



**University of  
Nottingham**

UK | CHINA | MALAYSIA

# **An Investigation Into Mass and Volume Reductions on Hydrogen-Electric Aircraft Propulsion Systems Using Biased Magnetics in an Interleaved DC-DC Buck Converter Topology**

Thesis submitted to the University of Nottingham for the degree of  
Doctor of Philosophy, March 2025.

**Bob Walmsley**

**20312449**

Supervised by

**Dr Christian Klumpner  
Dr Rishad Ahmed  
Dr Simon Hart  
Natalia Narozanska**

# Abstract

Hydrogen-electric aircraft offer the potential to support reductions in CO<sub>2</sub>, NO<sub>x</sub> and noise emissions, from the aviation sector. However, integrating fuel cells and batteries into aircraft propulsion systems introduces the requirement for additional onboard power electronic converters. Power electronic converters utilise semi-conductor switching devices, and energy storage components, such as capacitors and inductors. Currently, these passive components account for approximately 50% of the converter's packaged volume. Reducing their mass or increasing power density could lead to overall aircraft mass reduction and package size reduction; providing a compelling incentive to investigate techniques for improvement.

This research includes two primary objectives. The first objective was to develop a novel hydrogen-electric aircraft simulation tool, capable of optimising propulsion system parameters for a selected measure of merit. The tool, designed for preliminary or conceptual commuter aircraft specifications, enables hybridisation of power inputs for a mission analysis and trade studies. Specifically, it assesses the impact of different power converter technologies and drag polar models on overall aircraft mass. Results indicate that a simplified drag polar model led to an overestimation of aircraft mass by approximately 6.6%, when using baseline converter technologies. Additionally, increasing the converter technology level showed diminishing returns in mass reduction, but still achieved a 1.6% decrease in aircraft mass when baseline technologies were doubled. Furthermore, in-flight battery recharging resulted in a

0.89% increase in total aircraft mass.

The second objective focused on enhancing the performance of magnetic components within an interleaved buck converter topology. A novel approach was investigated, leveraging permanent magnets to provide simultaneous DC biasing for a pair of AMCC-100 inductor cores, and placing them into an interleaved converter. Experimental testing, using the University of Nottingham's Galvano Electrochemical Impedance Spectroscopy (GEIS) test equipment, demonstrated significant improvement in current handling capabilities, before saturation, ranging from 87% to 125%, depending on magnet quantity. The complete magnetic arrangement was subsequently validated through experimental implementation in an interleaved buck converter rig, confirming the positive impact of biased magnetics on converter performance.

Overall, this study contributes to the advancement of hydrogen-electric aircraft propulsion systems, by introducing a simulation framework for investigating aircraft mass and propulsion system configuration, and demonstrating novel technique to improve the power density of power electronic converters.

## Acknowledgements

I would like to begin by thanking my primary academic supervisors, associate professor Christian Klumpner, and associate professor Rishad Ahmed, who have kindly and compassionately provided me with all of the support and guidance over the course of my PhD project, and to who I owe a great debt of gratitude. Their advice, encouragement and patience has been invaluable to me, and for this I will always be grateful, and pay it forward where I can. I would also like to thank my industrial supervisors from the sponsoring company of this project, EVOLITO.Ltd, these being Dr Simon Hart, and Natalia Narozanska, who have guided the project from an industrial perspective, and likewise given me great advice, and supported me through to the end. To all of these people my thanks are endless, and any opportunities which arise due to completing a PhD degree, I owe to them.

I would also like to thank Kay Philips for supporting me with the day-to-day goings on, required to bring a PhD to fruition, including the assistance provided for the application an academic extension, the booking of conferences, and navigating the University's financial system, when I couldn't.

Thanks goes to the Engineering and Physical Research Council (EPSRC) for their financial support of this study, and to Professor Volker Pickert and Professor Patrick Wheeler for granting me a position on the Sustainable Electric Propulsion (SEP) CDT.

Thanks to all of my friends, colleagues and supporting technicians from the SEP-CDT, and the Power Electronics and Machine Control (PEMC) Research Institute, who have provided solid guidance and support, as well as lifting the mood on those bad days, and being all-round, great people. Associate professor Al Watson needs to be thanked for supporting me through the extension application process, and for his compassionate understanding of the circumstances. Abdullahi Abunakar needs a special thanks, for the immense amount of support he provided in getting the experimental rig working correctly.

A huge thanks goes to Dr Felix Finger and Dr Andres Revilla Aguilar, who have

kindly taken time from their busy schedules to assist me in understanding their respective research, which has supported this project greatly. Additionally, thanks to James Drummond of Mathworks, who has provided great guidance, with any issues encountered in MATLAB and SIMULINK.

My dear friends and family need considerable thanks, for their love and compassion, as well as financial support, while I have been taking on one of the biggest challenges of my life. I hope I can one day return the favour, and we can all enjoy the fruits of this labour.

Finally, I'd like to say a huge thank you to my partner, Alison, who has been an unbelievable source of support and inspiration, and for the constant reminders that I am capable of achieving a PhD. Thanks also to Brenda the cat for her generally uplifting spirit, and additionally, to Arlo the cat, for his company while writing this thesis.

## Research Contributions

From a tool functionality perspective, what are the clear and original contributions?  
What new knowledge has been generated, that it is not public knowledge?

The main research contributions of this thesis are as follows:

### **Development of a novel hydrogen-electric aircraft sizing methodology:**

This methodology enables the evaluation of hydrogen-electric aircraft mass sensitivity to the quality of modelling assumptions. Specifically, it demonstrates how the selection of aerodynamic model, with respects to a simplified or extended drag polar, in combination with input parameter fidelity, directly impacts the accuracy of the calculated Maximum Take-Off Mass (MTOM). This contribution advances the field by providing a structured methodology to asses modelling fidelity in early-stage hydrogen-electric aircraft conceptualisation.

### **Identification of mass-critical propulsion system components:**

Application of the novel sizing methodology has highlighted that away from the hydrogen storage, the most mass-sensitive subsystems are the DC-DC converters, particularly so, within the hydrogen branch of the propulsion system. This guides further research requirements for converter optimisation with regards to power density, and volumetric efficiency, yielding research priorities for future research on hydrogen-electric aircraft propulsion systems.

### **Development of a simplified fuel cell performance model optimised for cruise:**

A reduced order fuel cell model, without the requirements for detailed Nernst equations or explicit sizing of balance of plant equipment, enables rapid trade studies with the offering of cruise efficiency as a tunable input, in addition to tunable inputs for the fuel cells dynamic response for further trade studies. This contribution provides a model for use in methodologies where in depth fuel cell development is not a primary consideration.

### **Demonstration of the effects of fuel cell dynamic response modelling on**

**aircraft mass:**

A comparative study has shown that negating a fuel cell's dynamic response can yield sized aircraft with an underestimation on the final MTOM, at low hybridisation levels, relative to that of an aircraft which considers the fuel cell's response to changing power demands. This contribution highlights the importance of including the dynamic response models within the propulsion system modelling, to avoid and underestimation on the resulting aircraft masses, thereby improving the fidelity of hybrid-electric aircraft studies.

**Assessment of in-flight battery recharging as an operational mode:**

The methodology demonstrated that the introduction of in-flight battery recharging, during the cruise phase of the flight, increases aircraft MTOM by less than 1%, when compared to an aircraft not factoring in-flight recharge during cruise. This study has also shown the operational advantages of the in-flight recharge operational mode. This contribution provides new knowledge into the trade-offs between the mass penalties and options for operations flexibility for aircraft using hydrogen-electric propulsion systems.

**Critical evaluations of electromagnetic modelling tools:**

A comparative study of PLECS, for the closed loop converter simulation when considering biased magnetics, and ANSYS, for finite element analysis of magnetics has demonstrated the severe limitations of PLECS as an evaluation tool for biased inductors and specifically magnetic circuit modelling. This contribution sets out guidance on tool selection, and magnetics validation, for future work in magnetic component design, analysis and validation.

**Experimental validation of permanent magnet biased inductors:**

Original experimental data, based on the patented topology of [1], has shown positive improvements for the current handling capabilities under varying levels of magnetic bias. This work validates the use of permanent magnets to bias inductor cores for the potential improvements to inductor parameters, such as reduced turns count or core volume reduction, when designing inductors.

**Demonstration of improved converter performance through magnetic biasing of inductor cores:**

Original experimental work has confirmed that incorporating permanent magnet biased inductors into an interleaved converter configuration delays the onset of inductor saturation relative to that using non-biased inductors, thereby increasing the converter power density. This establishes a validity pathway for improving high-power converter design.

*”Everything is theoretically impossible,  
until it is done.”*

ROBERT A. HEINLEIN

# Contents

<b>Abstract</b>	<b>i</b>
<b>Acknowledgements</b>	<b>iii</b>
<b>Research Contributions</b>	<b>v</b>
<b>List of Figures</b>	<b>xii</b>
<b>Abbreviations</b>	<b>xvii</b>
<b>Chapter 1 Introduction</b>	<b>1</b>
1.1 Hydrogen-Electric Aircraft . . . . .	1
1.2 Fuel Cells in Aerospace . . . . .	4
1.3 Objectives of the Research . . . . .	9
1.4 Thesis Structure and Contents . . . . .	11
<b>Chapter 2 Literature Review</b>	<b>13</b>
2.1 Introduction . . . . .	13
2.2 Hydrogen-Electric Aircraft Technologies and Conceptual Design . .	14
2.3 DC-DC Converters . . . . .	47
2.4 Biased Magnetics . . . . .	56
2.5 Conclusion . . . . .	65
<b>Chapter 3 Hydrogen-Electric Aircraft Modelling</b>	<b>68</b>
3.1 Model Input Parameters and Methodology Navigation . . . . .	71
3.2 Top Level Aircraft Requirements and Aerodynamic Assumptions . .	83
3.3 Hydrogen-Electric Aircraft Constraint Diagram . . . . .	87
3.4 Aircraft Sizing . . . . .	95
3.5 Aircraft Structural Mass Determination . . . . .	118
3.6 Aerodynamic Adjustments . . . . .	130

3.7	Fuel Cell, Hydrogen Storage and Propulsion System Modelling . . .	137
3.8	Motor, Inverter, Converter and Power Distribution Mass . . . . .	156
3.9	Gearbox Mass . . . . .	156
3.10	Hydrogen-Electric Aircraft Study . . . . .	158
3.11	Hydrogen Aircraft Study Conclusion . . . . .	175
<b>Chapter 4</b>	<b>Multiphase - Interleaved Buck Converter</b>	<b>178</b>
4.1	Closed Loop Converter Modelling . . . . .	179
4.2	Buck Converter Parameters . . . . .	189
4.3	Inductor Design . . . . .	193
4.4	Standard Inductor Galvano Electrochemical Impedance Spectroscopy Testing . . . . .	205
4.5	Interleaved Buck Converter Inductor Simulations with Closed Loop Control . . . . .	214
<b>Chapter 5</b>	<b>Biased Magnetics For Interleaved Converters</b>	<b>222</b>
5.1	Biased Inductor Galvano Electrochemical Impedance Spectroscopy Testing . . . . .	226
<b>Chapter 6</b>	<b>Experimental Interleaved Buck Converter Hardware &amp; Supporting Equipment</b>	<b>237</b>
6.1	Support Equipment . . . . .	243
<b>Chapter 7</b>	<b>Experimental Results</b>	<b>248</b>
<b>Chapter 8</b>	<b>Conclusions and Future Work</b>	<b>260</b>
8.1	Main Contributions . . . . .	260
8.2	Future Work . . . . .	262
	<b>Bibliography</b>	<b>264</b>
	<b>Appendices</b>	<b>278</b>
<b>Appendix A</b>	<b>Part Power Tables for Honeywell TPE331-10</b>	<b>279</b>
<b>Appendix B</b>	<b>Dornier 228 Brochure Specifications</b>	<b>283</b>
<b>Appendix C</b>	<b>85kW Fuel Cell Time Response Fitting Plots</b>	<b>285</b>

Appendix D	Evolito D500 Data Sheet	288
Appendix E	AMCC METGLAS © Alloy 2605SA1 Core Material Properties	291
Appendix F	PLECS Closed Loop Simulation Results for MEC Inductor	293
Appendix G	Biased Inductor Galvano Electrochemical Impedance Spectroscopy Testing for Magnets within Inductor Airgap	300
Appendix H	Experimental Interleaved DC-DC Buck Converter Waveforms	302
Appendix I	Voltage Waveforms	323
Appendix J	Magnetising Current Waveforms	334

# List of Figures

1.1	Universal Hydrogen’s Turboprop Fuel Cell Retrofitted Concept . . .	2
1.2	Propulsion System Topology . . . . .	3
1.3	Bombardier Fuel Cell Based Emergency Power System Response with Time . . . . .	6
1.4	Bombardier Fuel Cell Based Emergency Power System Voltage with Time . . . . .	6
3.1	Methodology Flow Chart . . . . .	69
3.19	Methodology Flow Chart . . . . .	139
4.1	Interleaved Buck Converter Topology . . . . .	179
4.2	Interleaved Buck Converter Topology with 'n' Components . . . . .	180
4.3	Current Waveforms of the interleaved buck converter: a) Inductor one and two current imbalance. b) Inductor one and two current imbalance enhanced view. c) Combined converter output current. d) Converter output voltage with closed loop control . . . . .	182
4.4	Interleaved Buck Converter with Voltage PID Controller . . . . .	183
4.5	Interleaved Buck Converter with Voltage and Current PID Controllers	184
4.6	PSO’s place within the stochastic optimisation algorithms family tree	186
4.7	a) Inductor one and two currents balanced. b) Inductor one and two current balance enhanced view. c) Combined converter output current. d) Converter output voltage . . . . .	188

4.8	a) Inductor one and two currents balanced. b) Inductor one and two current balance enhanced view. c) Combined converter output current. d) Converter output voltage . . . . .	190
4.9	AMCC METGLAS © Alloy 2605SA1 General Core Dimensions . .	195
4.10	Inductor Core Cross-section and Window Area . . . . .	195
4.11	AMCC METGLAS © Alloy 2605SA1 Core Loss vs Flux Density .	202
4.12	Airgap and Inductance vs Number of Turns . . . . .	205
4.13	GEIS Inductor Current Input Waveform . . . . .	206
4.14	University of Nottingham’s Galvano Electrochemical Impedance Spectroscopy Equipment . . . . .	207
4.15	Experimental Inductor: Inductance vs Current at 100Hz . . . . .	208
4.16	Standard Inductor Value Percent Change with Current at 100Hz . .	210
4.17	Simple Buck Converter with Additional ESR . . . . .	212
4.18	Standard Inductor Inductance Values Across Multiple Frequencies .	213
4.19	a) Simple Inductor Diagram. b) Magnetic Equivalent Circuit for Inductor presented in a. . . . .	215
4.20	Single Inductor MEC Representation in PLECS Magnetics Blocks .	217
4.21	a) MEC Inductor Flux Density Waveform at converter Load of 2 Amps b) Output Voltage Waveform for Converter Load of 2 Amps	219
4.22	Single Inductor MEC Representation in PLECS Magnetics Blocks with Bias Winding . . . . .	221
4.23	Preliminary FEA Investigations a) Inductor Core with Winding. b) Inductor Core with Winding and Biasing Magnet . . . . .	221
5.1	Proposed Biased Inductor with Airgap Magnets, and Side Mounted Biasing Magnets . . . . .	223
5.2	Experimental Inductor: Bias scheme with ‘n’ magnets in series and parallel . . . . .	225
5.3	Experimental Biased Inductors: Inductance vs Current at 100Hz . .	226

5.4	Experimental Biased Inductors: Inductance Percent Difference Relative to Baseline Inductor at 100Hz . . . . .	227
6.1	Buck Converter Digital Signal Processing Board . . . . .	239
6.2	Buck Converter Gate Driver Board . . . . .	240
6.3	Buck Converter Sensor Board . . . . .	241
6.4	5 kW Power Supply Unit for the DC Bus . . . . .	243
6.5	Differential Voltage Probe . . . . .	244
6.6	Rogowski Coil . . . . .	245
6.7	YOKOGAWA DLM2024 . . . . .	246
6.8	Interleaved Buck Converter Programmable Load . . . . .	247
7.10	Rate of Change of Current ( $di/dt$ ) Across a Range of Inductor Currents (Amps/Second) . . . . .	258
F.1	a) MEC Inductor Flux Density Waveform at converter Load of 2 Amps b) Output Voltage Waveform for Converter Load of 2 Amps	293
F.2	a) MEC Inductor Flux Density Waveform at converter Load of 4 Amps b) Output Voltage Waveform for Converter Load of 4 Amps	294
F.3	a) MEC Inductor Flux Density Waveform at converter Load of 6 Amps b) Output Voltage Waveform for Converter Load of 6 Amps	294
F.4	a) MEC Inductor Flux Density Waveform at converter Load of 8 Amps b) Output Voltage Waveform for Converter Load of 8 Amps	295
F.5	a) MEC Inductor Flux Density Waveform at converter Load of 10 Amps b) Output Voltage Waveform for Converter Load of 10 Amps	295
F.6	a) MEC Inductor Flux Density Waveform at converter Load of 12 Amps b) Output Voltage Waveform for Converter Load of 12 Amps	296
F.7	a) MEC Inductor Flux Density Waveform at converter Load of 14 Amps b) Output Voltage Waveform for Converter Load of 14 Amps	296

F.8	a) MEC Inductor Flux Density Waveform at converter Load of 16 Amps	b) Output Voltage Waveform for Converter Load of 16 Amps	297
F.9	a) MEC Inductor Flux Density Waveform at converter Load of 18 Amps	b) Output Voltage Waveform for Converter Load of 18 Amps	297
F.10	a) MEC Inductor Flux Density Waveform at converter Load of 20 Amps	b) Output Voltage Waveform for Converter Load of 20 Amps	298
F.11	a) MEC Inductor Flux Density Waveform at converter Load of 22 Amps	b) Output Voltage Waveform for Converter Load of 22 Amps	298
F.12	a) MEC Inductor Flux Density Waveform at converter Load of 24 Amps	b) Output Voltage Waveform for Converter Load of 24 Amps	299

# Abbreviations

**AP** Area Product.

**BIF** Bias Improvement Factor.

**BoP** Balance of Plant.

**BSFC** Brake Specific Fuel Consumption.

**CAA** Civil Aviation Authority.

**CFD** computational fluid dynamics.

**DoD** Depth of Discharge.

**EASA** European Aviation Safety Agency.

**ESR** Equivalent Series Resistance.

**FAA** Federal Aviation Administration.

**GEIS** Galvano Electrochemical Impedance Spectroscopy.

**HHV** Higher Heating Value.

**HoP** Hybridisation of Power.

**IATA** International Air Transport Association.

**MAC** Mean Aerodynamic Chord.

**MEA** More Electric Aircraft.

**MEC** Magnetic Equivalent Circuit.

**MLT** Mean Length Per Turn.

**MMF** Magnetomotive Force.

**MTOM** Maximum Take Off Mass.

**OEM** Operational Empty Mass.

**PEMAD** Power and Energy Management and Distribution.

**PEMC** Power Electronics and Machine Control.

**PEMFC** Proton Exchange Membrane Fuel Cell.

**PMBI** Permanent Magnet Biased Inductors.

**PSO** Particle Swarm Optimisation.

**RANS** Reynolds Averaged Navier Stokes.

**RoC** Rate of Climb.

**SFC** Specific Fuel Consumption.

**SiC** Silicon Carbide.

**SoC** State of Charge.

**SUAVE** Stanford University Aerospace Vehicle Environment.

**TAS** True Air Speed.

**TLARs** Top Level Aircraft Requirements.

**TSFC** Thrust Specific Fuel Consumption.

---

# Chapter 1

## Introduction

### 1.1 Hydrogen-Electric Aircraft

Aviation has become an indispensable and pivotal part of contemporary society, shaping, and facilitating passenger travel and cargo transportation, as well as specialised missions for military operations, medical evacuations, fire-fighting, surveying, search and rescue, to name a few key roles.

Air-traffic density has doubled approximately every fifteen to twenty years [2] [3], making it one of the fastest growing sectors. The International Air Transport Association (IATA) expects 7.2 billion passengers to travel in the year 2035, which is a 90% increase, relative to the 3.8 billion who have flown in 2016 [4]. With the predicted expansion in the civil aviation sector to meet capacity needs, the environmental impact of such has come under great assiduity. Thus, aircraft manufacturers face ever tightening emission standards, and the requirement for aggressive technological advancements. Flightpath 2050 [5] outlines a number of overarching objectives, including, a reduction in CO<sub>2</sub> emissions by 75%, NO<sub>x</sub> emissions by 90% and noise emissions by 65% by 2050, with respects to flights in 2016, relative to the

capabilities of typical new aircraft in 2000.

Hydrogen-electric propulsion systems for aircraft have been identified as a potential technology to support the required reduction in emissions from the aviation sector [6]. To date there are no commercially available hydrogen-electric commuter aircraft available on the market; however, research efforts from the likes of ZeroAvia [7], with their ambitions to offer a hydrogen-electric powertrain, achieving 2-5MW, designed for 40-80 seat, CS-25 category aircraft, by 2027, are underway. A retrofitted Dornier 228, from the latter, has been used for a series of successful experimental flights. Similar efforts from Universal Hydrogen, with a higher capacity, retrofitted DeHavilland Dash-8 aircraft, have also yielded successful experimental flights; figure 1.1 shows the layout of the propulsion systems major components within the aircraft [8]. Table 1.1, from [9] provides a snapshot into additional aircraft which have been used to further the development of hydrogen fuelled aircraft, dating back to the 1950s; multiple examples use liquid hydrogen, ( $LH_2$ ), with turbo machinery while others utilise pressurised gaseous hydrogen, ( $GH_2$ ), in conjunction with fuel cell technology.

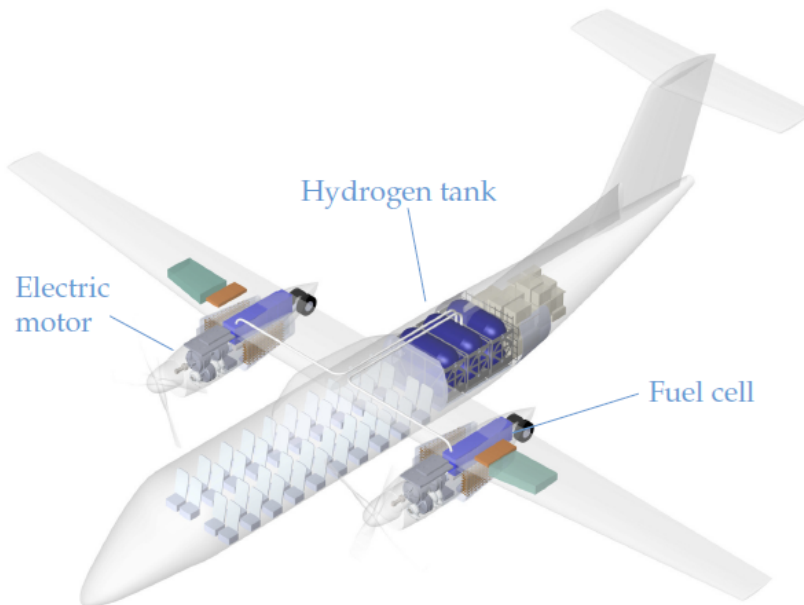


Figure 1.1: Universal Hydrogen's Turboprop Fuel Cell Retrofitted Concept

Table 1.1: Flown Hydrogen Fuelled Aircraft

Aircraft	First Flight	Storage	Propulsion	Notes
NACA-modified B57	1957	LH2	Turbojet	Single hydrogen-powered engine
Tupelov Tu-155	1988	LH2	Turbofan	Single hydrogen-powered engine
Boeing Fuel Cell Demonstrator Aircraft	2008	GH2	Proton Exchange Membrane Fuel Cell	Fuel cell powered cruise
Antares DLR-H2	2009	GH2, 350 bar	33kW fuel cell	
AeroVironent Global Observer	2011	LH2		
Boeing Phantom Eye	2012	LH2	Modified Ford 2.3L ICE	
H2FLY HY4	2016	GH2	45kW Proton Exchange Membrane Fuel Cell	
ZeroAvia Piper Malibu Demonstrator	2020	GH2, 350 bar	Fuel Cell	Partially fuel cell powered
ZeroAvia Dornier 228 Demonstrator	2023	GH2		Batteries and fuel cell each powering half of port side
Universal Hydrogen Dash-8 Demonstrator	2023	GH2	Megawatt-class Proton Exchange Membrane Fuel Cell	Single hydrogen-powered engine

A hydrogen-electric aircraft propulsion system, using a Proton Exchange Membrane Fuel Cell (PEMFC) and gaseous hydrogen, ( $\text{GH}_2$ ), is comprised of a number of fundamental components, namely, gear box, motor, inverter, fuel cell DC-DC boost converter, battery DC-DC boost converter, battery, fuel cell and hydrogen storage; a simple example of such a system is available as per figure 1.2. The quantities of each of these components will vary, depending on aircraft, configuration and certification requirements.

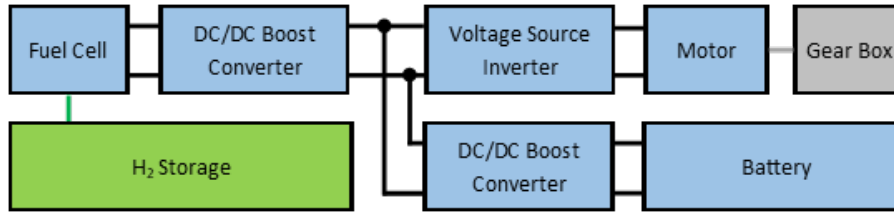


Figure 1.2: Propulsion System Topology

The battery within the fuel cell propulsion architecture is used to handle transients brought about by fluctuating power demand, and rapid changes in throttle setting. However, in certain applications it is also used to supplement the fuel cell's power at different stages throughout the flight [9][10].

## 1.2 Fuel Cells in Aerospace

Fuel cell technology exists in numerous forms, and have seen use in applications such as transportation, stationary power plants, marine power systems and also in aerospace applications [11][12][13]. Proton Exchange Membrane Fuel Cell (PEMFC) technology, which converts chemical energy into electrical energy, has garnered great interest due to their offering of high energy conversion efficiency, rapid start-up, limited sensitivity to orientation, and of most importance, high power density, relative to batteries, and this is a particularly attractive benefit for aerospace, where mass is one of the most dominant factors when designing an aircraft to be commercially competitive [14] [15].

PEMFC are not without their drawbacks. One of these is the fuel cell response rate, which is both an intrinsic property of the technology, and compounded by the balance of plant equipment, which is the term given to the required supporting ancillaries necessary to make the fuel cell stack operate, such as air-compressors, thermal management equipment and humidifiers. This can translate into an inability for the fuel cell to provide the required power demand during transients [16]. Souleman et al. models and simulates this scenario, with a fuel cell based emergency power system in a More Electric Aircraft (MEA), based on fuel cells, lithium-ion batteries and super-capacitors, using MATLAB and SIMULINK [10]. A representative emergency flight profile of a Bombardier aircraft is used for this simulation, and the supporting system utilises the following:

- 12.5 kW (peak), 30-60V PEMFC, with nominal power of 10 kW.
- 48V, 40 Ah, Li-ion battery system.
- 291.6V, 15.6 F, supercapacitor system (six 48.6V cells in series)
- 12.5 kW fuel cell DC-DC boost converter, with regulated output voltage and

input current limitation.

- Two DC-DC converters for discharging (4 kW boost converter) and charging (1.2 kW buck converter) the battery system. These converters are also output voltage regulated with current limitation. A single bidirectional DC-DC converter can also be used to reduce the weight of the power system.
- 15 kVA, 270V DC in, 200V AC, 400 Hz inverter system.
- 3 phase AC load with variable apparent power and power factor, to emulate the MEA emergency load profile.
- 15 kW protecting resistor to avoid overcharging the super-capacitor and battery systems.

With an understanding of the system's major components, the following scenario describes an emergency landing scenario from 0 seconds to a complete landing and disembarkation at 330 seconds, including the system's response in time to varying loads, while attempting to maintain a DC bus voltage of 270V. The reader can follow the events using figure 1.3, which shows the fuel cell's response (blue line) to the load change (yellow line), and in addition figure As can also be observed in figure 1.4 can be used to track the voltage of the 270V DC bus, as the emergency scenario plays out. Prior to an in depth breakdown of the events, it can be clearly observed that the fuel cell lags considerably behind the load change. In response to this lag, additional power is provided by both the super-capacitor (green line), and batteries (orange line). As a brief generalisation of the plots, the super-capacitor's response time is less than the battery's response time, but its charge is limited, and as the charge is diminished, the battery's power input to the DC bus increases.

- At 0 Seconds: All main generators are operational and providing the necessary loads for the aircraft. The fuel cell hybrid power system is turned on in

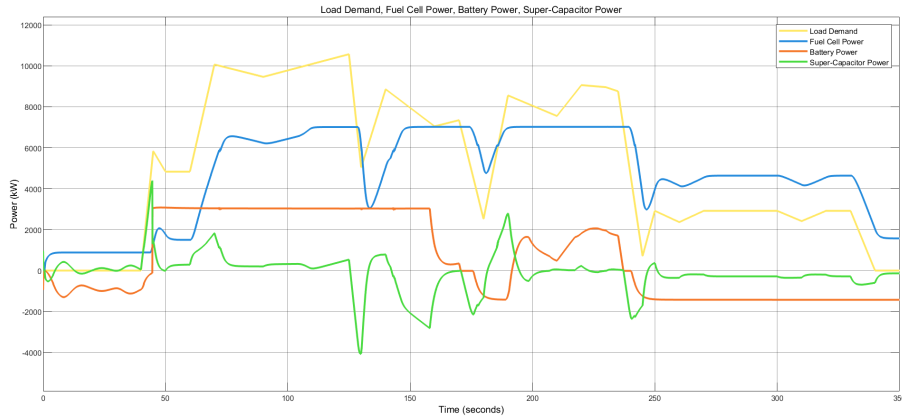


Figure 1.3: Bombardier Fuel Cell Based Emergency Power System Response with Time

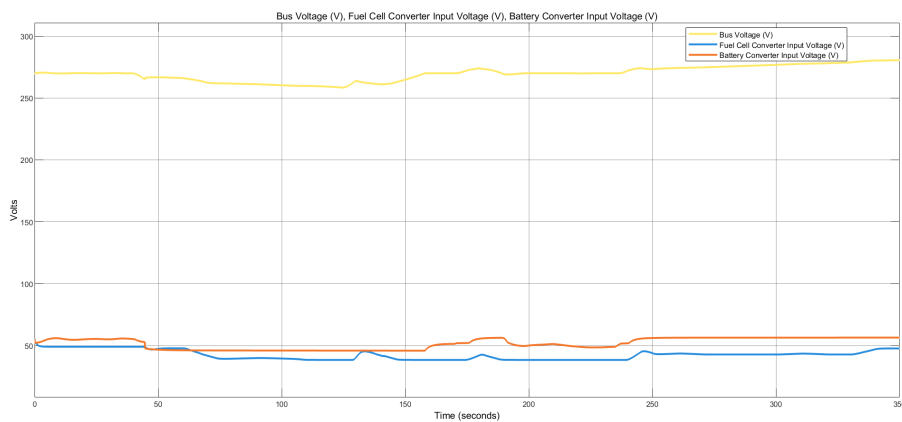


Figure 1.4: Bombardier Fuel Cell Based Emergency Power System Voltage with Time

perpetration for landing, and on standby for an emergency landing scenario. Figure 1.3, shows the blue line of the fuel cell power, slowly ramping up.

- At 5 Seconds: The fuel cell operates at an optimal power ( 1kW), to begin recharging the onboard battery, while the supercapacitor supports the regulation of the 270V DC bus.
- At 40 Seconds: An emergency onboard sees the the loss of all generators. The fuel cell hybrid power system is now employed to provide power to all essential loads. The supercapacitor rapid dynamics allow it to instantaneously provide the extra power to the system, while the fuel cell power gradually ramps up, due to its slower dynamics.

- At 45 Seconds: The supercapacitor is discharged to a point below the required 270V for the DC bus, and the battery steps up to provide power, and regulate the bus voltage back to the nominal 270V.
- At 60 Seconds: An emergency hydraulic pump is started, which causes the supercapacitor to provide the extra transient load power, and once again the fuel cell power slowly increases to support the demand.
- At 61.5 Seconds: The battery supports the regulation of the DC bus voltage to 270V, and simultaneously supports the fuel cell, by providing any additional power which the load requires.
- At 70 Seconds: The fuel cell has reached its maximum power output, which is governed by the DC-DC converter input voltage range; additional power to the load is provided by the battery.
- At 125 Seconds: The load power reduces to a value below the fuel cells maximum power output, and due to the fuel cell's slow dynamics, the extra power it provides during the transients is used to charge the supercapacitor.
- At 130 Seconds: A secondary emergency hydraulic pump is turned on, and the fuel cell hybrid power system displays a similar behavior to that of the first pump switch on, with the supercapacitor supporting the additional transient power.
- At 170 Seconds: The load power reduces below the fuel cell's maximum power, and the transient energy is transferred into both the supercapacitor and the battery.
- At 180 Seconds: Once again, the aircraft's power demand increases; this time due to the actuation of the flaps / slats and landing gear. The supercapacitor responds to this while the fuel cell and battery begin to ramp up their input.

- At 185 Seconds: The battery discharges to regulate the DC bus voltage, and continues to support the fuel cell with the extra load power.
- At 235 Seconds: The aircraft successfully touches down, and the power demand decreases significantly. The extra power from the fuel cell's slow response time is siphoned into the supercapacitor and battery.
- At 250 Seconds: As the aircraft is taxiing, the fuel cell provides the full load power required.
- At 330 Seconds: The aircraft is evacuated, and the load power reduces to zero, while the fuel cell continues to recharge the battery, as it ramps down to its optimal power level.

All of this together, forms a hybrid power generation system, ensuring that the load is supplied with the necessary power; this also supports the decisions from ZeroAvia to use batteries in conjunction to a PEMFC to supply the required power to the load. However, the percentage power split of battery power to hydrogen fuel cell power is not reliably reported. As such, an initial investigation will be required to determine the optimal power split, and the flight phases in which the power split is to be adopted, in a bid to yield the most mass efficient aircraft. The splitting of power between a number of energy sources to maintain a common DC bus voltage is also explored in [17] and [18].

As can also be observed in figure 1.4, the fuel cell's voltage output is less than 60V, where as the nominal bus voltage is 270V DC, with a minimum value of 258.4V, -4.3% off nominal, and maximum a of 280.5V, +3.8% off nominal. The plot shows that the bus voltage is not particularly well controlled, and is somewhat wayward when it comes to rigidly maintaining the required 270V DC, required on the bus; One possible cause of this relates to the controller itself, as this was not fully explored during the simulation. It is not uncommon for fuel cell based systems to

have a lower fuel cell output voltage, relative to load or bus voltages, and hence the necessity for the DC-DC boost converter, which is required to step up the voltage. It stands to reason that the power split between battery and fuel cell, and the fuel cell response time will have an influence on the mass and volume of the respective DC-DC converters. Aircraft are supremely sensitive to mass, and the take off mass drives cost, energy efficiency, and emissions, and as such the lightest aircraft will prevail [19]. Therefore efforts are required to reduce the mass and volume of the components within these devices to further support the mass and efficiency benefits brought about by the optimal power split.

### 1.3 Objectives of the Research

Based on the above introduction, a number of research objectives have been outlined to support the research efforts for future hydrogen-electric aircraft. A number of focuses are required for this project, the first being an investigation into the optimal power split between fuel cell and battery power systems, to yield the aircraft with the lowest mass, and the second part of this study, based on the optimised power split, is an investigation into further aircraft mass reductions, through mass and volume reduction of the DC-DC converter's most heavy and voluminous components.

This research project is aimed at developing a tool, with the capability of determining the optimal power split between battery power, and fuel cell power, in order to realise an aircraft with the lowest Maximum Take Off Mass (MTOM), whilst simultaneously identifying areas of the propulsion system which have the greatest mass sensitivity, and compounding mass increasing factors. Additional studies aim at investigating the effects of the parameter input quality into the simulation tool, on final aircraft mass, as well as different operational modes for the mission analysis,

pertaining to in-flight battery recharging.

Based on the results of the optimisation study, methods will be investigated to support a reduction for the mass and volume of the passive components within the DC-DC converter devices.

The work done as part of this research project and described in this document seeks to achieve the following objectives:

- To propose a novel hydrogen-electric aircraft sizing tool, capable of determining optimised propulsion system parameters for a selected measure of merit (MoM), based on preliminary or conceptual commuter aircraft specifications, and hybridisation of power, as inputs into a mission analysis.
- Perform trade studies for the assessment of the impact of various power converter technology levels, and various drag polars, on overall aircraft mass, in addition to investigating different operational strategies for the mission analysis, with regards to in-flight recharging.
- Parameterisation and development of an interleaved buck converter model, complete with voltage and current closed loop control for the simulation of the converter when considering the use of inductors modelled as Magnetic Equivalent Circuit (MEC).
- Correctly size and design an inductor capable of fulfilling the requirements of the parameterised interleaved buck converter, before testing the inductor to ascertain baseline values for saturation, when subject to Galvano Electrochemical Impedance Spectroscopy (GEIS) experimental validation.
- Investigate improvements into the performance of magnetics, when under the consideration of permanent magnet biasing, and compare these results against a baseline inductor, using the same GEIS experimental validation techniques

as for the baseline inductor. The results are used to determine any theoretical geometry alterations to support mass and volume reduction of the magnetics.

- Experimentally validate the proposed novel combination of Permanent Magnet Biased Inductors (PMBI) topology within an interleaved buck converter and ascertain any benefits.

## 1.4 Thesis Structure and Contents

An outline of the thesis structure is presented below, and summarises the strategies employed to satisfy the objectives presented in section 1.3.

- Chapter 2 - Provides a comprehensive literature review, considering hydrogen-electric aircraft and their conceptual design, including descriptions of battery, fuel cell, and hydrogen storage technology. Additionally a general overview of DC-DC converter technology, and any supporting background for improvements to DC-DC Converter technology is provided. Finally, the theory of biased magnetics are introduced to complete the most pertinent areas of interest for this project.
- Chapter 3 - Discusses the proposed modelling methodology for the hydrogen-electric aircraft, including initial sizing constraints diagrams, for complex and simple drag polars. A methodology, bespoke to hydrogen-electric aircraft, for structural mass determination, using legacy sizing methodologies is discussed, in addition to new methods for modelling hydrogen fuel cells for conceptual aircraft design. A number of test cases are simulated, pertaining to aircraft mass, for sweeps in converter technology, aircraft mass for drag polar fidelity, and finally aircraft mass using in-flight battery recharging.
- Chapter 4 - Presents the modelling on an interleaved buck converter, with

a brief discussion of particle swarm optimisation control parameter determination, for voltage and current balance control. The paramaterisation of the converter is discussed, as well as the sizing and design of an experimental inductor to suit the converter. Galvano Electrochemical Impedance Spectroscopy (GEIS) testing is undertaken on the experimental inductor, to provide a pre-bias baseline, which will be compared to an equivalent biased inductor. The PLECS simulation tool is used to simulate the closed loop control of the converter, with the baseline inductor represented as a Magnetic Equivalent Circuit (MEC).

- Chapter 5 - Introduces the Permanent Magnet Biased Inductors (PMBI) which will be used for experimental validation in the interleaved buck converter. Initial testing using various quantities of permanent magnets to form a bias flux in the core, is undertaken using the same GEIS from the testing of the baseline inductor. The results of the tests are compared to that of the baseline inductor, and any inferences to theoretical reductions in inductor mass and volume are made.
- Chapter 6 - The experimental hardware for the interleaved buck converter and supporting equipment used to perform the testing is discussed in this section.
- Chapter 7 - The results of the experimental work undertaken on the interleaved DC-DC buck converter rig, to validate any potential benefits of using biased magnetics within this specific topology are discussedCC, and final conclusions about the benefits of biasing inductors is drawn here.
- Chapter 8 - Concludes the work undertaken in this project, in addition to highlighting the main and novel contributions of the work undertaken. Suggestions are included in this section for future work.

---

# Chapter 2

## Literature Review

### 2.1 Introduction

Based on the initial introduction section, and the research objectives, it is clear that this is a multi-domain, multi-physics research project, touching on the disciplines of magnetic, electrical, thermal, chemical and aerospace sciences. As such, a comprehensive literature review aims to capture the essence of the necessary past, current and future technologies or methodologies required, to support the research goals. A series of discussions will follow, which touch upon the the propulsion system elements highlighted in figure 1.2, when also considered within the context of the overarching methodologies associated with hydrogen-electric aircraft propulsion system design and modelling.

## 2.2 Hydrogen-Electric Aircraft Technologies and Conceptual Design

As previously stated, the objective of this research is not to design a new or novel aircraft, but rather, explore the sizing and optimisation for specific elements and operating scenarios of a hydrogen-electric propulsion system. However, in order to arrive at a viable conclusion, it is entirely necessary to frame a conceptual aircraft propulsion system within realistic aircraft performance values. Erroneous predictions for aerodynamics and weight will manifest in an aircraft which does not meet the Top Level Aircraft Requirements (TLARs), when built, or from a research perspective, will not reflect the results of experimental validation [20]. In order to mitigate methodology risk, and increase the scientific accuracy of the novel branches of this research, an assessment of aircraft conceptual design strategies, and their associated technology is essential, such that the development of an appropriate system model is possible, and yields accurate results for system components, whose performance and operation can be authenticated via experimental analysis.

The sizing of the aircraft is a fundamental process of any aircraft design programme, and this takes place during the conceptual design phase [20] [19]. This important phase allows the determination of the aircraft's dimensions, MTOM, required thrust,  $T$ , power, and wing area,  $S$ . This information feeds into what will become a mission analysis, where the performance of the aircraft can be determined during the entirety of the mission profile.

### 2.2.1 Battery Technology

As a starting point for the the discussion of the propulsion system's major components, batteries are considered first. It is important to understand the common

terms which are used when addressing or defining battery technology; a concise, yet detailed description of these terms is provided in the list presented below, as taken directly from [21]. Here, details of the fundamental parameters pertaining to batteries, and their units of measure, symbols, and description for each are provided.

- **Stored Capacity**, denoted by the symbol, **Q**, and given in unit of Amp hours, **Ah**. This describes the amount of charge which is transferred by a flowing current, over a given time. As it is defined as Ampere supplied for one hour, a higher capacity battery, will provide a longer run-time for a given discharge current, or alternatively, it has the ability to yield a higher current over a given discharge time.
- **Stored Energy**, denoted by the symbol, **E**, and given in unit of Watt hours, **Wh**. This represents the amount of energy which is supplied, by combining voltage and current, or power for a given time, as per the below equations:

$$Power = Current \cdot Voltage$$

$$Energy = Current \cdot Voltage \cdot Time$$

$$Energy = Capacity \cdot Voltage$$

- **Specific Energy**, denoted by the symbol, **E\***, and given in unit of Watt hours per kilogram, **Wh/kg**. This is the amount of electrical energy stored per unit of battery mass. The higher the value of the specific energy for a battery, the lighter the battery is for a given amount of energy. The specific energy is also referred to as the energy density.
- **Specific Power**, denoted by the symbol, **P\***, and given in unit of Watts per kilogram, **W/kg**. Akin to the specific energy, is the amount of power which can be drawn, per unit of battery mass. The higher the specific power of the battery the lighter the battery is for a given power requirement.

- **Discharge C-Rating**, denoted by the symbol,  $C_{\text{discharge}}$ , and given in unit of per hour,  $1/\text{h}$ . This is the maximum current that can be drawn from the battery, given by:

$$C_{\text{discharge,rating}} = \frac{P^*}{E^*}$$

$$C_{\text{discharge,rating}} = Q \cdot C_{\text{discharge,rating}}$$

It is also possible for the discharge C-rating to give information about the time in which it will take to be discharged. At a discharge rate of 1C, the battery is depleted within 1 hour, and at 2C this would reduce to 0.5 hours, and at 3C, this would reduce further to 0.33 hours. It therefore stands to reason that at 10C a fully charged battery would in fact be depleted within 6 minutes. Discharging the battery at rates greater than those recommended by the data sheets, has the potential of causing battery degradation or total destruction due to the heat that it would encounter.

- **Charge C-Rating**, denoted by the symbol,  $C_{\text{charge}}$ , and given in unit of per hour,  $1/\text{h}$ . This is the maximum current which can be used to charge the battery, given by:

$$Current_{\text{max,charge}} = Q \cdot C_{\text{charge,rating}}$$

Similarly to the discharge C-rating, the charge C-rating provides useful information about the time in which the battery can be charged. For a C-rating of 1C, the battery can be charged within one hour, and for a 2C charge rate this is improved to 0.5 hours, and likewise at a C-rate of 3C, this is reduced further to 0.33 hours. Generally, the charging C-rate is lower than that of the discharge C-rate, and charging at C-rates above the recommended values, has the potential to overheat, and destroy the battery.

- **State of Charge**, generally abbreviated to **SoC**, and given as a percentage. The SoC pertains to the ratio of the remaining battery capacity, to its nominal capacity. At a SoC of 100%, the battery is considered "full", and when this SoC is at 50%, it is reasoned to be "half-full". It is necessary to employ measures to prevent battery degradation, and one means of supporting this, is to prevent the battery from discharging below an industry standard 20% SoC. Without any form of deep discharge protection, the battery is exposed to internal damage, and/or the cycle life will be greatly reduced. As an alternative to the SoC, a parameter referred to as the Depth of Discharge (DoD) is utilised. The DoD is calculated as  $1 - \text{SoC}$ .

As already discussed, the only hydrogen fuelled aircraft that have flown to date, are experimental concepts, and not yet available for airlines to purchase. That being said, a number of all-electric aircraft are available on the market, as of the time of writing this report, and as such provide a suitable jumping off point for an assessment of the current battery technology available and used to power the propulsion system of all-electric aircraft. Figure 2.1 shows the major components which constitute the propulsion system for an aircraft with an all electric architecture.



Figure 2.1: All-Electric Aircraft Propulsion Systems

Off the shelf Li-Ion Samsung INR18650-30Q cells, have seen use in NASA's cancelled, modified Tecnam, X-57 all-electric aircraft project [22]. These cells are promoted to have a capacity of 3Ah, and a rated discharge of 10A, yielding a C-rating of approximately 3.3. This particular cell technology benefits from a specific energy of approximately 240 Wh/kg, and when considering a one third reduction due to pack overheads, such as casing, sensing and cooling, this would decrease to a value of approximately 160 Wh/kg. The commercially available, flight certified,

pilot trainer, Velis Electro from Pipistel aircraft [23], offers a total nominal capacity, split between two units, of 20 kW/h, at 345V, this is coupled to a propulsion system with a maximum take off power of 57.6 kW, which corresponds to a 2.88 C-rating, not too dissimilar to the NASA Maxwell aircraft. Based on the provided cruise power of 35kW, this gives the aircraft an airborne time of approximately 35 minutes (neglecting energy used for take-off), which is suitable for pilot training needs, where a number of circuits are completed before a debrief, while the aircraft recharges. The Rolls-Royce ACCEL project, aimed at achieving the worlds fastest electric aircraft, developed the Spirit-of-Innovation [24], a modified Sharp Nemesis NXT race aircraft, equipped with an all electric propulsion system, of which the main components, the triple stacked 200kW axial flux motors, and 750V, 216kWh battery, were developed by EVOLITO and Electroflight respectively; the sponsors of this project. This aircraft is designed to have a continuous power of 375kW and in combination with the 216kWh battery, results in a C-rate of approximately 1.74 and 35 minutes flight time, although at a peak power demand of 750kW, this translates into a C-rate of approximately 3.5, aligning well with the current battery technology used within the previously mentioned aircraft. To provide more of a perspective on the landscape of specific power and energy for batteries, relative to their specific chemistry, a Ragone plot, from [25], featuring relatively recent specific energy, and specific power values, used for cells in automotive applications, is presented in figure 2.2. This plot, also features the super capacitor, which is a technology that holds its place somewhere between a traditional capacitor and a battery, [26], and has been shown previously in the Bombardier fuel cell based emergency power system. Super capacitors have a supremely high power density, at the expense of having the lowest specific energy, relative to the other energy storage technologies. As previously observed, they have the ability to offer rapid discharging and charging, storing the energy electrostatically.

A common theme amongst the aircraft already discussed, is that they are either

## 2.2. HYDROGEN-ELECTRIC AIRCRAFT TECHNOLOGIES AND CONCEPTUAL DESIGN

---

small single, to 4 seat aircraft, designed for short training sessions, racing aircraft designed to compete in races which are a few minutes in length, or experimental aircraft with the intended purpose of proving an increasing technology readiness level. However, during the course of this project, a number of start-up aircraft developers have proposed considerably larger all-electric or hybrid-electric aircraft.

Elysian aircraft [27], started in 2021, propose an all-electric, 90 seat aircraft, with a range of 800km, but to date have no tangible products, and limited information about the powertrain is available; specifically information regarding the batteries, which would power the worlds largest all electric-aircraft, if the production stage is entered. A considerably more successful start-up, who are scheduled to have their maiden-flight in the second quarter of 2025, for a hybrid-electric aircraft, which will utilise batteries, and a range extending generator, placed in parallel, and connected across four motors, has been developed by Hart Aerospace [28]. This aircraft offers a more modest, 30 seats, with a proposed all electric range of 200km and hybrid range of 400km, with improvements expected in conjunction with increases in technology levels. Again, information regarding the battery technology has not been disclosed.

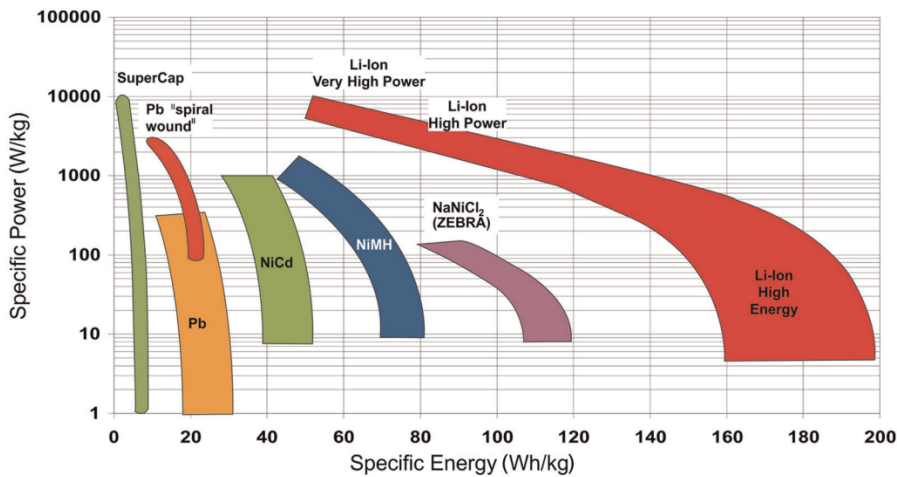


Figure 2.2: Ragone plot of various battery technologies with specification at cell level for automotive applications (Cell Level) [25]

Currently, available battery technology offers specific energies of approximately 200 Wh/kg at pack level. It is required that batteries with 400-500 Wh/kg at pack

## 2.2. HYDROGEN-ELECTRIC AIRCRAFT TECHNOLOGIES AND CONCEPTUAL DESIGN

level, which is more than double of the battery technologies at the time of writing, will be required to fully support the use of electric propulsion systems for all electric aircraft, and to see improvements in hybrid aircraft, such as Hart Aerospace’s ES-30 aircraft. The near term battery technology will be used in this study.

Batteries are generally modelled as a discharge curve, such as that given in figure 2.3 developed by [29]. As can be observed, batteries don’t discharge linearly across their full capacity range. A number of numerical models exist to handle this, such as that from [30]. However, these models imply that voltage and current maybe an input into the system, and as such corresponding models for motors which accept the output voltage are also required; these could be set up as look-up-tables.

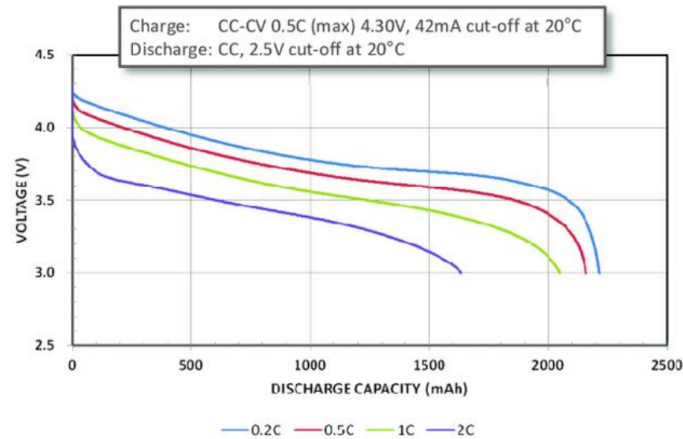


Figure 2.3: Representative Discharge Curves for Panasonic Batteries) [29]

The work of [31] presents a worked methodology for a composite, single seat, low wing, non-aerobatic recreational battery powered aircraft, with the intent of exploring a suitable battery powered powertrain and assessing its feasibility. The inputs into the analysis include the aircraft’s geometry, details regarding the powerplant, the aircraft’s weight, and it’s all important drag polar. The drag polar, amongst other details which pertain the the aircraft’s geometry will be dealt with later in this thesis, however, it is given as  $0.02+0.0526 \cdot CL^2$ , where  $CL$  is the coefficient of lift. The take-away point from this example being how the all electric powertrain is sized, particularity focusing on the details surrounding the battery, in addition to

2.2. HYDROGEN-ELECTRIC AIRCRAFT TECHNOLOGIES AND  
CONCEPTUAL DESIGN

---

Table 2.1: All-Electric Aircraft Design Example Input Parameters [31]

Parameter	Value	Parameter	Value
Take off mass (kg)	450	Propeller diameter (m)	1.524
Wing area (m <sup>2</sup> )	9.3	Wing span (m)	8.14
Wing taper ratio	0.5	Flight deck max. width (m)	1
Mean aerodynamic chord (m)	1.14	Aspect ratio	7.12
'g' load	+4 to -2	Battery Voltage (V)	300
Battery mass (kg)	100	Pilot mass (kg)	80
Motor mass (kg)	40	Structural mass (kg)	230
Power loading (kW/kg)	0.133	Max. cruise altitude (ft)	10000
Max. speed (kt)	100	Sortie duration (h)	1

providing the author with a flavour of the additional details which are required to size an aircraft with a novel propulsion system. The aircraft's inputs are detailed in table 2.1.

In the example provided by [31], the parameters from table table 2.1 are used to resize the battery, and determine the new battery mass  $m_{bat}$ , using equation 2.2.1, when the maximum power from the motor at take off is expected to be 60kW.

$$m_{bat} = \frac{R \cdot W \cdot D}{0.9\eta \cdot E^* \cdot L}$$

Where:

R = Range

W = Aircraft Weight

D = Aircraft Drag

$\eta$  = Propulsion system efficiency

L = Aircraft Lift

Although the equation is somewhat limited, due to its lack of accounting towards energy for take off, and any diversion, or loiter phases, of particular note, is the use of the specific energy of the battery (given as 200 Wh/kg) to size the aircraft's

battery, rather than implementing a model with a discharge curve. The use of the specific energy battery model in combination with maximum discharge (c) rates is also adopted by [21], and [32]. This is referred to as the "energy in a box" method of battery modelling, and lends itself well to conceptual aircraft design, where the adoption of a battery discharge curve would add an additional level of complexity, and would have the potential to increase simulation times. Additionally, the ability to use only a small number of inputs into the battery model, opens up additional research questions, as regards to how the specific energy and discharge rates of future battery technology, influences aircraft mass, and airline operations.

### 2.2.2 Hydrogen Storage

The literature has also highlighted a number of important factors which pertain specifically to hydrogen fuelled aircraft under design consideration; one of the major considerations being the issue surrounding hydrogen storage. Dependent upon the hydrogen to be carried onboard the aircraft, either GH<sub>2</sub> or LH<sub>2</sub>, and the hydrogen storage conditions, determines the storage requirements. Hydrogen, in its gaseous form, has a particularity low volumetric energy density, when under the conditions of ambient temperature and pressure; Unlike traditional aviation fuels, and hence the requirement for GH<sub>2</sub> compression, to achieve reasonable energy densities. Various fuel states observed in experimental aircraft were provided in table 1.1, and table 2.2 provides the properties of hydrogen across both liquid and compressed gaseous states at various pressures, with the properties of the commonly used Jet A-1 fuel, used for comparison [9] [31]. This table also demonstrates and supports the disparity between the energy storage of fossil fuels, hydrogen, and batteries, and highlights, that although hydrogen propulsion systems maybe more involved and complex than pure battery-electric aircraft, the benefits of additional energy storage for lower mass is advantageous.

2.2. HYDROGEN-ELECTRIC AIRCRAFT TECHNOLOGIES AND  
CONCEPTUAL DESIGN

---

Table 2.2: Properties of Available Fuels Used for Aerospace Propulsion

Metric	Jet A-1	LH <sub>2</sub>	GH <sub>2</sub> (350 bar)	GH <sub>2</sub> (700 bar)
Specific Energy (MJ/kg)	43.2	120	120	120
Energy Density (MJ/L)	34.9	8.5	2.9	4.8
Storage Temperature (K)	Ambient	20	Ambient	Ambient
Storage Pressure (bar)	Ambient	$\approx 2$	350	700

As table 2.2 shows, the specific energy of hydrogen per kilogram, is approximately three times greater than that of the traditional aviation fuel, however, achieving a stored kilogram of hydrogen is an additional concern. When looking at the energy density in regard to  $MJ/L$ , it is clear to see that at ambient temperature and pressure the Jet A-1 far out classes the energy densities of the hydrogen, by approximately twelve times for hydrogen compressed to 350 bar, and approximately seven times for hydrogen compressed to 700 bar. Even the most competitive storage state for hydrogen, liquid, is only one quarter as efficient in terms of energy density.

In regards to modelling the hydrogen storage, within the aircraft sizing, a number of methods are provided in literature. The first methodology, provided by [9], describes the 'hydrogen tank gravimetric efficiency' model; this is given by equation 2.1.

$$\eta_{tank} = \frac{W_{H_2}}{W_{H_2} + W_{tank}} \quad (2.1)$$

Where  $W_{H_2}$  is the weight of hydrogen that the tank is designed to hold,  $W_{tank}$  is the empty weight of the tank, and  $\eta_{tank}$  is the tank storage efficiency. Based on this, it is possible to use values of tank efficiency taken from literature, in combination with hydrogen mass and volume values taken from the aircraft sizing methodology, to rapidly determine the mass of the tank which fulfills the storage requirements.

The works of [33] present a different method for calculating the mass of the storage requirements for the aircraft. This method uses the ideal gas law to determine the volume of hydrogen and relates this to the geometry of a cylindrical tank with

hemispherical caps; the tank thickness is then determined, and a material density used to determine the mass of the tank. The works of [34] presents research for the energy efficiency of onboard hydrogen storage, with cryogenically cooled liquid hydrogen, stored within thermal tanks, offering the greatest efficiency, when compared to gaseous hydrogen storage efficiency.

### 2.2.3 Fuel Cells

Fundamentally, a fuel cell is a device capable of generating electrical power, directly from a continually flowing source of hydrogen or a hydrogen containing fuel, in combination with a continually flowing supply of oxygen, and the electrical power is generated via an electrochemical process [35]. This electrochemical process is in essence the reverse of electrolysis, and will be described in the proceeding text, with the aid of figure 2.4 from [29]. In order to understand how electrical power, or more specifically electrical current is generated as a function of the reaction between hydrogen and oxygen, it is necessary to consider the reaction that takes place at the anode and cathode. Considering a fuel cell of the acid electrolyte type, it can be stated that at the anode, hydrogen is oxidised, resulting in the release of electrons, and the generation of  $H^+$  ions (protons), as expressed by equation 2.2. In parallel to the anode and cathode, is a circuit which is external to the fuel cell, and this could represent a motor, converter, or some other electrical element of the propulsion system. The electrons ( $e^-$ ) flow as a current around this external circuit, and reconvene at the cathode side of the cell, once their useful work is done. At this stage, the air flowing across the cathode, supplies oxygen which combines with the electrons and the  $H^+$  ions that have diffused through the cell's membrane (electrolyte), to form water, and as a byproduct of the reaction, heat is generated; and this will have to be regulated using additional equipment. The reaction is given by equation 2.3

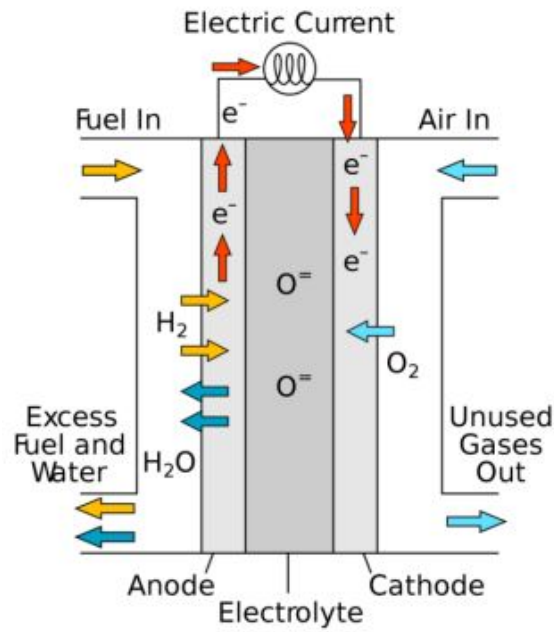
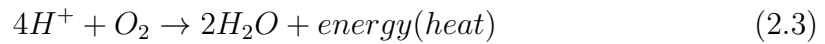


Figure 2.4: Single Fuel Cell Operation



Any additional water produced by the cell is removed, to prevent cell performance degradation due to flooding, and any unused or unreacted gasses are vented out of the system. The continual flowing of gasses through the cell produces an output 'open cell' voltage of less than 1 Volt, and has a thermodynamic limitation on the maximum voltage it can produce, per area of cell; this can be observed in the polarisation curve of figure 2.5, taken directly from [35].

Due to the low voltage output of a single cell, it is necessary to "stack" cells, and connect them in series, to generate suitable levels of voltage and power. These levels do not necessarily need to be inline with the system it is designed to power, as supporting DC-DC converters can be used to augment the voltage and current levels; as will be discussed later.

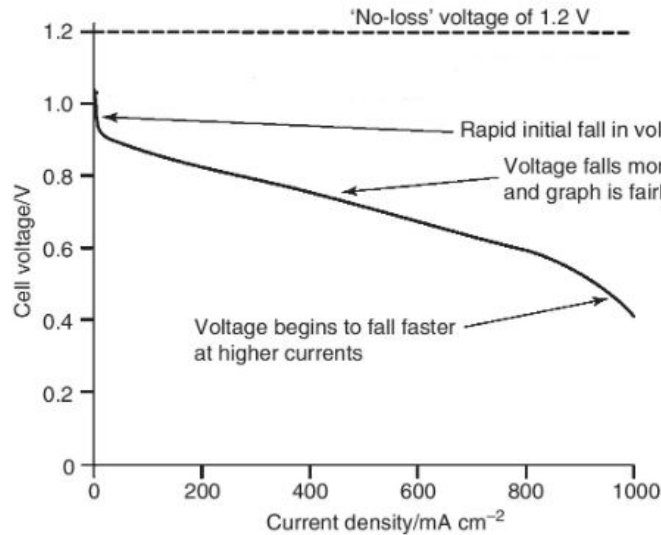


Figure 2.5: Single Cell Polarisation

Fuel cells are not limited to a single form, and are generally classified by the material which is used for the electrolyte layer, between the anode and cathode. From [35] and [29], six main classifications of fuel cells are referenced, these being the alkaline fuel cell (AFC), the proton exchange membrane fuel cell (PEMFC), the direct methanol fuel cell (DMFC), the phosphoric acid fuel cell (PAFC), the molten carbonate fuel cell (MCFC), and the solid oxide fuel cell. Table 2.3 provides a summary of the pertinent features of each fuel cell variant, and highlights an example of their application. For the purposes of this project, the PEMFC is adopted due to its aforementioned use in recent experimental aircraft, and its legacy use in the automotive field.

### 2.3

Focusing on the modelling of the fuel cell for the purposes of this project, the intricacies of the Proton Exchange Membrane Fuel Cell (PEMFC), and their design are dealt with, in great depth, by [35], [14], [36]. These textbooks provide detailed equations which permit for the development of a high fidelity fuel cell models, and their supporting balance of plant (BoP) equipment, such as humidifiers, turbo-normalising compressors, condensers, combustors, preheaters and heat exchangers,

2.2. HYDROGEN-ELECTRIC AIRCRAFT TECHNOLOGIES AND  
CONCEPTUAL DESIGN

---

Table 2.3: Fuel Cell Variants

Fuel Cell	Mobile Ion	Operating Temperature	Applications
Alkaline (AFC)	$\text{OH}^-$	50-200°C	Spacecraft
Proton exchange membrane (PEMFC)	$\text{H}^+$	30-100°C	Transportation applications, and low power stationary supplies
Direct Methanol DMFC	$\text{H}^+$	20-90°C	Portable applications: laptops, mobile phones
Phosphoric acid (PAFC)	$\text{H}^+$	220°C	Large power supplies (200kW+)
Molten carbonate (MCFC)	$\text{CO}_3^{2-}$	650°C	Medium to large MW supplies
Solid oxide (SOFC)	$\text{O}^{2-}$	500-1000°C	Low to high power stationary supplies

to name a few. The knowledge required to develop a fully functioning, and adaptable model is an entire project within itself, and moreover, these models do not lend themselves well to low computational effort, conceptual aircraft design methodologies, which form part of the research objectives. However, the knowledge within this literature supports an understanding of the nuances of topic and the supporting equations deliver an insight into the operation and function of the fuel cell, and its ancillary components.

The work of [37], presents a performance and failure analysis for a retrofitted Cessna 208 caravan, with a fuel cell power system, in combination with liquid hydrogen. Within this body of work, the author begins by presenting the open circuit voltage equation, which represents the maximum potential achieved by a cell, when there is no load attached; this equation is presented as equation 2.4, also referred to as the Nernst equation, and forms the foundation of the polarisation curve, presented previously. The work goes on to expand upon the Nernst equation, and details the losses, which contribute to the diversion away from the 'No-loss' line of figure 2.5, and whose dominance varies, depending upon the region of the polarisation curve, with the introduction of the activation losses,  $V_{act}$ , the ohmic losses,  $V_{Ohmic}$ , and the concentration losses,  $V_{conc}$ . In combination with the Nernst voltage equation, the cell voltage,  $V_{cell}$ , curve can now be given by equation, 2.5. The resultant curve

can then be used to calculate the fuel cell power when provided with the number of cells,  $N_{cells}$  in series, and the respective area of the cells,  $A_{cells}$ .

Details are given for the calculation of the individual losses. However, a considerable number of specific inputs are required for this, and go into details such as electrolyte membrane thickness, anode and cathode transfer coefficients, electrode roughness factors, but to name a few. As with the work within the textbooks discussed previously, this methodology for calculating the fuel cell characteristics, does not lend itself well to a rapid sizing methodology, when limited information is known about the cell, and its supporting balance of plant equipment; making it less than ideal for the proposed research.

Additionally, [37] the work of does not include any of the dynamics of the fuel cell, or discuss the idea of using a battery for propulsive purposes. The final aircraft does not include any batteries or a battery branch, and is ultimately powered by four 140kW fuel cells, attached to a common bus, via the necessary DC-DC converters, rather than sizing a single fuel cell which can be optimised for performance over a chosen flight segment. Likewise, the work of [38] presents a methodology for sizing aircraft, fuelled by both liquid and gaseous hydrogen, including the balance of plant equipment for the fuel cell; but, presents no details regarding any supporting battery branch for transient conditions or propulsive power during a particular section of the flight profile. The resulting aircraft all stipulate that the aircraft is free of any battery, and subsequently the masses calculated for these results have the potential to be inaccurate, and not inline with models showing the requirement of batteries and supercapacitors to cover transient periods.

$$E_{oc} = E_o - (8.5 \cdot 10^{-4}) \cdot (T_{stack} - 298.15K) + \frac{R \cdot T_{stack}}{2 \cdot F} \cdot \ln \left( \frac{P_{H_2} \cdot P_{O_2}^{0.5}}{1} \right) \quad (2.4)$$

Where:

$E_o$  = The  $H_2|O_2$  redox standard potential of 1.229V, as also identified by the 'No-loss' notation in figure 2.5

$R$  = Universal gas constant

$T$  = Stack operating temperature

$F$  = Faraday constant (96,485 C/mol)  $P_{H_2}$  = Partial pressure of the  $H_2$   $P_{O_2}$  = Partial pressure of the  $O_2$

$$V_{cell} = E_{oc} - V_{act} - V_{Ohmic} - V_{conc} \quad (2.5)$$

The work [39] presents research on the development of a generic fuel cell model, based on the application to a fuel cell vehicle, and also used for the previously discussed Bombarider fuel cell emergency power model. The work, once again takes advantage of the Nernst equation, observed in the text books and previous studies, however, it has that advantage of being conveniently packaged as the stalwart model in the MATLAB/SIMULINK environment, and provides a number of pre-programmed fuel cell stacks, including, a 1.26kW, 6kW and 50kW PEMFC, in addition to a 2.4kW AFC, and a 3kW and 25kW SOFC. The polarisation curves for voltage and power, are presented in figure 2.6, for the 6kW PEMFC. Although seemingly advantageous, the methodology is only suitable if the aircraft requires the power levels as exactly programmed in the fuel cell block, and although only 15 inputs are required for the model to work, when considering a variation on the programmed fuel cells, relative to the multitude for the other methods, there is still a requirement to have information regarding the airflow rates, operating temperatures, and voltage and current at specific points on the polarisation curve, which may induce inaccuracies for a custom fuel cell stack. However, this fuel cell model does come with the added advantage of not only incorporating the fuel cell dynamics, but also being able to select the nominal stack efficiency point, which could

## 2.2. HYDROGEN-ELECTRIC AIRCRAFT TECHNOLOGIES AND CONCEPTUAL DESIGN

---

be selected as the desired efficiency during the longest parts of the flight; namely cruise. Selecting the cruise efficiency, has the opportunity to open up a trade study to show the effects of efficiency selection on overall aircraft mass, as a lower efficiency (lower power) fuel cell, would be of lower mass than a higher efficiency fuel cell, thus reducing the mass compounding effect over the flights, but, the peak power of the lighter fuel cell may now be able to cover peak powers, and as such additional battery, and battery branch mass may be required.

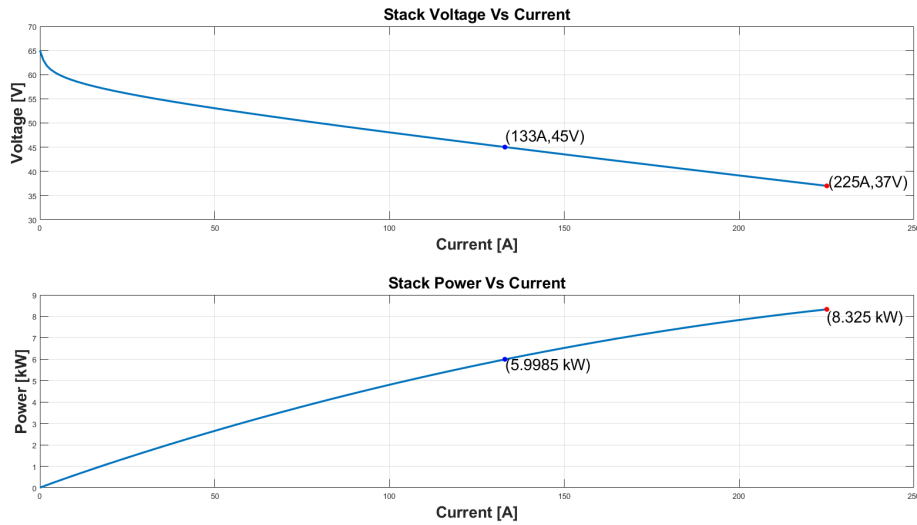


Figure 2.6: 6kW Fuel Cell Polarisation and Power Curve

In a bid to improve on the previously described modelling methods, and provide a useful research contribution, the modelling of the hydrogen fuel cell for this project aims to build on previous work, and take advantage of the normalisation of the polarisation curve to size a fuel cell specifically for the aircraft under consideration, as well as permitting for the desired cruise efficiency to be a direct input parameter, in addition to developing a means to incorporate the fuel cell dynamics, such to reflect that of the scenario observed for the Bombardier emergency landing system model, whereby the power supplied by the fuel cell with respects to a change in system power, is not instantaneous, and some level of battery input is required. In addition the number of specific inputs pertaining to items such as partial pressures, and membrane thicknesses should be omitted from the new model, in a bid to

Table 2.4: Power Density of Motors for Aerospace Applications

Manufacturer	Topology	DC Bus Voltage (V)	$P_{\text{rated}}$ (kW)	$P_{\text{peak}}$ (kW)	$\rho$ kw/kg
McLaren	Surface PM	545	100	120	4.6
YASA	Axial Flux PM	800	75	200	6
Protean	Outer Rotor SPM	400	54	75	2.2
Siemens	Hallback Array SPM	580	260	-	5.2
Honeywell	Wound-field Synchronous	300-600	260	-	5.2
ENSTROJ	Axial Flux PM	700	200	-	9.8

reduce the overall number of inputs which may not be known to the design team. An additional research question can also be posed, with respects to the effects on sized aircraft MTOM when incorporating fuel cell dynamics within the model, which [37] and [38] neglect. This is dealt with as an independent study, and is featured in the main body of the text.

### 2.2.4 Motor and Inverters

As this project does not focus on the design or modelling of the motor and inverters, explicitly, but does require their effects for the determination of overall aircraft mass, and to some degree, the efficiency of the aircraft, the decision is made to use rudimentary models, and assume a power density, and fixed efficiency when considering them in the full aircraft system model. The works of [40], presents a host of electrical machines used within aerospace applications, and more importantly, their power densities, as well. A selection of these motors are available to view in table 2.4

In addition to the empirical motor data presented, it would be possible to achieve higher fidelity motor models, through the use analytical motor sizing equations. For example [41], develops an analytical motor model for a three phase surface mounted permanent magnet synchronous machine. From this paper, the machine is sized, based on a set of fundamental steps, as shown in figure 2.7. The system level analysis, for system level simulations, including the control loop and filter design are captured by steps 1 through 12, at which point the candidate machine's

mass, volume, efficiency, power factor, stator resistance, stator inductance, and flux linkage are determined. An extension beyond step 12, can be used for more advanced machine design. A synopsis of steps 1 to 12 is provided below:

- Step 1 - The required machine design inputs are provided.
- Step 2 - The fundamental winding factor,  $k_{w1}$  is calculated. At system level analysis, this stage can be bypassed, and a value of 0.9 can be hard coded
- Step 3 to Step 6 - An approximate rotor sizing, followed by a stator sizing based on general machine sizing equations are considered.
- Step 7 - The windings are dimensioned under the consideration of full-pitch or fractional pitching windings.
- Step 8 - The stator resistance,  $R_s$  is calculated.
- Step 9 - The nominal operating point and voltage limits are considered in the dq current plane, from which feasible stator inductance,  $L_s$ , and magnetic flux linkage,  $\lambda_m$  are determined.
- Step 10 - The power losses and efficiency are calculated.
- Step 11 - All results are checked and filtered, if they are within the desired efficiency, power factor, and geometrical limits.
- Step 12 - The filtered candidate machines' mass are calculated from their known geometry.

A similar method from [42] is also considered, for a different topology to that of [41]; this additional methodology applies specifically to axial flux permanent magnet machines, such as those developed by this projects sponsor, EVOLITO LTD. However, these analytical models does not uphold for the proposed aircraft design methodology. One of the major issue with these methodologies stems from

## 2.2. HYDROGEN-ELECTRIC AIRCRAFT TECHNOLOGIES AND CONCEPTUAL DESIGN

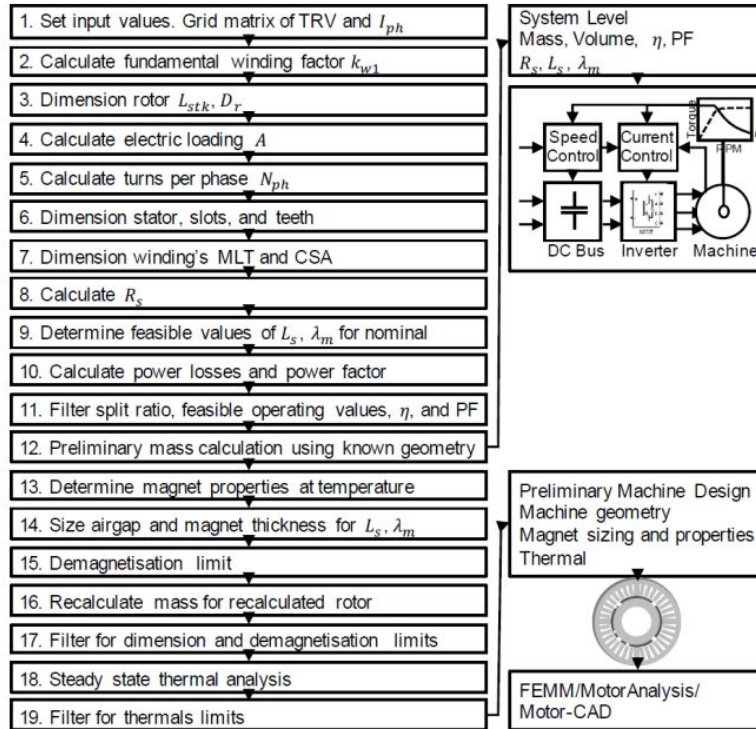


Figure 2.7: Machine Sizing Flowchart from [41]

the necessity to have some known voltage across the DC bus, which does not support the selected 'energy in a box' model used for the battery, which will permit for rapid aircraft sizing. An additional drawback to these models is the requirement for a vast number of inputs which extend down into material selection, with respects to their density, and the selection of magnets, in certain cases. It therefore stands to reason, that taking advantage of known power density values for motors, is the optimal solution for the sizing methodology, and as with the previous powertrain components discussed, it is possible to perform sweeps of technology levels to assess and leverage any benefits from future technologies, with regards to overall aircraft mass.

It is the function of the inverter, to convert the DC voltage (and current) values on the DC bus, into a usable sinusoidal wave form, of the required number of phases, for the propulsion motor(s) [43]. Models for such components exist in software such as PLECS [44], with a model of a simple voltage source inverter given in figure 2.8,

whereby the minimum quantity of specific components can be observed. Here, six switching devices, which could be MOSFETS or GAN devices, are controlled by a switching circuitry, usually from a digital signal processor in physical applications, and the switches are switched according to some switching regime, such a space vector pulse width modulation, to produce the required signals, to drive the motor, at a speed governed by the frequency of the switching, which in this image are represented by a series of resistive and inductive loads. A number of capacitors may be placed across the DC link to permit for filtering and attenuate any ripple brought about by the switching. PLECS, provides an environment for in depth inverter design, with the capability to incorporate thermal and loss models which can be imported from manufacturers data sheets

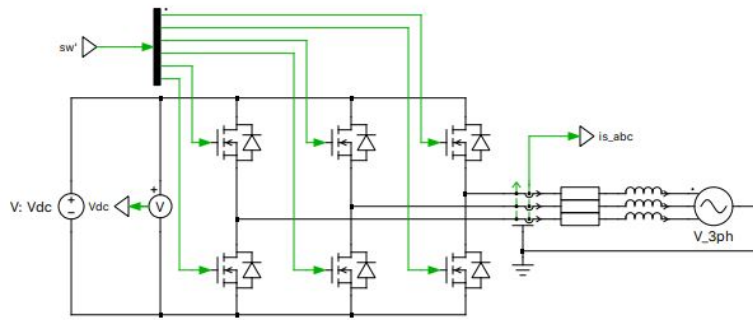


Figure 2.8: PLECS Example of a Three Phase Voltage Source Inverter [44]

Similar to the motor sizing methodology, the work of [41], whom adopts look up tables for specific components, has produced a sizing methodology for inverters and filter design. However, once again these models require a depth which is greater than what is required by the sizing methodology, and having additional convergence loops to build an inverter, in the event that additional switches are required in parallel for current handling capabilities, or spanning a model across two software platforms moves away from the objectives of the research, and as such, inline with the other components, the power density will be factored into the model, rather than the design of a bespoke inverter with individual switches, and bulk capacitance requirements is opted for.

### 2.2.5 Ancillary Propulsion System Components

The major components which comprise the propulsion systems of electric and hydrogen-electric aircraft have been discussed within the previous subsections; however, additional supporting hardware is required for component networking, and safety. These components are namely, cabling, bus-bars, circuit breakers and contactors to name a few. Within the literature which pertains specifically to aircraft and vehicle sizing, which has been referenced thus far, there is no mass accreditation for these components, and only minimal reference made, with the exception of the Bombardier emergency system, which does incorporate the contactors within the electrical model, but, has no requirement for accounting the mass. These components are not specific to only electric and hydrogen-electric aircraft powertrains, but are also found commonly in the electric vehicles, including cars, trains and ships, which provide excellent resources, to support the discussion of each, and a brief description of each of these components, and their place within the aircraft electrical system are discussed below.

- **Cables** - In the context of the electric and hydrogen-electric propulsion system, the cables form the main interconnections between the battery or fuel cell, bus-bars and the propulsion motor(s), via, the inverter(s), converter(s) and power management system(s) within each respective branch. The selection of the cable requires a number of considerations, such as the current carrying capability, insulation types, due to the Corona effects, shielding, due to EMI requirements, and weight optimisation. This does also not include the cabling required for the general aircraft systems such as onboard lighting, or actuation systems, including electric flap / slat actuation motors.
- **Bus-bars** - Generally observed as copper conductors which consolidate and distribute current between the major subsystems. Bus-bars have the advantage of offering low resistance, for reduced resistive losses, and improved cur-

rent handling capabilities, relative to flexible cabling. Having a set of common rails in which to connect subsystems, reduces the complexity of the electrical system layout, and improves the reliability of the system, through reduced connections and terminals.

- **Circuit breakers** - The purpose of circuit breaking equipment, is to provide a level of protection for the electrical system, through disconnection of power during an over current event or fault condition within the respective subsystem. Circuit breaking equipment is not exclusive to electrified aircraft, and are a fundamental element of all aircraft; and particularly in commercial aircraft. Circuit breakers are featured in the cockpit, for easy access by the pilot(s), and traditionally used magnetic and thermal actuation, however, solid-state circuit breakers now replace, or supplement these, due to their reduced mass, and rapid response times, to fault conditions.
- **Contactors** - In conjunction to circuit breakers, contactors are electrically controlled switches, which are used to connect (or disconnect) high-voltage circuits, and by virtue, play a crucial role in electric or hydrogen-electric aircraft system start up, or shut down processes, pre-charge operations, and emergency isolation. Aerospace certified contactors are designed to withstand high current and voltage levels, in addition to minimising arc formation during operation.

The modelling of the cabling for a hydrogen-electric aircraft is an additional complexity for the sizing methodology, and although, previous sizing equations, for conventional aircraft, such as that from [45], equation 2.6, does give some indication for the mass of the electrical system, given as a function of the avionics and fuel system, as per equation; as such this does not uphold for electric or hydrogen electric aircraft. The work of [46] presents a methodology for power cable estimation in electric aircraft propulsion systems, by comparing three different strategies, which

surround selection of cables from off-the-shelf options, design based on steady-state thermal limits, and design based on transient thermal limits, considering conductor and insulator materials, as well as their dimensions; preliminary results for the cable, thermal and weight estimation from transient and steady state models are presented in table, with the useful values of mass per unit length, ( $m_{tot}$ ), for various values of ampacity, at ambient temperatures, relative to reference values, based on the American wire gauge (AWG); as can be observed the reference values show strong confidence with the calculated values of  $m_{tot}$ . Although, the methodologies presented offer some insight into the sizing of the cables, a number of inputs which go beyond that of the proposed conceptual design are required, including the battery voltage, insulation breakdown voltage, dielectric permittivity of the insulating material and insulation thickness, which does not align with the battery model selected for this project; a more advanced battery model, and a selection of empirical cable data values, could lend itself well to adopting the cable mass estimation methodologies presented in [46]. However, The sizing of the cable mass, in the context of conceptual aircraft design, isn't necessarily a simple question of having some knowledge of the power handling capabilities of the cable mass or indeed calculating the mass per meter values, because, as well as attempting to reduce the number of inputs into the methodology, additional considerations are required to be factored in. In order to appropriately size the quantity, lengths, and as such mass of the high voltage cabling, an additional level geometrical accuracy, and the levels of redundancy or safety is required when the aircraft is being sized. Based on this, there is a requirement to understand the relative positions of all of the major components within the aircraft and consider emergency scenarios. The relative positions of the components within the aircraft raise further questions, and can be influenced by the technology levels used. For example, Hart aerospace [28] propose a "blister" pack located on the underside of the fuselage to store the battery, as per figure 2.9, and based on this, there would be a requirement for high voltage cabling to be taken towards the motors, mounted on the wings, via DC-DC converts and

## 2.2. HYDROGEN-ELECTRIC AIRCRAFT TECHNOLOGIES AND CONCEPTUAL DESIGN

---

power management systems, which maybe located elsewhere within the aircraft, and some network of cabling would be required to support redundancy. However, in a scenario of future battery technology, which the model in this project permits for, it may be possible to move the battery to the wings, and connect a battery independently to a motor, possibly without the need for a bus bar, or taking advantage of shrinking the entire package by using an integrated drive system [47], where all of the DC-DC converter, motor, cooling, control and power management are all packaged in a single unit, reducing the need for interconnecting cables, and furthered again by advances in technology, such as 3D printed bus-bars, to increase the overall power density of the unit. Placing a hydrogen fuel cell within the system would force the requirement for additional cable, and again, some knowledge of it's placement within the aircraft, for the determination of the cable length; a placement which may be an unknown. All of these factors result in the sizing of the aircraft's high voltage cable mass being open to error and something of a subjective topic; additionally the assigning of a coefficient to the aircraft mass, or some component masses to cover the cable mass would require further optimisation studies which consider fuselage and wing lengths, technology levels of all of the major components, and some for of failure rates analysis to compliment the major propulsion system components.



Figure 2.9: Hart Aerospace battery location proposal

$$W_{electrical} = 12.57 \cdot (W_{fuelsystem} + W_{avionics})^{0.51} \quad (2.6)$$

## 2.2. HYDROGEN-ELECTRIC AIRCRAFT TECHNOLOGIES AND CONCEPTUAL DESIGN

---

Table 2.5: Cable thermal and weight estimation from the transient and steady models developed by [46]

AWG	Conductor Radius (cm)	Ampacity (A)	Ref Temp. °C	Transient Temp °C	Steady State Temp. °C	Ref $m_{tot}$ Ref (kg/m)	Calc. $m_{tot}$ (kg/m)
10	0.129	50	75	77	77	0.086	0.088
8	0.1632	70	75	75	74	0.140	0.143
6	0.2057	95	75	78	77	0.1949	0.196
4	0.2595	125	75	76	76	0.2694	0.279

Where:

$W_{electrical}$  is the weight of the electrical system (in pounds)

$W_{fuel}$  is the weight of the fuel system (in pounds)

$W_{avionics}$  is the weight of the aircraft's avionics (in pounds)

Aerospace contactors are available as off-the-shelf components, from distributors such as TE connectivity, whom have presented a useful white paper on the subject of current and legacy contactors [48] [49]; explaining in detail, the operation of the device, including pre-charge circuitry, and additionally, provides information for the characteristics of switch off capabilities and overload behaviour. The adoption of higher voltages, in addition to designs for legacy 28VDC system, which are not suited for high voltage switching due to their inability to generate adequate arc voltage interruption, within an acceptable packaging size, require the use of additional components such as arc splitting plates, runners, blow-out magnets and better internal switching atmospheres, and systems such as the 270VDC and the 540VDC, which are often split into positive and negative channels, must now be controlled by either 2 contactors or new two-pole switching designs. From publicly available commercial data, a selection of high voltage DC contactors from the automotive sector, used in EV and HEV applications are available in table ???. For the power density calculation of the contactor, the decision is made to use the rated power, based on the continuous current rating, observed during steady state operation, rather than the interrupt or switching rating, which permits for greater current over shorter time periods; for example, the BSBC8V from [50], is rated at a continuous 500A,

## 2.2. HYDROGEN-ELECTRIC AIRCRAFT TECHNOLOGIES AND CONCEPTUAL DESIGN

Table 2.6: Off-the-Shelf Contactor Technology

Contactor Model/ Manufacturer	Rated Power	Approx. Mass	Power Density
BSBC8V-500A, 1000V [50]	$500\text{A} \cdot 1000\text{V} = 500\text{kW}$	0.4kg	$\approx 1250 \text{ kW/kg}$
BSBC8V-200A, 1000V [51]	$200\text{A} \cdot 1000\text{V} = 200\text{kW}$	0.35kg	$\approx 570 \text{ kW/kg}$
EVQ500 [52]	$500\text{A} \cdot \sim 1000\text{V} = 500\text{kW}$	0.93kg	$\approx 538 \text{ kW/kg}$
EVQ200 [53]	$200\text{A} \cdot \sim 1000\text{V} = 200\text{kW}$	0.43kg	$\approx 465 \text{ kW/kg}$

however, it has the capability to support a heavy load tolerance of 600A for 120 seconds, 900A for 30 seconds, and 1000A for 10 seconds. These data points provide realistic bounds for contactor mass contributions in propulsion system mass estimation. However, in conjunction to the cable mass estimation, it is required that some level of understanding of the necessary redundancy and network topology is supplied to methodology, as the contactors would be placed inline between various subsystems, therefore the same argument is stated for the contactors as it was for the cables in regards to the reasons for the additional complexity when attempting to model them as part of the sizing methodology.

Based on the previous discussions for cabling, and switching, including their complexity to model accurately with some level of confidence in the results, and in order to reduce the computational complexity of the model, the modelling of bus-bars, circuit breakers, and contactors is omitted from this project. It stands to reason that this would have some impact on the final MTOM value of the aircraft, with respects to a possible underestimation in certain respects, if the models described above were implemented, however, as previously described, the above models do not lend themselves well to conceptual aircraft sizing methodologies, where fast simulation times are a factor. Additionally, applying a coefficient to cover the mass of these systems, as a function of the aircraft's MTOM, has the potential to induce greater inaccuracy for the final results, if a thorough trade study to ensure that the coefficients are accurate in accordance with the selected technology levels, and redundancy values, has not already been undertaken.

## 2.2.6 Hydrogen-Electric Aircraft Design Methods

Stalwart methods for aircraft conceptual design have evolved from the early methodologies developed for both powered and non-powered aircraft, dating back to the 1920s and 30s [54] [55] [56]. Although, their original work still forms the basis of proceeding works, despite great advances in aerospace technology, and computation used for such development and design purposes. The design of an aircraft or aircraft system is generally an undertaking filled with complexity, and very much a process of multi-iteration, multi-phase and as is previously described, multi-disciplinary, spanning many engineering disciplines. Fundamental objectives of the conceptual aircraft design model include, the usually conflicting, high numerical accuracy, with low computational time.

The classic Bréguet range and endurance equations, taught in most undergraduate aerospace engineering studies, allow for the calculation of the aircraft's Maximum Take Off Mass (MTOM), under the consideration of a simple a mission performance analysis, when a traditional fuel burning engine is used, and the mass of the energy carrier (fuel) depletes. This concept is dealt within the main body of the thesis, but the reader is referred to aerospace design textbooks for further insight [31][20] [57][58][59]

This does not hold true for propulsive energy and power carriers whose mass does not deplete during flight, such as aircraft propulsion systems powered, or part powered by batteries or super-capacitors.

Designs for hybrid-electric, and hydrogen-electric aircraft propulsion architectures have become well documented, more so the former, and new methods for aircraft sizing have emerged. [6] identifies numerous propulsion system configurations for hybrid-electric and all electric aircraft.

The most prominent work on sizing aircraft with novel propulsion systems, comes

out of FH Aachen University [21], where literature suggests a move away from the classical fuel fraction methods presented in legacy literature, with a step towards an energy analysis using kinetic energy, potential energy, and energy expended to aerodynamic drag, termed the transport energy, and shown in equation 3.42

$$\Delta E = \underbrace{\frac{m \cdot g \cdot V}{L/D} \cdot \Delta t}_{\Delta E_{AeroDrag}} + \underbrace{\frac{m \cdot \Delta V^2}{2}}_{\Delta E_{Kinetic}} + \underbrace{m \cdot g \cdot RoC \cdot \Delta t}_{\Delta E_{Potential}} \quad (2.7)$$

where  $\Delta E$  is the change in energy for a given time step,  $\Delta T$ , based on the aircraft's weight, given by the product of mass,  $m$ , and the gravitational constant,  $g$ , its velocity,  $V$ , and where appropriate, the rate of climb,  $RoC$ , and lift to drag ratio,  $L/D$ .

With a known energy demand for each flight phase, the energy is apportioned to any non-consumable energy carriers,  $E_{nc}$ , such as batteries or super-capacitors, determined by the hybridisation of energy,  $H_{E,phase}$ , given by equation 2.8

$$H_{E,phase} = \frac{\Delta E_{nc}}{\Delta E} \quad (2.8)$$

In addition to the hybridisation of energy, a complementing term, the hybridisation of power, is also introduced, denoted as  $H_{P,PH}$  for parallel-hybrid aircraft, and  $H_{P,SH}$  for serial-hybrid aircraft. In the case of a parallel-hybrid configuration this is the ratio of the power requirement of the EM,  $P_{EM,max}$ , specified by the the split point of the total power demand,  $P_{max}$ , this is shown in equation 2.9.

$$H_{P,PH} = \frac{P_{EM,max}}{P_{max}} \quad (2.9)$$

For serial-hybrid configurations, a modification is made to equation 2.9, as failure to do so would lead to a value of one, for every scenario, due to all of the power coming from the EM, with no consideration taken to the range extending engine.

Therefore, the power of the engine is factored into the denominator, as per equation 2.10; a value of one in this scenario dictates that the engine is providing all of the power, and a value tending to infinity suggests an all electric aircraft.

$$H_{P,SH} = \frac{P_{EM,max}}{P_{ICE,max}} \quad (2.10)$$

The hybridisation of power is a fixed value which forms part of the initial design criteria, and in the case of [21] part of the optimisation variables.

The energy from every time step is split according to the  $H_E$ , to determine the energy from non-consumable mass carriers,  $\Delta E_{nc}$ , and the energy from the consumable mass carrier,  $\Delta E_c$ , and the power for the EM,  $P_{EM}$ , and ICE,  $P_{ICE}$ , is given by equations 2.11 and 2.12 respectively. During each time step, a validation must be performed to ensure that the power of either branch of the system does not breach the hybridisation on power.

$$P_{EM} = \frac{\Delta E_{nc}}{\eta_{stT,EM} \cdot \Delta t} \quad (2.11)$$

$$P_{ICE} = \frac{\Delta E_c}{\eta_{stT,ICE} \cdot \Delta t} \quad (2.12)$$

As can be observed in the above equations, new terms have been introduced,  $\eta_{stT,EM}$  and  $\eta_{stT,ICE}$ , these pertain to the shaft to thrust efficiencies for the branches containing the electric motor and the ICE, and are constituted of the product of the efficiencies of individual components or modules in the efficiency chain. Efficiency chains from multiple sources have been compiled to highlight to the reader, some of the representative configurations, see figure 2.10. Initial sizing literature has shown fixed values for the efficiency of modules along the efficiency chain, to permit for swift analysis; however, FH Aachen are looking towards the development of a variable efficiency sizing methodology.

## 2.2. HYDROGEN-ELECTRIC AIRCRAFT TECHNOLOGIES AND CONCEPTUAL DESIGN

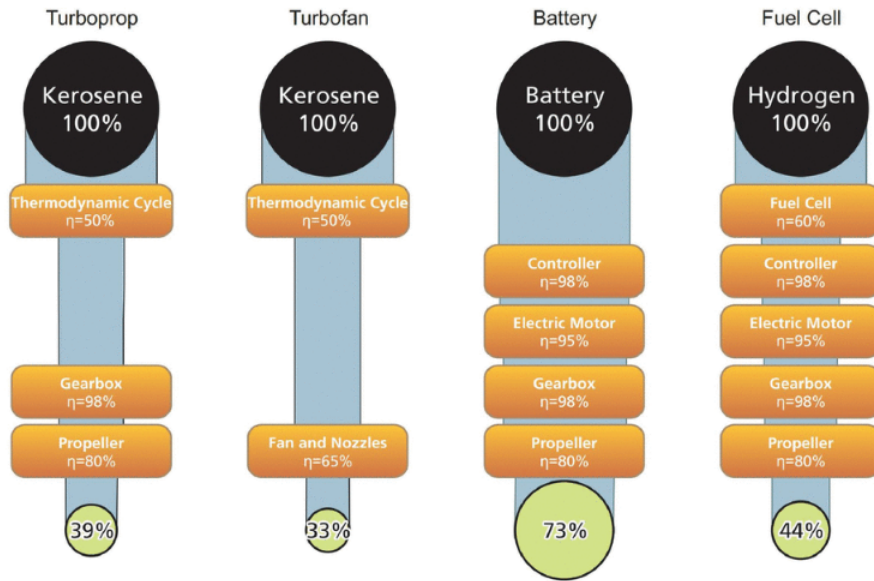


Figure 2.10: Efficiency Chains for Various Propulsion Systems

As shown in [20][21] the sizing process begins with the development of a constraint analysis. An arbitrary, yet representative example of the completed constraint analysis is shown in figure 2.11

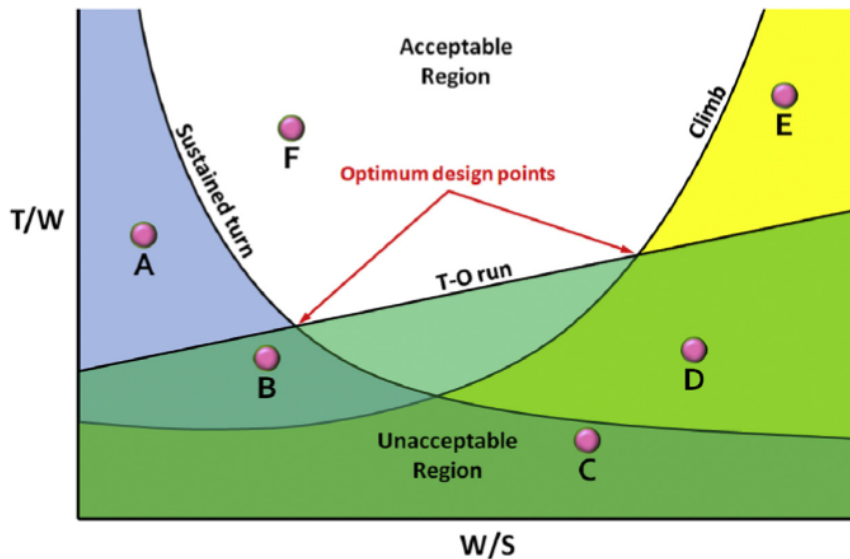


Figure 2.11: Gudmundsson's Constraint Diagram Concept

The constraint diagram takes advantage of constraint diagram equations, which are presented in the main body of this report, and permit for the determination of a power to weight ratio with respects to a wing loading. An initial assessment of the

aircraft mass permits for the maximum installed power to be determined, based on the optimal design points from the constraint diagram, permitting they fall within the acceptable region. The works of [60] make use of the constraints diagram.

It is also worth noting that two forms of the equation used to determine the aircraft drag coefficient during flight, have been observed in sizing methodologies for hydrogen-electric and electric aircraft design. These equations are the simplified drag model, and the extended drag model given in equation 2.13 and 2.14 respectively. The simplified drag model assumes that the minimum coefficient of drag,  $C_{Dmin}$ , occurs when the lift is zero, and applied to an un-cambered airfoil. The extended drag model applies to airfoils' which include camber, such as the DO-A5 airfoil used on the Dornier 228's main wing section [61]. The DO-A5 presents a maximum camber of 2.5%, at 75% along the chord length, and is denoted by the purple dashed line in figure 2.12. Symmetrical airfoils, typically used for the horizontal and vertical stabiliser, or small, home built aircraft main wing sections don't possess any camber, as shown by the airfoil used for the horizontal stabiliser of the Cessna 175 Skylark, in figure 2.13 [62] [63]. Two separate studies for the Dornier 228, which see the aircraft re-powered, with the first study from [21], demonstrating a hybrid-propulsion system, using batteries and a turbo-shaft engine, and the second study from [38], demonstrating a hydrogen fuel cell powered aircraft (without batteries), appear to calculate the aerodynamic properties of the aircraft differently, with [21] using the extended drag polar, and [38] using the simplified drag polar. .... The effects of these, and their variations in calculated power will be examined in the main body of this report.

$$C_D = C_{Dmin} + K \cdot C_L^2 \quad (2.13)$$

$$C_D = C_{Dmin} + K \cdot (C_L - C_{Lmind})^2 \quad (2.14)$$

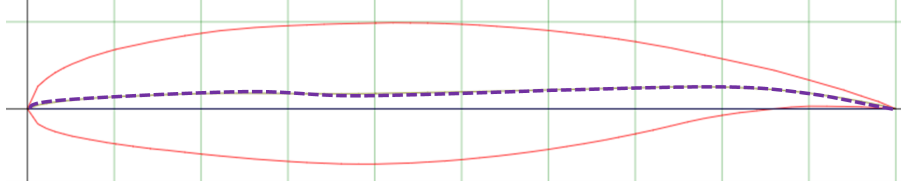


Figure 2.12: DO-A5 Dornier 228 Main Wing Airfoil

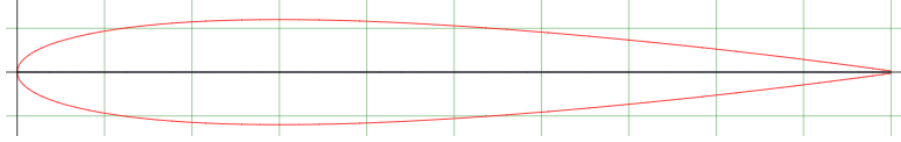


Figure 2.13: NACA 0012 Airfoil for Cessna 175 Horizontal Stabiliser

In addition to providing a means for establishing the power requirements for a time step, the work of [21] also provides a methodology to calculate the brake specific fuel consumption of a custom reciprocating engine, which is sized according to the maximum power of the constraints diagram. This equation is presented equation 2.15. This is a useful asset, as it permits for fuel burn calculations when sizing a conventional reference aircraft, and the engine performance data is unavailable. As sizing of a conventional aircraft, forms part of the sizing methodology, this equation could be implemented.

$$BSFC = \frac{BSFC_{opt} \left( (1.6 \cdot BSFC_{minP}) \cdot \left( \left( \frac{100 \cdot P}{P_{max}} - 80 \right)^2 \right)^{0.54} + 100 \right)}{100} \quad (2.15)$$

Where:

$BSFC$  = Brake Specific Fuel Consumption (BSFC) at a given power condition

$BSFC_{opt}$  = Best obtainable BSFC

$BSFC_{minP}$  = BSFC at the minimum usable fuel consumption, relative to  $BSFC_{opt}$

$P$  = Power at given flight condition

$P_{max}$  = Maximum power produced by the engine

A novel paper from [37] proposes a fuel cell retrofitted Cessna Caravan. This par-

ticular paper does not factor in any propulsive power from batteries, to cover the transient periods during changes in power, or purely for propulsive power, during take-off and climb, and takes advantage of the legacy thrust equations from aircraft design textbooks, in order to determine the power requirement for the fuel cell. Additional novelty from this paper comes in the form of a failure modes and reliability analysis, to assess the failure rates of the propulsion systems main components, and is potentially one of the reasons why the model does not consider any fuel cell transient behavior, or the acknowledgment of any batteries for propulsive purposes. [64] presents a generic platform for a fuel cell vehicle. The works of [65] provides research surrounding integrated optimal design for hybrid electric powertrains of future aircraft. [66] focuses on the power distribution and propulsion system for an all-electric short-range commuter aircraft, in the form of a case Study. Additional information regarding drag polar data for a specific variant of commuter aircraft is given by [67] for the Jetstream 31 National Flying Laboratory. [68] presents research exploring vehicle level benefits of revolutionary technology progress via aircraft design and optimization.

## 2.3 DC-DC Converters

This section begins with a consideration of the voltage levels observed onboard aircraft. Aircraft have a range of onboard voltages, these are in place to provide power to the various systems, ranging from the high power actuation devices for the control surfaces, down to the low power avionics and passenger in-flight entertainment services. The power for the aircraft can be generated from a multitude of sources, whether this is the accessory drive of a turbo-fan engine, an alternator of an internal combustion engine on a light aircraft, energy stored in batteries, or less conventionally for aircraft, a fuel cell. A number of common aircraft voltages are shown in figure 2.14 from [69], and a simplified example of a power distribution sys-

tem from a twin engine aircraft with an auxiliary power unit from [70], presented as figure 2.15, in addition to a similar example to validate the system, from [71], given as figure 2.16 which also provides reference to the specific bus voltages included in some aircraft, although this does vary depending on the particular aircraft [72].

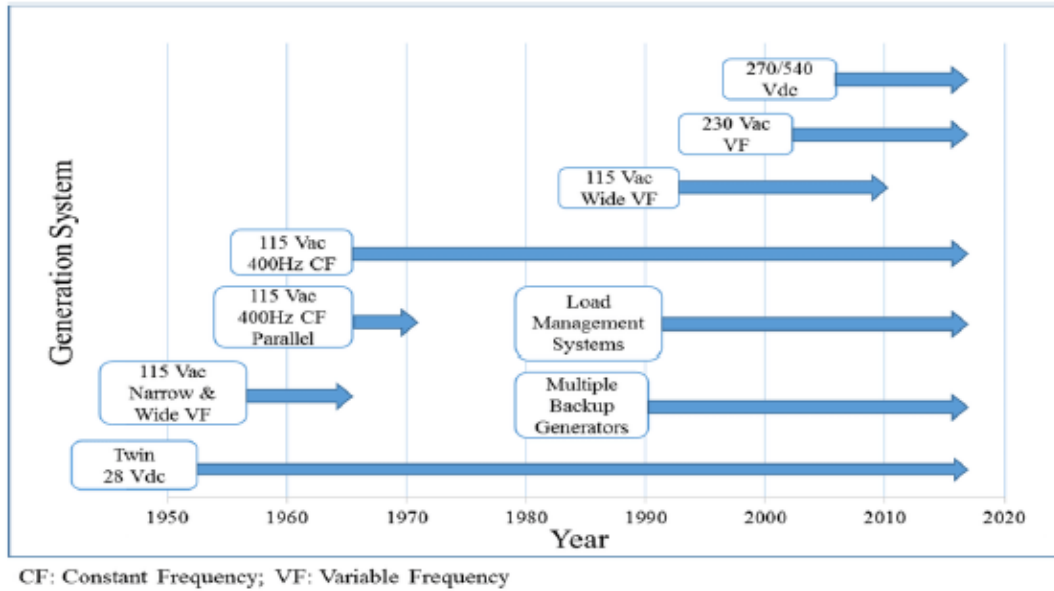


Figure 2.14: Various Aircraft Voltages used Onboard Aircraft with Time [69]

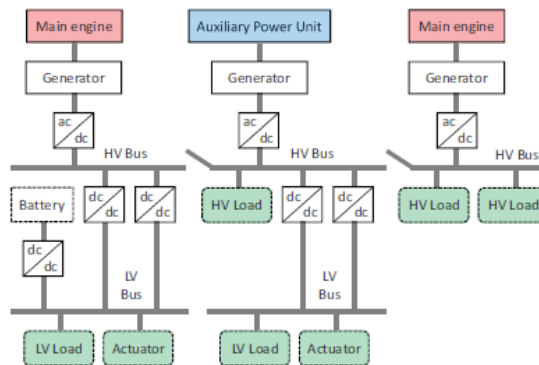


Figure 2.15: Simplified Example of Twin Engine Aircraft Power Distribution System [70]

The previous discussion for the Bombarider fuel cell based emergency power system also discusses the power and voltage levels used within the system; however, this system steps up the voltage from the fuel cell, rather than stepping down the voltages as observed in figure 2.16. The common requirement to all of these systems is the requirement for power converters, where, depending on the requirements, could

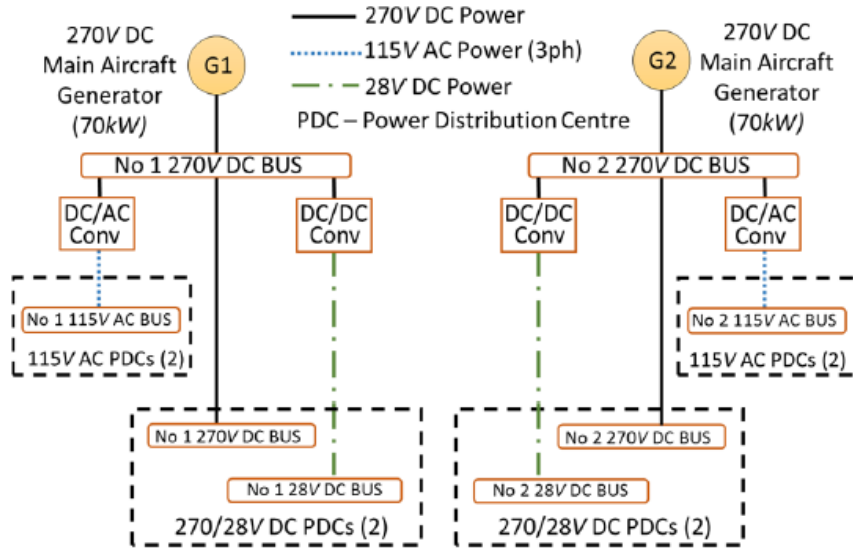


Figure 2.16: Simplified Example of Twin Engine Aircraft Power Distribution System with Bus Voltages[71]

be used to augment AC voltage waveforms to DC voltage waveforms, through an AC-DC converter, known as a rectifier, or vice versa, in a DC-AC converter, also referred to as an inverter, as discussed previously. Alternatively, converters can be used to step DC voltages up or down, depending on the downstream bus requirements, such as the 270V to 28V step down from figure 2.16.

Depending on the application or downstream bus requirements, the required voltage is stepped in a particular direction. In order to achieve this, one of the main variants of converter can be utilised. From [73], a number of converter topologies are identified, however, of particular note are the following basic switch mode power supply topologies:

- **Buck Converter** - Regulates the output voltage to a level lower than the input voltage.
- **Boost Converter** - Increases the output voltage to a level higher than the input voltage.
- **SEPIC (Single Ended Primary Inductor Converter)** - This allows the

output voltage to be greater or lower than the input voltage.

- **Buck-Boost Converter** - Produces an output voltage of the same polarity as the input, which can be either greater or lower.
- **Cuk Converter** - This provides a continuous current while inverting the polarity.

Despite all of these converters having dissimilar objectives, they do share the same common components, those being:

- **Inductor (L)** - The inductor stores and transfers energy between the input side and the load side, regulating the current flow.
- **Capacitor (C)** - Multiple capacitors may be placed in a switched mode power supply, to filter and smooth voltage fluctuations across the input DC supply, and load.
- **Switching Device** - These are commonly MOSFETS or IGBTs, and they act as an 'electronic switch' to control the energy transfer, as a function of their duty-cycle on time.
- **Diode** - Converters which do not take advantage of complimenting switches, may take advantage of a simpler approach and use a diode, which provides a path for current, but prevents reverse current.
- **Controller / Digital Signal Processor (DSP)** - It is the job of the controller / DSP to provide the switching pulse width modulation (PWM) to the gate drivers, associated with the switching devices. Additionally these devices may also be used to detect input signals from sensing equipment, such as current and voltage sensors, to support closed loop control.

Application notes from [74] describe the fundamental theory of the buck converter, and describes the law of inductance, whereby, when voltage is applied to an inductor, this will induce a current, and this current will vary with respects to time. The fundamental law, governing the voltage across an inductor given by equation 2.16, and represented in figure 2.17. The statement is made that when the current waveform is plotted with respects to time, the value of  $di/dt$  is defined as the slope of the current plot at any given point. From figure 2.17 the left-hand most plot, shows that current which is entirely DC, with zero ripple and as such constant with time, having a  $di/dt$  value of zero, and the resultant voltage across the inductor is going to be zero. The plot in the center shows a current which is increasing with time, as as such has a positive of  $di/dt$ , yielding a positive inductor voltage, and the inductor is building a magnetic field, and classified as 'storing energy'. Finally the, the right-had most plot, is the inverse of this, and represents a current that decreases with time, resulting in a negative value for  $di/dt$  and inductor voltage.

$$V = L \cdot \frac{di}{dt} \tag{2.16}$$

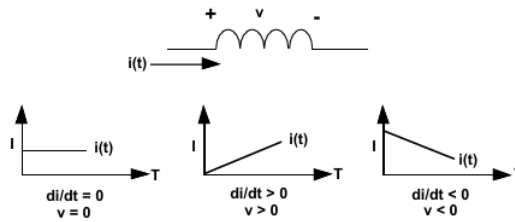


Figure 2.17: Inductor Voltage-Current Relationship [74]

It is possible to use the most simple buck converter model, to show the current paths as the switch transitions between on, given by figure 2.18, and off given by figure 2.19. For the MOSFET on stage, when the MOSFET is turned on, this connects the inductor to the supply; the potential is then made across the inductor, causing a rise in the current going through the inductor; this is shown in the buck converter current flow waveform from [74], in figure 2.20, during the  $T_{ON}$  period, at which

time the current simultaneously flows into both the output capacitor, causing it to charge, and the load.

The  $T_{ON}$  period is governed by the duty cycle,  $D$ , which is a function of the input voltage from the supply, and the required output voltage. This is expressed in equation 2.17. At the end of the duty cycle, the MOSFET is turned off, and as such the input voltage into the inductor from the supply is removed. However, the inductor does not have the ability to change its current instantaneously, this results in the voltage across the inductor, adjusting to try and hold the current constant. Eventually, the negative voltage, caused by a decrease in current, will cause the current to begin flowing through the diode, via the load, in conjunction with the discharging capacitor. This decrease in current is observed during the  $T_{OFF}$  period in figure 2.20

$$D = \frac{V_{out}}{V_{in}} \quad (2.17)$$

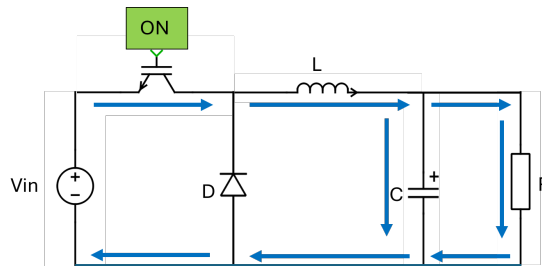


Figure 2.18: Buck Converter Current Flow: MOSFET ON

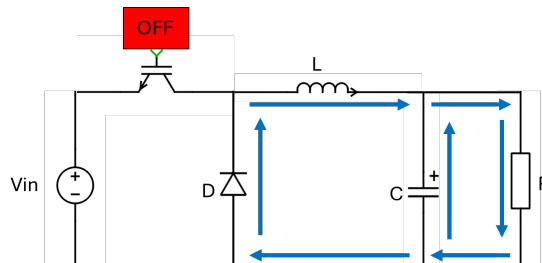


Figure 2.19: Buck Converter Current Flow: MOSFET OFF

With an understanding of the current waveforms through an inductor, in a buck converter, it can be related back to one of the overarching objectives of this research

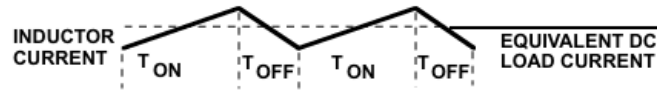


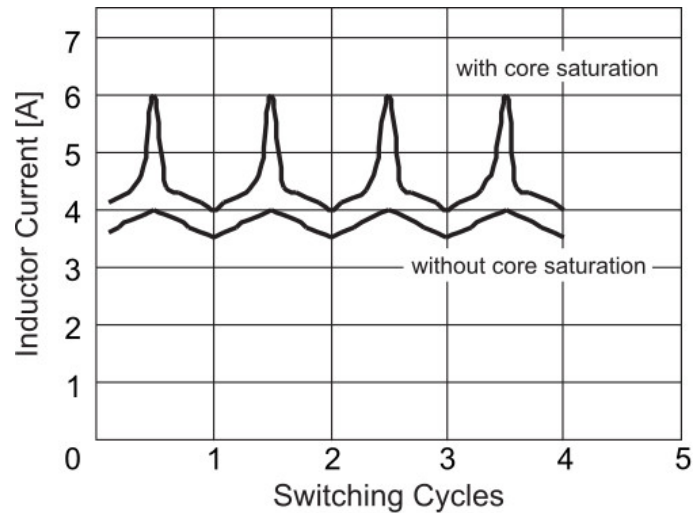
Figure 2.20: Buck Converter Current Flow: Waveform [74]

which pertains to the saturation of inductors. A more in depth discussion on inductors will be considered, in the next section, however, it is worth noting how the current waveforms of an inductor change, when saturation is experienced, as this also relates to the waveforms when experimental validation is considered. Inductor saturation occurs at the point when the core of an inductor reaches its maximum flux density, this causes a considerable decrease in inductance, and a rapid increase in  $di/dt$ . Reaching saturation has the effect on the inductor's ability to regulate current, which in turn leads to increases in the core losses, excessive heat, and instability in the circuit [75].

Figure 2.21, from [76], shows the inductor current waveform for a saturated and non-saturated inductor core. It is clear to see the similarities between the core without saturation in figure 2.21, and the waveform given in 2.20, albeit both waveforms are experiencing slightly different duty cycles, but this is incidental, as visually, both  $di/dt$  values look to be low. However, turning attention to the waveform of the saturated current, it is clear to see that it matches the description of a saturated core from [75], with large values for  $di/dt$ . This waveform also appears to be non-linear, unlike the non-saturated equivalent.

From what has been discussed previously, it is evident that the resultant saturation, where the core reaches its maximum flux density, is related to the current, which brings the topic into an initial means of preventing inductor saturation, and prevents the requirement for a single large current carrying inductor, in a high power DC-DC converter. This can be achieved through what is referred to as interleaving.

Interleaving a converter implies that multiple phases operate in parallel, with a phase shifted switching pattern, controlling the number of switches in the circuit.



Inductor Current Waveform With and Without Core Saturation.

Figure 2.21: Buck Converter Current Flow: Saturated Inductor Waveform [76]

Figure 2.22 best describes this topology, where it can be seen that rather than the single phase buck converter presented previously, there are now two parallel paths for the current to travel through, this in effect halves the current that each inductor would normally be exposed to, while still permitting for the full current required by the load, when the currents from each inductor combine at the node point before the capacitor. The number of interleaves can also be increased beyond two, as presented by the work of [77], with their design and control of a 6 phase Interleaved Boost Converter based on Silicon-carbide semiconductors fuel cell electric vehicle, and [78] with their design and comparison of a 10-kW interleaved boost converter for photo-voltaic application using Silicon and Silicon-carbide devices.

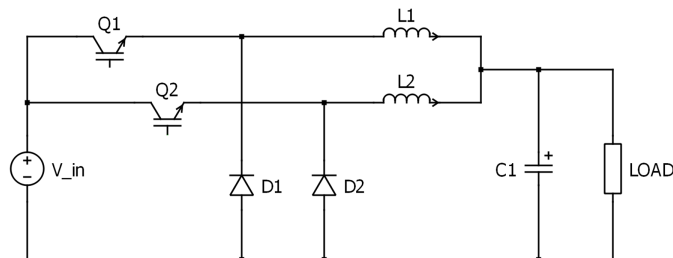


Figure 2.22: Interleaved Buck converter Topology

The interleaving of converters does not just benefit from the advantage of shared

load current, as this also leads to additional benefits as a byproduct; Including:

- **Reduced Input and Output Current Ripple** - This is made possible due to the phase shifting of multiple switching stages, such that the ripple currents of individual phases have the potential to cancel one another out; however, this does depend on the number of phases in the system, and the operational duty cycle, as shown in figure 2.23 from [79]. Reducing the current ripple has the effects of improvements to converter efficiency and reduces requirements for bulky filtering components.
- **Reduced Size Passive Components** - A ripple reduction also provides the benefit of physically smaller capacitors and inductors.
- **Enhanced Transient Response** - As there are more phases responding to changes in demand, interleaved converters have the ability to respond quicker, relative to non-interleaved equivalents.

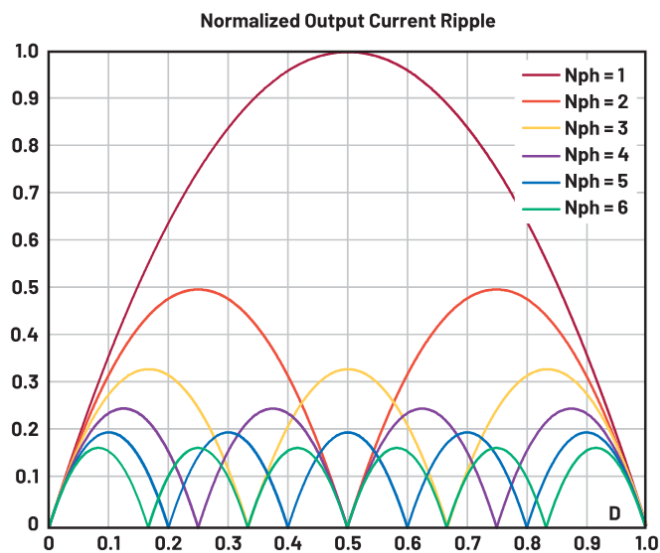


Figure 2.23: Interleaved Buck Converter Ripple Cancellation as a Function of Phases and Duty Cycle [79]

Multiphase Buck converter design is considered practically, in the application notes of [80], which provides a step by step process for the development of a multiphase

buck converter. This reference also reiterates the current cancellation and provides a visual reference for a two phase interleaved buck converter, which is repeated here as figure 2.24, and also shows the duty cycle for each phase, denoted as PH1 and PH2; this also support the relationship between the  $T_{ON}$  of the switch and the increase in current with respects to time.

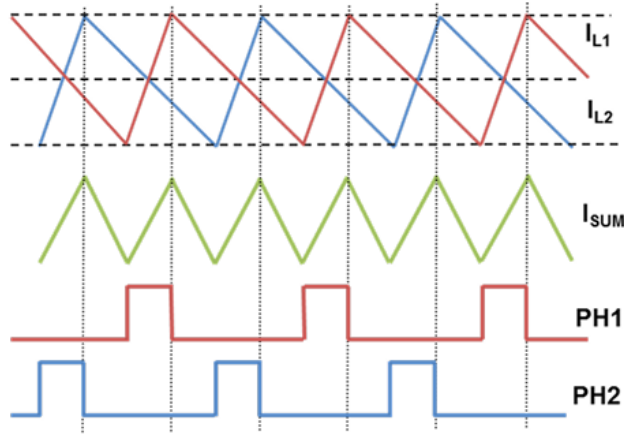


Figure 2.24: Inductor Current Waveforms [80]

From the work of [81], a power-dense, interleaved, bi-directional DC-DC converter for use in automotive applications achieved a power density of 15.7 kW/kg.

## 2.4 Biased Magnetics

This project centers around investigating the effects of mass reduction in converter technology, used onboard aircraft. To support this research effort, and provide some practical meaning to the results of the aircraft simulations, one of the most heavy and voluminous components of the converter, namely, the inductor, whose size and weight places limits on achieving continually higher power densities [82] [83], is investigated in depth, in a bid to provide improvements to converter power density, and volumetric efficiency.

Inductors are considered the largest and heaviest components of the converter. In

certain applications, they rely on magnetic cores, such as ferrites, or laminated steels to store the energy in a magnetic field [84]. When a standard inductor is placed in a unidirectional DC-DC converter, it operates solely in the positive current range, as per figure 2.25. This figure also demonstrates that the linear inductance region in the negative current range remains entirely unexploited.

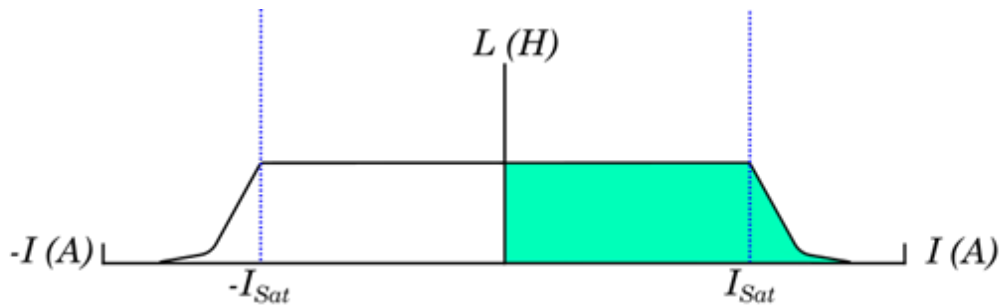


Figure 2.25: Non-Biased Inductor Operating Range

The concept of Permanent Magnet Biased Inductors (PMBI), identified during the 1950's, when applied in a unidirectional DC-DC converter allows the utilisation of the inductance values which would otherwise be only accessible to negative currents, as in figure 2.26. This allows improvements to the power density of the converter, as an inductor which is under 100% bias achieves equivalent inductance values as the non-biased, with only a 50% requirement for the core's cross sectional area or alternatively, only 50% of the required number of turns [85].

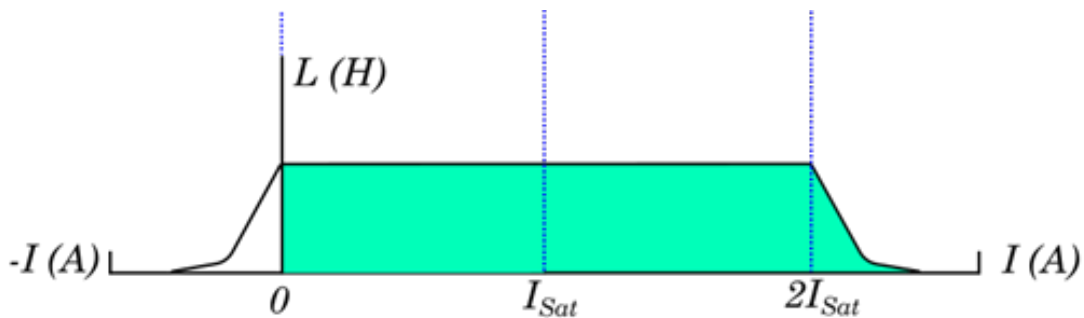


Figure 2.26: Biased Inductor Operating Range

The fundamentals of biasing an inductor are well presented in [86], which begins by highlighting that the saturation limits of ferromagnetic core materials are indepen-

dent of magnetic field polarity, and presents a symmetric saturation flux density,  $B_{sat}$  and  $-B_{sat}$  in the first and third quadrants of the B-H loop. This can be observed in figure 2.27, and how it is related to the linear inductor values for both positive and negative currents.

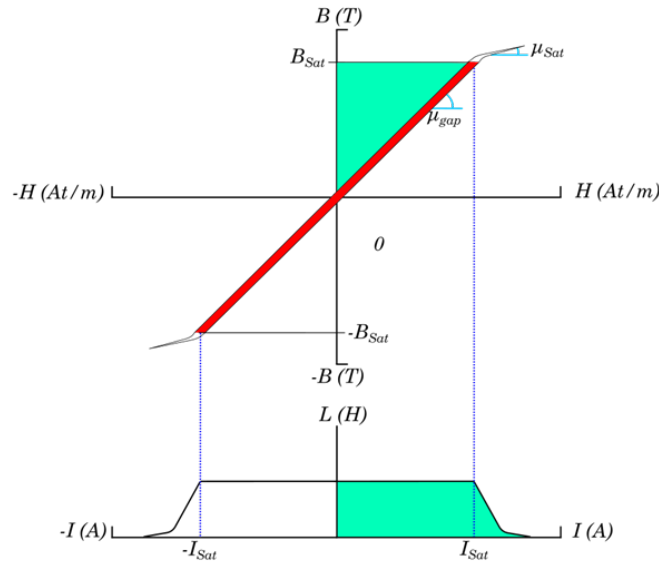


Figure 2.27: Non-Biased Inductor B-H Loop

The magnetic flux circulates through the highly permeable inductor core material, akin to current flowing around an electrical circuit with limited resistance, where  $\mu$  is the permeability in figure 2.27, and its value defines the slope of the BH loop of an inductor. However, the magnetic core which has the advantages of high permeability, has the disadvantage of low capabilities for energy storage; the implementation of an air-gap within the core's length extends the inductors ability to store energy, and who's length determines the linear inductance value, such that an inductor with a 'smaller' air-gap exhibits a larger linear inductance value, with a decreasing saturation current limit, while a 'longer' air-gap, reduces the value of linear inductance, but increases the current limit value. This relationship is validated by the maximum current and inductance product, which must remain constant and equal, when considering the 'small' and 'longer; gap using the same core properties; the inductance current product is given in equation 2.18.

$$L \cdot I_{max} = B_{sat} \cdot A_c \cdot N \quad (2.18)$$

Where:

$L$  = Inductance (H)

$I_{max}$  = Maximum current at saturation point (A)

$B_{sat}$  = Saturation Flux-density (T)

$A_c$  = Core cross-sectional area

$N$  = Number of turns

Using permanent magnets allows for an initial bias to be set into the core. This in turn moves the previously non-accessible linear inductance region from the negative current range, into the positive current range, whereby, at zero current the flux-density is located on the positive scale, in the second quadrant, as per figure 2.28, which shows an inductor with 100% bias. This figure also highlights why the PMBI is used in unidirectional applications; if the current provided to the inductor is in the negative range, saturation will be almost instantaneous, if the PMBI is set at 100% saturation.

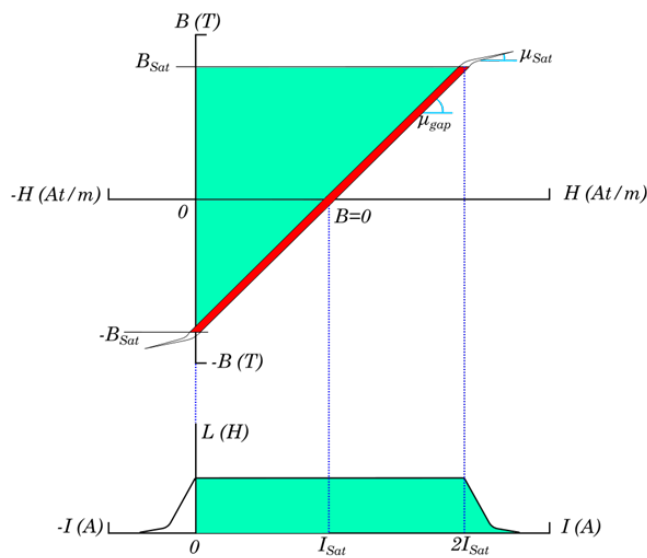


Figure 2.28: Biased Inductor B-H Loop

A standard inductor operates from zero amps, and its maximum flux density increment,  $\Delta B$ , can be defined as the zero to  $B_{sat}$  value, where as a PMBI operates from some bias point in the second quadrant, between zero and  $-B_{sat}$ , up to  $B_{sat}$ . Therefore the flux density increment for a PMBI,  $\Delta B_{PMBI}$  is given as the flux density bias value,  $B_{bias}$ , summed with the core's  $B_{sat}$  value. From [86] the term Bias Improvement Factor (BIF) is introduced, which highlights a ratio between the maximum flux density increment of the PMBI and the non-biased; this is presented as equation 2.19, and can be used to readjust the inductance current product equation, for that of an inductance current equation for a PMBI, given by equation 2.20.

$$BIF = \frac{\Delta B_{PMBI}}{\Delta B} = \frac{B_{bias} + B_{sat}}{B_{sat}} \quad (2.19)$$

$$L \cdot I_{max,PMBI} = \frac{B_{sat} \cdot A_c \cdot N}{BIF} \quad (2.20)$$

For a BIF of 2, where the  $b_{bias}$ , is equivalent to that of  $B_{sat}$ , this indicates that it is possible to attain either twice the value of inductance, or more useful to this research, twice the current. Alternatively, it is possible to reduce either the number of turns, or the core cross-sectional area by 50%, with respects to the non based counterpart. Partial saturation, where the BIF is between 1 and 2, or over saturation where the BIF is greater than 2, may also be useful in certain applications, particularly for the over saturation, where they can be used in applications for high DC currents with smaller AC peak-to-peak currents.

Different design advantages to the inductor, can be achieved depending upon the level of BIF introduced. From [86], an EE core with permanent magnets introduced into the air-gap to achieve a 100% bias and subsequently a BIF of 2; a summary of each of these configurations and improvements is shown in table 2.7

Table 2.7: EE Core Permanent Magnet Biased Inductor Design Variation

Design	Exploited Parameter(s)	Design Benefits
Inductor A	$2I_{\text{sat}}$	<ul style="list-style-type: none"> <li>• 200% <math>I_{\text{sat}}</math></li> <li>• 200% <math>J_{\text{max}}</math></li> <li>• 400% <math>E = L \cdot I_{\text{sat}}^2/2</math></li> </ul>
Inductor B	$N/2$	<ul style="list-style-type: none"> <li>• 50% <math>N</math></li> <li>• 50% <math>J_{\text{max}}</math></li> <li>• 25% <math>R_{\text{DC}}</math></li> </ul>
Inductor C	$A_c/2$	<ul style="list-style-type: none"> <li>• 50% <math>A_c</math></li> <li>• 50% core volume</li> <li>• 70% MLT</li> <li>• 70% <math>R_{\text{DC}}</math></li> </ul>
Inductor D	$A_c/\sqrt{2}$ & $N/\sqrt{2}$	<ul style="list-style-type: none"> <li>• 70% <math>A_c</math></li> <li>• 70% <math>N</math></li> <li>• 80% MLT</li> <li>• 60% <math>R_{\text{DC}}</math></li> <li>• 70% core volume</li> </ul>

---

Inductor 'A' takes advantage of the 100% bias by increasing the saturation current,  $I_{\text{sat}}$ , permitting for the same core size, and DC winding resistance, but allowing for the benefit of doubling of the saturation current to that of,  $2I_{\text{sat}}$ , and this also translates into a capability to store four times the amount of energy, relative to that of the standard inductor, as the energy is proportional to current squared. Reducing the number of turns required by half, such as that seen in inductor 'B', allows for a reduction in the copper losses. Inductor 'C' lends itself well to mass reduction advantages, by reducing the cross sectional area by half translates into a 50% reduction in the core weight, and as an additional benefit, also reduces the winding's Mean Length Per Turn (MLT), by approximately 70%, which in turn, reduces the total winding resistance, relative to the non-biased inductor. Finally, inductor 'D', this differs somewhat to the other inductors, whereby the exploited parameters, are spread between the the cross sectional area, and the number of turns by a factor of 0.707 for each, resulting in a reduction of approximately 70% for the core volume, 80% for the MLT and 60% reduction for the DC resistance, relative to the non-biased equivalent.

The review paper given by [86] does an excellent job at capturing the landscape of research for Permanent Magnet Biased Inductors (PMBI) technology. Additionally it makes use of a considerable number of resources and builds well on the legacy literature of the same topic, such as that from [87], which appears to be their primary source, along with [88].

### 2.4.1 PMBI Materials

The bias flux,  $\phi_{\text{bias}}$ , and the permanent magnet's properties for the PMBI, have a dependency on the  $B_{\text{sat}}$  of the inductor core material, and the operational frequency. Whereby, operations at higher frequencies require a core material with a higher resistivity. [86] provides a useful figure, showing the saturation flux density, and

remanent flux density for soft magnetic materials, and hard magnetic materials respectively; this figure is recreated here, for the readers convenience, given as, figure 2.29.

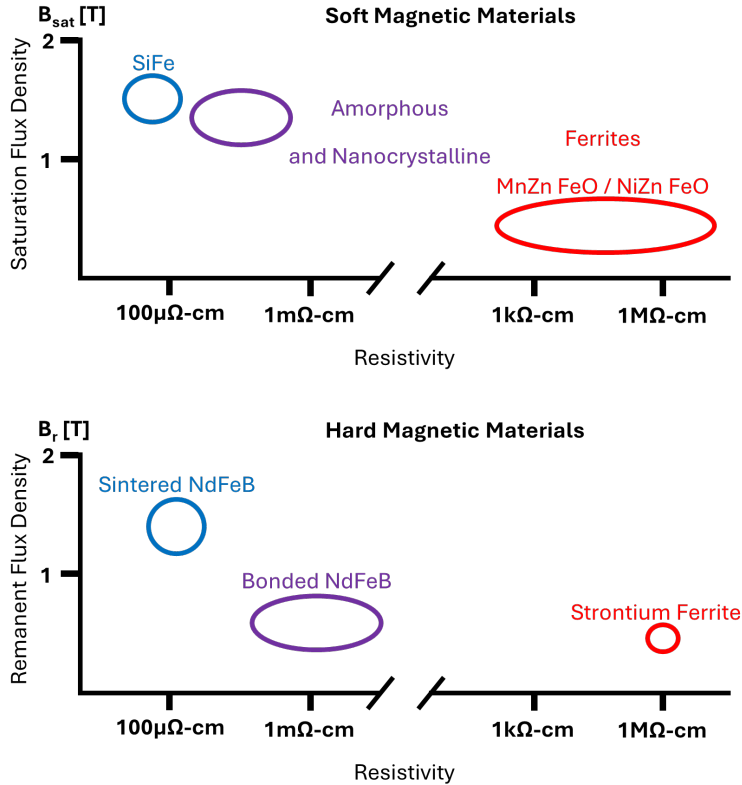


Figure 2.29: PMBI core and permanent magnet materials

It is also stated that from the soft magnetic materials, SiFe laminations used for the core, offer a high saturation flux density, in combination with a low resistivity, making them useful for applications at lower frequencies; less than 1 kHz. On the opposite end of the scale, the ferrites MnZn and NiZn demonstrate a somewhat lower saturation density, but offer a much higher electrical resistivity, making them suitable for higher frequency operation; approximately 500kHz for MnZn [89], and approximately 3MHz for NiZn [90]. The Nanocrystalline and amorphous offerings [91] provide a higher resistivity relative to the the SiFe material, and offer saturation values in the same region.

It stands to reason that a core material which is slated as having a high saturation flux density value,  $B_{sat}$ , requires suitable magnets to be able to provide equivalent

Table 2.8: Permanent Magnet Material Grades and Parameters

	Sintered Neodymium NdFeB	Sintered Samarium Cobalt, SmCo	Bonded Neodymium NdFeB	Strontium Ferrite
$B_{r_{min}}$ [T]	1	0.9	0.3	0.2
$B_{r_{max}}$ [T]	1.48	1.1	0.76	0.45
$H_{c_{min}}$ [kA/m]	780	600	160	125
$H_{c_{max}}$ [kA/m]	915	800	517	288
$H_{cj_{min}}$ [kA/m]	955	1200	398	210
$H_{cj_{max}}$ [kA/m]	2786	1830	1230	400
$BH_{max}$ [kJ/m <sup>3</sup> ]	256	200	110	24
Permeability $\mu_r$	1-1.1	1-1.2	1.2-1.5	1.1-1.3
Resistivity $\rho$ [Ω-cm]	$150 \cdot 10^{-6}$	$100 \cdot 10^{-6}$	$14 \cdot 10^{-3}$	$>10^6$
Curie Temp. $T_c$ [°C]	310	727-825	360	460
Temp <sub>d</sub> Coef Br [%/°C]	-0.12	-0.001-0.045	-0.1	-0.18
Temp <sub>B</sub> Coef Hcj [%/°C]	-0.6	-0.02-0.3	-0.4	0.4

saturation values, where a 100% bias or over saturation is specified. From [86], a table of permanent magnet materials and grades are presented, in table 2.8, and it is commented that Neodymium permanent magnets are typically found in sintered form, and achieve the highest value for energy products,  $BH$ , and offer a seemingly low resistivity, while the Strontium-Ferrite material, yields the greatest resistivity, it does possess a lower maximum energy product,  $BH$ .

Of particular interest, due to the aerospace related nature, and featuring a magnetically biased inductor, is the work of [92], which details a magnetically biased inductor for an aerospace switched reluctance drive. In this particular study, a relatively unseen core configuration with respects to biasing, as seen in other papers is used. A pot-core construction using soft magnetic composite materials is investigated in this study, and a figure of this topology, with the magnets identified is available in figure 2.30. Rather than an inductor designed for energy storage in a converter, this particular application uses the bias flux from the permanent magnets to help reduce the ripple currents brought about by the switched reluctance machine, in a bid to reduce the DC-link capacitance required in the drive system. Additional novelty was introduced when the pot-core topology was located axially with the DC-link capacitors, in a bid to reduce the overall system volume, as well

as support the reduction in ripple current. From [86], this particular study have achieved a 10% bias, which may appear minimal, but any greater value of BIF, maybe in excess of the bias flux required to cancel the currents.

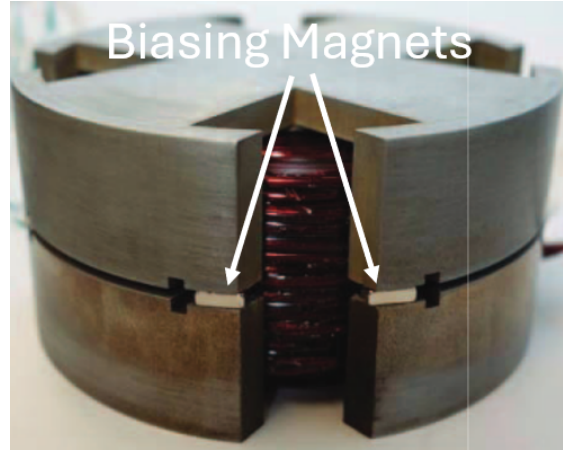


Figure 2.30: Permanent Magnet Biased Inductor for Current Ripple Filtration in an SRM drive system [92]

From [1] a patent is presented, and details a biased inductor topology which permits for permanent magnets to be used outside of the airgap, and placed on an external face between two cores, such that a magnetic flux path is established, and circulates through both cores uni-directionally, taking the path of least reluctance. This can be visualised using the figure 2.31, taken directly from the patent. This particular topology in combination with the concept of the interleaved converter opens up the potential of applying a single set of biasing magnets to the inductor cores, in order to increase the power density of the converter, through either a reduction in core mass, and volume, or through leveraging the additional current gain before saturation; this concept is depicted in figure 2.32.

## 2.5 Conclusion

In conclusion, and based on the literature reviewed, there is a clear need to quantify the effects of mass reduction resulting from technological improvements. How-

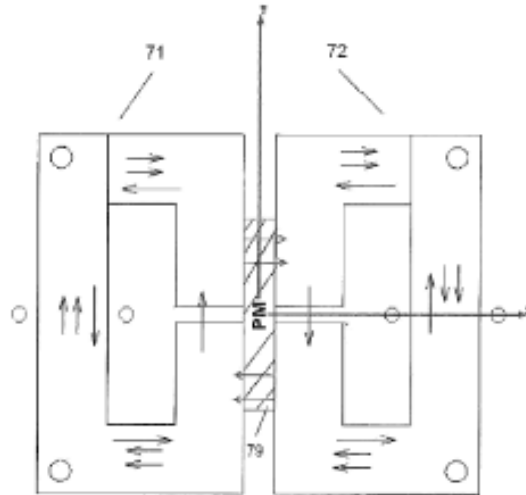


Figure 2.31: Patented Permanent Magnet Biased Inductors (PMBI) Core Topology [1]

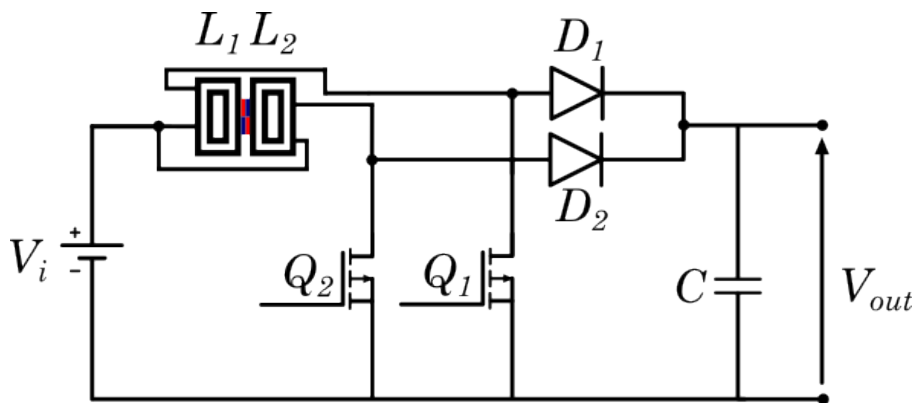


Figure 2.32: PMBI Inductors in a Multiphase Boost Converter

ever, implementing every component or subsystem in full detail would lead to a model of excessive complexity. To address this, a simplified modelling approach is adopted, to represent the primary components of the propulsion system, including the motor, inverter, converter, and power management system. The masses of these components are determined as functions of their respective power density, and the aircraft's power requirements, enabling the development of sizing tool, balancing computational efficiency, with high model fidelity.

Furthermore, gaps in the literature highlight the requirement for a parametric model capable of incorporating the transient behaviour of fuel cell power, during changes

in load, and for modelling the subsequent requirement for supplementary power support from additional sources, such as a battery or super capacitors. In response this research proposes a fuel cell model which factors in transients based on fuel cell technology level, while requiring only minimal user inputs.

Although a number of drag polars have been identified in the literature, the influence of their selection on overall aircraft mass remains undocumented. Further investigation into this relationship is therefore proposed as another key contribution from this study.

The second work package considers a specific focus on the PMBI technology. Using the proposed topology for the core biasing presented in [1], in conjunction with an interleaved converter, there is potential to yield an increase in specific power density for a converter when compared to an equivalent converter using standard non-biased magnetics, and additional, original research garnered from adopting the topology identified in [1], in a practical experimental DC-DC converter rig.

Although efforts to capture as much pertinent information to support the project has been undertaken, and presented in the literature review, the reader will also encounter a number of additional, relevant and important references throughout this document, which have been put in place to support the development of models and methodologies as and when presented.

---

## Chapter 3

# Hydrogen-Electric Aircraft

## Modelling

Determination of the optimal propulsion system configuration, and thus the influence on the corresponding components required for the DC-DC converters, specifically the passive components, relies on the modelling of a conceptual hydrogen-electric aircraft.

A methodology, and complimenting sizing tool, for such has been developed, and is presented in flowchart form, in figure 3.1. Initial inputs are used, and cascaded down through a series of functions, which will be discussed in their respective chapters. In order to guide the reader through the methodology flowchart, and to substantiate the minimum inputs or alternatives to the input recommendations required for the tool, chapter 3.1 (below) is provided.

For fulfilment of the 'Input Parameters' block, a reference aircraft has been selected for the purposes of extracting Top Level Aircraft Requirements (TLARs) and mission requirements. The aircraft in question is the 19 seat, CS-23 category, commuter aircraft, Dornier/RUAG Do228NG; shown in figure 3.2. In addition to

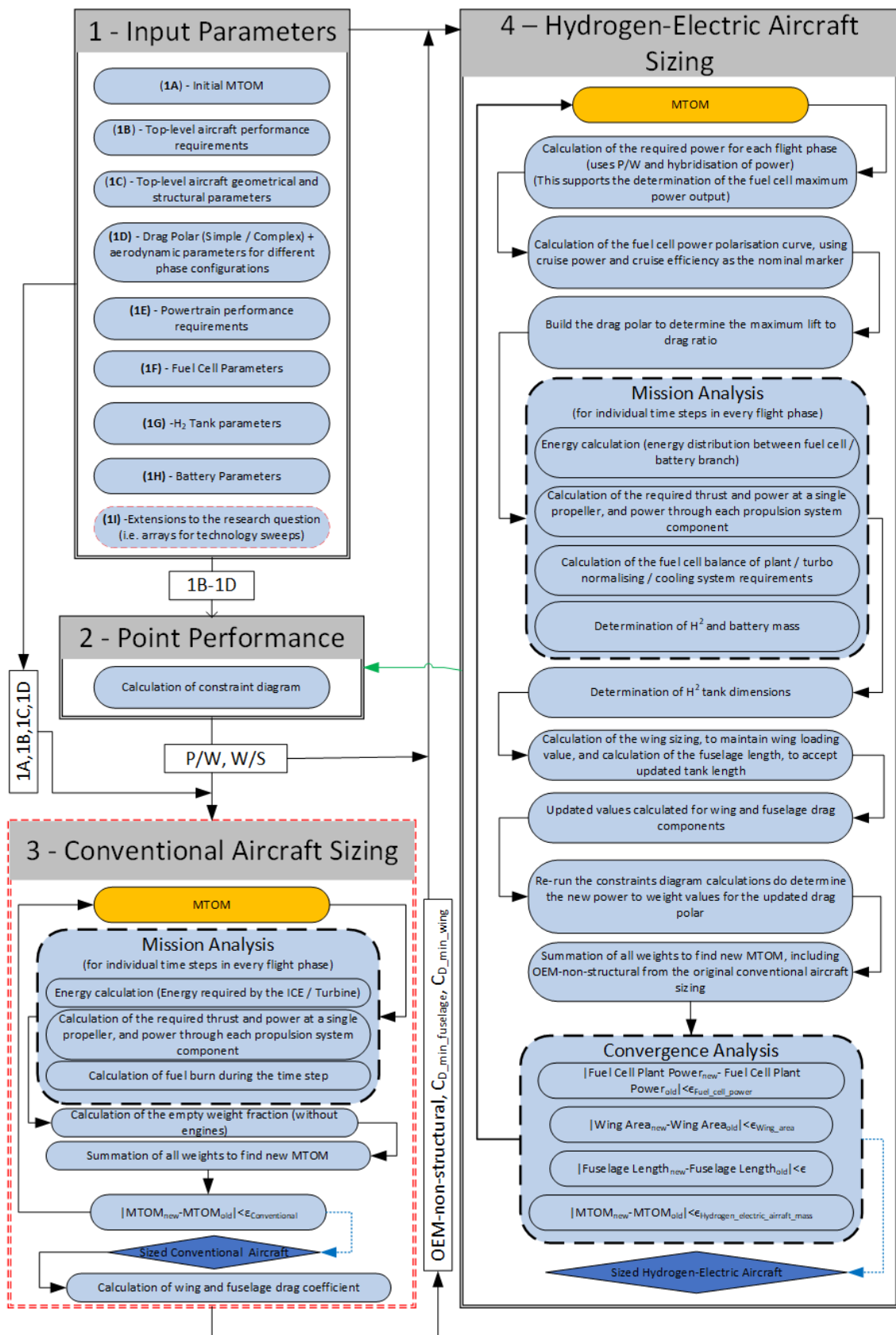


Figure 3.1: Methodology Flow Chart

---

being used as the test bed for ZeroAvia’s hydrogen-electric propulsion aircraft campaign, this aircraft has been the subject of numerous studies for hybridisation, CFD drag polar extrapolation, and hydrogen propulsion conversion, as well as being supported by available performance data; making it an ideal candidate for this study [7][38][93][21][94].

In order to make the sizing tool applicable to use cases where aircraft data is unavailable, this author offers alternative equations and generic values, available from literature in the public domain, which can be used as inputs into the model. The major draw back to this, comes in the form of limited accuracy, due to the potential for generic values to propagate mass compounding factors, leading to erroneous masses for some of the aircraft components or fuel masses. As such, no study will be completed using these generic values, and they are included purely for reference purposes and to highlight that it is possible to size a hydrogen-electric aircraft with limited resources, or the necessity to complete complex computational fluid dynamics (CFD) studies.



Figure 3.2: Do28NG Hydrogen Propulsion Test Bed [95]

## 3.1 Model Input Parameters and Methodology Navigation

The technical discussion, and corresponding equations for each section of the methodology flowchart are presented separately, within their respective chapters. This section aims to outline the minimum set of inputs required by the simulation tool, and to provide additional context and navigation for each section of the flowchart, as well as an understanding of the interactions between the subsystems.

Focusing initially on section 1, identified as 'Input Parameters', input 1A, specifies the requirement for an initial Maximum Take Off Mass (MTOM). The simulation tool requires this initial value to be entered by the user, serving as a starting point for the simulation. The selection of the initial MTOM is, to a certain extent, at the user's discretion; however, to improve convergence time and assist the simulation in identifying an optimal aircraft configuration for the mission, it is recommended that the selected value reflects that of an equivalent conventional aircraft within the same class. Several resources provide guidance for determining this initial mass, notably [96] [19], which offer empirical data for existing aircraft of the class, and methods for estimating an initial MTOM, respectively.

With an initial mass defined, the next step is to incorporate the aircraft performance parameters into the model inputs. These are denoted in flowchart section 1, as inputs 1B, the 'Top-level aircraft performance requirements', TLARs, which are discussed in detail, within their respective subchapter. To provide initial context, however, a brief overview is also presented here.

The TLARs consist of several performance specifications that the designed aircraft is expected to be able to achieve. They are derived through a combination of regulatory requirements, issued by governing aviation bodies, including European Aviation Safety Agency (EASA), the Civil Aviation Authority (CAA) and the Federal

Aviation Administration (FAA), each of which defines minimum standards, such as aircraft maximum stall speed, one engine inoperative (OEI) climb out performance, reserve fuel and diversion requirements.

In addition to the aforementioned regulatory requirements, customer and market requirements also inform the TLARS. These include parameters such as payload (which can be constituted from passengers, cargo, or a combination of both), range and cruise speed. Airlines typically perform extensive trade studies, and market analysis to ensure that the next generation of aircraft within their fleet, permit for viable and economically sustainable operations.

A further user defined input, referred to as the 'throttle constraint' is also necessary. This constraint ensures that the aircraft operates at a full power condition, only during take-off, consistent with the operating limits of the motor(s), which generally, have the capability to operate at full power conditions, for short durations only; in the order of a few seconds. The throttle constraint is a unitless factor, where take-off and climb with one engine inoperative, are assigned a value of 1, and subsequent flight phases defined as a fraction of full power. In this study, values of 0.9 are used for climb (with all engines operating), and 0.8 for cruise, loiter and diversion phases, with 0 assigned for descent.

For the calculation of the take-off parameters, additional environmental inputs are required, including the aircraft's starting altitude, as well as the runway friction coefficient. Published data provides typical values for various runway materials; here, a value of 0.04 is adopted, representing a concrete runway.

The final input for the TLARs, pertains to propeller efficiency across different phases of the flight. Propeller efficiency is primarily determined by the propeller configuration. Fixed pitch propellers achieve peak efficiency values within a narrow flight regime, while constant speed propellers can vary the blade pitch, to maintain higher values of efficiency across multiple phases of flight. Representative efficiency values

Table 3.1: **1B** - Top Level Aircraft Requirements - Performance

Parameter	Unit	Parameter	Unit
Take off distance	Meters	Diversion speed	Meters per Second
Start airport altitude	Meters	AEO ROC at SL	Meters per Second
Cruise altitude	Meters	OEI ROC at SL	Meters per Second
Destination airport altitude	Meters	Range	Kilometers
Diversion altitude	Meters	Diversion range	Kilometers
Loiter altitude	Meters	Loiter time	Minutes
Cruise speed	Meters per Second	Payload	Kilograms
Stall speed	Meters per Second	Reserve fuel	Percent
Take off throttle constraint	[-]	Climb throttle constraint	[-]
Cruise throttle constraint	[-]	Diversion throttle constraint	[-]
Loiter throttle constraint	[-]	Descent throttle constraint	[-]
Propeller efficiency	[-]	Runway friction coefficient	[-]

for each of these propeller variations may be obtained from stalwart aircraft design references, manufacturer data, or advanced analysis, such as blade element theory.

The values used in the simulation for the Dornier 228, taking advantage of the constant speed propeller, are based on the work of [21], [20] and [19]. The specific values for which, are 0.8 (i.e, 80% efficiency), for all flight phases. The complete list of TLARs inputs, along with their respective units, are presented in table 3.1.

To develop the aircraft sizing and simulation tool, such that it has the capability to determine the total aircraft mass for an optimally sized propulsion system, it is necessary to provide sufficient input parameters to enable the calculation of the geometry and mass of the primary structural components, namely the airframe. The determination of the structural mass is addressed progressively, beginning in chapter 3.4. For this process to occur, a number of geometrical and structural parameters must be supplied as inputs, as specified in section 1, inputs 1C, 'Top-level aircraft geometrical and structural parameters'; all of which are listed in table 3.2, and discussed further within this chapter.

It should be noted that an asterisk is placed against the Operational Empty Mass (OEM) fraction, and the Specific Fuel Consumption (SFC) in the table. These

parameters pertain exclusively to the optional conventional aircraft sizing routine, described by section 3, 'Conventional Aircraft Sizing', and are explained in greater detail, later in this subchapter.

Several of the parameters listed in table 3.2 are used to initialise the simulation tool, but will vary throughout the aircraft resizing process. For example, an increase in fuselage length to accommodate the H<sub>2</sub> tank(s), results in a corresponding increase in fuselage area, and consequently overall aircraft mass will increase. This mass increase necessitates the resizing of the wings, thus increasing the wing span, and area values.

Parameters expressed as ratios, such as aspect ratio, or thickness to chord ratio, remain constant throughout the aircraft sizing process, and are therefore hard-coded into the tool. Similarly, fuselage width and height, remain as fixed values, and are not subject to variation.

The source of certain parameters, such as structural surface area, tail arm length, or thickness to chord ratios, may require additional clarification. Thickness to chord ratios are a function of the chosen airfoil, and can be obtained from online databases, such as that of the NACA repository [63]. Where the airfoil is unspecified, representative textbook values may be used. Likewise, aircraft surface areas, and tail arm lengths, can be estimated using legacy data, such as those presented by [45], or derived by referencing comparable existing aircraft. Alternatively, modern open source tools, such as openVSP, can be employed to generate useful values, as will be demonstrated in chapter 3.5.

As outlined in the objectives of this study, an investigation is conducted to evaluate how variations in the selected drag polar influence the resulting aircraft mass. To facilitate this analysis, a number of aerodynamic inputs are required to populate the variables within each respective drag polar, and provide the aerodynamic data necessary for constructing the constraints diagram. The concept of the constraints

Table 3.2: **1C** - Top Level Aircraft Requirements - Geometry & Structure

Parameter	Unit	Parameter	Unit
Wing area	Sq. Meters	Wing aspect ratio	[-]
Number of propellers	[-]	OEM fraction*	[-]
Wing 25% MAC sweep	Meters	Wing taper ratio	[-]
Aircraft ultimate load factor	G. Constant	Wing t/c ratio	[-]
Horizontal tail area	Sq. Meters	Horizontal tail 25% MAC sweep	Meters
Horizontal tail taper ratio	[-]	Horizontal tail aspect ratio	[-]
Horizontal tail span	Meters	Vertical tail height	Meters
Vertical tail area	Sq. Meters	Vertical tail t/c ratio	[-]
Vertical tail 25% MAC sweep	Meters	Horizontal tail t/c ratio	[-]
Vertical tail taper ratio	[-]	Tail arm length	Meters
Fuselage surface area	Sq. Meters	Fuselage length	Meters
Fuselage height	Meters	Fuselage width	Meters
Wing Span	Meters	SFC*	Kg/(KW or N)/hr

Table 3.3: **1D** - Top Level Aircraft Requirements - Aerodynamic Inputs

Parameter	Nomenclature
Minimum drag coefficient	$C_{D,min}$
Take off drag coefficient	$C_{D,TO}$
Take off lift coefficient	$C_{L,TO}$
Maximum lift coefficient	$C_{L,max}$
Lift induced drag constant	K
$\Delta$ CLmax take off flaps	$\Delta C_{L,max,Take-off}$
$\Delta$ Clmax landing flaps	$\Delta C_{L,max,Landing}$
Lift coefficient at $\alpha_0$	$C_{L,0}$
Oswald's span efficiency factor	e

diagram was discussed within the literature review, and is subsequently analysed for the Dornier 228 case study in chapter 3.3, and appearing as the 'calculation of the constraint diagram' within section 2 of the methodology flowchart. Table 3.3, titled 'Aerodynamic Inputs', provides context for section 1, inputs 1D, and lists the specific parameters used. A detailed discussion of these aerodynamic inputs, including rationale for their selection and methods for determining each value is presented in chapter 3.2; prior to the construction of the constraints diagram.

In section 1, inputs 1E, the requirement arises to define performance parameters for the primary powertrain components, excluding the battery and fuel cell. For the purposes of this project, the powertrain comprises of the motor(s), inverter(s),

Table 3.4: **1E** - Top Level Aircraft Requirements - Powertrain Performance Inputs

Parameter (Nomenclature)	Unit	Parameter (Nomenclature)	Unit
Gearbox efficiency: $\eta_{gb}$	[-]	Motor efficiency: $\eta_{em}$	[-]
Inverter efficiency: $\eta_{inv}$	[-]	DC-DC Converter efficiency: $\eta_{dc-dc}$	[-]
PMAD efficiency: $\eta_{pmad}$	[-]	Fuel Cell (cruise) efficiency: $\eta_{fc}$	[-]
Motor PD: $\hat{\rho}_{em}$	[kW/kg]	Motor VPD: $v\hat{\rho}_{em}$	[kW/m <sup>3</sup> ]
Inverter PD: $\hat{\rho}_{inv}$	[kW/kg]	Inverter VPD: $v\hat{\rho}_{inv}$	[kW/m <sup>3</sup> ]
Converter PD: $\hat{\rho}_{dc-dc}$	[kW/kg]	Converter VPD: $v\hat{\rho}_{dc-dc}$	[kW/m <sup>3</sup> ]

DC-DC converter(s) for both fuel cell and battery, and the power management and distribution equipment responsible for handling the power split, according to the selected level of hybridisation. Each of these components requires the specification of its specific power, also referred to as power density (PD), and its efficiency, which are entered as inputs into the sizing tool.

Additionally, the propeller is mechanically coupled to a gearbox, which follows its own dedicated sizing process, detailed in chapter 3.9. Accounting for the gearbox efficiency allows assessment of its impact on the overall propulsion system sizing, and additionally, enables future investigations into novel, high efficiency propeller or gearbox technologies.

The volumetric power density (VPD) of each component can also be included as an optional input, supporting studies that consider the interactions between airframe volume and propulsion system layout; however, these parameters are not essential for a purely mass based sizing study. Table 3.4, summarises all of the necessary propulsion system inputs, including the non-essential VPD parameters.

Finally, while this work assumes constant efficiency values for all components (with the exception of the fuel cell), it would be possible to extend the methodology by incorporating more advanced efficiency models or component efficiency maps. Such enhancements could yield greater fidelity in future studies of powertrain performance and integration.

Table 3.5: **1F** - Top Level Aircraft Requirements - Fuel Cell Performance Inputs

Parameter	Unit	Parameter	Unit
Fuel Cell PD	Kilowatts per kilogram	Fuel Cell Time Constant	Seconds
Fuel Cell Efficiency at cruise	[-]	Fuel Cell VPD	[kW/m <sup>3</sup> ]

One of the novel components of this project, identified through gaps in previous research, concerns the implementation of a fuel cell model with a dynamic response to variations in aircraft power demand across different flight phases, as well as the selection of the operational efficiency during the cruise segment of the mission profile. The modelling of the fuel cell is addressed in detail, within its dedicated section; chapter 3.7.1.

To simplify the model for use within the sizing framework, the fuel cell is represented through a concise set of user defined inputs, denoted in section 1, as inputs 1F, 'Fuel Cell Parameters', within the methodology flowchart. These required parameters include the specific power of the fuel cell, the dynamic response time,  $\tau$ , and the desired efficiency at cruise.

Further clarification of the fuel cell response time, is provided later in the text. In brief, it represents the technological responsiveness of the fuel cell system, showing how rapidly it can adapt to changes in power demand, influenced by component level characteristics, such as balance of plant dynamics or the performance of turbo-normalising compressors, as well as the reaction rates of the fuel cell electrolyte membrane material.

By enabling user defined control, over the fuel cell power density, response time, and cruise efficiency point, the model support a broad range of trade studies. These studies allow for assessment of the potential performance and operational benefits associated with higher fuel cell technology readiness levels. Table 3.5, highlights the aforementioned parameters, and their respective units.

In support of the fuel cell hydrogen system as a whole, it is necessary to define the

Table 3.6: **1G** - Top Level Aircraft Requirements - H<sub>2</sub> Storage Tank Performance Inputs

Parameter	Unit	Parameter	Unit
Tank storage efficiency	[-]	Tank radius	Meters
Hydrogen storage temperature	Kelvin	Hydrogen storage pressure	Pascals

technology level of the H<sub>2</sub> storage tank; corresponding to section 1, inputs 1G, 'H<sub>2</sub> Tank Parameters', within the sizing methodology flowchart. Akin to the inputs for the power train, the H<sub>2</sub> tank also adopts the principle of efficiency; however, in this scenario, it refers to storage efficiency, i.e., the storage capability as a function of the mass or volume of the contained hydrogen. This concept is expanded upon in much greater detail in chapter 3.7.4. The density of the hydrogen within the tank, which also supports the sizing process, requires the input values for the hydrogen storage temperature at altitude, and the associated storage pressure. Table 3.6, presents the required parameters for the determination of the hydrogen storage tank sizing. The tank radius, is taken as half of the fixed fuselage width. A dedicated optimisation study exploring alternative tank sizes and configurations presents an opportunity for an extending the current sizing tool, and for further research.

The final, major element of the sizing inputs in section 1, pertains to the battery, defined as input 1H, 'Battery Parameters'. The inputs required for the battery model are comparatively few , and include the specific power, the specific energy (ED), battery efficiency, deep discharge protection limit, and discharge rate. These parameters are consistent with the discussion in the literature review, and are representative of a battery model that does not explicitly incorporate a discharge curve, as observed for some of the more advanced battery modelling approaches. All battery parameters and their respective units are presented in table 3.7.

A final, optional input is also available within the sizing methodology. This input, denoted by inputs 1I, 'Extensions to the research question (i.e. arrays for technology sweeps)', is represented by a dashed red line in section 1, of the flowchart. It

Table 3.7: **1H** - Top Level Aircraft Requirements - H<sub>2</sub> Battery Parameter Inputs

Parameter	Unit	Parameter	Unit
Battery PD	Kilowatts per kilogram	Battery efficiency	[-]
Battery SE	Kilowatts per Hour	Battery deep discharge protection	[-]
Battery discharge rate	[-]		

allows any of the preceding single value inputs to be replaced with arrays of values, thereby enabling the sizing tool to perform parameter sweeps. These sweeps permit for the determination of the optimal aircraft mass and configuration for multiple variable sets that would otherwise be treated as singular inputs.

For example, in this project, technology level sweeps are conducted for the DC-DC converter power density. However, this optional input capability allows for multi-variable sweeps, such as simultaneously varying both battery discharge rate and specific power, to assess how advancements in battery technology could influence the overall mass of the aircraft relative to current battery technologies.

With a complete understanding of the system inputs, it is now possible to provide context as to how the inputs propagate throughout the methodology, and interact within the process flow. Specifically, inputs 1B, 'Top-level aircraft performance requirements', and 1D, 'Drag Polar (Simple / Complex) + aerodynamic parameters for different phase configurations', are utilised in section 2, 'Point Performance'.

The point performance stage, concerns the construction of the constraints diagram, previously introduced in the literature review, and expanded upon, with the associated equations in chapter 3.3. The primary purpose of the constraints diagram is to determine the required power to weight, ( $P/W$ ), as a function of wing loading, ( $W/S$ ), defined as the aircraft weight divided by a wing area, for each performance constraint line. Each line is governed by a unique set of equations, corresponding to a specific flight phase, or performance condition.

Once values for the power to weight ratio and wing loading have been established for

all flight conditions, the methodology advances to section 2. If the non-structural operational empty mass of the aircraft (excluding propulsion system), along with the conventional fuselage and wing parasitic drag coefficients,  $C_{D,\min,\text{fuselage}}$  and  $C_{D,\min,\text{wing}}$ , are already known and hard coded, the hydrogen-electric aircraft sizing process proceeds directly into section 4. However, if these parameters are not yet defined, section 3, 'Conventional Aircraft Sizing' becomes active, providing the necessary foundation, before transitioning into the main hydrogen-electric sizing routine.

The premise of section 3, 'Conventional Aircraft Sizing', is to correctly size the baseline conventional aircraft, that will later be adapted to incorporate a hydrogen-electric propulsion system. This process enables a detailed breakdown of the aircraft masses, allowing for the extraction of the non-structural operational empty mass (OEM). In addition, the parasitic drag components of the conventional configuration, namely  $C_{D,\min,\text{fuselage}}$  and  $C_{D,\min,\text{wing}}$ , are evaluated. These values are subsequently required during the hydrogen-electric aircraft sizing routine, as changes in the wing and fuselage geometry will alter the corresponding drag characteristics.

To perform the conventional sizing, the methodology calls upon several key inputs from section 1, these being, inputs 1A, 'Initial MTOM', the starting point initial MTOM estimation, input 1B, 'Top-level aircraft performance requirements', 1C, 'Top-level aircraft geometrical and structural parameters' and 1D, 'Drag Polar (Simple / Complex) + aerodynamic parameters for different phase configurations'.

Within section 3, a new methodology, involving an energy based mass calculation regime is adopted. As discussed in the literature review, this method evaluates the energy consumption for each time step, including the energy losses, derived through the use of component efficiency chains. These energy values are translated into power, which is subsequently related to a series of fuel burn equations. When integrated across the entire mission profile, the method yields the total mission fuel

mass requirement.

The total aircraft mass is then determined through the summation of the fuel mass, propulsion system mass, payload mass, and the structural and non-structural masses, determined through the operational empty mass fraction (discussed in chapter 3.4). This produces an updated aircraft mass, 'MTOM<sub>new</sub>', which is compared against that of the previous iteration, 'MTOM<sub>old</sub>'. The process repeats until the absolute difference between these values satisfies the user defined convergence criterion,  $\epsilon_{Conventional}$ , which is set according to the desired simulation accuracy .

Once convergence is achieved, the finalised aircraft configuration is passed to a subroutine that calculates the refined parasitic drag coefficients for both the wing and fuselage. With the non-structural operational empty mass and drag coefficients established, section 3 successfully completes its role within the overall sizing methodology.

Section 4, 'Mission Performance', utilises all inputs defined in section 1 ('Input Parameters'), together with the outputs from section 2 ('Point Performance'), and section 3 ('Conventional Aircraft Sizing'). The process begins as in section 3, with input 1A, an initial estimate for the aircraft's MTOM. This value is iteratively updated until all convergence criteria are realised.

The corresponding power to weight ratio and wing loading values are then used to determine the power requirements for the fuel cell and associated ancillary systems. The cruise power is used to define the nominal power of the fuel cell, while a check is performed to ensure that the system is capable of supplying take-off power, where this is required, by the current level of hybridisation being investigated.

A 'Mission Analysis' is subsequently conducted, which accounts for every time step of the flight profile. During this analysis, the energy demand for each component is calculated, accounting for its efficiency, and position within the propulsion

system architecture. This data is then passed to the appropriate subroutine to determine the power requirements of the fuel cell, its balance of plant (BoP), the turbo-normalising compressor and the cooling system. Simultaneously, the battery energy demand is assessed according to the hybridisation of power level, and any in-flight recharging requirements are incorporated. The instantaneous  $H_2$ , and battery masses are also updated at each time step.

Once the mission analysis is complete, the  $H_2$  tank is dimensioned. The tank width is held constant, while its length is permitted to increase as required. This growth in the tank length necessitates a lengthening of the fuselage, which is implemented within the geometry recalculation subroutine. Within this routine, the wing geometry is also resized to maintain the prescribed wing loading.

Following the geometric update, the parasitic drag of the wings and fuselage is recalculated. The revised drag coefficients alter the drag polar, which in turn effects the constraint diagram established in section 2. Consequently, the constraint diagram subroutine is invoked once again (as indicated by the green arrow on the diagram), to update the power to weight ratios, based on the new aerodynamic properties. If mass convergence has not yet been achieved, a new iteration of the sizing loop is initiated.

As in Section 3, a summation of all mass components is performed at the end of each iteration. However, the hydrogen-electric aircraft sizing routine in section 4, introduces additional convergence criteria. Each mission analysis run, may trigger a resizing of the fuel cell, thereby altering the hydrogen mass, balance of plant, and cooling requirements. These changes influence the fuselage length, wing area, and aerodynamic characteristics, which in turn modify the fuel cell power demand, creating an iterative feedback cycle.

These stopping criterion are denoted as  $\epsilon_{Fuelcellpower}$ , for the fuel cell stopping criterion, the units for this particular criterion are in Watts, and the tool user can

define a value suitable for the simulation requirements. The next stopping criterion is  $\epsilon_{Wingarea}$  which checks convergence for the wing area, and is given in the units of meter; The stopping criterion here should be minimal, to ensure that the wing is not unnecessarily over-sized. The fuselage stopping criterion, also in meters, is given by  $\epsilon_{Fuselagelength}$ , and this detects any additional growth brought about by the hydrogen tank resizing. Finally, just as with section 3, a stopping criterion to detect convergence on the mass is given as the final requirement for the tool to meet; this is denoted as  $\epsilon_{Hydrogenelectricalaircraftmass}$ , and as before, the units are in kilograms. Once all of the stopping criterion are satisfied, the process is completed, and the methodology moves into the 'Sized Hydrogen Electric Aircraft' diamond, of section 4, and the aircraft with the selected figure of merit, which in this scenario is that of the lowest mass, is correctly sized.

The preceding descriptions of the sizing process, and methodology, at this stage may appear to be somewhat lacking in technical information, and give rise to additional questions from the reader, regarding some of the finer details of the sizing steps. These questions and ambiguities aim to be closed within the main body of the thesis.

## 3.2 Top Level Aircraft Requirements and Aerodynamic Assumptions

The reference aircraft for the model is sized for a given set of top level requirements and mission requirements, including reference speeds, distances and contingencies, all with respects to the necessary certification requirements, akin to that of the real aircraft, which in this scenario, are taken from the CS-23 easy access rules for normal, utility, aerobatic and commuter category aircraft regulations [97], pilots operating handbook, and the aforementioned previous studies, which will be placed

### 3.2. TOP LEVEL AIRCRAFT REQUIREMENTS AND AERODYNAMIC ASSUMPTIONS

Table 3.8: Top Level Aircraft Requirements [94]

Parameter	Value	Parameter	Value
Take off distance (m)	793	Diversion Speed (m/s)	85
Start airport altitude (m)	0	AEO ROC at SL (m/s)	8
Cruise altitude (m)	3000	OEI ROC at SL (m/s)	2
Destination airport altitude (m)	0	Range (km)	396
Diversion altitude (m)	1000	Diversion range (km)	270
Loiter altitude (m)	450	Loiter time (min)	30
Cruise speed (m/s)	115	Payload (kg)	1960
Stall speed (m/s)	34.5	Reserve fuel (%)	5

in competition in order to yield the most accurate set of inputs into the sizing tool. These competing values are shown in table 3.8 [94], from herein referred to as study A, and table 3.9 [38], from herein referred to as study B, for their respective studies. It can be seen that table 3.8 is somewhat more populated for parameters pertaining to diversion and loiter requirements. However, the data presented within table 3.9 is consistent with 3.8, with the exception of the stall speed constraint, which shows a 10.5% increase; the influence from this will be available to see during the later discussion of the constraints diagram. The reader at this point may question the necessity of looking across two separate sets of values for resizing an aircraft, and the logic behind this decision can be quite simply stated as the following; a study may appear to be comprehensive, with complex computational fluid dynamics and complex equations, however this does not necessarily mean that it is correct, and vice-versa, a somewhat more 'simple' looking study may not present the most high fidelity equations or analysis, but the value of the study when used in a slightly different context may lead more acceptable results for the new study in question. Additionally, the author would also like to observe the potential for any diminishing returns that may result from expending time into pursuing high fidelity aerodynamic models, relative to those taken from text books, and other data already available in the field.

In addition to the TLARs, there is also a requirement for a complementing set of

### 3.2. TOP LEVEL AIRCRAFT REQUIREMENTS AND AERODYNAMIC ASSUMPTIONS

Table 3.9: Top Level Aircraft Requirements [38]

Parameter	Value	Parameter	Value
Take off distance (m)	793	Diversion Speed (m/s)	[-]
Start airport altitude (m)	0	AEO ROC at SL (m/s)	8
Cruise altitude (m)	3000	OEI ROC at SL (m/s)	[-]
Destination airport altitude (m)	0	Range (km)	396
Diversion altitude (m)	[-]	Diversion range (km)	[-]
Loiter altitude (m)	[-]	Loiter time (min)	[-]
Cruise speed (m/s)	115	Payload (kg)	[-]
Stall speed (m/s)	38.1	Reserve fuel (%)	[-]

Table 3.10: Aerodynamic Properties Estimation [38]

Parameter	Value
Minimum drag coefficient: [-]	0.0288
Take off drag coefficient: [-]	0.05
Take off lift coefficient: [-]	0.7
Maximum lift coefficient: [-]	2.2
Lift induced drag constant: [-]	0.0592
Lift to drag ratio: [-]	10.98

aerodynamic properties for the aircraft. As previously discussed, the aerodynamic properties of commercially available aircraft are seldom seen in the public domain. Fortunately, the studies which present the separate sets of TLARs, also discuss means to generate the drag polar for the aircraft. Study B, uses initial assumptions based on empirical data for CS-23 category aircraft, which are refined using a vortex lattice methodology, within Stanford University’s, conceptual aircraft design software Stanford University Aerospace Vehicle Environment (SUAVE)[98]. The Aerodynamic properties of the Dornier 228 presented in study B, are shown in table 3.10. Study B uses the simplified drag polar as previously discussed.

Study A, attains an extended drag polar, using the higher order method of Reynolds Averaged Navier Stokes (RANS) CFD simulations, presented in [94], rather than going for a classical drag build up approach, usually presented in aircraft design textbooks. The author makes use of NASA’s open source parametric geometry software, OPENVSP [99], and three view drawings of the aircraft to create a reference

### 3.2. TOP LEVEL AIRCRAFT REQUIREMENTS AND AERODYNAMIC ASSUMPTIONS

---

geometry, which could be transferred to Siemens' simulation package, StarCCM+, for the study to be completed. The author of this project also attempted to repeat the results of this test, for validation purposes. However, post completion of the reference geometry, time constraints, and limited access to the required software prohibited this validation step. It will be noted in the further research and recommendations section, this will be addressed. The reference geometry created by this author, including the modelling of the DO-A5 airfoil profile for the main wing, is presented in figure 3.3. The aerodynamic properties estimation based on the CFD from study A, are given in table 3.11. It is important to note that study A also includes the changes to the coefficient of lift due to the effects of high-lift surfaces (flaps), at different settings.

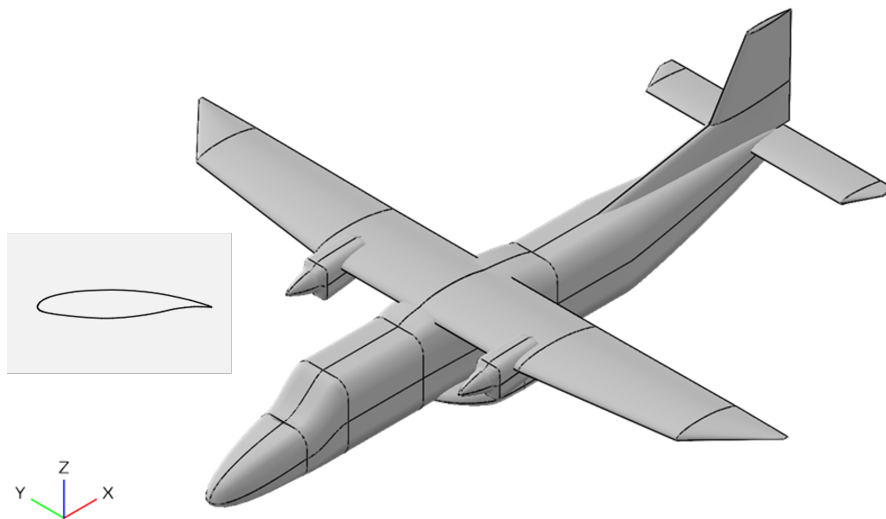


Figure 3.3: Dornier 228 Reference Geometry in OPENVSP

In the event that it is not possible to attain suitable aerodynamic properties from previous research, it is practical to use drag-build up methods [31] [19]. With a set of acceptable TLARs and the aerodynamic properties of the aircraft obtained, it is possible to move onto the constraint analysis section of flow chart. As a further alternative, [20] presents a useful table of typical aerodynamic characteristics for various aircraft; a small selection of which are detailed in table 3.12.

Table 3.11: Aerodynamic Properties Estimation [94]

Parameter	Value
Minimum drag coefficient: [-]	0.029
Take off drag coefficient: [-]	0.1694
Take off lift coefficient: [-]	1.34
Maximum lift coefficient (CLmax): [-]	1.7
Lift induced drag constant: [-]	0.0561
Lift to drag ratio: [-]	[-]
$\Delta$ CLmax take off flaps [-]	0.73
$\Delta$ Clmax landing flaps [-]	0.97

Table 3.12: Aerodynamic Characteristics for Various Aircraft Types

Aircraft Type	$C_{D,min}$	$C_{D,TO}$	$C_{L,TO}$	Comments
Twin Turboprop	0.025-0.035	0.035-0.045	$\approx 0.8$	Flaps in TO Position
Single Engine GA	0.028-0.035	0.038-0.045	$\approx 0.7$	Flaps in TO Position
Jet Transport	0.020-0.025	0.030-0.038	$\approx 0.8$	Flaps in TO Position

### 3.3 Hydrogen-Electric Aircraft Constraint Diagram

The  $P_{max}$  of the aircraft is an output from the constraints diagram, discussed previously, and referenced as section 2, within the aircraft design methodology flowchart, and using inputs 1B, 'Top-level aircraft performance requirements', and 1D, 'Drag Polar (Simple / Complex) + aerodynamic parameters for different phase configurations', as the primary input; figure 3.4, a condensed version of the main methodology flowchart, shows the relative position of the proceeding discussion, specifically for the constraints diagram calculation, within the process flow, as identified by the green highlighted box of section 2. The equations for each constraint, take-off distance, cruise speed, rate of climb and stall speed, are dealt with separately, with their own set of respective equations. The output of  $T/W$  to  $W/S$ , is transposed to reflect the use of power rated equipment, i.e motors, and presented in terms of power to weight  $P/W$  to  $W/S$ . This is achieved with with equation 3.1, assuming propeller efficiency,  $\eta_p$  as a functions of airspeed.

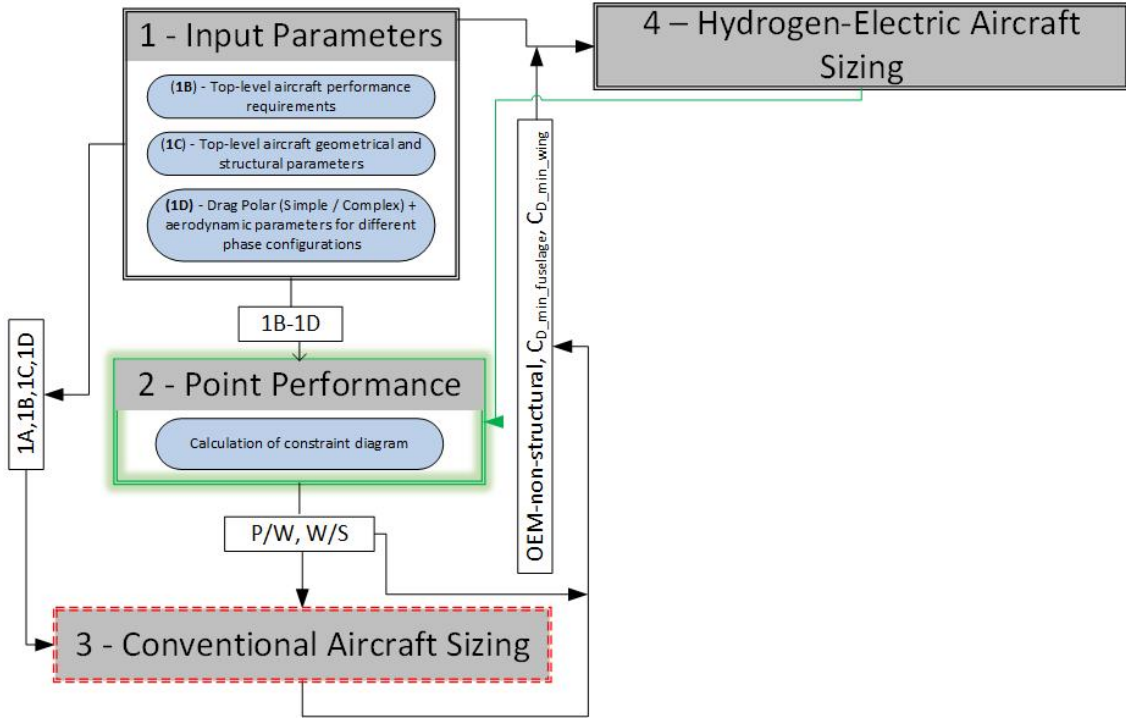


Figure 3.4: Flowchart Discussion Position - Point Performance

$$P = \frac{T \cdot v}{\eta_p(v)} \quad (3.1)$$

Where:

$P$  = Power

$T$  = Thrust

$v$  = Velocity

$\eta_p$  = Propeller efficiency

As previously discussed, study A and B use different forms of the drag polar, and as such the equations pertaining to each constraint vary due to this; these equations are presented below.

### 3.3.1 Take-Off Distance Constraint

Equations 3.2 through 3.4 describe the equations for the take-off distance constraint used in study A, extended from the work of [20]. These equations are used to describe the  $T/W$  required in order to achieve a specific ground run distance, during take-off, under the conditions of averaged acceleration. equation 3.5 pertains to the take-off distance constraint from study B, taken directly from [20]; again, averaged acceleration is assumed.

Study A:

$$\left(\frac{T}{W}\right)_{TOD} = \frac{v_{TO}^2}{2 \cdot g \cdot S_G} + \frac{q \cdot C_{D,TO}}{\frac{W}{S}} + \mu \cdot \left(1 - \frac{q \cdot C_{L,TO}}{\frac{W}{S}}\right) \quad (3.2)$$

Where

$$v_{TO} = 1.1 \cdot \sqrt{\frac{2 \cdot \frac{W}{S}}{\rho \cdot C_{L,TO}}} \quad (3.3)$$

And simplifying to

$$\left(\frac{T}{W}\right)_{TOD} = 1.21 \cdot \frac{\frac{W}{S}}{g \cdot S_G \cdot \rho \cdot C_{L,TO}} + 1.21 \cdot \frac{C_{D,TO}}{C_{L,TO}} - 0.21 \cdot \mu \quad (3.4)$$

Study B:

$$\left(\frac{T}{W}\right)_{TOD} = \frac{v_{TO}^2}{2 \cdot g \cdot S_G} + \frac{q \cdot C_{D,TO}}{\frac{W}{S}} + \mu \cdot \left(1 - \frac{q \cdot C_{L,TO}}{\frac{W}{S}}\right) \quad (3.5)$$

Where for study A and B:

$T/W$  = Thrust to weight ratio

$v_{TO}$  = Take-off speed

$g$  = Gravitational constant

$S_G$  = Ground run distance

$q$  = Dynamic pressure at condition (equation 3.6)

$C_{D,TO}$  = Drag coefficient at take-off conditions

$W/S$  = Wing loading

$\mu$  = coefficient of friction on runway (taken as 0.04 [20])

$C_{L,TO}$  = Lift coefficient at take-off conditions

$\rho$  = Air density at take-off altitude

Equation 3.6 describes the dynamic pressure that the aircraft will experience at a given condition; it is imperative to know that this is not a fixed value, and changes depending on the flight condition, as a function of the altitude and aircraft's velocity squared.

$$q = 0.5 \cdot \rho \cdot v^2 \quad (3.6)$$

### 3.3.2 Cruise Speed Constraint

The following equations, 3.7, and 3.8, are used to determine the  $T/W$  necessary, to achieve the prescribed cruise speed at a cruise altitude.

Study A:

$$\left(\frac{T}{W}\right)_{cruise} = \frac{q}{\frac{W}{S}} \cdot \left( C_{D,min} + k \cdot \left( \frac{\frac{W}{S}}{q} - C_{L,0} \right)^2 \right) \quad (3.7)$$

Study B:

$$\left(\frac{T}{W}\right)_{cruise} = q \cdot C_{D,min} \cdot \left( \frac{1}{\frac{W}{S}} \right) + k \cdot \left( \frac{1}{q} \right) \cdot \left( \frac{W}{S} \right) \quad (3.8)$$

Where for study A and B:

$C_{D,min}$  = Minimum drag coefficient

$k$  = Lift induced drag constant; this was discussed in the literature review, but is presented below in equation 3.9

$C_{L,0}$  = Lift coefficient at 0° angle of attack

$$k = \frac{1}{\pi \cdot AR \cdot e} \quad (3.9)$$

Where:

$AR$  = Wing aspect ratio

$e$  = Oswalds's span efficiency factor

### 3.3.3 Rate of Climb Constraint

The Rate of Climb (RoC) constraint equation yields the  $T/W$  required for a given rate of climb with respects to the wing loading,  $W/S$ . As well as the vertical climb rate,  $v_v$ , both equations require a velocity for the aircraft along the horizontal axis,  $v_y$ . Study A, achieves this for a case using the advanced drag polar, developing a set of equations, presented here as 3.11, and 3.12, where  $v_{aux}$ , is used as an interim variable, and assumes that the lift-to-drag ratio,  $L/D$ , is 86.6% of the maximum lift-to-drag ratio,  $L/D_{max}$  for the case of a propeller driven aircraft. This is not an arbitrary value that has been selected for the lift-to-drag ratio percentage, but is once again taken from stalwart aircraft design text books [19] [31]

Study A:

$$v_{L/D,max} = \left[ \left( \frac{m \cdot g}{\frac{\rho}{2} \cdot S} \right)^2 \cdot \frac{k}{C_{D,min} + K \cdot C_{L,0}^2} \right]^{1/4} \quad (3.10)$$

$$v_{aux} = \frac{m \cdot g \cdot (2 \cdot k \cdot \frac{L}{D} \cdot C_{L,0} + 1)}{\frac{L}{D} \cdot \rho \cdot S \cdot (C_{D,min} + k \cdot C_{L,0}^2)} \quad (3.11)$$

$$v^2 = v_{aux} - \sqrt{v_{aux}^2 - v_{L/D,max}^4} \quad (3.12)$$

$$C_L = \frac{m \cdot g}{\frac{\rho}{2} \cdot v^2 \cdot S} \quad (3.13)$$

$$\left(\frac{T}{W}\right)_{RoC} = \frac{RoC}{v_y} + \frac{q}{\frac{W}{S}} \cdot \left(C_{D,min} + k \cdot \left(\frac{W}{S} - C_{L,0}\right)^2\right) \quad (3.14)$$

Study B:

$$\left(\frac{T}{W}\right)_{RoC} = \frac{RoC}{v_y} + \frac{q}{\left(\frac{W}{S}\right)} \cdot C_{D,min} + \frac{k}{q} \cdot \left(\frac{W}{S}\right) \quad (3.15)$$

Where:

$m$  = Aircraft mass

$S$  = Aircraft wing area

*Note -  $m$  and  $S$  combine with the gravitational constant term to put the analysis in terms of  $W/S$ .*

$L/D$  = Lift-to-drag ratio

$RoC$  = Rate of climb

$v_{L/D,max}$  = Velocity at maximum lift-to-drag ratio

### 3.3.4 Rate of Climb Constraint - One Engine Inoperative (OEI)

Not discussed in study B, is the event in which an aircraft with multiple propellers, or rotors, suffers a failure of one of the propulsion devices, at take-off, when the aircraft is above the  $v_1$  decision speed, and must continue with the take off. In this event the aircraft must climb with a reduced RoC to account for the loss of power.

Study A, makes the simple adjustment to the standard climb constraint equation to factor in the loss of a propulsion device, or branch.

Study A:

$$\left(\frac{T}{W}\right)_{RoC,OEI} = \frac{NoD}{NoD - 1} \cdot \left(\frac{T}{W}\right)_{RoC} \quad (3.16)$$

Where:  $NoD$  = number of propulsion devices

### 3.3.5 Stall Speed Constraint

The final constraint is the stall constraint, and unlike its' counterparts discussed previously, here the constraint is not a function of the  $T/W$ , but rather, has the wing loading as it's result, in the form of an isobar on the constraint diagram, and relies on the maximum lift coefficient,  $C_{L,max}$  and the aircraft stall speed,  $v_{stall}$ .

Study A:

$$\left(\frac{W}{S}\right)_{stall} = \frac{\rho}{2} \cdot v_{stall}^2 \cdot C_{L,max} \quad (3.17)$$

Study B:

$$\left(\frac{W}{S}\right)_{stall} = q_{stall} \cdot C_{L,max} \quad (3.18)$$

### Results of the Constraints Diagram

Plotting both sets of equations to their respective sets of aerodynamic, and mission parameters, yields a constraint diagram, as per figure 3.5, for the aircraft according to study A and B. It is clear to see that there are a number of disparities between both studies. These will be discussed, such that the most accurate set of competing results, when compared to the reference aircraft will be used.

The maximum wing loading, dictated by the stall constraint isobar, will be addressed first, and a compromise made for the wing loading, from which to take

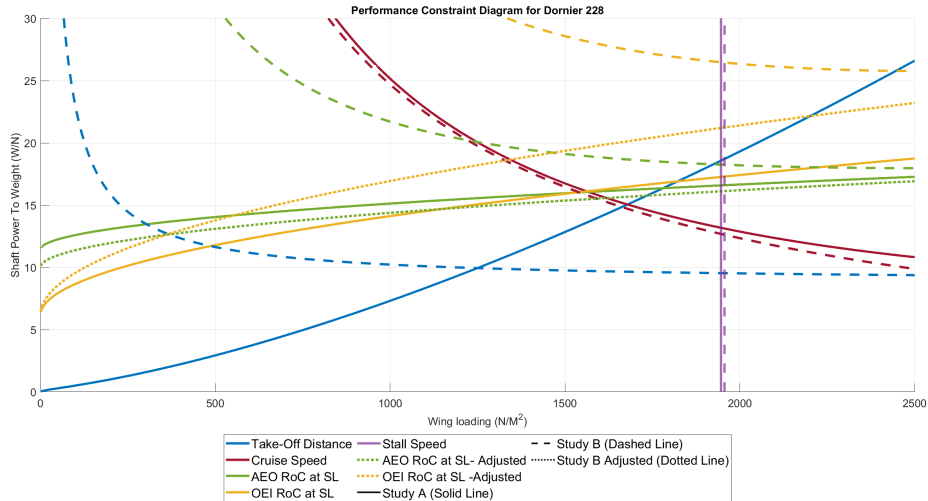


Figure 3.5: Dornier 228 Constraint Diagram

the remainder of the power to weight values. The equations of study A calculates a maximum wing loading of  $1946.5 \text{ N/m}^2$ , while Study B calculates a maximum wing loading of  $1956 \text{ N/m}^2$ . This represents a difference of  $9.5 \text{ N/m}^2$ , or  $0.49\%$ . To give both studies more context, it is important to consider the real aircraft, which has a given Maximum Take Off Mass (MTOM) of  $6400 \text{ kg}$ , or when converted to Newtons,  $62784\text{N}$ , and dividing by the reference wing area of  $32\text{m}^2$ , yields a wing loading of  $1962 \text{ N/m}^2$ . This translates to a  $15.5 \text{ N/m}^2$ , or  $0.8\%$  difference from study A, and a  $6 \text{ N/m}^2$ , or  $0.3\%$  difference from study B. The comparison between the values for shaft power to weight for each flight condition and study will be taken with reference to the stall isobar for study A; using either isobar would be acceptable as the values for the stall line are acceptably close. In order to align the two studies somewhat, the take off and climb constraint lines for the aircraft of study B, are subjected to the more advanced equations which pertain to take off and climb, used for aircraft A, as the initial values obtained, far exceed any rational result.

These power to weight values are now available to use and in input into the hydrogen-electric mission performance function of the sizing tool.

## 3.4 Aircraft Sizing

Although this project requires the sizing of a hydrogen-electric aircraft, which is in turn used to determine the potential benefits when improvements are made to the power converter technology, it is first necessary to consider the sizing of the conventional aircraft, within the context of traditional methodologies, before moving onto the discussion of a conventional aircraft sized by the updated methodology, as shown in the methodology flowchart. This is also referred to as a class 1 analysis, for aircraft mass estimation, for a conventional aircraft.

Note that although both aircraft variants are different in terms of their propulsion system, they are identical in respect to the build up of their total take off mass, these masses being described by the fundamental masses in equation 3.19

$$MTOM = M_{OEM} + M_{payload} + M_{fuel} \quad (3.19)$$

Where  $M_{payload}$  is the mass of aircraft's payload; this includes passengers, luggage and any additional cargo.  $M_{fuel}$  is the mass of the fuel required for the aircraft's mission. And, of particular note for this section is  $M_{OEM}$ , which describes the aircraft's Operational Empty Mass (OEM). Traditionally the OEM includes the structure, engines, landing gear, fixed equipment, avionics, furnishings and anything else that is not considered as payload or fuel.

The  $M_{payload}$  is provided as part of the TLARs, and as such the remaining unknowns for the conventional aircraft are the  $M_{fuel}$  and the  $M_{OEM}$ . These however, in traditional sizing are dependent on the MTOM, and an iterative approach to determine the final MTOM is used. [19] expresses these masses as functions of MTOM, using fractions of the total take off mass, these being  $\frac{M_{OEM}}{MTOM}$ , for the OEM mass fraction, and  $\frac{M_{fuel}}{MTOM}$ , for the fuel. This yields the following set of equations which can be

used to describe the aircraft's total mass as a function of the mass fractions.

$$MTOM = M_{payload} + \left( \frac{M_{OEM}}{MTOM} \right) * MTOM + \left( \frac{M_{fuel}}{MTOM} \right) * MTOM \quad (3.20)$$

$$MTOM - \left( \frac{M_{OEM}}{MTOM} \right) * MTOM - \left( \frac{M_{fuel}}{MTOM} \right) * MTOM = M_{payload} \quad (3.21)$$

$$MTOM = \frac{M_{payload}}{1 - \left( \frac{M_{OEM}}{MTOM} \right) - \left( \frac{M_{fuel}}{MTOM} \right)} \quad (3.22)$$

The fuel fraction estimation is something of an involved process which is dependent upon the flight mission, the aircraft's aerodynamic properties, and the specific fuel consumption of the engine. The fuel fraction must also be sympathetic to mission reserve fuel, and trapped fuel which cannot be scavenged from the tanks.

Various mission profiles exist for different aircraft, and the mission of the specific aircraft maybe governed by customer TLARs, but, will ultimately be overshadowed by airworthiness regulations, such as the CS-23 standards previously mentioned [97]. A simple cruise mission may be identified by the following characteristics, including, takeoff, climb, cruise, descend, loiter in the event of a temporary airport or runway closure, and finally a landing phase. This is depicted in figure 3.6.

For commercial transport, additional range or flight time is required; this could be for a longer loiter period or for a diversion to an alternate airport. The CS-23 regulations stipulate for commercial aircraft under visual flight rules, operators must account for an additional 30 minute (minimum) fuel reserve, intended to ensure that the aircraft has sufficient endurance for a safe diversion or alternate operations; this

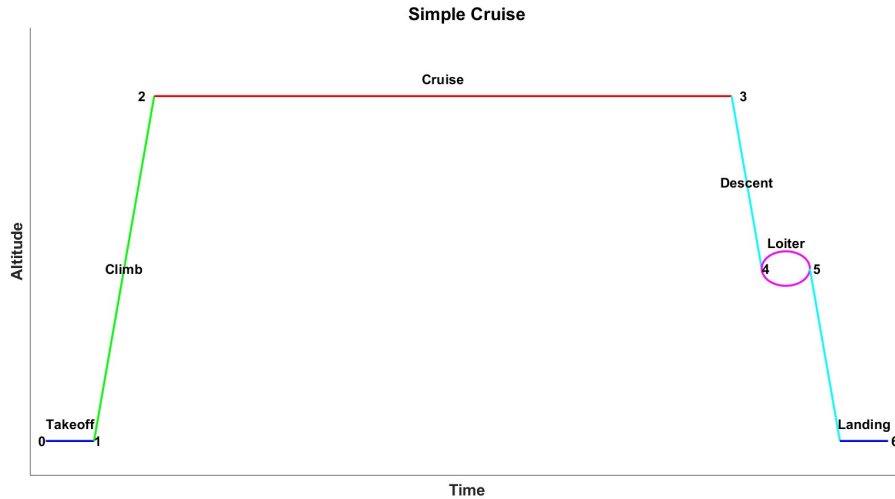


Figure 3.6: Simple Cruise Profile

is available in figure 3.7.

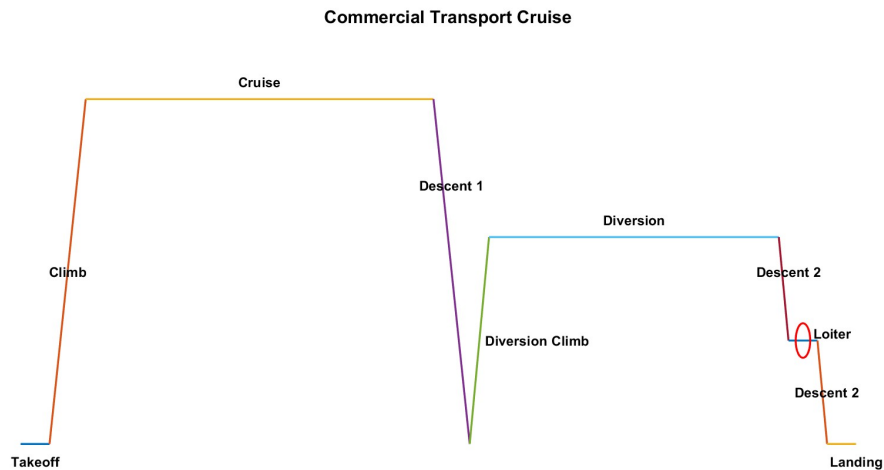


Figure 3.7: Commercial Transport Cruise Profile

Determination of the fuel mass fraction for an aircraft which does not experience a sudden drop in mass during the flight, such as a fighter aircraft dropping weaponry, assumes that the fuel used during each mission segment, is proportional to the aircraft weight during that mission segment. The various mission segments are numbered, as shown in figure 3.6, with '0' denoting the beginning of the flight profile. The mission segment weight fraction for some 'i<sup>th</sup>' segment is given as  $\frac{W_i}{W_{i-1}}$ . The total fuel weight fraction  $\frac{W_{i,end}}{W_0}$  is given by the product of all of the mission

Table 3.13: Historical Mission-Segment Weight Fractions

Flight Segment	$\frac{W_i}{W_{i-1}}$
Warm-up and takeoff	0.970
Climb	0.985
Landing	0.995

segments. Hence, for figure 3.6, the fuel fraction is reflected by equation 3.23.

$$\frac{W_6}{W_0} = \frac{W_6}{W_5} \cdot \frac{W_5}{W_4} \cdot \frac{W_4}{W_3} \cdot \frac{W_3}{W_2} \cdot \frac{W_2}{W_1} \cdot \frac{W_1}{W_0} \quad (3.23)$$

At this stage the weight fractions are unknown. Historical weight segment fractions are available from [19] for the warm-up and take off segments, climb segment and landing segment, given in table 3.13. The downside to using these values, which are more akin to a jet transport aircraft, is somewhat apparent, in that the values may be subject to change, depending on the aircraft variant under consideration, and this could lead to some mis-estimation for the final aircraft mass. Values for the descent segment are also ignored by this legacy methodology; again leading to further inaccuracy.

With values for the warm-up and take-off, climb and landing, this leaves the requirement to determine the fuel weight fractions for the cruise and loiter phases. This can be achieved using the Breguet range and endurance equations. The change in weight or mass of an aircraft with respects to fuel burn, in a time step can be realised by equation 3.24.

$$\Delta Weight = -SFC \cdot Thrust \cdot \Delta t \quad (3.24)$$

Where:

$\Delta Weight$  = Change in aircraft weight

SFC = Specific fuel consumption

Thrust = Thrust produced by the aircraft

$\Delta t$  = Time step

Note that the Specific Fuel Consumption (SFC) is presented with a negative sign, as this symbolises that the aircraft is consuming fuel. SFC, also termed Thrust Specific Fuel Consumption (TSFC) for thrust producing engines, is the rate of fuel consumption divided by the resulting thrust. This is usually measured in the mass of fuel flow per hour, per unit of thrust force, such as pounds of fuel per hour per pound of thrust; this can be converted to milligrams per Newton-second. Analogous to TSFC for aircraft producing thrust via a propeller, is Brake Specific Fuel Consumption (BSFC). Thrust and power can be related by a function of velocity and propeller efficiency, as per equation 3.25.

$$Thrust = \frac{\eta_p \cdot Power}{V} \quad (3.25)$$

Where:

$\eta_p$  = Propeller efficiency

V = Velocity

Continuing with range with respects to change in aircraft mass, equation 3.26 shows this relationship, as an elemental change in distance with respects to an elemental change in mass.

$$\Delta s = V_\infty \cdot \Delta t = \frac{V_\infty \cdot \Delta Mass}{SFC \cdot Thrust} \quad (3.26)$$

Where:

$\Delta s$  = Change in distance

$V_\infty$  = Free-stream velocity of the aircraft (assumed constant)

During the cruise and loiter phases, the aircraft is in a state of equilibrium, where lift,  $L$ , equals weight,  $W$ , and thrust,  $T$  equals drag,  $D$ . The ratio of lift to drag,  $L/D$  is assumed constant across the entire flight segment, even though in practical terms the lift will change as result of the aircraft burning fuel, and reducing in mass, which therefore alters the value of lift. The  $L/D$  can be incorporated into the elemental distance equation to yield equation 3.27. It is also worth noting, that depending on the propulsion variant, either propeller or jet, the values for  $L/D$  are taken as 86.6% of  $(L/D)_{\max}$  for an aircraft with jet engines, or  $(L/D)_{\max}$  for propeller driven aircraft; this is specific to the cruise phase only, and will change to 86.6% of  $(L/D)_{\max}$  for an aircraft with propellers, and  $(L/D)_{\max}$  for an aircraft with jet engines, during the loiter stage.

$$\Delta s = - \left( \frac{V_{\infty}}{SFC} \right) \cdot \left( \frac{L}{D} \right) \cdot \frac{\Delta Weight}{Weight} \quad (3.27)$$

Holding the  $L/D$ , SFC, and velocity as constant when integrating equation 3.27 to get the total distance, or range,  $R$ , allows the constant terms to be taken out of the integration, generating the following equation, 3.28.

$$R = \left( \frac{V_{\infty}}{SFC} \right) \cdot \left( \frac{L}{D} \right) \cdot \ln \frac{W_{i-1}}{W_i} \quad (3.28)$$

Rearranging to give the fuel weight fraction for the cruise segment is show in equation 3.29

$$\frac{W_{i-1}}{W_i} = \exp \left( \frac{-R \cdot SFC}{V_{\infty} \cdot \frac{L}{D}} \right) \quad (3.29)$$

The fuel fraction for the loiter phase, also known as the endurance,  $E$ , phase is handled with a slight alteration to equation 3.29. The endurance is a measure

of the aircraft in a particular configuration for a given time, rather than a given distance, as previously discussed with the range equation. Equation 3.30 presents the equation for Breguet endurance, and transposing yields the mass fraction for the loiter phase, in equation 3.31.

$$E = \left( \frac{L}{D} \right) \ln \frac{W_{i-1}}{W_i} \quad (3.30)$$

$$\frac{W_{i-1}}{W_i} = \exp \left( \frac{-E \cdot SFC}{\frac{L}{D}} \right) \quad (3.31)$$

When all of the fuel mass fractions per segment are combined into single equation, it is possible to describe the complete fuel mass fraction for the flight profile in figure 3.6 as follows. The addition of extra segments to the flight profile, such as a diversion, can be added by simply placing the appropriate mission segments value or equation into the fuel fraction equation.

$$\frac{W_6}{W_0} = 0.995 \cdot \exp \left( \frac{-E \cdot SFC}{\frac{L}{D}} \right) \cdot 1 \cdot \exp \left( \frac{-R \cdot SFC}{V_\infty \cdot \frac{L}{D}} \right) \cdot 0.985 \cdot 0.970 \quad (3.32)$$

As previously mentioned, some degree of reserve and trapped fuel must be accounted for, in the order of approximately 5% of the total fuel mass. This is taken care of in equation 3.33, to yield the final fuel fraction, where, RFF is the reserve fuel factor.

$$\frac{M_{fuel}}{MTOM} = (1 + RFF) \cdot \left( 1 - \frac{W_6}{W_0} \right) \quad (3.33)$$

The values for  $L/D$  can be determined through the drag polars presented earlier, or by using methods commonly presented in aerospace textbooks [19][31][58]. Al-

Table 3.14: General Specific Fuel Consumption Values for Various Propeller Aircraft

Aircraft Type	Cruise Phase (mg/W-s)	Loiter Phase (mg/W-s)
Piston-prop (fixed pitch)	0.068	0.085
Piston-prop (variable pitch)	0.068	0.085
Turboprop	0.085	0.101

Table 3.15: General Specific Fuel Consumption Values for Various Jet Aircraft

Aircraft Type	Cruise Phase (mg/N-s)	Loiter Phase (mg/N-s)
Pure turbojet	25.5	22.7
Low-bypass turbofan	22.7	19.8
Turboprop	14.1	11.3

ternatively, if the aircraft is known or has a close relative, databases of values are available from the manufacturers of the PIANO aircraft design software [100].

If the BSFC is unknown, using [19], it is possible to ascertain representative values for the various aircraft classes, these are provided for the readers reference in table 3.14 for propeller aircraft, and table 3.15 for jet propelled aircraft.

In order to improve the accuracy of the BSFC values in the analysis, it is important to note that turbojet and turbofan engines suffer in terms of fuel efficiency when they operate below their maximum thrust or power setting. Reducing the throttle results in a reduction in thrust, which is more than proportional to the value at which the fuel flow reduces, with a noticeable increase in SFC below approximately 90% thrust. Some engine manufacturers provide part power tables, which describe SFC as a function of thrust, across various altitudes and flight speeds. Where part power tables are unavailable, the author of [101] developed a semi-empirical equation to approximate the effect of part power on SFC, simulating a realistic increase in SFC as thrust is reduced; this is presented in equation 3.34, and is referred to as the Mattingly equation.

$$\frac{SFC}{SFC_{max,dry}} = \left( \frac{0.1}{\frac{T}{T_{max,dry}}} \right) + \left( \frac{0.24}{\frac{T}{T_{max,dry}}^{0.8}} \right) + \left( 0.66 \cdot \frac{T}{T_{max,dry}}^{0.8} \right) + \left( 0.1 \cdot M \left[ \frac{1}{\frac{T}{T_{max,dry}}} - \frac{T}{T_{max,dry}} \right] \right) \quad (3.34)$$

Where:

$SFC_{max,dry}$  = Maximum SFC for the engine at a given condition for altitude and speed. 'Dry' refers to an engine without an afterburner.

$T_{max,dry}$  = Maximum thrust from the engine at a given condition for altitude and speed. Using an engine without an afterburner.

M = Mach number.

The reference aircraft takes advantage of the Honeywell TPE331-10 turboprop engine, for which full power BSFC data is available [102], and presented in figure 3.8. Unfortunately, the manufacturer does not provide any part power tables, and as such these will need to be calculated, for accurate SFC values for the conventional reference aircraft, in the aircraft sizing tool.

The data presented uses shaft horsepower, and true airspeed, as opposed to thrust, and Mach number. Turboprop engines are in essence a turbine, similar to a turbojet engine, however the shaft of the turbine is connected to a gearbox which produces power, and is in turn connected to a propeller; the part power performance equation is therefore deemed acceptable to use for this type of engine.

True Air Speed (TAS), is related to Mach number, M, through equation 3.35, where  $a$  is the speed of sound, at altitude. As the speed of sound changes with altitude, an arbitrary value of TAS at sea level, will not yield the same Mach number as the equivalent TAS, at some increase in altitude, and as such it is not possible to use the data directly from figure 3.8; augmentation is required, such that it can be used with the Mattingly equation for part power tables.

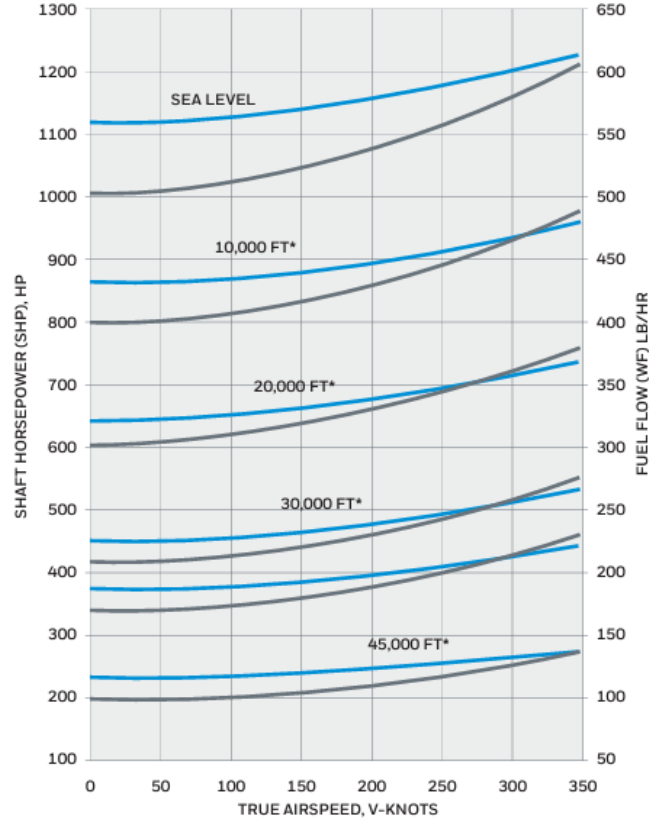


Figure 3.8: TPE331 Brake Specific Fuel Consumption (BSFC) plot (Blue Line = SFC and Grey Line = Power) [102]

$$M = \frac{TAS}{a} \quad (3.35)$$

The speed of sound at altitude can be calculated through equation 3.36.

$$a = \sqrt{\gamma \cdot R \cdot T} \quad (3.36)$$

Where:

$\gamma$  = Ratio of specific heats, and given as 1.4 for air at standard conditions

R = Specific gas constant for the medium. Air is given as  $287 \text{ J}/(\text{Kg} \cdot \text{K})$

T = Absolute temperature, in Kelvin

As an example to highlight the mismatch between Mach number and TAS at various

altitudes, this is provided using a commercial airliner who's entire career was based at flying beyond 'the speed of sound'. Concorde, has a cruising altitude of 60,000 feet and cruises at 2120 km/h, or 588.9 m/s when converted. At 60,000 ft, the air temperature is approximately 217 Kelvin, yielding a speed of sound of 295.5 m/s, and dividing the cruise speed by the speed of sound gives a cruising speed of Mach 2. The same scenario for a 588.9 m/s cruise at sea level (if this was indeed possible), where the standard atmosphere provides a temperature of 288.2 Kelvin, yields a speed of sound of 342 m/s, giving a Mach number of 1.72.

Using this information, the SFC data for the TPE331 is augmented to show power and fuel consumption with Mach number and altitude. Additionally an interpolation function is set up within the transposition code such that it is possible for the aircraft sizing tool to be able to calculate the SFC across the entire range of altitudes that the aircraft will experience. A value of 1000m, or 3281ft when converted, is included as a representative example of the interpolation, in figure 3.9.

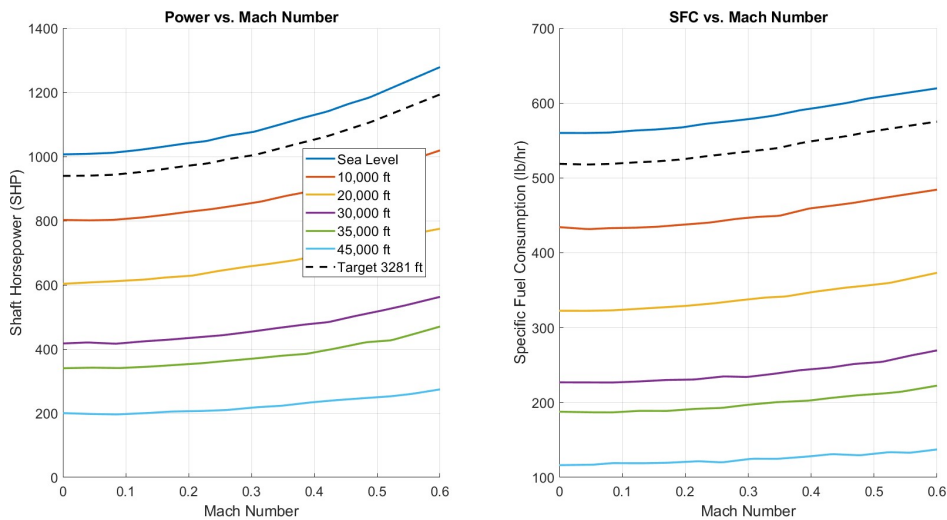


Figure 3.9: Brake Specific Fuel Consumption (BSFC) with Altitude and Mach Number

To enable the use of the Mattingly equation, it is necessary to convert the fuel flow data from a power with respects to fuel flow plot, to a thrust with respect to fuel flow plot. In order to achieve this, the first step is to convert the power

provided by the plot, in horsepower,  $P_{HP}$ , to a usable value in kilowatts,  $P_{kW}$ , by multiplying the value from the plot by 0.7457. The second stage requires the calculation of the velocity in meters per second,  $V_{m/s}$ , from the provided Mach number of the augmented plot, for the selected altitude. Dividing the values of power by the velocity, yields a value thrust, in kilo-Newtons, which is converted to thrust, in pound force,  $T_{lbf}$ , when multiplied by 224.81; this is shown in equation 3.37 for clarity. This is done for all of the altitude isopleth in figure 3.9. During the conversion process, the SFC values are converted from a value of pounds per hour,  $lb/hr$ , for the total horsepower, into a value of pounds of fuel per hour per pound force,  $lbs/hr/lbf$ . This is done by taking the corresponding value of SFC which relates to the power being converted to thrust, and dividing the SFC by the new thrust value; shown in equation 3.38. The new isopleths for SFC with Mach number, and thrust with Mach number are presented in A.6. As with the previous set of values before the conversion process, the value for 3281ft is also shown to demonstrate the interpolation capabilities of the tool. The ability to interpolate the fuel flow data allows the sizing tool to be able to calculate exact fuel flow values, and as such the fuel mass, across any mission profile, and flight conditions.

$$T_{lbf} = \left( \frac{P_{HP} \cdot 0.7457}{M \cdot a} \right) \cdot 224.81 \quad (3.37)$$

$$SFC_{lb/hr/lbf} = \frac{P_{HP} \cdot 0.7457}{M \cdot a} \cdot 224.81 \quad (3.38)$$

Using the thrust flow data and the Mattingly part power equation, it is possible to generate a series of part power tables for the engine. To represent how the fuel consumption and in-turn, the efficiency of the engine changes when the throttle is reduced, from full power. A representative example for the interpolated altitude of 3281ft is shown in figure 3.11, with the remaining part power tables for the various

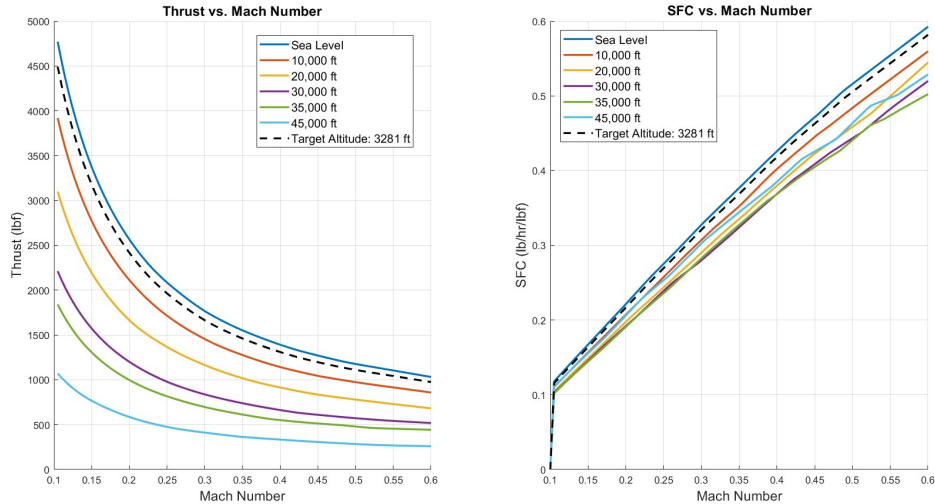


Figure 3.10: Thrust vs Mach Number and Corresponding Specific Fuel Consumption (SFC) with Mach Number

other altitudes, displayed in the appendix. Taking a twin engine aircraft which is cruising at  $85\text{m/s}$  with a thrust requirement of  $432\text{lbf}$  (per engine) at  $3281\text{ft}$ , for one hour, the fuel flow rate is determined through the interpolated part power tables as  $0.4263\text{ lbs/hr/lbf}$ , giving  $184\text{lbs}$  of fuel consumed per engine;  $368\text{lbs}$  total. However, if the aircraft design tool was to only consider the values initially provided by the un-interpolated data from the manufacturer, the same aircraft under the same conditions would be slated to consume  $0.27236\text{ lbs/hr/lbf}$ , which would yield a value of fuel consumed by each engine of  $117.6\text{lbs}$ , resulting in a total fuel consumption by both engines of only  $235.2\text{lbs}$ . This is a difference of approximately  $36\%$  from the correct value, and in addition, this mass would propagate error through the rest of the mass sizing, and cause the final aircraft mass to be severely underestimated. Likewise, the averaged value of BSFC provided by [19], of  $0.55\text{lb/hr/bhp}$  gives a fuel mass consumed of  $235.4\text{lbs}$ ; a near identical underestimation to the uncorrected tables.

Having a methodology for determining accurate inputs for the SFC variables of the Breguet cruise and loiter equations, focus now returns to the empty mass fraction determination.

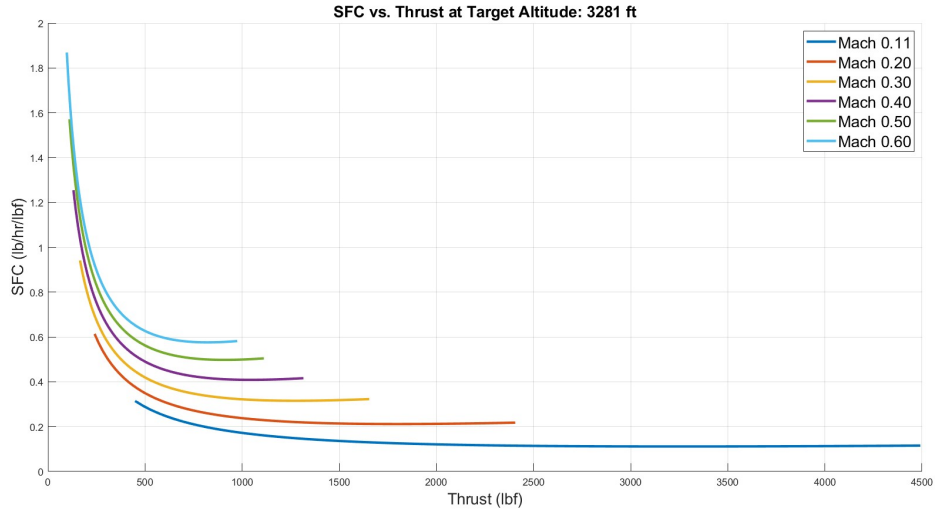


Figure 3.11: Part Power Table for TPE331-10 SFC at 3281ft

For the empty mass fraction for a conventionally powered aircraft, it is possible to estimate this value statistically, using historical data. [19] presents a useful chart for the empty mass fraction trends for various aircraft types; this is shown in figure 3.12; the aircraft presented here are not an exhaustive list and aircraft such as flying boats, gliders, agricultural, unmanned ariel vehicles and military jet fighters are omitted. It is reported that each line is plotted with equation 3.39, where the variables A and C for the various aircraft are given in table 3.16.

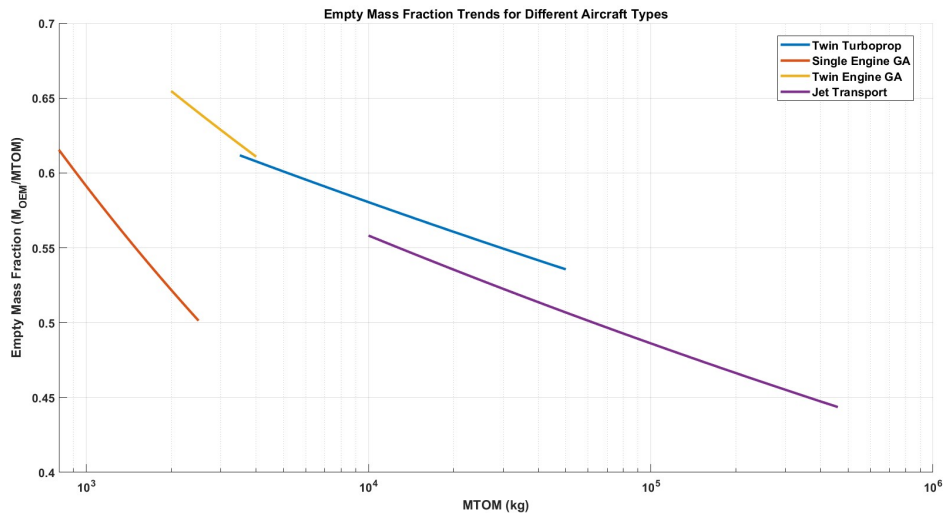


Figure 3.12: Empty Mass Fractions for Different Aircraft Types

Table 3.16: Empty Mass Fraction Equation Variables

Aircraft Type	A	C
Twin Turboprop	0.92	-0.05
Single Engine General Aviation	2.05	-0.18
Twin Engine General Aviation	1.4	-0.1
Jet Transport	0.97	-0.06

$$\frac{M_{OEM}}{MTOM} = A \cdot MTOM^C \quad (3.39)$$

For the aircraft in question (the Dornier 228), its reported MTOM of 6400kg places the empty mass fraction at approximately 0.6, which aligns with figures reported in previous texts. The empty mass fraction trend equation is a useful element of the tool, when used for designing other aircraft when little information is known.

No such data is available for aircraft powered by GH<sub>2</sub>, and batteries, and this is quite simply because outside of experimental and research domains, these aircraft do not exist, and this is one of the reasons why these novel aircraft cannot sized using traditional methods. In addition, legacy models do not have the capacity to deal with propulsive energy stored in 'non-consumable masses', i.e batteries. However, the traditional sizing process still finds a use with in the novel aircraft sizing tool.

To see how the traditional methodology works in conjunction with the new, novel methodology for sizing aircraft powered by batteries and GH<sub>2</sub>, the reference aircraft is subjected to sizing through mass fractions, for the mission profile from figure 3.7, in order to determine the empty mass value of the aircraft, and a comparison will be drawn against the physical aircraft. The values from both study A and Study B, for performance parameters and drag polar will be used as the input values into the calculations.

The first stage in the analysis required the determination of the maximum lift to drag values which are to be used in the Breguet equations. Study A makes

use of the extended drag polar, and uses the parameters from table 3.11, while study B uses the simplified drag polar and uses the parameters from table 3.10. Figure 3.13 highlights the lift to drag ratios for the two different studies; It can clearly be observed that study B which does not take advantage of a CFD study, is approximately 23% lower than that of study A. This suggests that study B will be cruising, diverting and loitering with lower aerodynamic efficiency, which points towards a higher fuel burn.

Extracting the drag polars also allows for the calculation of the thrust at cruise, diversion and loiter, which will be used in conjunction with the part power tables to generate accurate SFC values for the Breguet equations. This concept uses the principle of equilibrium in steady level flight, where lift equals weight, and thrust equals drag. It is possible to take the equation for lift and transpose for the coefficient of lift, as per equation 3.40. The calculated lift coefficient can then be placed into the drag polar for the respective study, to generate a value for the drag coefficient,  $C_D$ , allowing for the thrust to be calculated using the drag equation, given by equation 3.41. The Thrust, given in Newtons can then be converted to pound force, when multiplied by 0.2248; thus allowing the thrust value to be used in the Mattingly equation interpolations. To make the analysis more robust, the author implements a value for propeller efficiency ( $\eta_p$ ), of 0.85, in a bid to incorporate thrust losses between the propeller and the output shaft of the engine, during the cruise, diversion and loiter phases.

$$C_L = \frac{L}{0.5 \cdot \rho \cdot V_\infty^2 \cdot S} \quad (3.40)$$

Where:

$C_L$  = Coefficient of lift (N)

$\rho$  = Air density at altitude (kg/m<sup>3</sup>)

$V_\infty^2$  = Free-stream velocity (m/s<sup>2</sup>)

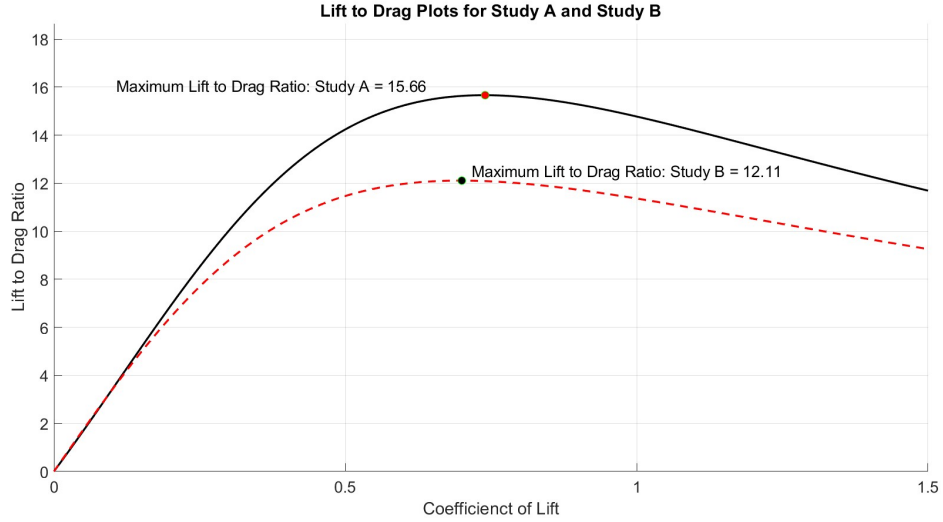


Figure 3.13: Lift to Drag Ratios for Study A and Study B

Table 3.17: MTOM Calculations for Dornier 228 - Study A & B

Study	Aircraft Mass (kg)	OEM (kg)	Fuel Mass (kg)	Cruise SFC	Diversion SFC	Loiter SFC
A	6434.65	3818.45	656.20	0.35153	0.34794	0.28544
B	6609.90	3917.19	732.73	0.34451	0.30956	0.23524
Difference %	+2.723%	+2.585%	+11.661%	[-]	[-]	[-]

$S = \text{Wing area (m}^2\text{)}$

$$Thrust = C_D \cdot 0.5 \cdot \rho \cdot V_\infty^2 \cdot S \quad (3.41)$$

The final mass for the aircraft is determined through an iterative process, whereby an initial guess is taken for the MTOM and used in the right hand side of the MTOM equation, at which point the absolute value of the new calculated mass, when subtracted from the original mass, is taken as a stopping criterion. The calculated mass is then used as the input for the new mass, and the system repeats until mass convergence is reached, based on the stopping criterion. 7000kg was chosen as the starting point for this study. The results of the studies are shown in table 3.17.

From table 3.17, when comparing the results of the two aircraft, it is clear to see a strong agreement between the calculated values for both the overall aircraft

MTOM, with approximately 2.7% between the two, and a similar situation for the OEM value with approximately 2.6% difference. The largest variance comes from the fuel mass with over a nearly 12% increase for aircraft B, with respects to aircraft A. As previously suggested, the simplified drag polar used for aircraft B, somewhat underestimates the aerodynamic properties of the aircraft, leading to unfavorably high thrust requirements for the cruise and diversion conditions, even though the part power tables favour the engines working closer to their more efficient operating points, as is demonstrated by the lower SFC values.

Extending the discussion of the results further, by comparing aircraft A and B with reference values for the Dornier 228, taken from manufacturer details, provided in in the appendix, figure B.1, and shown in table 3.18, it is possible observe positive agreements between the overall aircraft MTOM, with mere 0.54% increase between aircraft A and the reference, and a greater 3.28% increase for aircraft B, using a simplified drag polar. The OEM of aircraft B is in particularly close agreement with the reference aircraft, with less than 0.5% increase, and somewhat slightly less close, with a 2.09% decrease for aircraft A. However, there appears to be quite a disparity for the fuel masses of both the aircraft, when compared to the reference aircraft, with a more than 21% increase from aircraft A, and a staggering 35.69% for aircraft B. Even though both aircraft are in good agreement between theirselves, it is only when compared to a reference aircraft, that the error can truly be observed. The use of the simplified drag model and semi-empirical values from other literature has clearly compounded the fuel growth issue for Aircraft B. However, aircraft A, which was slated to have the advantage of aerodynamic accuracy, has also lead to somewhat erroneous values for fuel mass, and the author suggests that the use of fixed values used for taxi, take off, climb and landing, in the fuel fraction build up, have had a negative effect on the fuel values. Therefore, it is evident that the model needs amending to yield greater accuracy for the fuel / energy calculations.

In order to address the issues with the fuel and energy calculations, improvements

Table 3.18: MTOM Variance Between Reference Aircraft, Aircraft A & Aircraft B

Aircraft	Aircraft Mass (kg)	OEM (kg)	Fuel Mass (kg)
Reference D228	6400	3900	540
Difference % Study A	+0.54%	-2.09%	+21.52%
Difference % Study B	+3.28%	+0.44%	+35.69%

to the legacy model are suggested. The new model will still take full advantage of the work undertaken so far; hence comprehensive detail of the previous discussion.

An important note surrounding the aircraft’s Operational Empty Mass (OEM), is noteworthy at this point, and its level of importance will guide the updated system. The Operational Empty Mass (OEM) includes all of the items which are not fuel or payload. As such, this includes the aircraft’s fuel tanks and fuel storage. Fuel onboard most commuter and jet transport aircraft is stored, unpressurised, across two major structures, these being the wings and the wing box. Fuel stored in the wing, without the use of a fuel bladder, is referred to as a ‘wet wing’ and the tank is therefore the structure of the aircraft, and similarly for the wing box fuel storage. Using the structure of the aircraft to store fuel, in an unpressurised state means that the storage efficiency is close to 100%. The current technology for  $\text{GH}_2$  storage is limited, with an efficiency of approximately 10%. This, therefore does not align with the traditional sizing methodology, and the tank sizing must be dealt with separately. It also stands to reason that if the  $\text{GH}_2$  tank is lumped into the  $\frac{M_{OEM}}{MTOM}$ , the tank inefficiency would cause an unnecessary growth in components which are not ordinarily a function of the MTOM of the aircraft. For example, if a conventional aircraft is retrofitted with a hydrogen-electric propulsion system, the mass of items such as the avionics, climate control, de-icing equipment, furnishings, onboard equipment, galleys, electrical systems and toilet facilities should not be influenced by the inefficiency of the energy storage system, and it should only be a question of making adjustments to the aircraft structure, including fuselage, wings, vertical stabiliser and horizontal stabiliser to accommodate for the extra loads and

size, brought about by the GH<sub>2</sub> storage and new propulsion system.

As part of the updated system, and moving into section 3 of the sizing methodology flow chart, identified by the red dashed box, 'Conventional Aircraft Sizing', of figure 3.14, as well as sizing the conventional aircraft, the OEM of the conventional aircraft is required to be decomposed further, to yield a mass for the structural components of the aircraft, and a mass for everything else which is not the structure, and should not be influenced by the growth in MTOM when under the consideration of a hydrogen propulsion retrofit. This new term,  $OEM_{non-structure}$  can be taken as an absolute value into the hydrogen-electric mission profile.

This also changes the class of the analysis from a class 1 analysis using mass fractions, into a class 2 analysis which deals with specific elements of the aircraft in greater detail.

Moving to a class 2 analysis, and based on the potential inaccuracies that could be brought about by using legacy values for mission segment fractions, as well as not accounting for descent phases, a decision has been made to utilise the universal transport energy equation, repeated below for convenience, in a bid to yield greater accuracy for the energy used during each mission segment. This method also lends itself well to sizing the energy requirements for the hydrogen-electric aircraft, and permits for the energy to be split between the hydrogen system and the battery system, while still permitting for the sizing of a conventional aircraft, which itself is essential to be sized correctly, as this determines the  $OEM_{non-structure}$  value.

$$\Delta E = \underbrace{\frac{m \cdot g \cdot V}{L/D} \cdot \Delta t}_{\Delta E_{AeroDrag}} + \underbrace{\frac{m \cdot \Delta V^2}{2}}_{\Delta E_{Kinetic}} + \underbrace{m \cdot g \cdot RoC \cdot \Delta t}_{\Delta E_{Potential}} \quad (3.42)$$

As previously stated the transport energy equation permits for energy to be calcu-

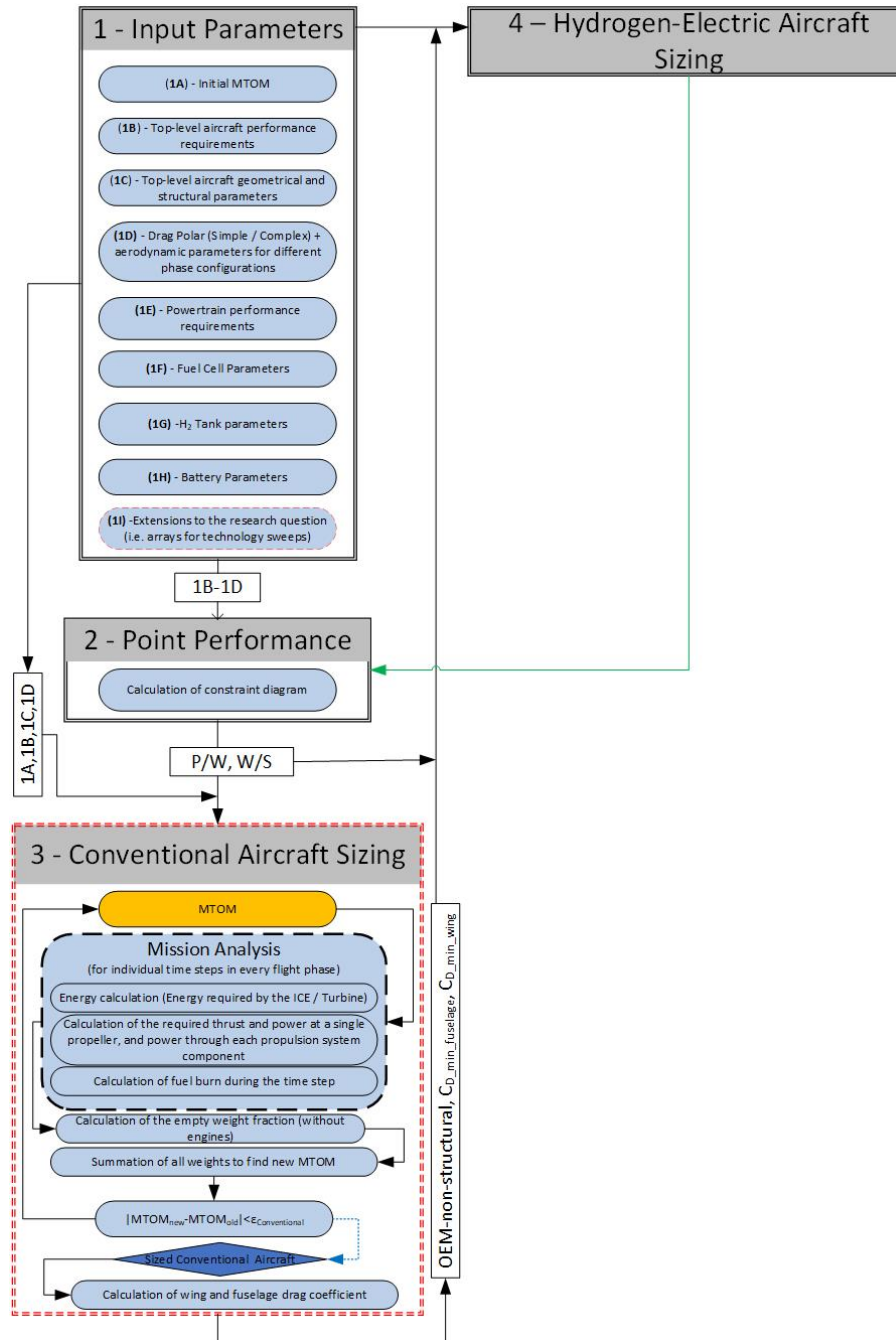


Figure 3.14: Flowchart Discussion Position - Conventional Aircraft Sizing

lated in every time-step of a mission profile. During the cruise segment, only the aerodynamic drag gives rise to the energy requirement; this allows the new model to take advantage of all of the previous lift, drag and thrust equations, as well as the drag polars presented previously. For the climb and descent phases, the potential energy is added or subtracted from the aero drag energy. The kinetic energy is added during acceleration. Finally, the energy during the take off phase, assumes that the aircraft is operating at full power for some pre-determined time, and this takes full advantage of the constraints diagram developed previously, as the initial estimation of mass can be used to calculate the installed power of the aircraft, based on the maximum power to weight ratio, with respects to the wing loading.

The required fuel for the time step is dealt with using either, the fuel mass equation for thrust, equation 3.43, or the fuel mass equation for power rated (reciprocating) engines, equation 3.44; However, the Brake Specific Fuel Consumption (BSFC) is determined using equation 2.15, rather than the Mattingly equation.

$$\Delta m_{fuel} = (1 + TFF) \cdot Thrust \cdot NoD \cdot TSFC \cdot \Delta t \quad (3.43)$$

Where:

$\Delta m_{fuel}$  = Required fuel in a time step

$NoD$  = Number of thrust producing devices.

$\Delta t$  = time step (s)

$$\Delta m_{fuel} = (1 + TFF) \cdot Power \cdot NoD \cdot BSFC \cdot \Delta t \quad (3.44)$$

Before dealing with the additional complexities of decomposing the OEM, and incorporating fuel cells with their supporting equipment, batteries and GH<sub>2</sub> tanks, the conventional aircraft is to be resized using the new methodology, for the pur-

Table 3.19: MTOM Calculations for Dornier 228 Using Energy Analysis - Aircraft A' & B'

Study	Aircraft Mass (kg)	OEM (kg)	Fuel Mass (kg)
A'	6354.18	3812.12	581.83
B'	6473.93	3877.51	636.41
Difference%	+1.88%	+1.71%	+9.38%

Table 3.20: MTOM Variance Between Reference Aircraft, Aircraft A' & Aircraft B'

Aircraft	Aircraft Mass (kg)	OEM (kg)	Fuel Mass (kg)
Reference D228	6400	3900	540
Difference % Aircraft A	+0.54%	-2.09%	+21.52%
<b>Difference % Aircraft A'</b>	-0.71%	-2.24%	+7.74%
Difference % Aircraft B	+3.28%	+0.44%	+35.69%
<b>Difference % Aircraft B'</b>	+1.16%	-0.58%	+17.85%

poses of validation, and to make a comparison between energy based methods, and legacy aircraft design methods, a previously discussed. The results of the resizing analysis are presented in table 3.19. The remodelled aircraft, from the energy based methodology are now referred to as aircraft A' and aircraft B', to differentiate when discussing the results of the previous analysis using the legacy study.

Once again, the results of both aircraft appear to be in good relation to one another with regards to their MTOM and OEM; both being less than 2% from another, and more importantly this shows some improvement from the previous method where both values were closer to 3% apart from one another. A similar improvement can be observed with the fuel mass, with 9.38% difference using the updated method, relative to 11.66% for the legacy methodology. However, the real comparison comes from putting these new values in competition with the reference aircraft, and those of the previous study, from table 3.18. The updated analysis is available in table 3.20.

From the updated study, it is immediately clear that the MTOM and OEM values

for aircraft A' align closely with the reference aircraft, at just 0.71% and 2.24% respectively, and compare well to the results of the previous study, with a negligible difference for OEM, and just 1.25% for MTOM between A' and A. The greatest improvement comes in the form of the fuel mass, with respects to the reference value, for aircraft A', showing 7.74% difference, relative to the near 22% of the legacy model. Moving onto aircraft B', yet again the MTOM and OEM agree with the real aircraft, and an improvement of approximately 2% is seen between aircraft B' and B for MTOM, and a slight underestimation for OEM, but still extremely close at just 0.58% away from the target value. Once again, the greatest improvements can be shown from the fuel mass, and although the value is still nearly 18% away from the reference value, this does however represent an exactly 50% increase in the accuracy of the estimation relative to aircraft B.

This clearly shows that the updated system has a much improved means of handling the energy consumption of the aircraft, and as well as increasing the accuracy of the results, it allows for the energy to be distributed across multiple sources, such as fuel, and as will be described later in this chapter, batteries and hydrogen.

Based on the results of the above study, it is clear to see that the improvements to the individual masses have clearly validated the justification for using the universal energy methodology for sizing the reference aircraft.

### **3.5 Aircraft Structural Mass Determination**

Moving to a class 2 estimation allows for the use of structural mass equations to be used, to determine the mass of key aircraft structural components; namely, the wings, empennage and fuselage. A number of authors propose various methods and equations to calculate the structural mass of the aircraft. These authors, and respective equation numbers are identified in table 3.21.

Table 3.21: Aircraft Structural Component Equation Reference

Author	Structural Component	Equation Number	Nomenclature
Raymer [19]	Wing	3.45	$W_{W, Raymer}$
	Horizontal Tail	3.46	$W_{HT, Raymer}$
	Vertical Tail	3.47	$W_{VT, Raymer}$
	Fuselage	3.48	$W_{Fuselage, Raymer}$
Nicolai [58]	Wing	3.49	$W_{W, Nicolai}$
	Horizontal Tail	3.50	$W_{HT, Nicolai}$
	Vertical Tail	3.52	$W_{VT, Nicolai}$
	Fuselage	3.53	$W_{Fuselage, Nicolai}$
Roskam [45]	Wing	3.54	$W_{W, Cessna}$
	Horizontal Tail	3.55	$W_{HT, Cessna}$
	Vertical Tail	3.56	$W_{VT, Cessna}$
	Fuselage	3.57	$W_{Fuselage, Cessna}$
Torenbeek [103]	Wing	3.58	$W_{W, Torenbeek}$
	Empennage	3.59	$W_{Empennage, Torenbeek}$
	Fuselage	3.60	$W_{Fuselage, Torenbeek}$

Each of these equations is discussed below separately, below. The reader should also be aware of the units used; the aircraft design tool automatically converts the units where necessary, to produce the final results in SI units.

For equation 3.45, the mass of the wing is increased with increasing values of wing surface area, fuel stored in the wing structure, aspect ratio, cruise speed (factored into dynamic pressure), taper ratio, ultimate loading factor, and more importantly the aircraft design gross weight, which is analogous to MTOM. The sweep of the wing, increases the values of certain elements of the equation when coupled to a positive exponent, and has the effect of reducing the values in the equation when subject to a negative exponent; a greater value for sweep will ultimately yield a heavier wing. The thickness to chord ratio will have the effect of reducing the wing mass. From this equation, it is expected that wing weight would be lower for a hydrogen-electric aircraft, as fuel is no longer stored in the wing. As an alternative, to make good use of the wings, it is decided that the fuel cell mass will take the place of the fuel, and works on the basis that the motors, fuel cells and necessary power

electronics are part of a integrated modular unit which bolts onto the wing. This also leads to the hypothesis that improved technology in respects to power density of the power train will translate into reduced wing mass. This makes the Raymer wing mass equation a good candidate for use in the hydrogen-electric aircraft sizing methodology.

$$W_{W, Raymer} = 0.036 \cdot S_W^{0.758} \cdot W_{fw}^{0.0035} \cdot \left( \frac{AR}{\cos^2 \Lambda} \right)^{0.6} \cdot q^{0.006} \cdot \lambda^{0.04} \cdot \left( \frac{100 \frac{t}{c}}{\cos \Lambda} \right)^{-0.3} \cdot (N_z \cdot W_{dg})^{0.49} \quad (3.45)$$

Where:

$S_W$  = Trapezoidal wing area (ft<sup>2</sup>)

$W_{fw}$  = Weight of fuel stored in wings (lbs)

$AR$  = Wing aspect ratio

$\Lambda$  = Wing sweep at 25% Mean Aerodynamic Chord (MAC) (deg)

$q$  = Dynamic pressure at cruise  $\left( \frac{lb}{ft^2} \right)$

$\lambda$  = Wing taper ratio

$\frac{t}{c}$  = Wing thickness-to-chord ratio

$N_z$  = Ultimate load factor

$W_{dg}$  = Aircraft design gross weight (lbs)

For the horizontal tail mass, calculated by equation 3.46, similar to the wing, the aircraft design gross weight, ultimate loading factor, cruise speed and horizontal tail area all, have the effect of increasing the tail mass. However, in this scenario, the negative exponent of the taper ratio suggests a mass reducing effect as taper ratio is increased, and is also supported by the mass reducing effects of increasing the thickness-to-chord ratio. The role of the sweep has the effect of decreasing the

component mass when the values are increased.

$$W_{HT, Raymer} = 0.016 \cdot (N_z \cdot W_{dg})^{0.414} \cdot q^{0.168} \cdot S_{HT}^{0.896} \cdot \left( \frac{100 \frac{t}{c}_{HT}}{\cos \Lambda_{HT}} \right)^{-0.12} \cdot \left( \frac{AR}{\cos^2 \Lambda_{HT}} \right)^{0.043} \cdot \lambda_{HT}^{-0.02} \quad (3.46)$$

Where:

$S_{HT}$  = Horizontal tail area (ft<sup>2</sup>)

$\Lambda_{HT}$  = Horizontal tail sweep at 25% Mean Aerodynamic Chord (MAC) (deg)

$\lambda_{HT}$  = Horizontal tail taper ratio

$\frac{t}{c}_{HT}$  = Wing thickness-to-chord ratio for horizontal tail

The equation for the vertical tail mass from Raymer, equation 3.47, is something of a special case, where by the configuration of the tail (conventional or "T" tail), acts as a binary case for the  $\frac{H_T}{H_V}$  term, with it being set to 1 in the case of a "T" tail, or 0 for a conventional tail, with an increasing mass suggested by a non-conventional tail. As before the ultimate loading factor, MTOM, cruise speed, vertical tail area, sweep, taper ratio, and aspect ratio have an effect of increasing the component mass, while the thickness-to-chord ratio decrease the mass, with increasing values.

$$W_{VT, Raymer} = 0.073 \cdot \left( 1 + 0.2 \cdot \frac{H_T}{H_V} \right) \cdot (N_z \cdot W_{dg})^{0.376} \cdot q^{0.122} \cdot S_{VT}^{0.873} \cdot \left( \frac{100 \frac{t}{c}}{\cos \Lambda_{VT}} \right)^{-0.49} \cdot \left( \frac{AR}{\cos^2 \Lambda_{VT}} \right)^{0.357} \cdot \lambda_{VT}^{0.039} \quad (3.47)$$

Where:

$\frac{H_T}{H_V}$  =  $H_T$  is the horizontal tail height above the fuselage (ft),  $H_V$  is the vertical tail height above the fuselage (ft). This is taken as 0 for a conventional tail and 1 for a 'T' tail

$S_{VT}$  = Horizontal tail area (ft<sup>2</sup>)

$\Lambda_{VT}$  = Vertical tail sweep at 25% Mean Aerodynamic Chord (MAC) (deg)

$\lambda_{VT}$  = Vertical tail taper ratio

Raymer's fuselage mass equation, given as equation 3.48, indicated that increasing values of fuselage surface area, ultimate loading, cruise speed and pressurisation factor will increase the mass of the fuselage. Increasing the length of the tail arm or fuselage, has a mass reducing affect on the aircraft, this is also supported by mass reductions for increasing height.

This equation lends itself well to the sizing methodology for the hydrogen electric-propulsion aircraft variant, as the increasing length of the fuselage brought about by the H<sub>2</sub> tank sizing iteration, and the subsequent increase in fuselage surface area will be able to capture the mass fluctuations, as the sizing routine iterates through its regime.

$$W_{Fuselage, Raymer} = 0.052 \cdot S_f^{1.086} \cdot (N_Z \cdot W_{dg})^{0.177} \cdot L_t^{-0.051} \cdot \left(\frac{l}{h}\right)^{-0.072} \cdot q^{0.241} + W_{press} \quad (3.48)$$

Where:

$S_f$  = Fuselage wetted area (ft<sup>2</sup>)

$L_t$  = Tail arm length (wing MAC to tail MAC) (ft)

$\frac{l}{h}$  = Fuselage structural length (ft) to fuselage structural height (ft) ratio

$W_{press}$  = Cabin pressurisation factor

In order to determine the initial input values for the fuselage wetted area, the model developed earlier in OPENVSP, is subject to a component geometry extraction, whereby the individual components of the aircraft are segregated at their intersections, to yield single components, which can be used for wetted area extraction; the separation of the major components from the single aircraft model is shown in figure 3.15, with each component identified by an individual colour, and the wetted

Table 3.22: Wetted Area of Individual Structural Components

Aircraft Component	Wetted Area (m <sup>2</sup> )
Fuselage	72.127
Wheel Fairing	14.28
Wing	58.56
Vertical Tail	11.66
Horizontal Tail	13.64

area of the major structural components are show in table 3.22.

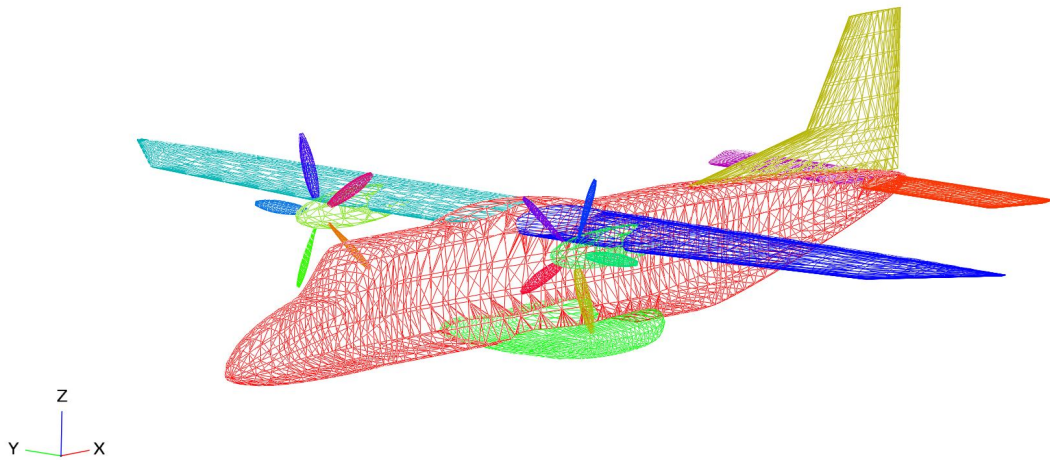


Figure 3.15: Dornier 228 Individual Structural Wetted Areas

For the purposes of any equations requiring the fuselage wetted area for the D228 use case, the sum of fuselage and the wheel fairing areas are used. In the event that wetted areas are not known, and access to OPENVSP is not possible, resources such as [96] and [104] can be valuable.

Nicolai's equation for wing mass, equation 3.49, demonstrates, similarly to Raymer, that increasing the values of ultimate load factor, design gross weight, aspect ratio, wing area, taper ratio, and a new term, the maximum speed at sea level, will result in an increase in wing mass, when their values are increased, and similarly the thickness-to-chord ratio will result in a reducing mass, when its value is increased. Unlike Raymer, no account for the fuel onboard is accounted for here, making the equation slightly less desirable to take forward for further analysis in the hydrogen-

electric system.

$$W_{W,Nicolai} = 96.948 \cdot \left[ \left( \frac{N_Z \cdot W_{dg}}{10^5} \right)^{0.65} \cdot \left( \frac{AR}{\cos\Lambda} \right)^{0.57} \cdot \left( \frac{S_W}{100} \right)^{0.61} \cdot \left( \frac{1 + \lambda}{2 \frac{t}{c}} \right)^{0.36} \cdot \sqrt{1 + \frac{V_{max}}{500}} \right]^{0.993} \quad (3.49)$$

Where:

$V_{max}$  = maximum level airspeed at sea level (knots)

The weight of the horizontal tail from Nicolai, given in equation 3.50 has an increasing mass, with an increasing value for all parameters, with the exception being that of an increasing root chord thickness, which results in a decreasing mass. A word of caution should be expressed here, in that the maximum root thickness is given in inches rather than feet, and a separate equation is required to calculate this value; this is given as equation 3.51, with the results in inches; it is much easier to attain data for the parameters used in 3.51, than it is to find a specific value for the parameter in question itself. Additionally, the equation is easily adapted for the vertical tail maximum root thickness.

$$W_{HT,Nicolai} = 127 \cdot \left[ \left( \frac{N_Z \cdot W_{dg}}{10^5} \right)^{0.87} \cdot \left( \frac{S_{HT}}{100} \right)^{1.2} \cdot \left( \frac{L_T}{10} \right)^{0.483} \cdot 0.289 \cdot \sqrt{\frac{b_{HT}}{t_{HT,max}}} \right]^{0.458} \quad (3.50)$$

Where:

$b_{HT}$  = Span of the horizontal tail (ft)

$t_{HT,max}$  = Maximum root chord thickness of the horizontal tail (inches)

$$t_{HT,max} = \left[ \left( \frac{2 \cdot S_{HT}}{b_{HT} \cdot (1 + \lambda_{HT})} \right) \cdot \left( \frac{t}{c_{HT}} \right) \right] \cdot 12 \quad (3.51)$$

The parameters for the vertical tail equation of Nicolai, equation 3.52, act in a near identical way when it comes to increasing the component mass when increasing their values, and no further discussion is required here.

$$W_{VT,Nicolai} = 98.5 \cdot \left[ \left( \frac{N_Z \cdot W_{dg}}{10^5} \right)^{0.87} \cdot \left( \frac{S_{VT}}{100} \right)^{1.2} \cdot 0.289 \cdot \sqrt{\frac{b_{VT}}{t_{VT,max}}} \right]^{0.458} \quad (3.52)$$

Where:

$b_{VT}$  = Span of the vertical tail (ft)

$t_{VT,max}$  = Maximum root chord thickness of the vertical tail (inches)

The final equation used from Nicolai's arsenal of mass calculating tools, is for the fuselage mass, given by equation 3.53. It can be quite simply distilled that, any increase, from any parameter, will result in an increase in the fuselage mass. Similarly to the Raymer fuselage equation, the changes in length brought about the hydrogen tank, will be translated into an increased structural mass.

$$W_{Fuselage,Nicolai} = 200 \cdot \left[ \left( \frac{N_Z \cdot W_{dg}}{10^5} \right)^{0.286} \cdot \left( \frac{l}{10} \right)^{0.857} \cdot \left( \frac{w+h}{10} \right) \cdot \left( \frac{V_{max}}{100} \right)^{0.338} \right]^{1.1} \quad (3.53)$$

Where:

$w$  = Total fuselage structural width (ft)

$l$  = Fuselage structural length (ft)

The equations presented by Roskam, affectionately termed as "Cessna", due to their

origins, are presented below, with the first being equation 3.54, for the wing weight. The equation suggests that an increase to the MTOM, wing surface area, ultimate loading factor or the aspect ratio, will result in an increase of the wing weight. No account is taken for the influence of the fuel mass as a stand-alone entity.

$$W_{W,Cessna} = 0.04674 \cdot W_{dg}^{0.397} \cdot S_W^{0.36} \cdot N_Z^{0.397} \cdot AR^{1.712} \quad (3.54)$$

For the horizontal tail mass given by equation 3.55, any increase in the gross design weight, horizontal tail surface area or aspect ratio, will yield an increase in the component's mass. The maximum root thickness (now used in feet) however, when increased, results in a reduction in the mass, due to its position in the denominator.

$$W_{HT,Cessna} = \frac{3.184 \cdot W_{dg}^{0.887} \cdot S_{HT}^{0.101} \cdot AR_{HT}^{0.138}}{174.04 \cdot t_{HT}^{0.223}} \quad (3.55)$$

Where:

$AR_{HT}$  = Aspect ratio of the horizontal tail.

Similar to the horizontal tail equation, Roskam's equation for determining the mass of the vertical tail, equation 3.56, implies that any increase in design gross weight, vertical tail area, or vertical tail aspect ratio will result in an increase in the component mass. Whereas, any increases to the maximum root thickness of the airfoil, will result in a reduction in the mass. The sweep, acts somewhat differently here in the denominator, and any increases in sweep will result in an increase in the structure's mass.

$$W_{VT,Cessna} = \frac{1.68 \cdot W_{dg}^{0.567} \cdot S_{VT}^{0.1249} \cdot AR_{VT}^{0.482}}{639.95_{t_{VT}}^{0.747} \cdot \cos\Lambda_{VT}^{0.882}} \quad (3.56)$$

Where:

$AR_{VT}$  = Aspect ratio of the vertical tail.

Roskam's equation for fuselage mass, given by equation 3.57, implies that any increase to either design gross weight, the number of passengers (and crew), and fuselage length will result in an increase in the structural mass of the aircraft. Somewhat counterintuitively, an increase in the maximum perimeter of the fuselage reduces the overall mass. Although a simple equation, once again it is possible to use the effects of fuselage lengthening brought about by the hydrogen tank to assess the effects on the fuselage mass.

$$W_{Fuselage,Cessna} = 14.86 \cdot W_{dg}^{0.144} \cdot N_p^{0.455} \cdot \left( \frac{l}{p_{max}} \right)^{0.778} \cdot l^{0.383} \quad (3.57)$$

Where:

$N_p$  = Number of personnel on board (crew + passengers)

$p_{max}$  = Maximum perimeter of the fuselage (ft)

The final set of equations, from Torenbeek, starts with equation 3.58, for determining the mass of the wing. Here, any increases to the sweep or span of the wing will ultimately result in an increase in mass, despite both being used as denominators across the equation. This is also true for the cases where design gross weight and ultimate loading factor. The maximum root thickness has a reducing influence on the component.

$$W_{W,Torenbeek} = 0.00125 \cdot W_{dg} \cdot \left( \frac{b_W}{\cos\Lambda} \right)^{0.75} \cdot \left( 1 + \sqrt{\frac{6.25 \cdot \cos\Lambda}{b_W}} \right) \cdot N_Z^{0.55} \cdot \left( \frac{b_W \cdot S_W}{t_{wmax} \cdot W_{dg} \cdot \cos\Lambda} \right)^{0.3} \quad (3.58)$$

Where:

$t_{wmax}$  = Maximum root chord thickness of the wing (ft)

Unlike the other authors work, Torenbeek has chosen to lump the horizontal and vertical tail together in a single equation, given in equation 3.59. Unusually, for structural mass sizing equation, the mass is not determined as a function of the design gross weight, but rather the ultimate loading factor, and the areas of the respective horizontal and vertical tail sections.

$$W_{Empennage,Torenbeek} = 0.04 \cdot (N_z \cdot (S_{VT} + S_{HT})^2)^{0.75} \quad (3.59)$$

The final equation for the masses is Torenbeek's fuselage mass equation, given as equation 3.60. Here, any increases to width or height will result in a lower fuselage mass, where as any increases to  $v_{max}$ , length or surface area, will result in an increase in the mass. however, there is no relationship between the fuselage mass, and the MTOM, or the ultimate loading factor; the increase in length due to the hydrogen tank will still be reflected in this case.

$$W_{Fuselage,Torenbeek} = 0.021 \cdot \sqrt{\frac{V_{max} \cdot l}{w + h}} \cdot S_f^{1.2} \quad (3.60)$$

In a bid to validate the most appropriate set of equations to be used, to determine the structural calculations within the hydrogen-electric aircraft sizing tool, each set of equations are placed in competition with one another, with respects to aircraft A' and B', in an attempt to observe any favorable trends. The results for structural masses from each author, for aircraft A' and B' are presented in table 3.23

As a first observation, it is clear to see that the mass predicted by the total structural mass given by the Roskam equations, is somewhat of an outlier, at nearly more than double the mass relative to the other studies for aircraft A' and B'. In this case, most of the mass disparity comes from the sizing of the fuselage, coming in

Table 3.23: Structural Component Mass for Aircraft A' and B' According to Sizing Methodology

Aircraft	Structural Component	Raymer (kg)	Nicolai (kg)	Cessna (kg)	Torenbeek (kg)
A'	Wing	597.38	621.79	638.78	285.21
B'	Wing	529.93	539.30	643.54	253.94
A'	Horizontal Tail	75.55	80.02	90.37	[-]
B'	Horizontal Tail	76.07	80.62	91.88	[-]
A'	Vertical Tail	55.69	25.79	0.54	[-]
B'	Vertical Tail	86.15	26.22	0.99	[-]
A'	Total Empennage	131.25	105.82	90.91	120.55
B'	Total Empennage	162.22	106.84	92.87	120.55
A'	Fuselage	654.55	518.51	2453.09	1241.99
B'	Fuselage	655.89	521.05	2459.69	1240.36
<b>A'</b>	<b>Total Structure</b>	1383.17	1246.12	3182.78	1647.75
<b>B'</b>	<b>Total Structure</b>	1348.05	1167.19	3196.096	1614.86

at approximately four times the value of that presented Raymer and Nicolai, and twice that of Torenbeek. An additional anomaly for the Roskam equations is found in the masses for the vertical tail, where a value of less than 1kg is obtained for both aircraft. However, the horizontal tail overcompensated for this, resulting in an empennage mass which is in good alignment with the the rest of the studies empennage masses. The Roskam equations will not be used for the final analysis based on the excessive fuselage mass, and inconsistencies with the mass for the horizontal and vertical tail structures.

Torenbeek's equations, although in good agreement with the Raymer and Nicolai, in terms of the empennage masses, are somewhat disproportionate with both the values for the fuselage and wing. The wing values are roughly 50% of the value of the sizing by Raymer and Nicolai, for both aircraft A' and B'. Additionally, Torenbeek only considers the structural mass as a function of the aircraft gross design weight, for the wing mass calculation only, while empennage and fuselage are based mainly around a geometric parameters. Torenbeeks equations therefore do not qualify for

the hydrogen-electric aircraft sizing regime.

The results between Raymer and Nicolai are in a relatively good agreement with one another. A percentage difference comparison does not really add much value at this stage, as there is no baseline structural values for reference. Based on this, Raymer's structural mass calculations will be used exclusively in the sizing regime, as there are advantages to using the wing mass calculation specifically, as it is possible to amend the fuel mass of the wing to now incorporate the lumped masses of the propulsion system, and ensure that its effects are captured in the mass build up of the new aircraft.

### 3.6 Aerodynamic Adjustments

The previous sections have discussed the idea of the aircraft's geometry changing as a function of increased mass and hydrogen tank length. If the wing loading is held at a constant value, but the mass increases on every iteration, this leads to a requirement for a larger wing surface area to support the additional mass of the aircraft, while maintaining the same lift distribution. Likewise, the length of the fuselage will increase with the length of the H<sub>2</sub> tank, thus increasing the fuselage surface area. These increases in geometric area, inevitably lead to a greater value of parasitic drag, which must be overcome by additional thrust, which potentially results in a requirement for an up-scaled propulsion system, and as a byproduct, an increased fuel burn. In order to be scientifically accurate, the change in parasitic drag,  $\Delta C_{D,min}$ , must be accounted for, and the respective drag polars adjusted.

The conventionally sized aircraft, is once again taken advantage of. The parasitic drag of the fuselage and wing, is first determined, to act as a baseline, and will be subtracted from the fuselage and wing parasitic drag of the new aircraft, during each sizing iteration, to determine a new parasitic drag value, as per equation 3.61. This

Table 3.24: Drag Calculation Assumptions

Parameter	Value	Unit
Free-Stream Velocity, $V_\infty$	55	$m/s$
Altitude	0	$m$
Density	1.225	$kg/m^3$
Dynamic Viscosity, $\mu_{altitude}$	$1.79e^{-5}$	$kg/m - s$
Flow State	Fully Turbulent	[-]
Smooth Paint Roughness, $k$	$0.634e^{-5}$	[-]

new calculation will form an additional convergence requirement for the aircraft sizing system.

$$C_{D,min} = C_{D,min,original} + (C_{D,min,new} - C_{D,min,conventional}) \quad (3.61)$$

### 3.6.1 Fuselage Parasitic Drag

The fuselage parasitic drag can be calculated by making an initial set of assumptions, for the calculation parameters, these being a reference free-stream velocity, an initial altitude, and a flow state, the values for this study are taken as those given in table 3.24.

The  $C_{D,min}$ , for any component,  $C_{D,min,c}$  is given by equation 3.62, and the parasitic drag of all of the components, is summed to give the final result. It is possible to use either SI or imperial units, to yield the same result.

$$C_{D,min,c} = \frac{C_{f,c} \cdot FF_c \cdot Q_c \cdot S_{wet,c}}{S_{ref}} \quad (3.62)$$

Where:  $C_{f,c}$  = Flat plate skin friction coefficient

$FF_c$  = Component form factor

$Q$  = Component interface factor. Generally taken as 1 for the fuselage, and 1 for a

high-wing, or well filleted low-wing

$S_{wet,c}$  = Component wetted area

$S_{ref}$  = Wing reference area

For turbulent flow, the flat plate skin friction coefficient is calculated using equation 3.63.

$$C_{f,c} = \frac{0.455}{(\log_{10} \cdot R)^{2.58} \cdot (1 + 0.144 \cdot M^2)^{0.65}} \quad (3.63)$$

The Reynolds number for the fuselage can be calculated from equation 3.64. In the case of the Reynolds number for the fuselage, the total length of the fuselage is used, where as, this will change when the wing is considered, and the Mean Aerodynamic Chord (MAC) will be used as the length.

$$R = \frac{\rho \cdot V_{\infty} \cdot l_{fuselage}}{\mu_{altitude}} \quad (3.64)$$

The form factor,  $FF_c$ , is determined through equation 3.65 ,

$$FF_c = \left( 0.9 + \frac{5}{f^{1.5}} + \frac{f}{400} \right) \quad (3.65)$$

Where:

$f$  = Relationship between fuselage length and average fuselage diameter,  $l/d$ . Not to be confused with lift to drag ratio

As the length of the fuselage grows,  $\Delta l$ , with the length of the hydrogen tank, a means of adding additional fuselage wetted area,  $S_f$ , is required, as shown in figure 3.16. For the fuselage this is a simple case, of adding an additional, extruded

hollow profile area onto the the existing fuselage area. As the D228 has a rectangular fuselage, the additional area will come from the change in length multiplied by the height, for both the sides, and the change in length multiplied by the width, for the roof section and belly section. This can be determined through equation 3.66. In the event that the aircraft does not have a rectangular fuselage, and is of the more traditional 'tadpole' or cylinder shape, the additional area can be given, by taking the area of an open ended cylinder, whose length is the change in length of the fuselage, as a best approximation.

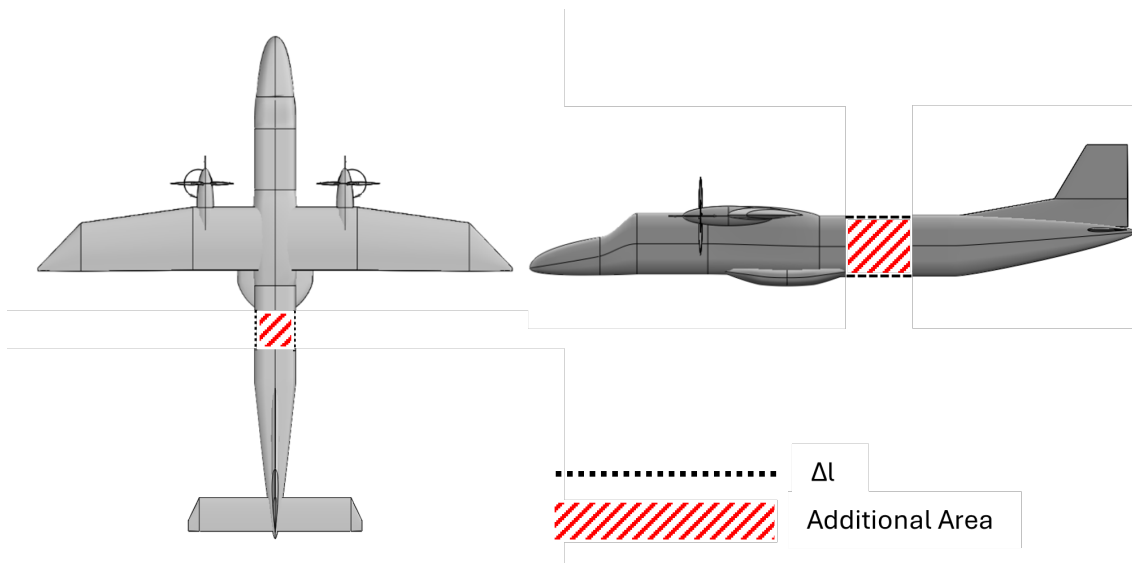


Figure 3.16: Dornier 228 Additional Wetted Area of the Fuselage

$$S_{f,new} = S_f + ((2 \cdot \Delta l \cdot h) + (2 \cdot \Delta l \cdot w)) \quad (3.66)$$

Using the conventional aircraft as a reference, in conjunction with above equations for calculating the reference parasitic drag of the fuselage, when it is configured to a standard length, using a conventional propulsion system, the parasitic drag,  $C_{D,min,fuselage}$ , is presented in table 3.25. An additional 5% is added to account for leakages and protuberances.

### 3.6.2 Wing Parasitic Drag

The parasitic drag of the wing is calculated in an almost identical means to the fuselage, with a minor change to the calculation of the Reynolds number, where the characteristic flat plate length is now the the MAC of the wing. It is possible to obtain the MAC, by working through equation 3.67, which determines the wingspan, equation 3.68 to determine the length of the wing root chord,  $C_{root}$ , which is then fed into equation 3.69 to determine the MAC, also referred to as  $\bar{C}$ .

$$b_W = \sqrt{AR \cdot S_{ref}} \quad (3.67)$$

$$C_{root} = \frac{2 \cdot S}{b_W \cdot (1 + \lambda)} \quad (3.68)$$

$$\bar{C} = \frac{2}{3} \cdot C_{root} \cdot \left( \frac{1 + \lambda + \lambda^2}{1 + \lambda} \right) \quad (3.69)$$

The value for,  $C_{f,c}$ , the flat plate skin friction coefficient, uses equation 3.63 in its original form. However, the equation for the wing's form factor,  $FF_W$ , is entirely different to that of the fuselage, and is presented in equation 3.70. With the new values for the wing Reynolds number, wing form factor, and wing skin friction coefficient, equation 3.62 is used again to determine the parasitic drag of the wing,  $C_{D,min,wing}$ , and can be summed with that from the fuselage to make the total for the two components, given as,  $C_{D,min,wing\&fuselage}$ . These values are presented in 3.25.

$$FF_W = \left[ 1 + \frac{0.6}{x/c_m} \cdot \left( \frac{t}{c} \right) + 100 \cdot \left( \frac{t}{c} \right)^4 \right] \cdot [1.34 \cdot M^{0.18} \cdot (\cos\Lambda_m)^{0.28}] \quad (3.70)$$

Where:

$x/c_m$  = Chord wise location of the of the maximum airfoil thickness point. For low speed wings, this is approximately 0.3 of the total chord length, and approximately 0.5 for higher speed wings

$\Lambda_m$  = Sweep of the maximum thickness line

To account for the changes in the  $S_{wet,c}$  for the wing,  $\Delta S_{wet,c}$ , a new value of  $S_{wet,wing}$  requires calculating, such that it can be subtracted from the original, to yield the difference. Equation 3.71 can take care of this, if the exposed area of the wing,  $S_{exposed}$  is known, and the wing thickness-to-chord ratio is less than 0.05; equation 3.72, deals with wing thickness-to-chord ratios above 0.05. The growth in wing area is shown by figure 3.17

$$S_{wet,wing} = 2.003 \cdot S_{exposed} \quad (3.71)$$

$$S_{wet,wing} = S_{exposed} \cdot \left[ 1.977 + 0.52 \cdot \left( \frac{t}{c} \right) \right] \quad (3.72)$$

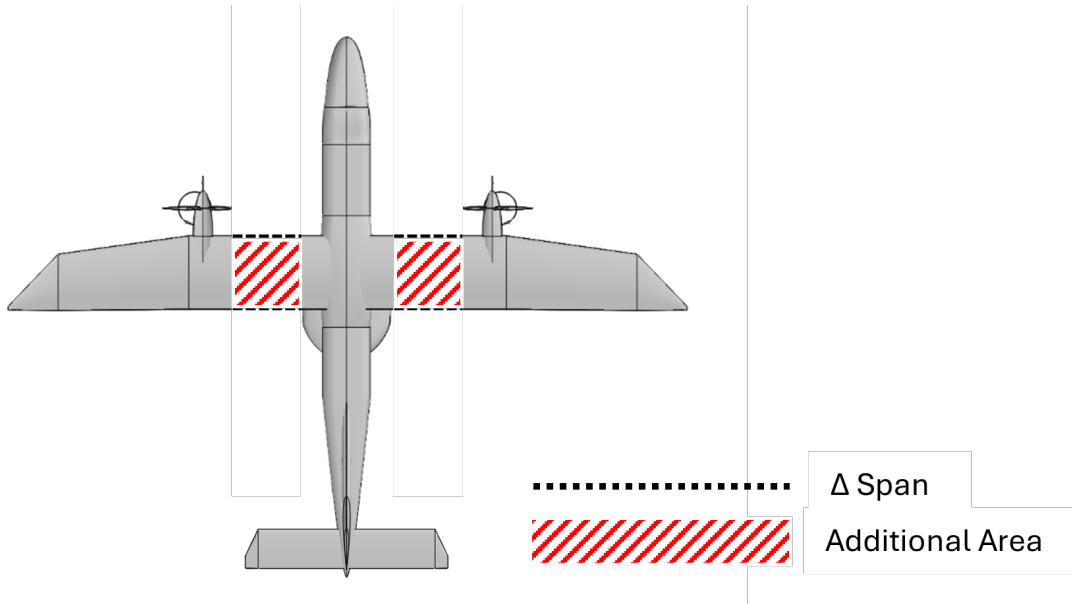


Figure 3.17: Dornier 228 Additional Wetted Area of the Wing

The exposed area of the wing,  $S_{exposed}$  is the reference area of the wing,  $S_{ref}$  minus

some value of area which is not exposed to lift, and is usually found to be the wing-box which runs over, under or through, the fuselage. For the analysis, the fuselage width will be known, and the wing root chord,  $C_{root}$ , calculated as part of the drag analysis, can be used to determine the value of the area above the fuselage, and thus not exposed. In order to not overestimate the non-exposed area, by not factoring in the wing taper from the center line, this area must be calculated; this area is highlighted in figure 3.18.

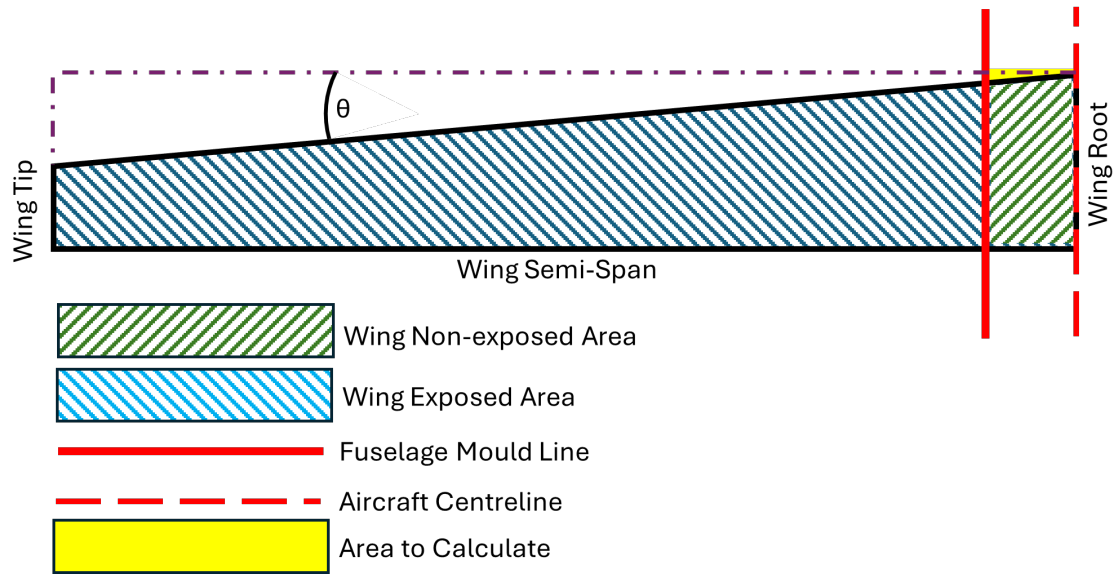


Figure 3.18: Exposed Wing Area Geometry

Using equation 3.73, the difference between the root chord and the tip chord, referred to as  $\Delta_{root}$ , can be calculated. This is used to form the 'dashed purple' line extending from the wing tip, which will be used trigonometrically to determine the angle, between the angle of the taper,  $\lambda_{angle}$ , given by equation 3.74, which can then be used in equation 3.75, to determine the area based on the angle, and the distance to the fuselage mould line from the aircraft centerline. The area of the non-exposed section can be calculated as the root chord multiplied by the fuselage width, and subtracting two times the the area calculated previously, using equation 3.76. Finally the exposed area is determined using the wing area, and the non-exposed wing area.

Table 3.25: Fuselage and Wing Parasite Drag for Conventional Aircraft

component	Parasitic Drag Value
Fuselage, $C_{D,min,fuselage}$	0.0067
Wing, $C_{D,min,wing}$	0.0073
Total, $C_{D,min,wing\&fuselage}$	0.014

$$\Delta_{root} = C_{root} - (\lambda \cdot C_{root}) \quad (3.73)$$

$$\lambda_{angle} = \tan^{-1} \left( \frac{\Delta_{root}}{0.5 \cdot b_w} \right) \quad (3.74)$$

$$\lambda_{angle,area} = 0.5 \cdot \left( \frac{w}{2} \right) \cdot \left( \left( \frac{w}{2} \right) \cdot \tan(\lambda_{angle}) \right) \quad (3.75)$$

$$S_{non-exposed} = (w \cdot C_{root}) - (2 * \lambda_{angle,area}) \quad (3.76)$$

$$S_{exposed} = S_{ref} - S_{non-exposed} \quad (3.77)$$

At this stage, no adjustments are to be made for the vertical and horizontal tail.

## 3.7 Fuel Cell, Hydrogen Storage and Propulsion System Modelling

With a means to successfully describe the structural mass build up for the new aircraft, and determine any variations in the aerodynamic properties based on al-

terations to the geometry, it remains for the propulsion system to be incorporated into the model. The propulsion system comprises of a fuel cells, batteries, motors, gear boxes, Power and Energy Management and Distribution (PEMAD) systems, power converters, H<sub>2</sub> tanks and inverters; each of these components will be dealt with individually. The proceeding discussions relate to section 4 of the methodology flowchart, 'Hydrogen-Electric Aircraft Sizing', repeated below in figure 3.19.

### 3.7.1 Fuel Cell Modelling

The PEMFC is the fuel cell of choice for this project. This decision is based on a multitude of factors, the first being, the type's successful use in ZeroAvia's campaign for hydrogen fuel cell aircraft, in both their Dornier 228, and Piper Malibu Mirage retrofitted experimental aircraft. In addition to being commercially available, at high power outputs, with established legacies, the PEMFC is a well documented and well researched power source, with a plethora of literature available on different techniques for developing models; each with varying degrees of fidelity, and as such complexity. The literature review section has already discussed some of these modelling techniques.

A running theme throughout this project is the requirement for accurate modelling with reduced simulation time, to permit for parameter sweeps and optimisation without excessive computational expense and consumption of time budget. Although the operating principles of the hydrogen fuel cell, described previously, could be considered 'simple', the full high fidelity design and simulation of such is somewhat beyond the scope of this project due to both the author's limited expertise in the field, and the complexities surrounding the precise sizing of Balance of Plant (BoP) equipment.

As such, a more applicable model is utilised here. The model in question is based

### 3.7. FUEL CELL, HYDROGEN STORAGE AND PROPULSION SYSTEM MODELLING

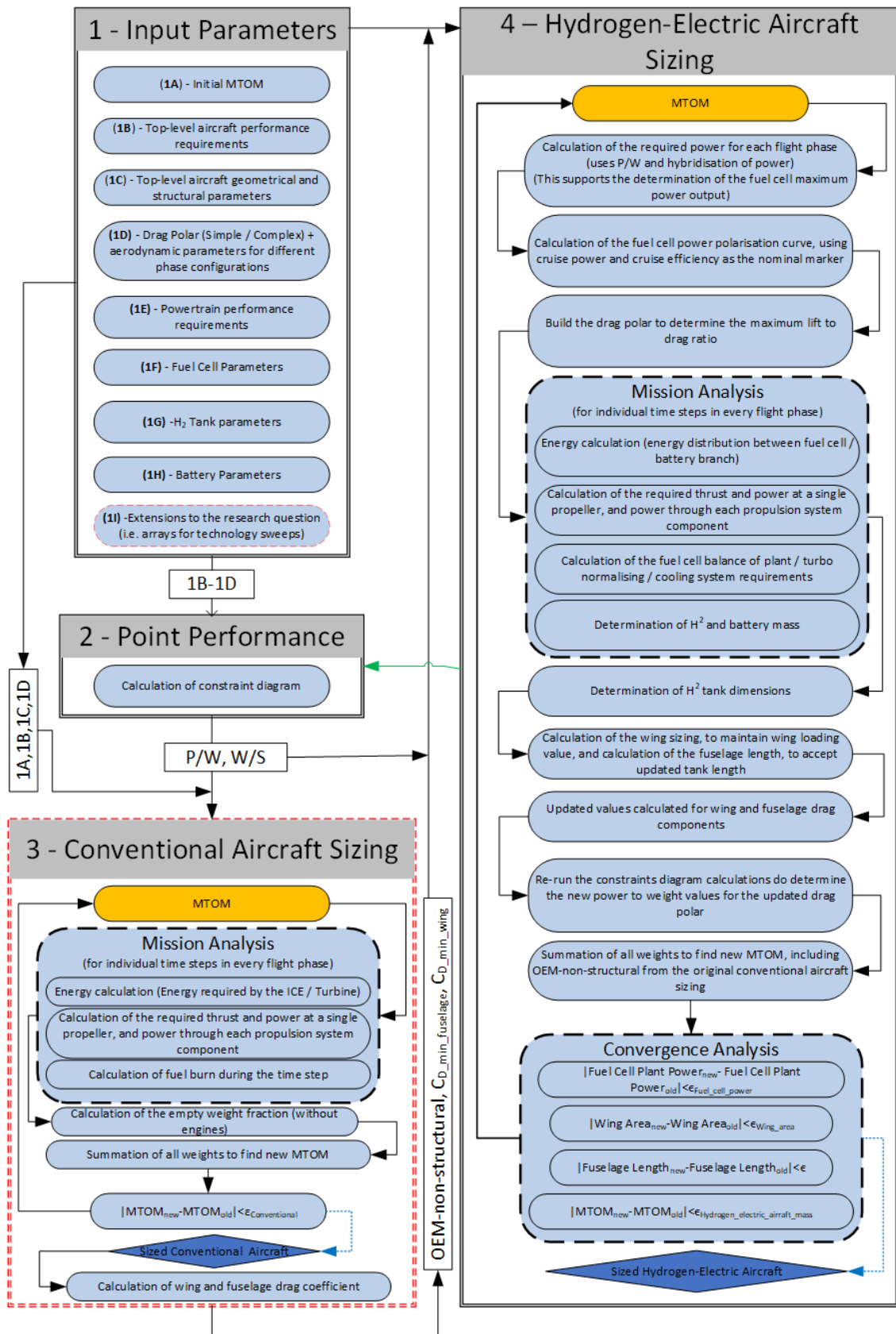


Figure 3.19: Methodology Flow Chart

### 3.7. FUEL CELL, HYDROGEN STORAGE AND PROPULSION SYSTEM MODELLING

---

around the generic dynamics of the fuel cell polarisation curve, which describes the relationship between output voltage and current density. An Empirical fuel cell polarisation curve model is adopted, based on the work in [105], which provides the fitting equation in 3.78, and its corresponding fitting parameters, which are subject to the current density,  $i$ , in  $A/cm^2$ .

$$V_{cell} = V_{OCV} - b \cdot \log\left(\frac{i + i_{loss}}{i_{loss}}\right) - (R \cdot i) - (m \cdot [\exp(n \cdot i) - 1]) \quad (3.78)$$

Where:

$$V_{OCV} = 0.956 \text{ (V)}$$

$$b = 0.06677 \text{ (V/decade)}$$

$$R = 0.1073 \text{ } (\Omega/cm^2)$$

$$i_{loss} = 0.001241 \text{ } (A/cm^2)$$

$$m = 0.005339 \text{ (V)}$$

$$n = 2.2353 \text{ } (cm^2/A)$$

Equation 3.78 describes the behavior of a single cell, shown in figure 3.20, for a range of current densities. To achieve the power and voltage levels required for practical purposes, a number of cells are stacked in series. This is the fuel cell stack; however, as this project does not concern itself specifically with the voltage of the fuel cell, only the overall power will be considered.

Extracting the power of an entire fuel cell stack for an aircraft, and making it tunable to system demands, by using data from a curve which describes only a single cell's voltage and current density, begins by turning the voltage versus current density curve into a power versus current density curve, through multiplication of the voltage with its corresponding current density. Figure 3.21, based on equation 3.78, shows this relationship, and additionally, shows the power with respects to the fuel cell's efficiency, which is directly related to the cell's voltage. As the figure

### 3.7. FUEL CELL, HYDROGEN STORAGE AND PROPULSION SYSTEM MODELLING

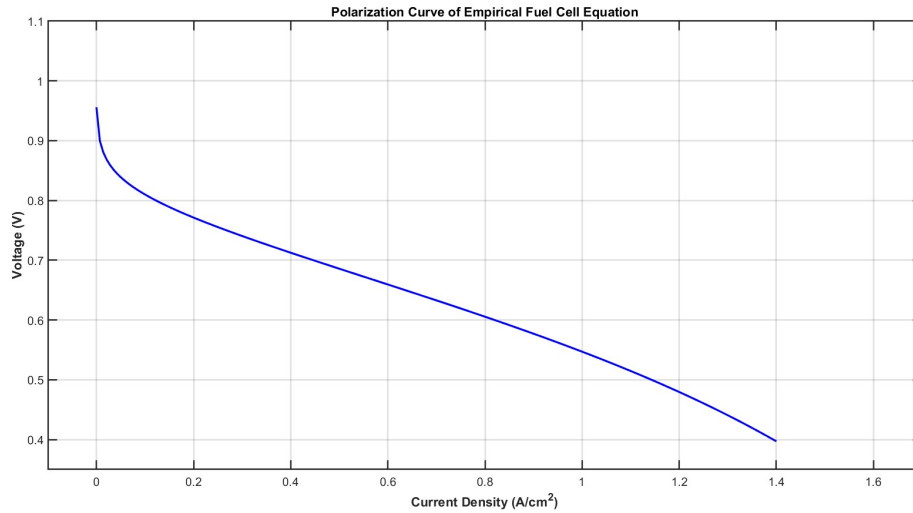


Figure 3.20: Polarisation curve of empirical fuel cell equation

shows, the peak power point appears at an efficiency of approximately 37%, as the efficiency drops off with an increase in power output. Importantly, as previously discussed, fuel cells should not be operated for long periods at this peak power point, as it has the potential to damage the stack, and reduce the service life; instead a more conservative operating point of between 50% and 60% should be chosen.

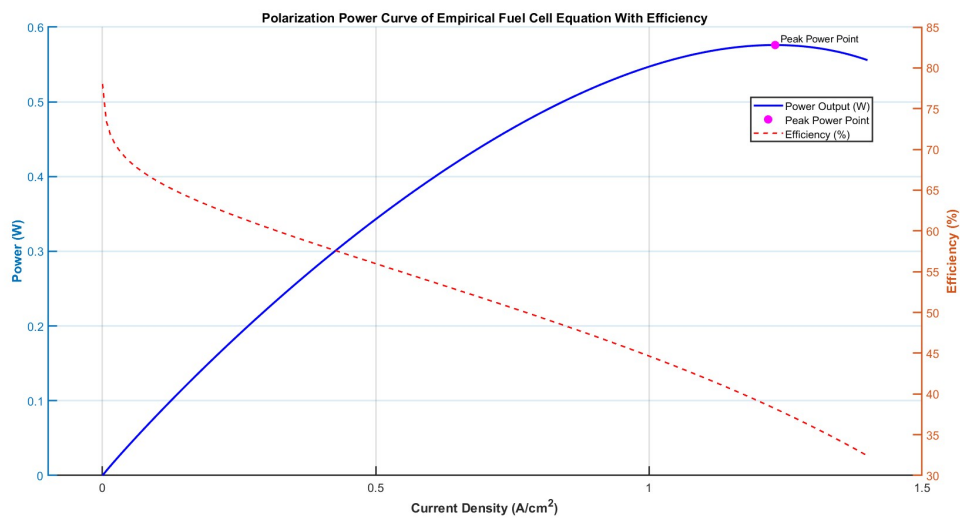


Figure 3.21: Polarisation Power curve of empirical fuel cell equation with efficiency

It is possible to use the power versus current density data by creating a normalisation factor,  $FC_{nf}$ , and scaling the power to usable levels for the aircraft. This is achieved by initially selecting a target efficiency operating point, and this will

be the approximate efficiency that the aircraft is expected to achieve during cruise. The efficiency point has a corresponding power density point,  $PDP_i$ , at the same index as the efficiency, which is extracted. A selected nominal power,  $P_{nominal}$ , for the fuel cell, which again, will be the cruise power, where the fuel cell is expected to operate most efficiently, is chosen. Dividing the nominal power by the extracted power density point yields the normalisation factor. The normalisation factor is then multiplied by each of the power densities in the array; this produces the same shape as the original single cell power output with respects to efficiency, but it is now scaled to a usable power for the aircraft, while still allowing for plotting against current density, and provides the efficiency values based on the power that the aircraft outputs during the flight profile, allowing for a variable efficiency model to be achieved, which will also have an influence on the fuel cell's cooling system sizing. Having the ability to scale the fuel cell by selecting the operating efficiency of the aircraft during cruise, allows for additional trade studies to be undertaken.

$$FC_{nf} = \frac{P_{nominal}}{PDP_i} \quad (3.79)$$

This model is demonstrated, whereby an arbitrary value of a 1 Megawatt cruise phase is selected, and the fuel cell is also sized to work at 55% efficiency. The results are shown in figure 3.22. The plot clearly shows the fuel cell has a nominal operating point of 1 Megawatt at 55% efficiency. This also shows that the nominal operating point is at approximately 62.5% of the peak operating power, with the remaining power potentially being sufficient to take care of the take-off and climb phase, with only minimal input power from an additional battery. This will also be addressed during a trade study.

Additional BoP is required to ensure that the fuel cell operates at the scaled conditions, and to ensure that it is fully able to provide both propulsive power,  $FC_{PP}$ , across the flight profile and altitudes, as well as producing power to sustain itself.

### 3.7. FUEL CELL, HYDROGEN STORAGE AND PROPULSION SYSTEM MODELLING

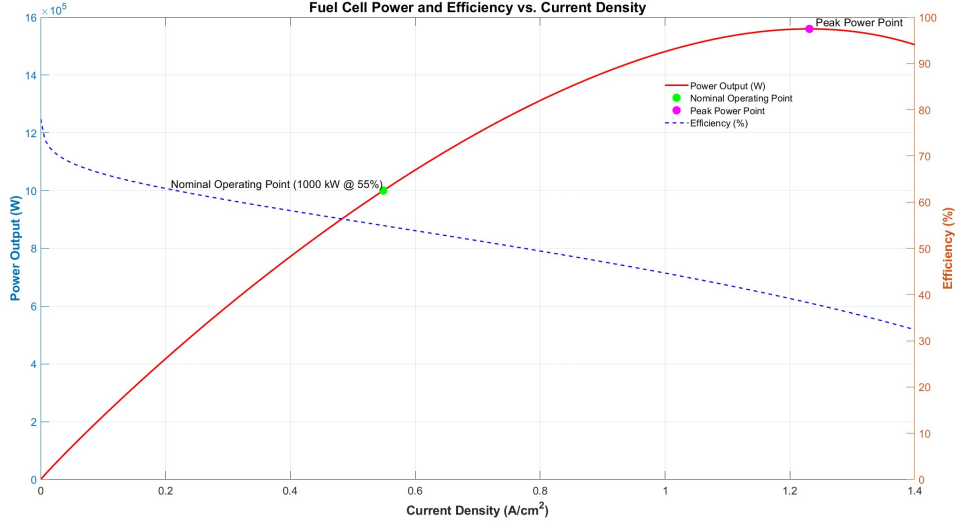


Figure 3.22: 1MW Continuous Power Fuel Cell

These are the turbo-normalising compressor,  $P_{TNC}$ , which acts as a compressor load, required to power a compressor unit which is used to increase the air pressure entering the fuel cell, ensuring that it operates at its optimum pressure, of 1 atmospheric bar for this study, as the aircraft climbs and the air density decreases with altitude. The other major component is the cooling system,  $P_{Cooling}$ , which must also be factored into the scaled fuel cell power, with the consideration of the power required for both a blower fan and the cooling system. The equation for the fuel cell power requirement,  $FC_{Power,Req}$ , thus becomes that given by 3.80. These systems are dealt with independently, below.

$$FC_{Power,Req} = FC_{PP} + P_{TNC} + P_{Cooling} \quad (3.80)$$

With the inclusion of the additional components the fuel cell sizing is now an integral part of the sizing iteration loops and requires its own convergence loop, to ensure that the aircraft has sufficient power, as the outer iteration loops for mass, and drag potentially continue to increase.

In addition to improving the fuel cell model, through the ability to select an operat-

ing efficiency point, and sizing the fuel cell around this point, the model is adapted further, to incorporate the dynamics of the response to changes in power.

As already discussed in the introduction section, fuel cells have a particular dynamic, in which their response is not instantaneous, when attached to a resistive and inductive (RL) load, and this response, as well as being part of the intrinsic nature of the physics of the fuel cell and load, is also subject to the fuel cell's supporting BoP, such as the response time of a compressor. In order to model the response rate of the fuel cell, without knowing manufacturer specifics, or performing an in depth analysis to determine the transfer function of the entire propulsion system, during every iteration of the sizing tool, some assumption has to be made. Inspired by the fuel cell polarisation curve fitting equation, a 'catch all' equation has been developed by the author, in a bid to ensure that the sizing tool's fuel cell response time is inline with that of existing fuel cells. This was achieved, by using the SIMULINK 6kW and 85kW fuel cell models, developed by [16], and performing a basic fitting; the results of the fitting for the 6kW study can be observed in figure 3.23, while the 85kW study, is placed in the appendix. The resulting equation, given as 3.81, requires the fuel cell power at each time step,  $ts$ , and the previous time step, where  $i$  represents the current flight index, and  $i - 1$  represents the previous flight index,  $\tau$  is the system response time, and finally a tunable gain parameter, based on fuel cell power levels, and response time, presented as  $g_{dynamic}$  is used.

$$FC_{Power,Req,i} = FC_{Power,Req,i-1} + (FC_{Power,Req,i} - FC_{Power,Req,i-1}) \cdot \left( 1 - e^{-\frac{ts}{\tau} g_{dynamic}} \right) \quad (3.81)$$

The values for  $g_{dynamic}$  for each study are presented in table 3.26, and used to determine a  $g_{dynamic} = f(\tau, FC_{power})$ . The derivation of the gain, as a function of response time and fuel cell power, starts by plotting the results of 3.26, to observe

### 3.7. FUEL CELL, HYDROGEN STORAGE AND PROPULSION SYSTEM MODELLING

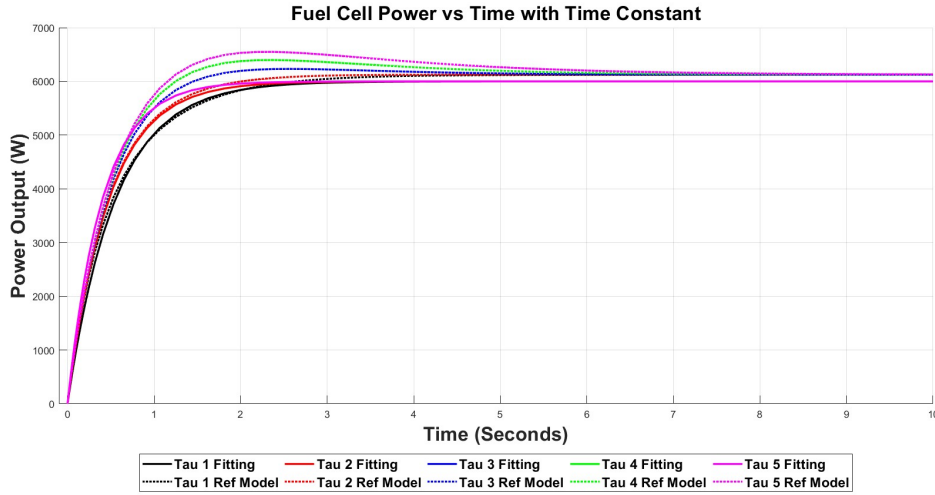


Figure 3.23: Fuel Cell Response Time Dynamic Equation

Table 3.26:  $g_{dynamic}$  for 6kW and 85kW Fuel Cell Response Time Study

$\tau$	$g_{dynamic}$ 6kW	$g_{dynamic}$ 85kW
1	0.55	0.3
2	0.95	0.55
3	1.2	0.9
4	1.6	1.1
5	2	1.3

any trends. Figure 3.24, demonstrates a quasi-linear increase in the gain value, with an increasing response time, and a decreasing value in gain with increasing fuel cell power; the equation for linear trend lines are presented in equations 3.82 and 3.83 for the 6kW and 85kW fuel cell respectively, and generalised in equation 3.84.

$$6kW_{g,trend} = (0.333 \cdot \tau) + 0.195 \quad (3.82)$$

$$85kW_{g,trend} = (0.255 \cdot \tau) + 0.065 \quad (3.83)$$

$$General_{g,trend} = (a(FC_{power}) \cdot \tau) + b(FC_{power}) \quad (3.84)$$

Based on the above data, and trends observed in figure 3.24, a power law assumption, with  $FC_{power}$  is made, forming equations 3.85 and 3.86, and a least squares

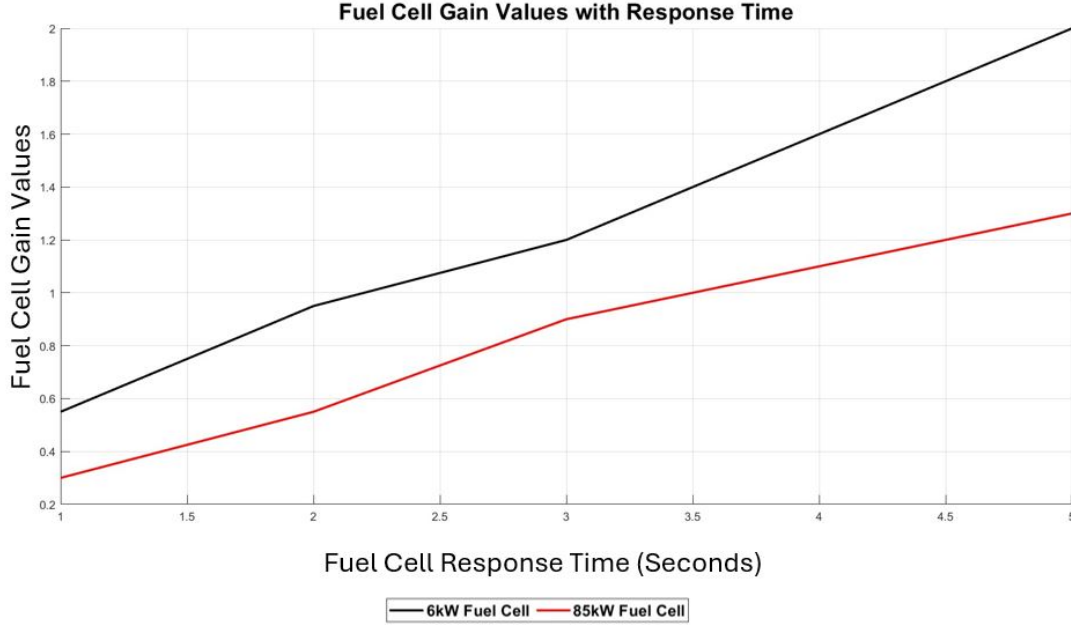


Figure 3.24: Fuel Cell Gain Values with Response Time

fitting is performed using MATLAB, so the general form of the equation, becomes that of equation 3.87.

$$a(FC_{power}) = c_1 \cdot P^{-n} = 0.444 \cdot FC_{power}^{-0.125} \quad (3.85)$$

$$b(FC_{power}) = c_2 \cdot P^{-m} = 0.41 \cdot FC_{power}^{-0.414} \quad (3.86)$$

$$g_{dynamic}(\tau, FC_{power}) = (0.444 \cdot FC_{power}^{-0.125}) \cdot \tau + (0.410 \cdot FC_{power}^{-0.414}) \quad (3.87)$$

A simple test to validate the entirety of the response formula is shown in figure 3.25, where it can be observed that the lower values of response time align almost perfectly, with the reference fuel cell. However as the system time response increases, the overshoot forces the reference fuel cell to deviate away from the powers predicted by the fuel cell power equation, to a much greater extent than that shown by the 85kW fuel cell study. During these studies the RL load is quantified by the square of the voltage over the nominal fuel cell power, and this rudimentary estimate for the load and system inductance may be giving rise to greater deviations

### 3.7. FUEL CELL, HYDROGEN STORAGE AND PROPULSION SYSTEM MODELLING

as the power exits the quasi-linear portion of the power plot; it is also worth noting that the materials and configuration of any practical fuel cells may also give some deviation due to membrane resistances and cell areas. However, as an initial approximation, when little is known about the specific inductance of the system or loads, the response formula does provide some representation of the general fuel cell dynamics, and as such, finds its place in the aircraft sizing tool; an updated study to refine this equation may be a useful asset to any future work.

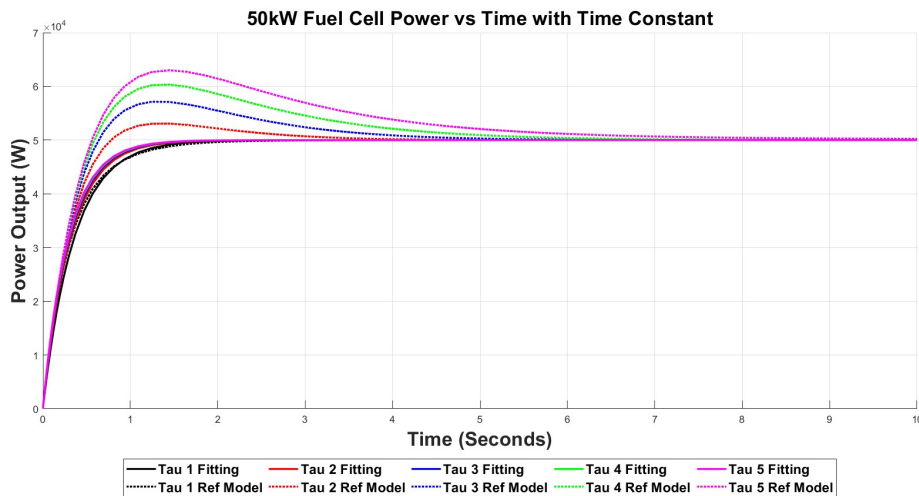


Figure 3.25: 50kW Fuel Cell Gain Values with Response Time

One of the drawbacks of such a simple means to determine the fuel cell response is that it cannot directly represent the fuel cell, as the Tremblay model displays some overshoot, which is to be expected from a fuel cell, which the equation does not capture, however, for systems with a response time of  $\leq 2$  seconds, the results are in good order, and the equations lends itself well. It is worth noting that there is a minor error between the final steady state powers of the equation and the SIMULINK model, possibly due to the resistor and inductor values used in the SIMULINK model.

### Fuel Cell Turbo-normalising Compressor

For the turbo-normalising compressor, the power requirement is a function of the temperature increase due to air compression, plus the air flow rate through the unit. The compressor's pressure ratio,  $PR_{TNC}$ , is used to calculate the rise in temperature, with respects to the ambient air temperature at altitude, when sea level pressure is given as the reference. The pressure ratio is related to the altitude, through equation 3.88, which makes the assumption that there will be a pressure loss in the order of 10% as the air is distributed across the cathodes of the fuel cell.

$$PR_{TNC} = \frac{P_{SL}}{P_{alt,i}} \cdot 1.1 \quad (3.88)$$

Where:

$P_{SL}$  = Sea Level Reference Pressure, Pascal

$P_{alt,i}$  = Pressure at flight indexed altitude, Pascal

The compressor's polytropic efficiency,  $\eta_{TNC}$ , and pressure ratio are used to calculate the change in air temperature for the ambient air entering the compressor, as given in equation 3.89.

$$T_{t2} = T_{t1} \cdot \left( \frac{1}{\eta_{TNC}} \right) \cdot (PR_{TNC})^{\left( \frac{\gamma-1}{\gamma} - 1 \right)} \quad (3.89)$$

Where:

$T_{t2}$  = Final temperature after the compressor stage, Kelvin

$T_{t1}$  = The ambient temperature at altitude, Kelvin

$\gamma$  = Ratio of specific heats, and given as 1.4 for standard air conditions; as observed in the Mach equation

The mass flow rate,  $\dot{m}$ , of the air is required for the calculation of the compressor unit power. This is dealt with using equation 3.90, and is a function of the power which must be provided by the fuel cell, it's polytropic efficiency, and the ratio of oxygen supplied, relative to the oxygen required for the reaction to take place between the cathode and anode of the cell. This is referred to as the stoichiometric ratio, presented as  $\gamma_{O_2}$ , and a value of between 1.5 and 2 is generally used, ensuring that the oxygen partial pressures are inline with what a fuel cell would expect to work at efficiently.

$$\dot{m}_{air} = (2.856 \cdot 10^{-7}) \cdot \gamma_{O_2} \cdot \frac{FC_{Power,Req}}{\eta_{FC}} \quad (3.90)$$

Using the result of equations 3.89 and 3.90, along with the heat capacity,  $C_p$  of the air, taken as 1005 Joules per kilogram, in conjunction with the efficiency of the motor driving the compressor,  $\eta_{TNC,motor}$ , and ambient air temperature, it is possible to arrive at the final equation to determine the power required for the turbo-normalising compressor, given in equation 3.91.

$$P_{TNC} = \frac{\dot{m}_{air} \cdot C_{p,air} \cdot (T_{t2} - T_{t1})}{\eta_{motor}} \quad (3.91)$$

### Fuel Cell Cooling System

For the cooling system, developed, and presented by a NASA study, from 2020 [106], this is dealt with as two separate components; these being the cooling fan, which creates an airflow across a heat exchanger, and the cooling pump, which cycles cooling fluid between the heat exchanger and the fuel cell, to remove any rejected heat power, for which a value can be determined using equation 3.93, based on the fuel cell's output power and the operating efficiency. A representative illustration of the system just described can be visualized in figure 3.26.

$$P_{rejected,heat} = \left( \frac{1}{\eta_{FC}} - 1 \right) \cdot FC_{Power,Req} \quad (3.92)$$

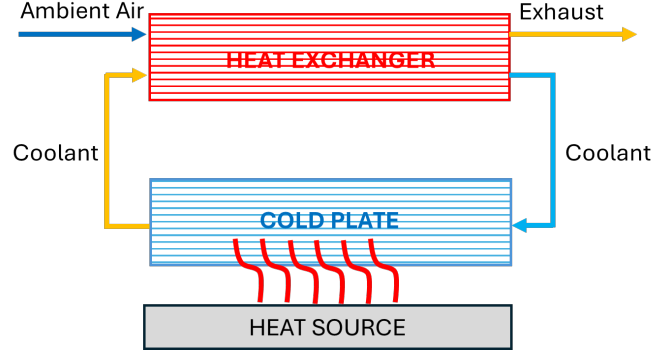


Figure 3.26: Fuel Cell Heat Exchanger Diagram

From [106], the equation for the cooling system power comes off the back an optimisation study which demonstrates a relationship between the power of the heat to be rejected by the cooling system, the cooling power, the aircraft mass, and the aircraft thrust. As this project is not explicitly focused on the detailed design of individual propulsion system components, equation 3.93 is assumed to be acceptable for this study, and includes the power demand for both the coolant circulation pump and the cooling fan. Equation 3.93, also introduces the term  $f(dT)$ , which is a correction factor that enables the cooling power equation to be used at other temperature difference,  $dT$ , values, outside of that used for the original optimisation study.

$$P_{Cooling} = (0.371 \cdot P_{rejected,heat} + 1.33) * f(dT) \quad (3.93)$$

$$f_{dT} = 0.0038 \cdot \left( \frac{T_{air}}{dT} \right)^2 + 0.352 \cdot \left( \frac{T_{air}}{dT} \right) + 0.1817 \quad (3.94)$$

### 3.7.2 Hydrogen Consumption Model

Hydrogen consumption is determined by initially calculating the molar flow rate of the hydrogen,  $\dot{n}_{hydrogen}$ , as a function of the fuel cell power, when subject to all of the systems efficiency values, and the Higher Heating Value (HHV), for  $\text{GH}_2$ , as per equation 3.95. The HHV used for the hydrogen fuel cell is given as 286 kJ/mol [107] [108] [109], due to formation of liquid water as the byproduct from the reaction.

$$\dot{n}_{hydrogen} = \frac{FC_{Power,Req,i}}{GH_{2,HHV}} \quad (3.95)$$

With the molar flow rate calculated, it remains to use the atomic weight of hydrogen,  $\mu_{hydrogen}$ , given as 0.00100784 kg/mol [110], to be able to calculate the mass flow rate,  $\dot{m}_{hydrogen}$ , and when multiplied by the time step,  $\Delta_t$ , yields the hydrogen consumption mass. As  $\text{GH}_2$  exists as two hydrogen atoms, the atomic mass value is multiplied by two. Equation 3.96.

$$m_{hydrogen,i} = (\dot{n}_{hydrogen} \cdot (\mu_{hydrogen} \cdot 2)) \cdot \Delta_t \quad (3.96)$$

The sum of the hydrogen mass, for every time step, constitutes the hydrogen consumption for the entire flight.

### 3.7.3 Battery Modelling

As an alternative to using a battery model which encompasses the dynamics of the discharge curve, the model presented by [31], representing the "energy in a box" method discussed previously, is an ideal candidate for the sizing tool, and permits for easy sweeps of various battery technologies, with various specific energy and

discharge values.

In flight recharge, by uprating the nominal power of the fuel cell, opens up the potentials to reduce battery mass and reduce on ground turn-around times.

### 3.7.4 Hydrogen Storage Modelling

The sizing of the hydrogen storage vessel, is both a question of science and economics; in this subsection, the two are blended. To support this hypothesis, the introduction of the payload-range diagram is necessary, which can be observed in figure 3.27 from [111]. As the name suggests, the payload range diagram represents the aircraft's load carrying capabilities with respects to the range capable when taking off from MTOM. The nominal mission with a full payload and maximum range capability, is represented by the horizontal line starting off from zero range and ending at the maximum achievable range for the maximum payload, at this point, the only means to achieve additional range is through a reduction in the payload carried by the aircraft; this is represented by the linearly declining range on the plot, which suggests a decreasing payload results in an increased range. After this range the aircraft reaches another point on the payload range diagram, where it is limited by the maximum fuel it can carry, with the maximum permissible payload. However, the aircraft reaches a point where there is no payload, but a maximum range; in aviation terms, this is referred to as the 'ferry range' of an aircraft. The 'ferry range' is generally only exploited when repositioning the aircraft to a new operating center or delivering to a new customer.

With existing, conventionally powered aircraft, any combination of payload or range, with respects to acceptable regions on the payload range diagram, do not influence the structure of the aircraft, i.e. if the aircraft operates with only 50% of the fuel tank capacity, this does not influence the structure of the aircraft, as the

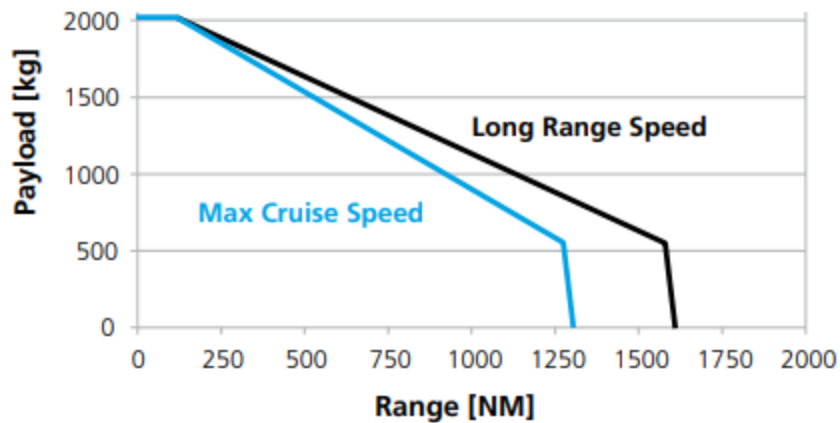


Figure 3.27: D228 Payload Range Diagram [111]

fuel is stored in the wing, and the same area / volume of wing is still required to provide the lift, so the mass stays the same and the aircraft requires no more or no less wing mass during its operational life, regardless of payloads or range, and still has the opportunity to operate a ferry flight without any modifications. The same cannot be stated for aircraft using  $\text{GH}_2$ , as the tank is now an additional component which is sized for the aircraft, and influences mass and geometry. If the hydrogen-electric aircraft was sized to carry out ferry operations using  $\text{GH}_2$  tanks, this suggests that for its operational life, where it carries out nominal missions with full or part payloads, it would be operating with an unnecessarily large tank, located in an unnecessarily fuselage, attached to an unnecessarily large set of wings, all of which translates into a compounding mass effect, solely due to the tank.

This author suggests that the aircraft should only be able to operate any extended ferry operations through the use of 'ferry tanks' such as those used in conventional aircraft, as shown in figure 3.28, from [112], and adapted for  $\text{GH}_2$ . As an alternative to aircraft delivery through ferrying, the option of shipping smaller aircraft is also available, where the aircraft can be reassembled at base [113], or perhaps more radically, and a homage to the sport of gliding or the 'Airspeed AS.51 Horsa' troop transporting glider, air-towing also offers potential to support the design of an aircraft without vast quantities of ferry capability [114] [115].



Figure 3.28: Example Ferry Tank from Turtle-pac [112]

As referenced in the literature review section, there are multiple methods to determine the size and mass of the tank. Initially the methodology presented by [33] was implemented, but initial results showed little confidence between values obtained and the values presented. As a result, the hydrogen tank efficiency model was used in conjunction with the calculations for the volume of a hemi-spherically capped cylinder,  $V_{Tank}$ , given by equation 3.97, where  $r$  is the tank radius, and governed by the minimum width of the fuselage, as shown in figure 3.29, which shows a cross section of the main cabin for the Dornier 228. The volume of the tank, is equivalent to the volume of the hydrogen,  $V_{H_2}$ , required for the flight, which leaves  $l_{tank}$  as the variable within the tool, and determined through a simple rearrangement of 3.97.

$$V_{Tank} = \left( \frac{4}{3} \cdot \pi \cdot r^3 \right) + (r^2 \cdot \pi \cdot l_{Tank}) \quad (3.97)$$

Naturally, the density of the hydrogen to be stored, and the storage pressure, determines the volume to be stored, and thus, the tank's length. ZeroAvia, use a pressure of 350 bar for their system, and this will be adopted for any future sizing studies. The resultant density of the hydrogen,  $\rho_{GH_2}$ , starts with a rearranged version of the ideal gas law equation [116], presented in equation 3.98, and termed the real gas law; this is used to determine the moles of GH<sub>2</sub>, for 1m<sup>2</sup> of hydrogen. This equation also includes the hydrogen compressibility factor,  $Z$ , which augments the results of

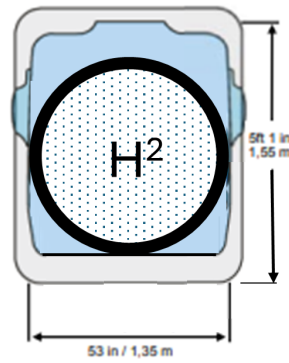


Figure 3.29: Fuselage and Tank Cross-Section

the ideal gas law, into a result which is akin to a gas behaving in a non-ideal manner [117]. Equation 3.98, is then substituted into equation 3.99, which uses the atomic mass of the  $\text{GH}_2$ , given in the previous subsection, to determine the density. For the simulation tool, a set of initial conditions are selected, these being a storage temperature,  $T$ , of 298.15 Kelvin, a pressure,  $P$ , of 350 bar, equivalent to  $350 \times 10^5$  Pascal, the volume is held constant at  $1 \text{ m}^3$ , so that the density from the equation is presented in  $\text{kg}/\text{m}^3$ ). The compressibility factor,  $Z$ , is a function of the temperature and pressure, as presented in standard  $\text{GH}_2$  compressibility tables, such as that from [117], which is used in a MATLAB interpolation function to determine the compressibility for the specific conditions outlined by the TLARs.

$$n = \frac{P \cdot V}{Z \cdot R \cdot T} \quad (3.98)$$

Where:

$n$  = moles of  $\text{GH}_2$

$P$  = Pressure of  $\text{GH}_2$  (*Pascals*)

$V$  = Volume of  $\text{GH}_2$  ( $\text{m}^3$ )

$Z$  = Compressibility factor

$R$  = Universal gas constant ( $\text{J}/\text{mol} \cdot \text{K}$ ), given as 8.314463.

$T$  =  $\text{GH}_2$  storage temperature (*Kelvin*)

$$\rho_{GH_2} = n \cdot (\mu_{hydrogen} \cdot 2) \quad (3.99)$$

The mass of the hydrogen determined by the flight mission is divided by the final density for the hydrogen, to yield the final volume, which is then used in the tank sizing equation previously presented.

$$V_{GH_2} = \frac{m_{GH_2}}{\rho_{GH_2}} \quad (3.100)$$

### 3.8 Motor, Inverter, Converter and Power Distribution Mass

Somewhat similar to the methods for the battery mass calculations, the mass for the motors, inverters, converters and power distribution and management are calculated through their power density values, discussed in the literature review section, with reference values taken from a range of resources, including [21] [118] [19] [31] [6]. In a bid to reduce computational expense, fixed values for efficiency are opted for.

### 3.9 Gearbox Mass

The mass of the gearbox (in pounds) is calculated using the methods presented in [119], before being converted to kg. Equation 3.101 is used to determine the parametric value,  $PV$ , which is fed into equation 3.102, which describes the linear regression of the empirical data figure. The  $P_{max}$  term is passed to the equation as the maximum power observed by the motor in a single branch of the system,

and is updated on every iteration of the sizing regime. For the  $RPM_{out}$  value, this is taken from the propeller manufacturers data sheet, associated to the Dornier 228; assumed constant, and given as 2200 RPM. The  $RPM_{input}$  is the speed of the motor (or stack of motors) which is coupled to the input shaft of the gearbox; this is taken as 7000 RPM, based on the efficiency maps of the stack-able D500 axial-flux motor from EVOLITO [118], for which the supporting data sheet is presented in the appendix. Finally, the efficiency is assumed to be constant at 97%, and is a conservative estimate based on the power expected to be delivered by a single branch of the propulsion system, and using values presented in figure 3.31, from [120].

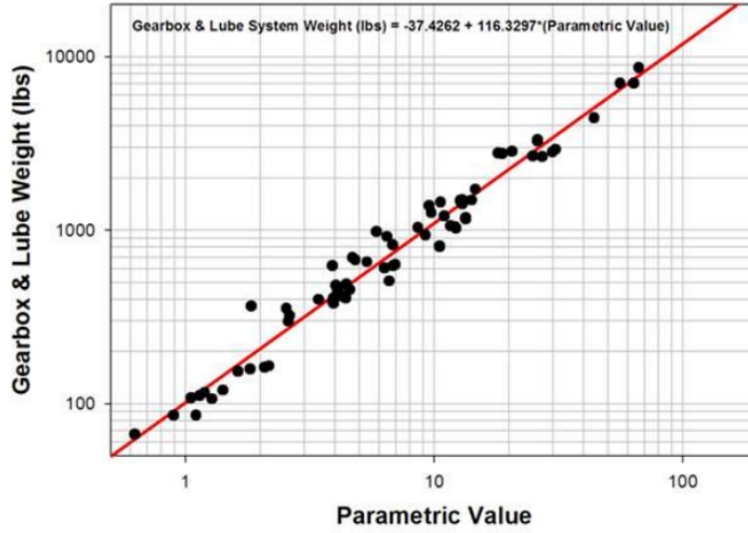


Figure 3.30: Gearbox Mass Correlations [119]

$$PV = \left( \frac{P_{max}}{RPM_{out}} \right)^{0.75} \cdot \left( \frac{RPM_{in}}{RPM_{out}} \right)^{0.15} \quad (3.101)$$

$$Mass_{Gearbox} = (-37.462) + (116.3297 * PV) \quad (3.102)$$

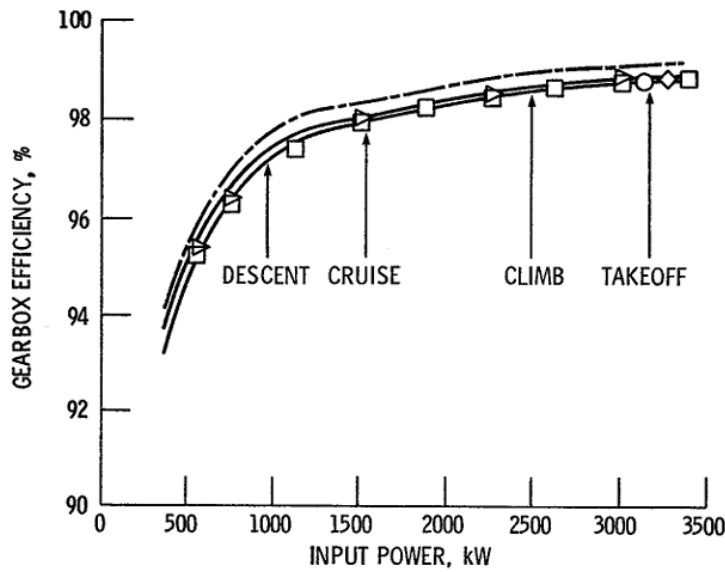


Figure 3.31: Analytical Gearbox Box Efficiency [120]

### 3.10 Hydrogen-Electric Aircraft Study

With a completed, comprehensive aircraft sizing model, it is possible to subject the reference aircraft to a series of studies, in which it will be possible to determine the optimum system parameters for some given measures of merit, such as minimum MTOM for a given mission or transport energy for a given mission, for example. As well as looking at the different power and energy management schemes, the model also opens up the potential to explore the advantages (or disadvantages) of various operational strategies, such as in-flight recharging of the batteries.

In a bid to reduce computational time for the simulations, a search pattern is employed, which prevents the simulation from searching through every possible hybridisation ratio value between zero and one. The first run of the simulation steps through the hybridisation values in steps of 0.1, which yields eleven correctly sized aircraft, and somewhere within the pack, will be an aircraft of 'lowest figure of merit'; this can be observed in figure 3.32. Although the figure identifies an 'initial optimum' this is not necessarily the global minimum for full range of hybridisation

of power sweep. In order to find this from the data, the initial optimum point is used as a reference, and the two aircraft sized at either side of this point set up the optimum search boundaries, for a more refined search, as the aircraft which matches the described measure of merit should lay somewhere between these two points; thus eliminating the necessity for a refined search of the full hybridisation of power spectrum.

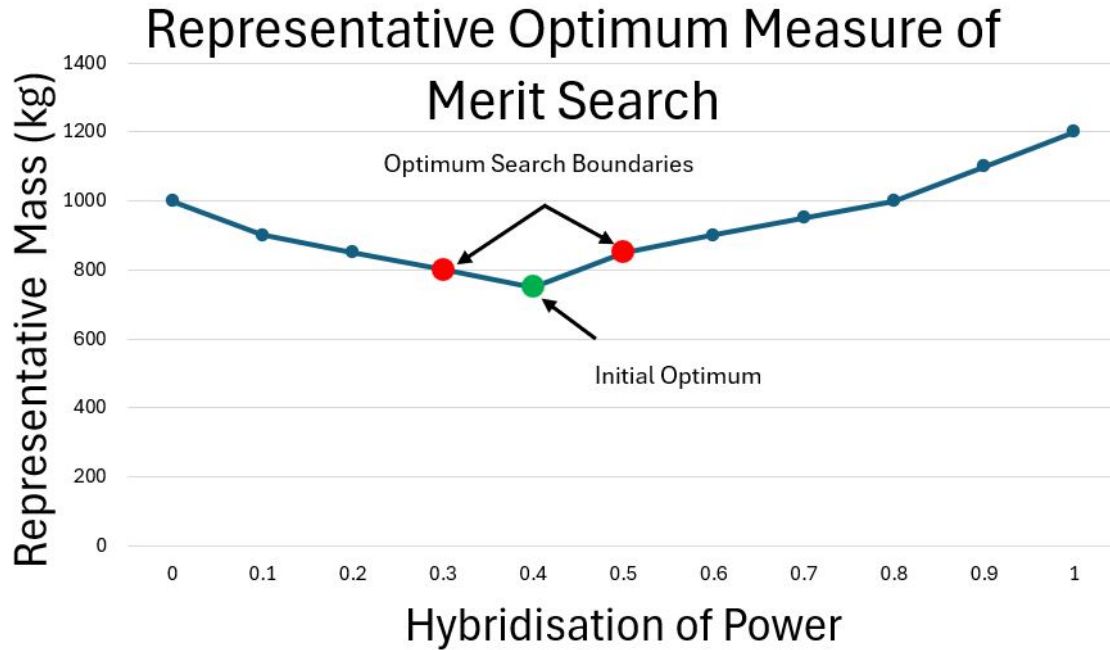


Figure 3.32: Representative Optimum Measure of Merit Search

To further reduce the computational time, an averaged atmosphere model is used, for calculating the density at altitude. This has been employed as a result of the delays encountered when the MATLAB 'ATMOSISA' function is utilised. Initial testing with both the averaged model, and the MATLAB 'ATMOSISA' function showed an average of less than 0.1% difference between the results, while decreasing the simulation times by a factor of approximately 25.

Initial studies, look quite simply at the retrofitting of the standard aircraft, with the new propulsion system, under current technology levels, with the exception of the battery, and a sweep of the hybridisation of power, from zero, where no batteries are used for propulsion, and are only in place to capture any of the transient power

Table 3.27: Top Level Aircraft Requirements - Study One

Parameter	Value	Parameter	Value
Take off distance (m)	793	Diversion Speed (m/s)	85
Start airport altitude (m)	0	AEO ROC at SL (m/s)	8
Cruise altitude (m)	3000	OEI ROC at SL (m/s)	2
Destination airport altitude (m)	0	Range (km)	396
Diversion altitude (m)	1000	Diversion range (km)	270
Loiter altitude (m)	450	Loiter time (min)	30
Cruise speed (m/s)	115	Payload (kg)	1960
Stall speed (m/s)	34.5	Reserve fuel (%)	5

demands that the fuel cell cannot keep up with, during take-off and climb. The sweep for the hybridisation of power goes all the way through to a hybridisation of power of one, which suggests that the battery is supplying the full power demand during take off and climb. No in flight recharge is considered, and by virtue of this the aircraft will have to be sized to carry additional battery mass for the diversion climb.

The author would like to note, that no battery power will be used for propulsion during the longer cruise, diversion and loiter stages. Previous studies have already shown that incorporating this operational mode leads to an excessively heavy aircraft.

Study one, pertains to the TLARs previously discussed, and presented in table 3.8, repeated below for the readers convenience, in conjunction with the extended drag polar aerodynamics. Additionally, the specifications for the powertrain, under consideration of study one, are available in table 3.28. The study considers 'near-future' battery technology, with a specific energy of  $500 \text{ Wh/kg}$ , and a discharge 'C' rate of 10, with a fuel cell response time of three seconds, while working under the considerations of 'current technology' component power densities.

Initial results for the study can be observed in figure 3.33. The lowest resulting aircraft mass is found at a hybridisation of power of 0.43, with a resulting mass

Table 3.28: Powertrain Specifications - Study One

Parameter	Value	Parameter	Value
Gearbox efficiency: $\eta_{gb}$	0.97	Motor efficiency: $\eta_{em}$	0.97
Inverter efficiency: $\eta_{inv}$	0.98	DC-DC Converter efficiency: $\eta_{dc-dc}$	0.98
PMAD efficiency: $\eta_{pmad}$	0.95	Fuel Cell (cruise) efficiency: $\eta_{fc}$	0.55
Compressor efficiency: $\eta_{comp}$	0.9	GH <sub>2</sub> storage efficiency: $\eta_{storage}$	0.1
Motor PD: $\hat{\rho}_{em}$ [kW/kg]	20	Motor VPD: $v\hat{\rho}_{em}$ [kW/m <sup>3</sup> ]	20000
Inverter PD: $\hat{\rho}_{inv}$ [kW/kg]	20	Inverter VPD: $v\hat{\rho}_{inv}$ [kW/m <sup>3</sup> ]	20000
Converter PD: $\hat{\rho}_{dc-dc}$ [kW/kg]	15	Converter VPD: $v\hat{\rho}_{dc-dc}$ [kW/m <sup>3</sup> ]	20000
Fuel Cell PD: $\hat{\rho}_{fc}$ [kW/kg]	2.1	Fuel Cell VPD: $v\hat{\rho}_{fc}$ [kW/m <sup>3</sup> ]	970
Compressor: $\hat{\rho}_{comp}$ [kW/kg]	2	Battery specific energy [Wh/kg]	500
Battery discharge 'C' rate [1/h]	10	H <sub>2</sub> pressure: bar	350

of 8324.3 kg; this is identified as the green point on the plot. From a regulatory perspective, this aircraft is 96.6% of the permissible MTOM permitted for 19 seater aircraft according to the CS-23 category aircraft regulations. The data from figure 3.33 suggests that aircraft at the extremes of hybridisation are nearly, equally as heavy as one another, despite the lack of required propulsion power required from either branch according to the size of the hybridisation, while the optimum, or lowest value of mass is found towards a 43% hybridisation for take-off and climb. In order to better understand why this is happening, and delve further into figure 3.33, the masses for the propulsion system components and structural masses are presented in a more granular format, as follows.

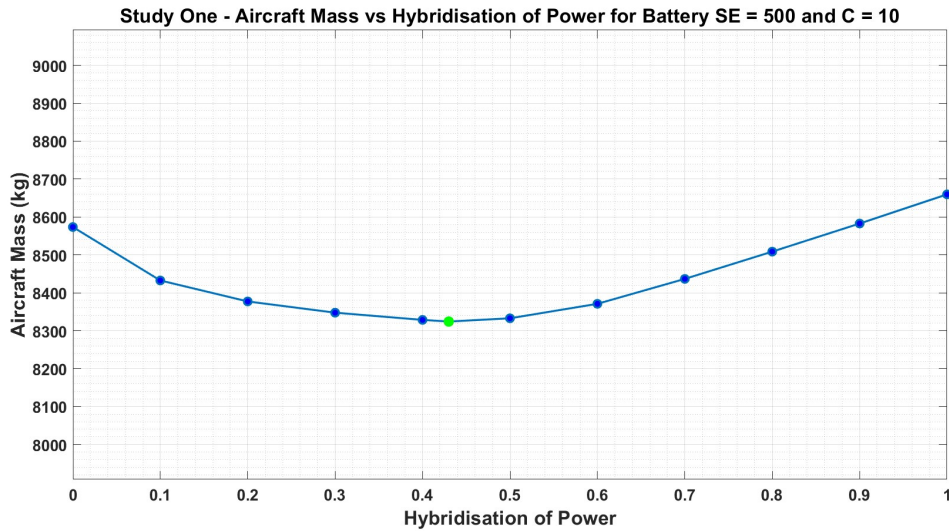


Figure 3.33: Aircraft Mass vs Hybridisation for Study One

Figure 3.34 presents the mass data for the H<sub>2</sub> tank, motors, gear-box, DC-DC converters for the battery and fuel cell, and the inverter masses. It is clear to see that the mass landscape, is entirely dominated by the mass of the H<sub>2</sub> tank. This is primarily due to the fact that it operates at such low efficiencies, relative to the rest of the components which make up the propulsion system. A quasi-linear trend is observed as hybridisation of power is increased, which stands to reason, as dependency for the fuel cell is reduced for the take-off and climb segments, thus reducing the mass of fuel required for storage, however, the mass still remains high as the cruise, loiter, and diversion stage is not influenced by the hybridisation levels. As this project does not focus on improvements to tank efficiency, and the main focus is on the power converter technology, the tank mass is removed from 3.34, and it is re-represented as figure 3.35, which provides a more enhanced view of the remaining masses.

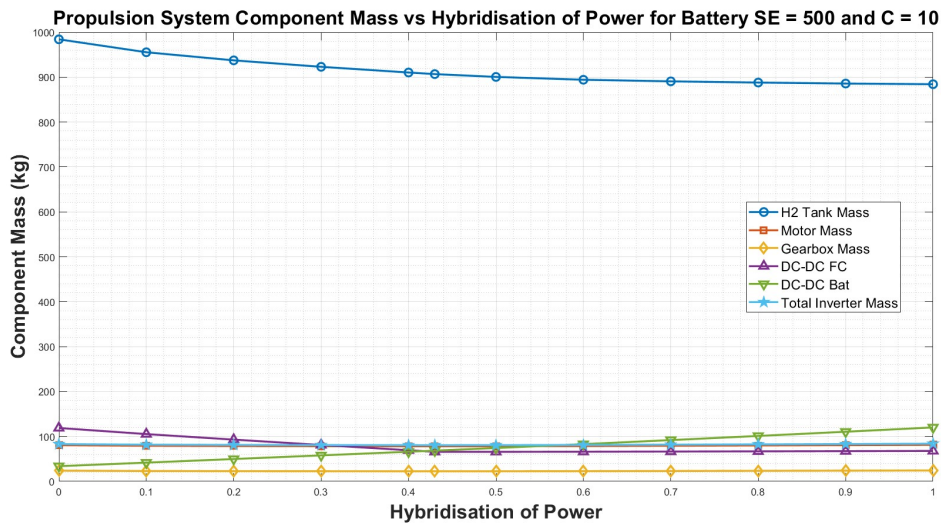


Figure 3.34: Propulsion System Component Mass vs Hybridisation for Study One

Figure 3.35 highlights that the motor, inverter and gear-box, show a low sensitivity to the variation in hybridisation levels, as well as complimenting one another's trends well, and showing little influence on final aircraft mass variations; the author suggests that very simply, this is because the mass of these components is a function of the overall power requirements of the aircraft, rather than being a function of the

power from an individual power or energy source, in a particular branch. However, the same cannot be stated for the fuel cell and battery DC-DC converters, as these can be seen to be highly sensitive to the hybridisation level, and can be identified as one of the major causes for the extremes in mass observed at the upper and lower end of hybridisation in figure 3.34. For a hybridisation of 0, where no battery is required for propulsion, a mass is still observed for the battery DC-DC converter, this is due to the necessity of a battery, which is required to capture the transients as a result of the fuel cell's system response time. If the fuel cell response time was instantaneous, the mass allocated to the battery DC-DC converter would approach 0, however, the fuel cell DC-DC converter mass would increase as a result, as it is now responsible for all of its power during the peak power demand at take-off. A trade off for a faster response time, would be a reduction in the battery mass, and in theory this mass would reduce to zero, as the fuel-cell no longer requires any support to meet peak power demand.

The trend of the battery DC-DC converter mass is entirely linear, and increasing with a positive gradient with the increasing hybridisation levels, as dependency on the battery branch of the propulsion system becomes greater. Inversely, as hybridisation levels increase, the mass of the fuel cell DC-DC converter decreases with a negative trend. However, unlike the battery DC-DC converter, the fuel cell DC-DC converter reaches a plateau point and maintains a linear trend with no gradient. This plateau appears to be caused by the fact that the fuel cell, regardless of hybridisation level, is still required to provide all of the power for the cruise, diversion and loiter stages, and as such the complementing DC-DC converter for these power levels is required. Improvements to the power density of the converters for both the battery and fuel cell will, therefore influence the aircraft mass sizing during the periods which are split by the hybridisation and the phases which are non-hybridisation dependent.

Looking at the mass of the battery system and H<sub>2</sub> system, with respects to hybridi-

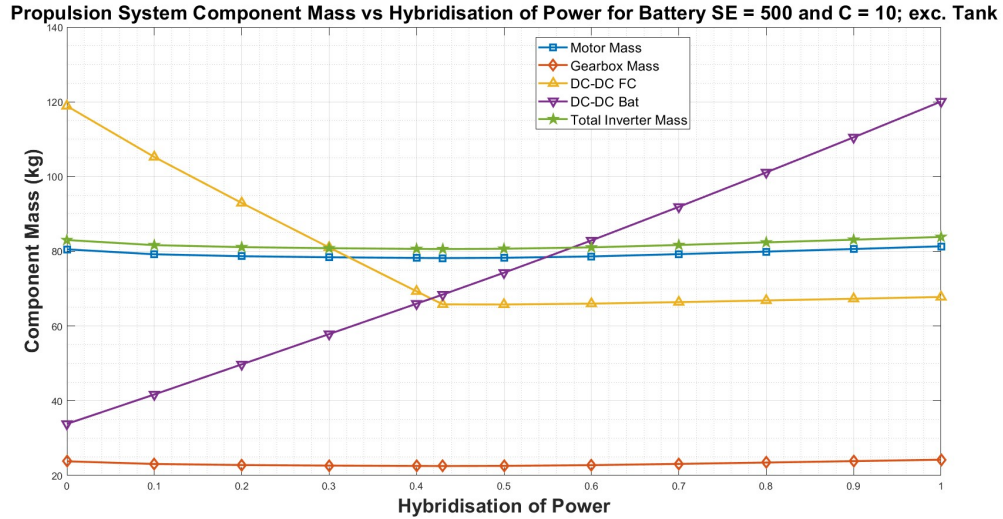


Figure 3.35: Propulsion System Component Mass vs Hybridisation for Study One (Excluding Tank)

Table 3.29: Study One: Battery and H<sub>2</sub> System Mass for Hybridisation of Power Sweep

Hybridisation Level	Battery Mass (kg)	H <sub>2</sub> Mass (kg)	H <sub>2</sub> Tank Mass	Fuel Cell Mass (kg)	BOP Mass (kg)	Total Mass (kg)
0	108.9	109.4	984.1	834.66	271.5	2308.56
0.1	134.3	106.2	955.4	822.9	182.87	2201.67
0.2	160.3	104.1	937.3	818.21	142.77	2162.68
0.3	186.4	102.5	922.9	815.59	116.68	2144.07
0.4	212.6	101.1	910.3	813.82	96.13	2133.95
0.43	220.5	100.7	906.7	813.41	90.65	2131.96
0.5	239.3	100.1	900.5	813.92	80.56	2134.38
0.6	267.1	99.3	894.1	816.72	80.84	2158.06
0.7	311.4	98.9	890.6	821.72	81.32	2203.94
0.8	358.9	98.7	887.9	827.21	81.87	2254.58
0.9	407.2	98.4	885.7	832.88	82.43	2306.61
1	456.4	98.2	884.2	838.78	83.01	2360.59

sation level, shown in figure 3.36, as the battery DC-DC converter mass increase from the previous plot suggests, the battery mass also increases with, hybridisation level, and the mass of the H<sub>2</sub> used, and the H<sub>2</sub> tank decrease, however, the mass of the battery increases at a greater rate than the decline from masses of the H<sub>2</sub> system, so the mass of the battery related elements of the aircraft increase. This is presented in table 3.29, which shows that the minimum mass for the battery and H<sub>2</sub> system, excluding the converters, occurs at the point which pertains to the aircraft of lowest mass.

Using the aircraft of lowest mass from study one, as a baseline, the component mass percent difference for the remaining aircraft in the pack according to the HoP are presented, to identify where the greatest percent changes occur. As can

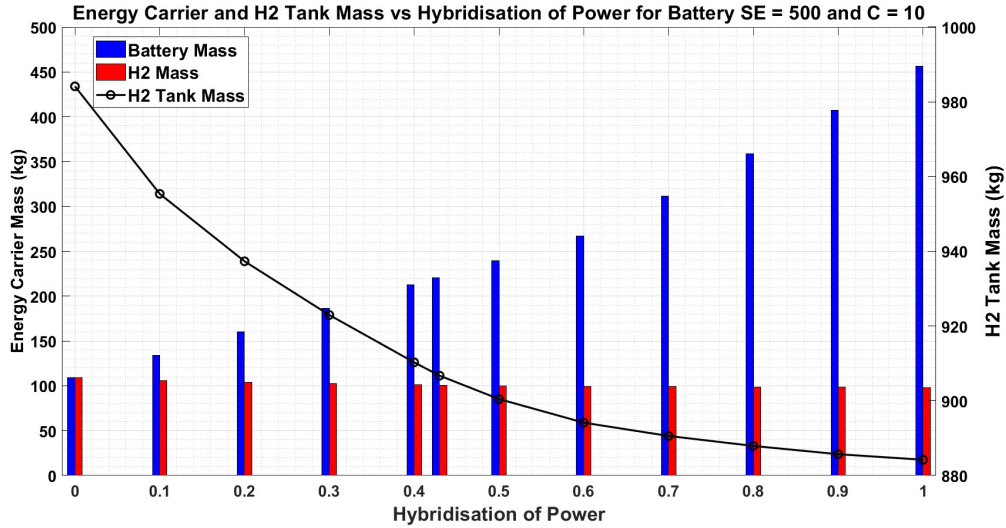


Figure 3.36: Energy Carrier and H2 Tank Mass with Hybridisation of Power

Table 3.30: Study One: Component Mass Percent Change with Regards to the Optimum Aircraft

	0	0.1	0.2	0.3	0.4	0.5	0.6	0.7	0.8	0.9	1
Wing	+3.78%	+1.64%	+0.81%	+0.36%	+0.07%	+0.13%	+0.7%	+1.7%	+2.8%	+3.9%	+5.1%
Fuselage	+1.96%	+1.13%	+0.68%	+0.35%	+0.08	-0.1%	-0.13%	-0.06%	+0.04%	+0.15%	+0.28%
Fuel Cell	+2.6%	+1.7%	+0.6%	+0.27%	+0.05%	+0.06%	+0.41%	+1.02%	+1.7%	+2.4%	+3.1%
H <sub>2</sub>	+8.5%	+5.4%	+3.4%	+1.8%	+0.4%	-0.7%	-1.39%	-1.78%	-2.1%	-2.3%	-2.48%
H <sub>2</sub> Tank	+8.5%	+5.4%	+3.4%	+1.8%	+0.4%	-0.7%	-1.39%	-1.78%	-2.1%	-2.3%	-2.48%
Battery	-50.6%	-39.1%	-27.3%	-15.5%	-3.6%	+8.5%	+21.2%	+41.2%	+62.8%	+84.7%	+107%
FC DC-DC	+80.7%	+59.9%	+41.2%	+23.2%	+5.3%	-0.05%	+0.3%	+0.9%	+1.6%	+2.3%	+3%
Battery DC-DC	-50.6%	-39.1%	-27.3%	-15.5%	-3.6%	+8.5%	+21.2%	+34.3%	+47.8%	+61.5%	+75.5%
Inverters	+3%	+1.3%	+0.6%	+0.3%	+0.05%	+0.1%	+0.6%	+1.4%	+2.2%	+3.1%	+4%
Motors	+3%	+1.3%	+0.6%	+0.3%	+0.05%	+0.1%	+0.6%	+1.4%	+2.2%	+3.1%	+4%
Gearbox	+5.6%	+2.4%	+1.2%	+0.5%	+0.1%	+0.2%	+1.1%	+2.5%	+4.2%	+5.8%	+7.5%
FC Cooling	+273.5%	+142.2%	+81.3%	+40.6%	+8.5%	-15.8%	-15.5%	-15%	-14.5%	-13.9%	-13.3%
FC Compressor	+22.7%	+5.1%	+0.6%	+0.3%	+0.05%	+0.06%	+0.4%	+1%	+1.7%	+2.4%	+3.1%

be observed, the converters for the fuel cell and battery, consistently demonstrate some of the greatest percent mass changes, relative to most other components, with the exception of the fuel cell cooling system mass, which appears to exhibit a large negative gradient as less dependency is placed on it at aircraft peak power requirements.

The next study looks to address another research question, and make an additional research contribution. This study sees the effects of a hydrogen-electric aircraft sized without the response model for the fuel cell, and balance of plant; i.e the response of the fuel cell, and balance of plant is in essence instantaneous with respects to any alterations in power demand, and as such there is no requirement for a battery or battery branch to cover any peaks or transients to meet the power

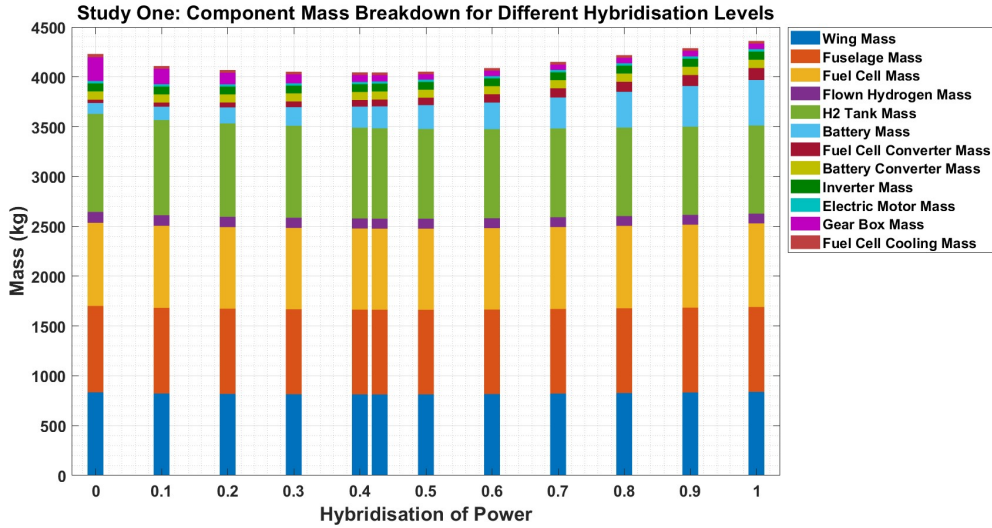


Figure 3.37: Component Mass vs Hybridisation for Study One

demand, unless dictated by the hybridisation of power. In order to show the effects of the removal of the dynamic response model, a decision is made to place study one in direct competition with the new study, which is from herein referred to as 'study one-B'. Based on this, all of the original top-level aircraft requirements and powertrain specifications, are upheld; the only alteration being, the removal of the dynamic gain function from the sizing code.

Initial results for study one-B indicate that the minimum MTOM achieved, is found at a hybridisation of power of 0.19, with a resulting mass of 8209.32 kg; as identified by the blue point on plot 3.38.

Taking the results of the lowest MTOM for both studies, this represents a 1.38% decrease relative to that of study one, and a 24% difference between the optimal hybridisation power points; with study one-B favouring a lower hybridisation of power. The results for study one-B, are plotted against study one, in figure 3.38, to give a visual representation of the general mass disparity. From the plot, an initial observation can be stated, this being that the masses tend towards convergence as the hybridisation of power increases. This can be explained by identifying that at a hybridisation of power of one, both aircraft are entirely dependent on the battery

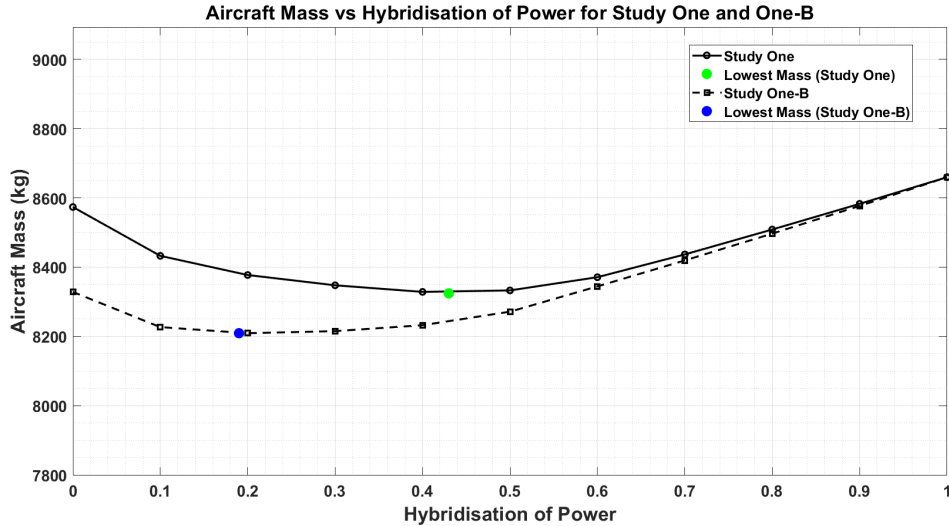


Figure 3.38: Aircraft Mass vs Hybridisation for Study One-B

branch of the propulsion system for both take-off and climb, with the fuel cell only coming into effect during cruise, diversion and loiter; therefore, both aircraft see the same demand for the battery and associated equipment, and as such are sized at the same rates. However, as the hybridisation of power approaches zero, i.e. the fuel cell is expected to provide all of the power for take-off and climb, there is an opportunity for the masses to diverge. This divergence arises from the fact that the model which uses the dynamic gain values for the fuel cell is disadvantaged by requiring a battery branch in the propulsion system which is capable of handling full power take off requirements; automatically adding an initial additional mass for the aircraft of study one. Convergence then begins as less demand is placed on the fuel cell, and the battery branch, which is identical for both aircraft, begins to become more prevalent. Similar to study one, the propulsion system masses (excluding the  $H_2$ ) are extrapolated from the results, and for study one-B, are shown in figure 3.39. The figure demonstrates near identical trends across all components, with the knee-point for the DC-DC converter of the fuel cell occurring at approximately 40% hybridisation of power, and linear trends for the motor mass, gearbox mass, battery DC-DC converter mass, and inverter mass. However, the starting point for the battery DC-DC converter mass is considerably different between the two studies,

with study one-B starting at 0 kg, as there is no battery requirement at this point, and as such 0 kg for the battery mass, as verified by figure 3.40. These masses inevitably therefore do not form mass compounding factors for the remainder of the flight, thus yielding an aircraft which sees a 2.86% reduction in MTOM with a hybridisation of power of zero, relative to the aircraft of study one, and as shown in figure 3.38, the rate of percentage reduction decreases, until a hybridisation of power of one, yields a 0% MTOM increase, as shown in table 3.31.

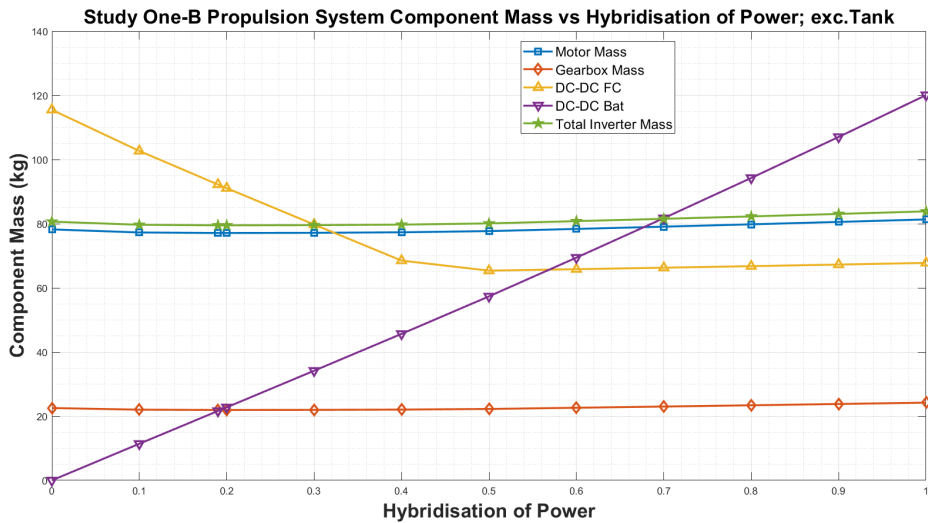


Figure 3.39: Aircraft Mass vs Hybridisation for Study One-B

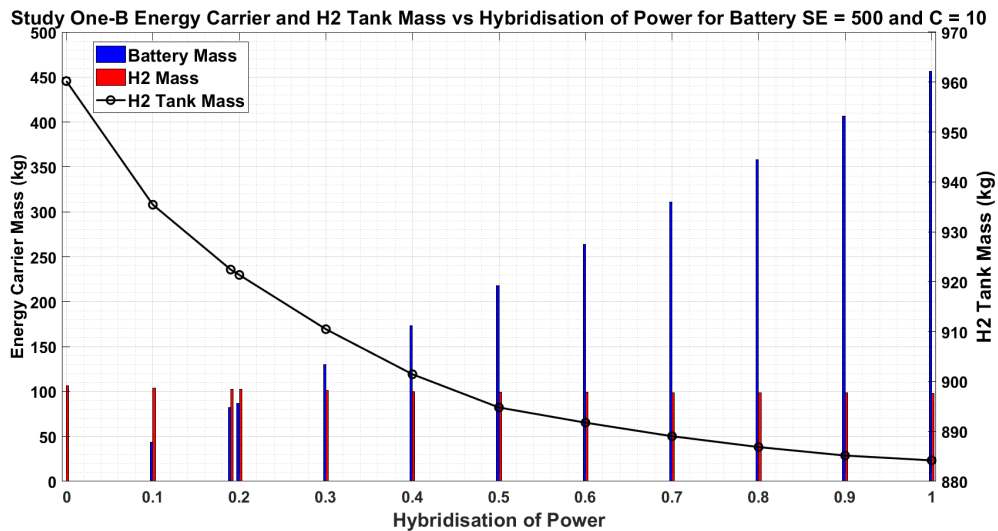


Figure 3.40: Aircraft Mass vs Hybridisation for Study One-B

The trends from study one-B, somewhat disagree with the original hypothesis. That

Table 3.31: Study One-B MTOM Mass Variation with Regards to Study One

Hybridisation Level	$\Delta$ MTOM (kg)	$\Delta$ MTOM (%)
0	-245.1	-2.86
0.1	-205.6	-2.4
0.2	-167.8	-2
0.3	-132.2	-1.6
0.4	-96.1	-1.15
0.5	-61.4	-0.74
0.6	-26.6	-0.32
0.7	-17.33	-0.21
0.8	-11.8	-0.14
0.9	-6	-0.1
1	0	0

being, that a greater dependency on hydrogen, for low values of hybridisation of power, would increase the total quantity of hydrogen required for the take-off and climb phases, and due to the inefficiency of the hydrogen storage, would inevitably lead to an aircraft which is somewhat heavier than that of the aircraft sized with the dynamic response of the fuel cell incorporated, mainly due to the tank and the compounding effect that it would have on the remainder of the flight. however, it appears that the requirement to have an electrical branch which is seized to handle full power take-off requirements tips the balance towards the aircraft with the more advanced fuel cell model yielding the greatest MTOM, at lower values of hybridisation of power; the lower initial masses then translate into a lower power requirement, and ultimately a reduction in the size of the power requirements, which influence the propulsion system mass components. This answers one of the research questions which surrounds an investigation into the effect of the fuel cell model on the mass of the sized aircraft, and in summary it can be stated that a fuel cell model which adopts the ability to achieve changed in power demand instantaneously will yield an aircraft which is undersized in comparison to that of a model which adopts some kind of response model, and the effects of this are worsened when low values of hybridisation are applied.

The main study for this section of the project, centers around studying the effects of the DC-DC converter power density, on the resulting aircraft mass; while the second half deals with methods to support the improvement in power density. Study two, focuses on the effects on aircraft mass when improvements to the DC-DC converter technology are introduced. Maintaining the TLARs from table 3.8, and powertrain specifications in table 3.28, with the exception of the converter specific power density, which is now a swept variable for the trade study, and is formed of an array featuring power densities at 5, 10, 15, 20, 25, 30, 35 and 40  $kW/kg$ . Again, as with study one, the aircraft will not in-flight recharge, and uses the same battery and fuel cell technology. The results for study two, showing the aircraft mass with respects to hybridisation of power across various DC-DC converter technologies, are shown in figure 3.41, and the respective MTOM for each converter technology are available in table 3.32, in addition to the percent mass change from the lowest technology level, the percent mass change from the previous technology level, and the percent mass change from the baseline technology level of study one. As improvements to the power density of the components would suggest, the aircraft featuring the converters with the highest level of technology, yield the lowest mass, with a total mass of 8182.6 kg for the optimum MTOM, at a converter power density of 40  $kW/kg$ , and this represents an approximate 1.7% in mass saving relative to the aircraft of study one, using the baseline technologies. Most noticeably, an interesting trend from figure 3.41, shows that as the technology levels increase, from the 5  $kW/kg$ , low technology value, there is a diminishing return on aircraft mass improvements, as improvements are made to converter power density; The percent difference in improvements between each aircraft with its respective converter technology, is shown in 3.32. Figure 3.41, provides a visual insight into the component mass breakdown, for the aircraft under consideration in study two. The trend for the diminishing returns to be a result of the converters acting as a mass compounding factor against the most influential mass increasing component, the  $H_2$ . However, in summary, it is possible to state that any improvements made to the converter technology, has

Table 3.32: Study Two: Optimum Aircraft Mass for Varying DC-DC Converter Power Densities

$\hat{\rho}_{dc-dc}$ [kW/kg]	Aircraft Mass (kg)	HP	$\Delta$ Mass% From 5 kW/kg	$\Delta$ Mass% From Previous $\hat{\rho}_{dc-dc}$	$\Delta$ Mass% From Baseline Technology	Absolute $\Delta$ Mass From Baseline Technology
5	8811.8	0.43	-	-	+5.86%	+487.5kg
10	8440.8	0.43	-4.21%	-4.21%	+1.4%	+116.5kg
15	8324.3	0.43	-5.53%	-1.38%	-	-
20	8267.2	0.43	-6.18%	-0.69%	-0.69%	-57.1kg
25	8233.4	0.43	-6.56%	-0.41%	-1.09%	-90.9kg
30	8210.7	0.44	-6.82%	-0.28%	-1.36%	-113.6kg
35	8194.6	0.46	-7%	-0.2%	-1.56%	-129.7kg
40	8182.6	0.44	-7.14%	-0.15%	-1.7%	-141.7kg

the positive impact on reducing overall aircraft mass.

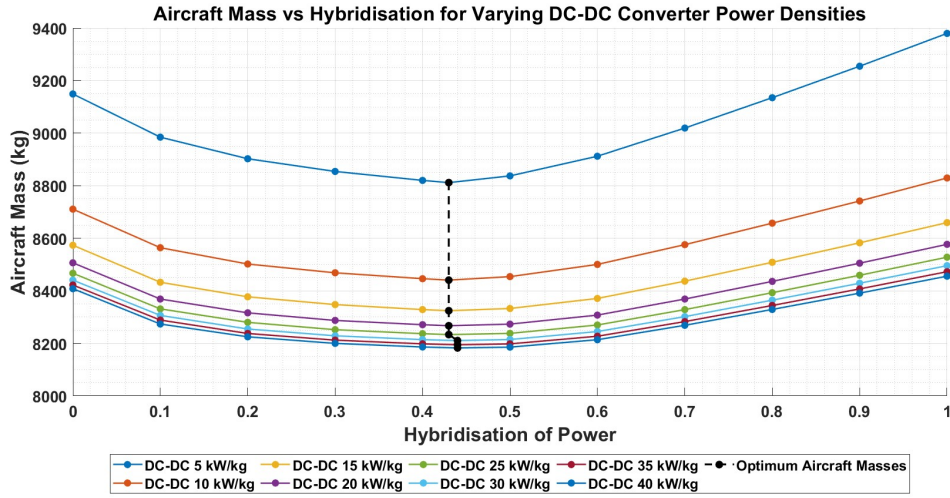


Figure 3.41: Study Two: Aircraft Mass vs Hybridisation for Varying DC-DC Converter Power Densities

As previously discussed, it is possible to subject the aircraft to an additional operational mode, this being an in-flight battery recharge scenario. Unlike the previous study, which relied on additional battery mass to support the requirements for a diversion climb, the new study, study three, will assess the influence of recharging the battery during the cruise segment of the flight, such that it is fully recharged, and available to supply any additional power required during the diversion climb, depending on the HoP split. Alternatively, from an airline operational perspective, this in-flight recharge mode, also gives operators the flexibility to have the aircraft recharge itself during flight, and potentially reduce on-ground turn around time, thus increasing the utilisation of the aircraft. As with the previous studies, all technology levels remains the same, however the DC-DC converter technology will act

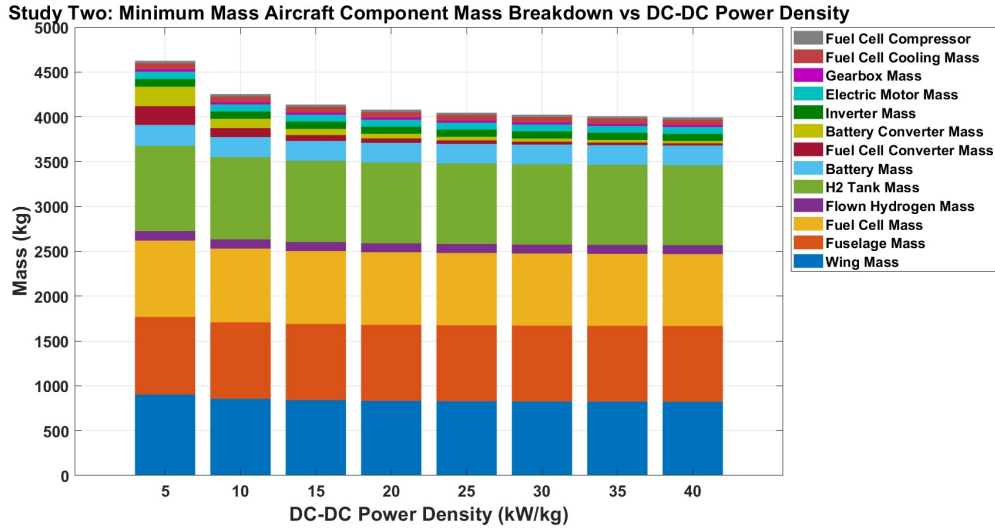


Figure 3.42: Study Two: Component Mass Breakdown Vs DC-DC Converter Power Density

as a variable to the trade study. Figure 3.44, shows the location in terms of HoP, the lowest mass aircraft, when considering in-flight recharge for current converter technology levels. This plot allows allows a comparison to be made against the result of study one. From this plot it can be observed that at a HoP of 0.32, the lowest aircraft mass, with a result of 8398.62kg is achieved. When compared against study one, this represents a 25.6% decrease in the level of HoP, which implies a greater dependency on the hydrogen propulsion system. This additional dependency on the hydrogen propulsion system, also gives rise to a 0.89% increase in the total aircraft mass. The component mass breakdowns for this study are available to view in figure 3.44.

Study one, which is also part of the data set from study two, presented in table 3.32, in conjunction with the aircraft as part of the trade study, is now presented against the aircraft of study three, when the same trade study is repeated, this is shown in table 3.34.

From table 3.34, it can be observed that at all converter technology levels, the aircraft considering in-flight recharge is marginally heavier than its non-in-flight recharge counterpart; however, for all cases this mass increase never exceeds 1%.

Table 3.33: Study Two: Component Mass Percent Change with Regards to Base-line Converter Technology

	5	10	15	20	25	30	35	40
Wing	+7.43%	+1.77%	-	-0.86%	-1.37%	-1.72%	-1.96%	-2.14%
Fuselage	+1.85%	+0.44%	-	-0.22%	-0.35%	-0.45%	-0.52%	-0.56%
Fuel Cell	+4.76%	+1.14%	-	-0.56%	-0.89%	-1.11%	-1.27%	-1.39%
H <sub>2</sub>	+4.93%	+1.18%	-	-0.58%	-0.92%	-1.26%	-1.42%	-1.54%
H <sub>2</sub> Tank	+4.93%	+1.18%	-	-0.58%	-0.92%	-1.26%	-1.42%	-1.54%
Battery	+5.64%	+1.35%	-	-0.66%	-1.05%	-0.13%	-0.32%	-0.46%
FC DC-DC	+217.57%	+52.1%	-	-25.5%	-40.6%	-50.61%	-57.74%	% -63.1
Battery DC-DC	+216.91%	+52.02%	-	-25.49%	-40.63%	-50.06%	-57.28%	-62.67%
Inverters	+5.86%	+1.39%	-	-0.69%	-1.09%	-1.36%	-1.56%	-1.7%
Motors	+5.86%	+1.39%	-	-0.69%	-1.09%	-1.36%	-1.55%	-1.7%
Gearbox	+10.93%	+2.63%	-	-1.29%	-2.05%	-2.57%	-2.93%	-3.21%
FC Cooling	+6.46%	+1.39%	-	-0.68%	-1.08%	-4.25%	-4.44%	-4.58%
FC Compressor	+4.76%	+1.14%	-	-0.56%	-0.89%	-1.11%	-1.27%	-1.38%

Table 3.34: Study Three: Comparison Between Aircraft Masses for No In-flight recharge and In-flight Recharge

$\hat{\rho}_{dc-dc}$ [kW/kg]	Study:1 Aircraft Mass (kg)	Study:1 HP	Study:2 Aircraft Mass (kg)	Study:2 HP	$\Delta\%$ Mass	$\Delta\%$ HP
5	8811.8	0.43	8900	0.42	+1%	-2.33%
10	8440.8	0.43	8520.2	0.37	+0.94%	-13.95%
15	8324.3	0.43	8398.6	0.32	+0.89%	-25.58%
20	8267.2	0.43	8339	0.32	+0.87%	-25.58%
25	8233.4	0.43	8303.4	0.29	+0.85%	-32.56%
30	8210.7	0.44	8279.8	0.29	+0.84%	-34.1%
35	8194.6	0.46	8263	0.29	+0.83%	-36.96%
40	8182.6	0.44	8205.5	0.29	+0.28%	-34.1%

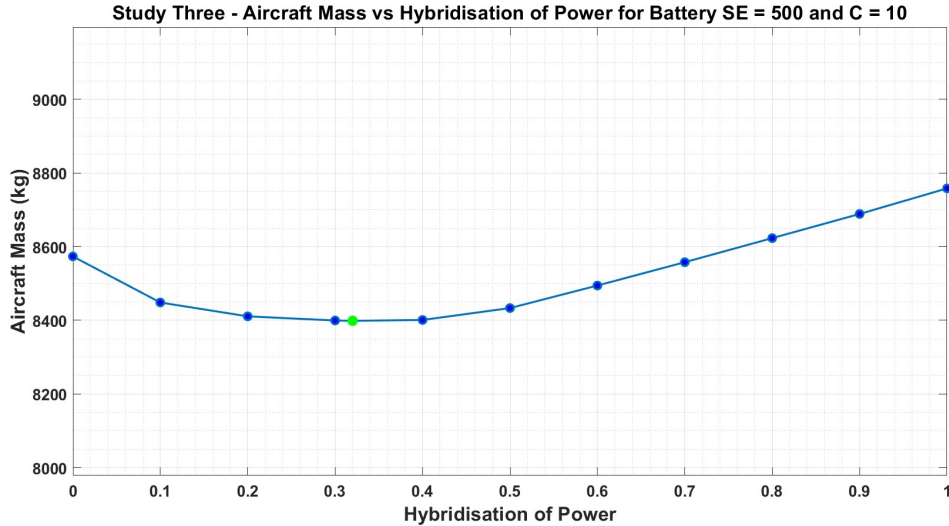


Figure 3.43: Aircraft Mass vs Hybridisation for Study Three

Additionally, for all cases the HoP is reduced, and shows a trend of greater reduction in HoP value with increasing value of converter technology level, with the lowest value of HoP experienced at 40 kW/kg. The data also suggests that even though the in-flight recharging does increase the aircraft mass, the mass growth is reduced with greater converter technology levels, and again supports a compelling incentive to focus efforts on these technology improvements.

As part of the aircraft sizing methodology, two branches of drag polar fidelity was considered, the simple and the complex, and the effects of the drag polar fidelity on the aircraft mass are considered in the next study; study four. As with the previous studies, all parameters are held, with the exception of the DC-DC converter technology level, and as with study two, the operational mode of in-flight recharge is not considered, such that it can be placed in direct comparison with the aircraft pack of study two.

From the data presented in table 3.35, one of the first observations is that the aircraft using the simple drag polar, places greater dependency on the hydrogen branch of the propulsion system; however, this dependency reduces with increases in DC-DC converter technology level. The aircraft sized using the simple drag

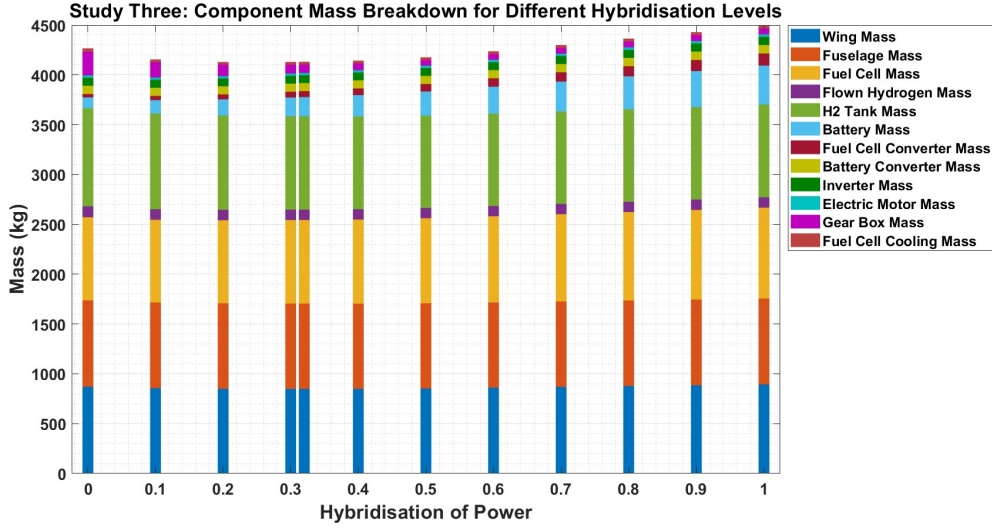


Figure 3.44: Component Mass vs Hybridisation for Study Three

Table 3.35: Study Four: Comparison Between Aircraft Masses for Complex and Simple Drag Polar

$\hat{\rho}_{dc-dc}$ [kW/kg]	Study:1 Aircraft Mass (kg)	Study:4 HP	Study:2 Aircraft Mass (kg)	Study:2 HP	$\Delta\%$ Mass	$\Delta\%$ HP
5	8811.8	0.43	9404.2	0.34	+6.72%	-21%
10	8440.8	0.43	9001.3	0.34	+6.64%	-21%
15	8324.3	0.43	8874.2	0.34	+6.61%	-21%
20	8267.2	0.43	8811.4	0.37	+6.58%	-13.95%
25	8233.4	0.43	8773.7	0.38	+6.56%	-11.63%
30	8210.7	0.44	8748.5	0.38	+6.55%	-13.63%
35	8194.6	0.46	8730.7	0.38	+6.54%	-17.4%
40	8182.6	0.44	8717.3	0.38	+6.53%	-13.63%

polar also presents greater increases in mass relative to the counterparts using the extended drag polar; however, this mass increase never exceeds 7%. Although the percentage increases may appear relatively small, when placed into absolute terms, the maximum mass difference observed is a considerable increase in terms of aviation standards, at 592.4 kg for the low technology converter, and 549.9 kg for the baseline technology converter.

### 3.11 Hydrogen Aircraft Study Conclusion

To begin the conclusion section of the hydrogen aircraft study, the most obvious and sweeping statement is made, this being, that hydrogen-electric aircraft are fundamentally heavier, than their fossil fuel burning counterparts, when considering

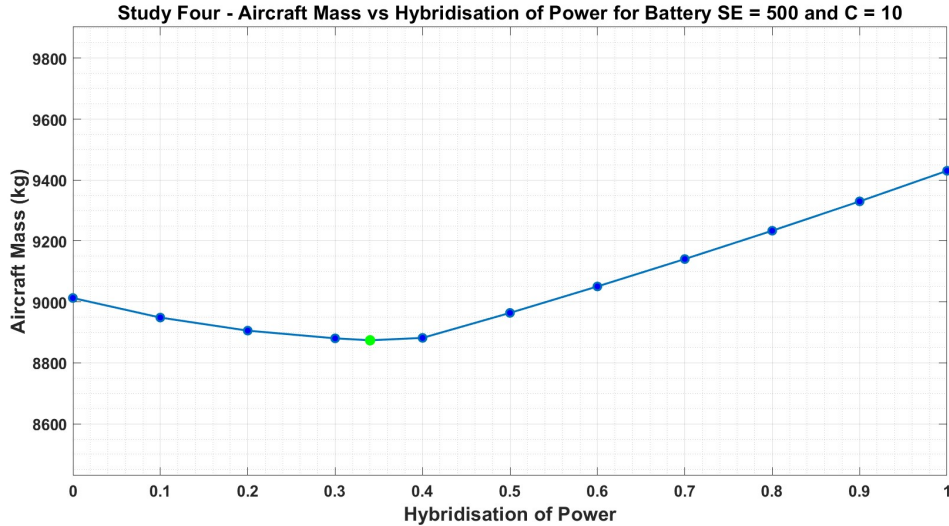


Figure 3.45: Aircraft Mass vs Hybridisation for Study Four

like-for-like aircraft in terms of equivalent range and payload carrying capability. However, the variation in mass between conventional and hydrogen-electric aircraft was not the focus of this thesis.

It has been observed that the DC-DC converter is one of the most sensitive components within the system, with regards to its impact on the overall mass of the sized aircraft. The overarching mass of the aircraft propulsion components is dominated by the  $H_2$ , due to the current inefficiency of hydrogen storage, and any increase in DC-DC converter mass, propagates, ultimately, acting as a mass compounding factor for this dominating component, through the requirements of additional  $H_2$  to transport these additional masses, when lower technology values are used. It has also been observed that the use of in-flight recharging yields a marginally heavier aircraft, and places a greater dependency on the hydrogen propulsion system; however this slight increase could still yield some operational advantage for the airline who may require fast on-ground turn around times. Also observed in the results are 'knee points', where additional improvements to the technology level of the DC-DC converter, begin to yield a diminishing return in the results. The likely cause of this, is suggestive that the improvements are akin to an exponential decay of improvement, which become limited due to the nature of the remainder of

the technology levels within the propulsion system remaining constant, causing the DC-DC converter mass improvements to plateau, as its effects are felt less.

Finally, the use of a low fidelity drag model corresponds to an increase in sized mass for an aircraft of equivalent technology levels, when using the complex drag polar; however values did not deviate above 7%. This suggests that the quality of the information presented to the sizing methodology should be carefully considered, depending on the degree of accuracy required for the final results.

---

## Chapter 4

# Multiphase - Interleaved Buck Converter

To assess the potential benefits of employing PMBI technology in power converters for enhancing power density, or reducing mass and volume, an initial bench mark converter is conceptualised. As this study primarily focuses on the impact of PMBI reducing mass and volume in magnetic components, or increasing energy handling capabilities, the selection of converter topology could be described as relatively arbitrary. Ultimately, the primary concern is the saturation point of the inductor, which can be examined in either a buck or boost converter configuration.

Based on the literature review of the various topologies available for DC-DC converters, and the common DC Bus voltages used in aircraft systems, the PMBI technology is to be used to gain additional novelty, through its implementation into an interleaved buck converter. As previously described, the buck converter steps down the voltage on the output side, resulting in an increase in the output current, relative to the input, assuming ideal power conservation ( $P_{in} = P_{out}$ ). The resulting increase in inductor current simplifies the experimental aspects of this study, as inductor saturation can be induced by implementing a significant voltage step down,

thereby increasing the current proportionality. This approach enables a practical, low power investigation, while effectively evaluating the advantages of the PMBI technology in combination with the interleaved topology.

The basic topology of a multiphase buck converter is shown in figure 4.1. In this particular scenario, the converter takes advantage of diodes ( $D_1$  and  $D_2$ ), to enable the current freewheeling during the off-state of the switch, and inductor discharge; however, it is also possible to substitute the diodes for a complimenting set of switches. For the switching cycles of this topology the reader is referred to [121].

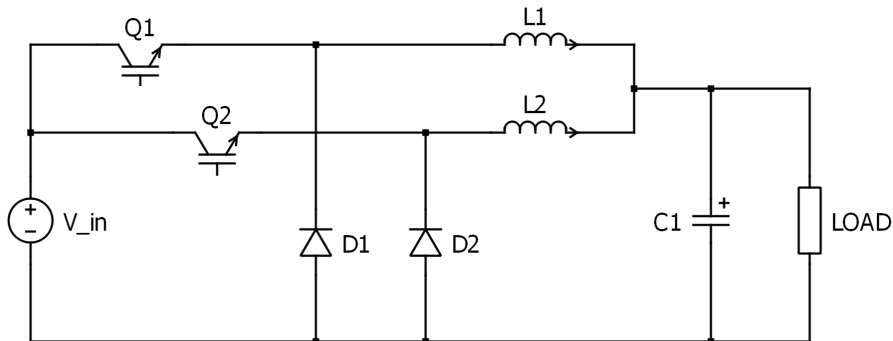


Figure 4.1: Interleaved Buck Converter Topology

One of the advantages of utilising interleaving, is that it permits for a potentially unlimited amount of phases to be included, enabling the sharing of high input currents, and depending on the quantity of phases and operating duty cycle, ripple cancellation can also be achieved. Ripple cancellation will not be the focus of this study. Figure 4.2, outlines how the additional phases are included within the converter.

## 4.1 Closed Loop Converter Modelling

In order to implement a buck converter featuring two interleaved phases, with closed loop control, it is traditional to derive the transfer function of the system, such that the corresponding PID controller values can be determined, and used within the

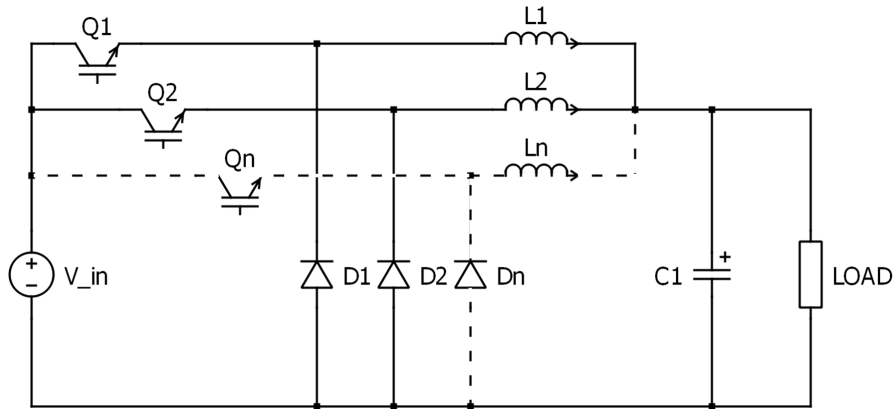


Figure 4.2: Interleaved Buck Converter Topology with 'n' Components

PLECS software simulation package, for control validation, and subsequent use with any hardware. This is an important step in the converter design process, as not only does the closed loop control of the output voltage, ensure that the desired voltage is attained and maintained within acceptable tolerances, it also deals with another phenomenon that pertains to interleaved converters; this being current imbalance between the inductors [121]. This is best explained using figure 4.3, which is based on the output current and voltage waveforms for an arbitrarily designed dual-phase buck converter, with the inclusion of output voltage control, and without current balance control; developed by the author, using the PLECS simulation package. As can be observed in figure 4.3.a, the current from inductor one (green line), is burdened with a higher current value, relative to that of inductor two; an enhanced view of the imbalance is available in figure 4.3.b. In this particular example the disparity between the two currents could be considered low, with very minimal variance between the two, however, this example only considers one operating condition, and other combinations of buck converter hardware, and modes of operation has the potential to cause a greater disparity between the two currents. Without the observations of the two inductor currents independently, this imbalance would have been un-noticed, as the sum of the two currents, which is the required output current as per the design specification for the converter, is quite simply the sum of the two currents, as per figure 4.3.c; therefore the sum of a lower current inductor,

combined with a high current inductor, will deceptively, show that the converter is working correctly. It is also observable from figure 4.3.d, that the voltage control loop is maintaining the output voltage within approximately 0.22% of the reference 28V, required by the converter specifications. In addition to guiding the design of the control system, the understanding of the current imbalance also guides the design requirements for current sensing equipment in the experimental hardware, as for this example both of the inductor currents are required to be sensed, and fed back into the control loop. From [121], the concept of single inductor current sense control for multiphase converters is explored; however, this is not employed here, but the theory presented for the balancing of the currents, using the error between the two inductor currents, proves useful.

The current imbalance has the potential to cause issues for both the inductors, and the converter as a whole. If one inductor is more highly burdened with current than the other, there is the potential that the burdened winding may not be rated for the additional current, thus exceeding thermal and electrical ratings, leading to a failure of the coil. Alternatively, the coil may be able to tolerate the additional current, however this will likely lead to an over-saturation of the magnetic flux density in the inductor's core, leading to a premature saturation, and resulting in a decrease in the inductor value, to a point which may be below the critical inductance value required for converter operation. The model which describes the voltage controlled scenario above, is available in figure 4.4.

In order to add the current balance control loop, the process generally begins with the development of a mathematical representation of the system, using a representation such as state space equations, which for the proposed converter represent the circuit as the state of the switches transition; this information is used to develop a Laplace transfer function, which is in turn used to calculate the gain values for the control system. The standard format for the states of the circuit,  $\dot{x}$ , are governed by equation 4.1, and the outputs, based on equation 4.1, are given by equation

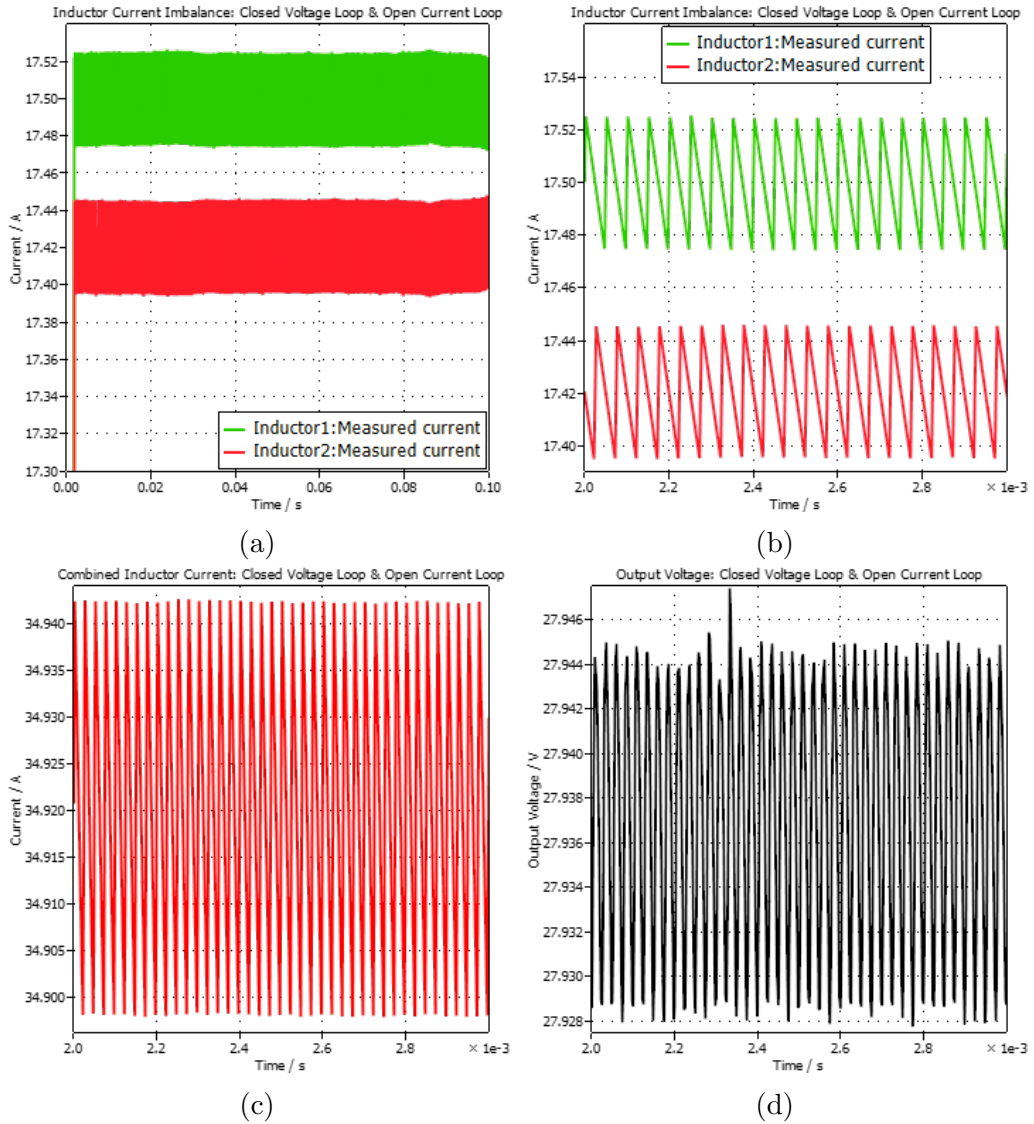


Figure 4.3: Current Waveforms of the interleaved buck converter: a) Inductor one and two current imbalance. b) Inductor one and two current imbalance enhanced view. c) Combined converter output current. d) Converter output voltage with closed loop control

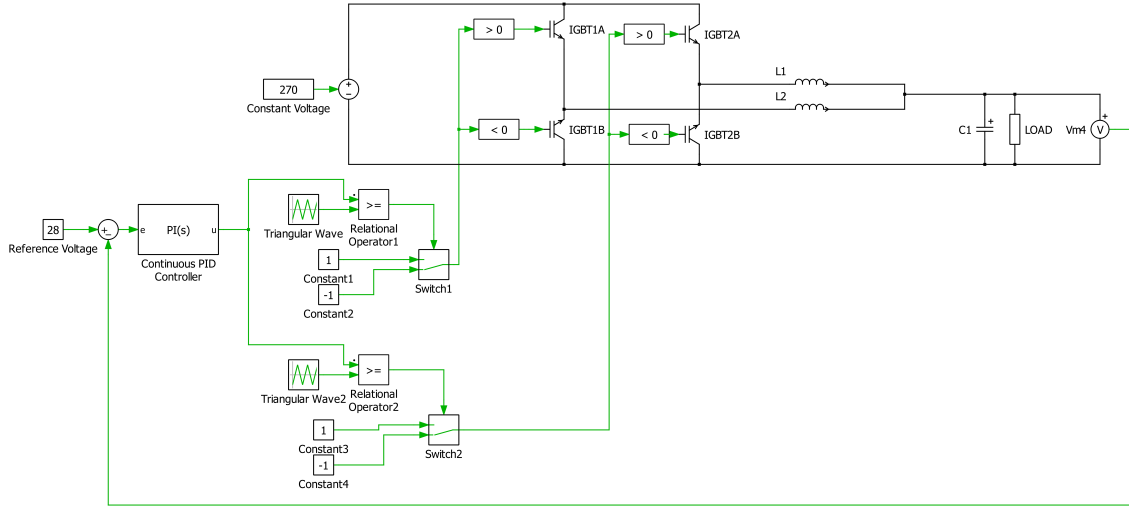


Figure 4.4: Interleaved Buck Converter with Voltage PID Controller

4.2. These equations define the system states,  $\dot{x}$ , and outputs  $y$ , based on matrices derived from the differential equations, governing each circuit state, which are then averaged, and converted from state space, into a transfer function using the standard form, given by equation 4.3.

$$\dot{x} = A_i \cdot x + B_i \cdot u \quad (4.1)$$

$$y = C_i \cdot x + D_i \cdot u \quad (4.2)$$

$$G(s) = C(sI - A)^{-1} \cdot B + D \quad (4.3)$$

From [121], the control of the voltage and current balancing is a function of the voltage duty cycle error, in combination with the error between the two currents,  $\epsilon$ , measured on the outputs of the inductors, where the inductor which observes the greater current, which from simulation has proved to be the one that switches on last, has its error value subtracted from the voltage duty error, and the opposite happens for the inductor which observes the lower current value, whereby the error is added to the duty cycle error, this translates into the switch's gate staying open for longer. This is described by equation 4.4, where input  $d_2$  is the duty cycle

associated to the inductor which would burden greater current, and input  $d_1$  being the duty cycle for the inductor which experiences the lower current value. The  $u$  term represents the outputs of the system, these being,  $d$ , the duty cycle error, and as previously mentioned,  $\epsilon$ , the error between the two inductor currents. The modified voltage control system, which now includes the current balance control, using the duty cycle, is available in figure 4.5.

$$\begin{cases} d_1 = d + \epsilon \\ d_2 = d - \epsilon \\ u = \begin{bmatrix} d \\ \epsilon \end{bmatrix} \end{cases} \quad (4.4)$$

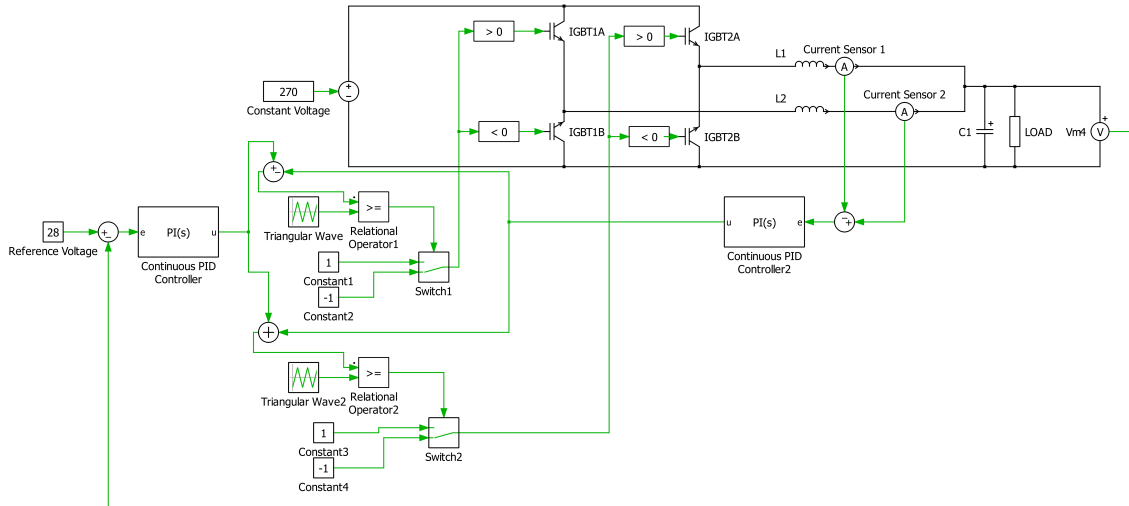


Figure 4.5: Interleaved Buck Converter with Voltage and Current PID Controllers

As is shown in figure 4.5, there are now two PI controllers, relative to the single PI controller used by the system with voltage control alone. Both of these PI controllers require tuning, with the correct PI values, to maintain control of the converter's voltage, and balance the currents. It should be noted that the author is not a control expert, and as such an alternative to the traditional control tuning methods is adopted. The tuning method selected here is Particle Swarm Optimisation (PSO) [122], which rather than defining a mathematical model of the system and working

towards a transfer function to determine the proportional, P, and integral, I, values for the controller, systematically works its way through varying values of P and I, to evaluate optimum control parameters, with minimal error.

PSO, a metaheuristic population based optimisation algorithm, and a member of the larger stochastic optimisation algorithms family, presented in figure 4.6, is an intelligent optimisation algorithm, which finds use in many fields, such as operations management, research, data mining and machine learning. In order to find a system optimum, a “search mechanism” is adopted, whereby output data is compared, and assessed by a selection of independents until all independents reach the same conclusion. In order to achieve this search mechanism a set of fundamental principles are required, where a group of particles moves within the solution space, adjusting their relative position based on;

- Communication – whereby measured values of the individual particles best know position, are disseminated to others in the search mechanism for comparison; this is referred to as a personal best, and generally denoted as, *pbest*.
- Learning – whereby, in abstract terms, the members of the search mechanism are able to comprehend that a value from another member of the search mechanism maybe closer to the optimal values required, hence a form of swarm intelligence that may be observed in nature is adopted within an algorithm, these values are referred to as, the global best, and commonly denoted as, *gbest*.

PSO contains a population of candidate solutions called a swarm of particles to the optimisation problem. Every particle in the swarm has a search space within the optimisation problem, and moves as a vector (with position and velocity) towards the optimum value, and all particles will be governed by the same set of predetermined rules, i.e. a mathematical model of the motion for the particle [123]. In order

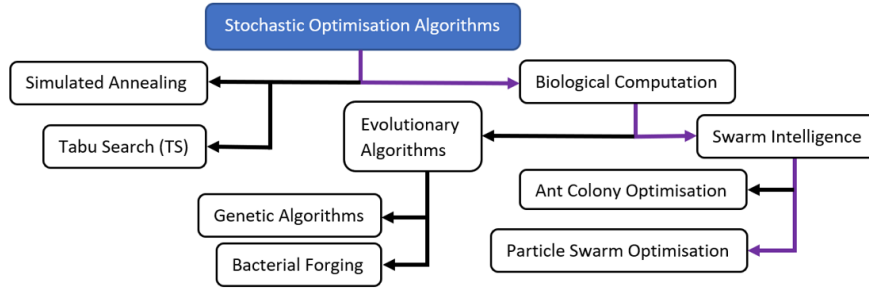


Figure 4.6: PSO's place within the stochastic optimisation algorithms family tree

for the search mechanism to work, each particle requires:

- A position of where it is in the search space, denoted as,  $x_i$ , where the subscript,  $i$ , pertains to the individual particle.
- A velocity, which describes how the particle moves, denoted as,  $v_i$ .
- A value of fitness, which is a measure of how optimum the current position is.
- A value for the personal best position of the particle, already given as,  $pbest$ .
- A reference of the global best position given by the full swarm, already denoted as,  $gbest$ .

For each iteration, denoted as,  $t$ , of the optimisation, the velocity of each particle,  $i$ , and the position of each particle, are given by the standard equations used to set-up a PSO study, with an updated velocity given by equation 4.5, and an updated position given by equation 4.6 .

$$v_i^{(t+1)} = \omega \cdot v_i^{(t)} + c_1 \cdot r_1 \cdot (pbest_i - x_i^{(t)}) + c_2 \cdot r_2 \cdot (gbest_i - x_i^{(t)}) \quad (4.5)$$

Where:

$\omega$  = Inertia weight, which provides a balance between exploration and exploitation.

$c_1, c_2$  = Cognitive and social coefficients, which control the influence of the  $pbest$

and  $gbest$ .

$r_1, r_2$  = Random numbers in  $[0,1]$ , which add to the stochastic behavior.

$v_i^{(t)}$  = Current velocity of the particle.

$x_i^{(t)}$  = Current position of the particle.

$pbest_i$  = Particle's personal best position.

$gbest_i$  = Best global position provided by the swarm.

$$x_i^{(t+1)} = x_i^{(t)} + v_i^{(t+1)} \quad (4.6)$$

The PSO begins by initialising a swarm of particles, the size of which is selected as an input parameter to the study, with random positions and velocities. The fitness of each particle is then evaluated, using the objective function; the objective function in the case of the buck converter, being a minimisation of the voltage and current error. The values given for the  $pbest_i$  of each particle is taken, and the  $gbest_i$  compared against a stopping criterion; the process stops if the criterion is met, i.e when the fitness becomes a relatively small value. It is unlikely that the objective function is met using the random positions, and as such based on the  $pbest_i$  and the  $gbest_i$ , the particle is moved to the next position, based on equation 4.5, and the search continues, each iteration updating the  $pbest_i$  and the  $gbest_i$  until convergence is met. A maximum number of iterations can be established, to prevent the code from searching through using an infinite number of swarms. The inertial property, denoted by  $\omega$  is a value generally lower than 1. A value closer to 1, for the  $\omega$  term promotes exploration, where as a lower value promotes exploitation. The values of  $c$ , are usually set somewhere between 1.4 and 2.

Using the PSO technique to determine optimal PI values, the scenario from the previously unbalanced system is re-run, with the additional control loop to balance the current, to demonstrate the functionality of the current balancing loop, in com-

combination with the P and I values determined by the PSO. The specific values for the PI controllers are not noteworthy here, as this is an arbitrary example to validate functionality of the model as a whole, and the next section deals with the specific parameters for what will become the final converter, to be simulated, and translated into physical hardware. Figure 4.7 represents the updated study, where it is clear to see in figure 4.7.b, that the inductor currents are now perfectly balanced with one another, and the output voltage is still being regulated with only 0.2% of the required 28V output voltage.

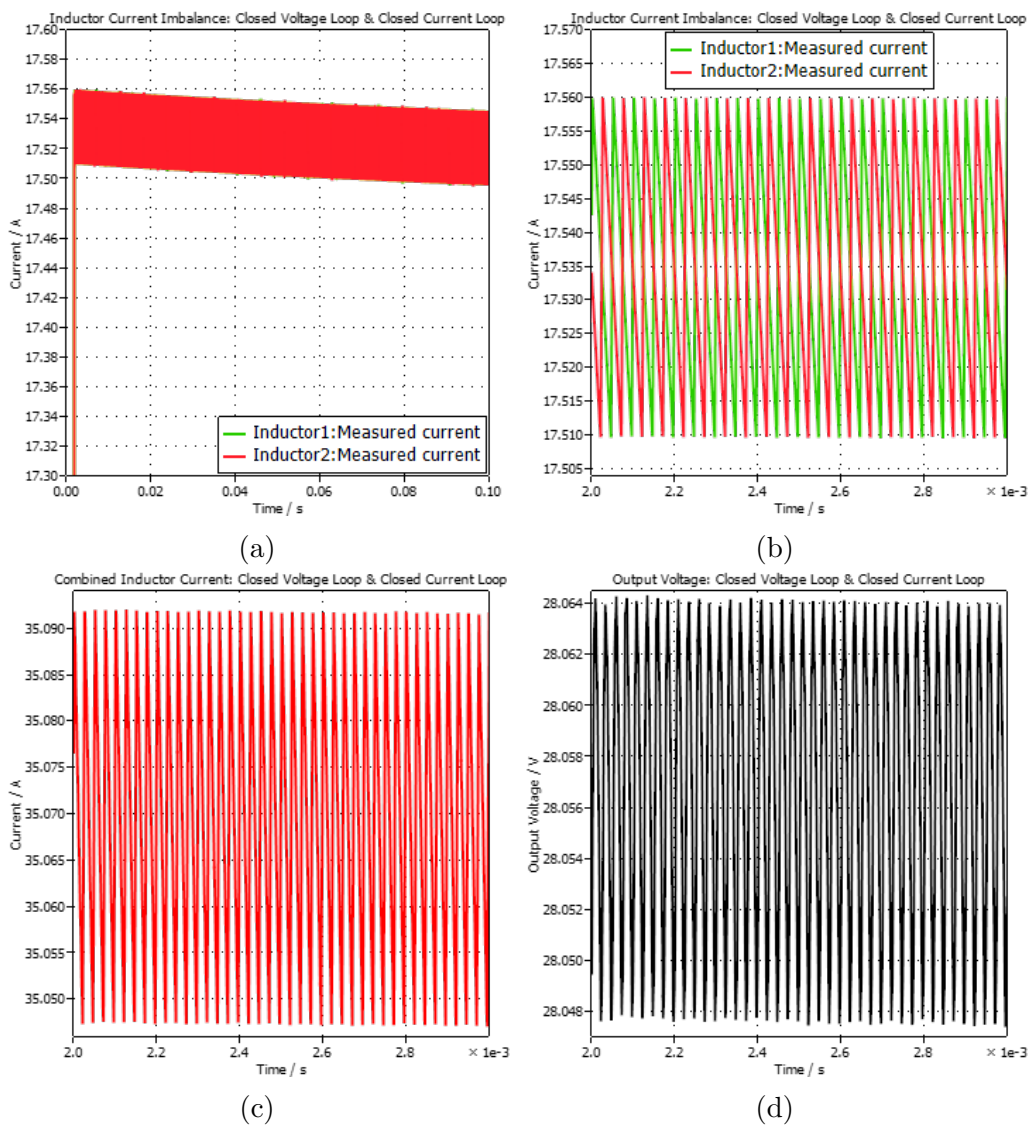


Figure 4.7: a) Inductor one and two currents balanced. b) Inductor one and two current balance enhanced view. c) Combined converter output current. d) Converter output voltage

Additional testing of the PSO tuned parameters show that the current balancing capabilities, and voltage holding capabilities are well maintained under load changes, however, the voltage exhibits transients during the step. The step repose for the currents is shown in figure 4.8.a, through figure 4.8.f. The current balance during steady state, both before and after the change in load, is perfectly maintained. Figure 4.8.g, highlights a minor flaw with the control system, that being the voltage drop during the load change, at 0.05 seconds. The voltage plummets towards zero, and in a practical sense, when considering load changes on an aircraft, this voltage drop would be unacceptable, and a more robust controller would be required. However, for the purposes of experimentally testing a buck converter in the laboratory, this voltage drop will be addressed by utilising an 'electronic load', which would take advantage of the continuous current mode functionality, and placing this in conjunction with a power supply operating at constant voltage and variable current, will negate the voltage drop.

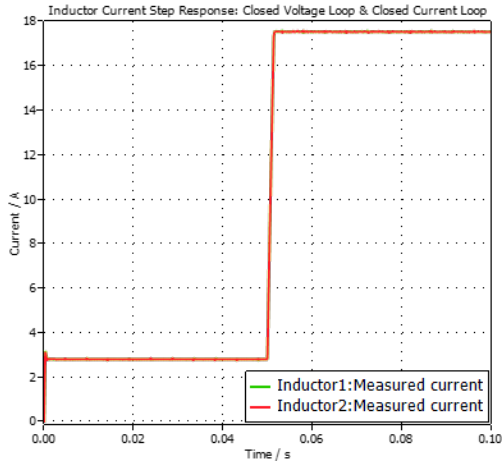
## 4.2 Buck Converter Parameters

It remains for the specifications of the experimental converter to be defined, for the purposes of experimentally validating the use of biased magnetics, relative to non biased, standard magnetics, in an interleaved buck converter topology.

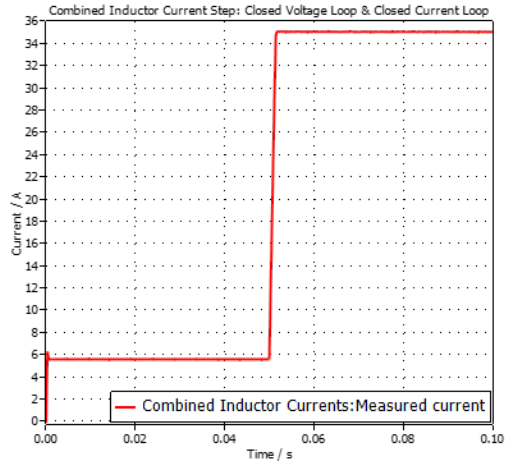
As this is an interleaved configuration, taking advantage of two pahses, the buck converter is defined in a "2n" topology, to prevent an odd number of inductors being required.

As a starting point for the specifications, the buck converter will conform to two common DC bus voltages, which are an aircraft standard 270VDC,  $V_{in}$ , and stepping down to 28VDC,  $V_{out}$ , in accordance with the literature review. The voltages are also used to determine the duty-cycle for the converter and inductor design, and

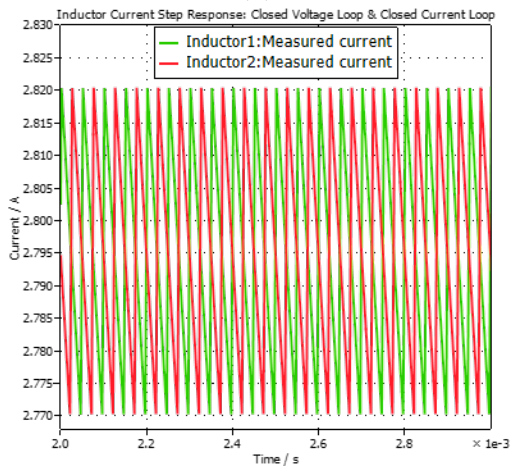
## 4.2. BUCK CONVERTER PARAMETERS



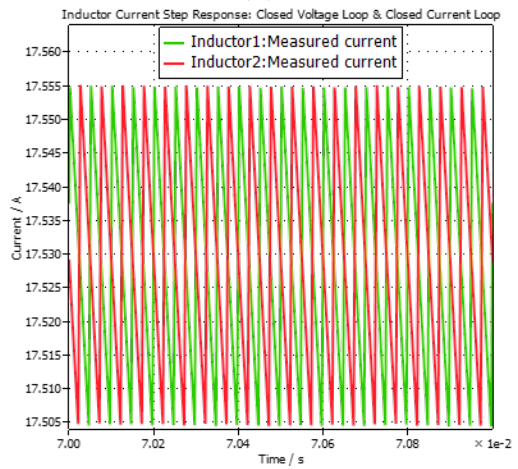
(a)



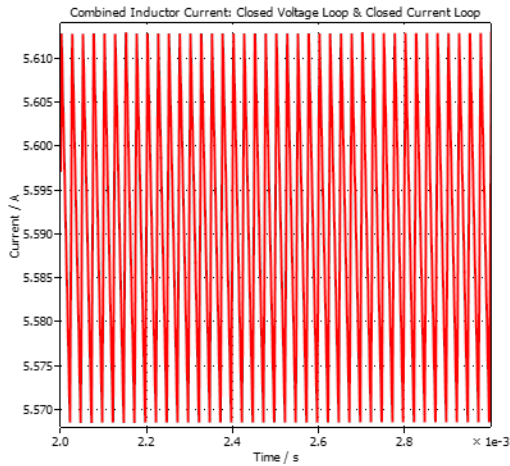
(b)



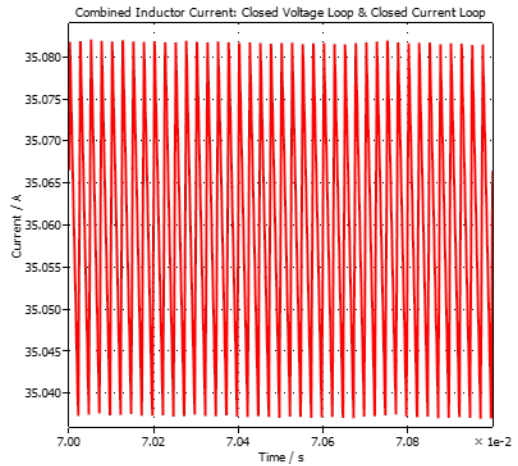
(c)



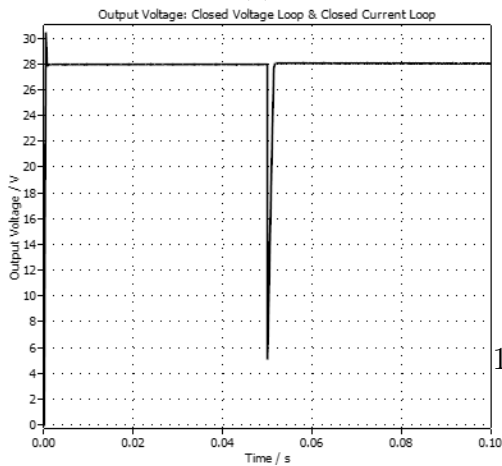
(d)



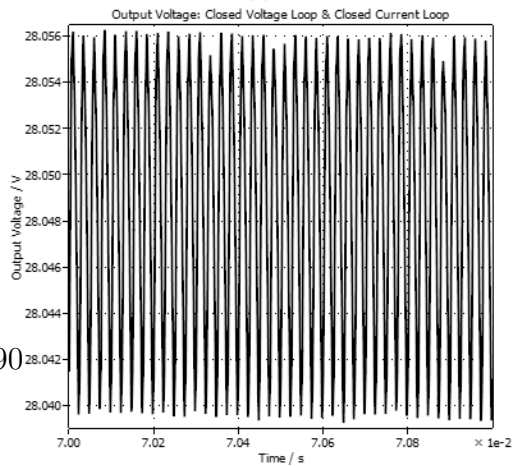
(e)



(f)



(g)



(h)

specifically for a buck converter, stepping down the voltage, this is given by equation 4.7. It stands to reason that a variable input voltage, or output voltage will therefore require a variable duty-cycle, which is determined by a voltage and current controller in the loop with the converter. For the proposed converter, and initial inductor designs, a duty-cycle of 0.1037 is required; the controller will vary this duty cycle somewhat to ensure that the currents are balanced across both inductors.

$$D = \frac{V_{out}}{V_{in}} \quad (4.7)$$

Standard inductor sizing for the converter beings by defining the number of phases,  $n$ , required for the system. In this scenario, as already stated, a two phase system is employed,  $n = 2$ . The selection of an output current,  $I_{out}$ , in combination with the output voltage determines the output power of the converter. For this study, in order to test the theory of the biased inductors in an interleaved configuration, a relatively low power output is desired. Based on this, a reasonable 40 Amp load current is chosen, as this also aligns with the maximum current output of test equipment described in the next section, and in combination with the 28V output yields a total power output of approximately 1.12kW for the system; this is also sympathetic to the maximum power threshold of the electronic load, which will be used during experimental validation, and is stated to be 1.8kW maximum. As an interleaved converter is considered, the current is distributed across the two inductors, therefore the saturation current for the standard non-biased inductors is required to be considerably less than 20 Amps, such that when the biased inductors are implemented, there is sufficient leeway in the system to explore potential additional current handling capacity from the inductors, without exceeding the maximum proposed power limit. The output current ripple is selected as 5%, and forms the current ripple (peak-to-peak) term,  $I_{pp}$ , given in equation 4.8, and is the product of the mean phase current multiplied by the ripple percentage. Additionally, the

Table 4.1: MIL-STD-704F 28V Bus and 270V Bus Standards

Steady State Characteristics	Limits	
	28 Volt DC System	270 Volt DC System
Steady State Voltage	22 to 29 Volts	250 to 280 Volts
Distortion Factor	0.035 Maximum	0.015 Maximum
Ripple Amplitude	1.5 Volts Maximum	6 Volts Maximum

converter’s operational frequency,  $f_{sw}$ , is required at this stage.

The converter’s operational frequency, i.e. the frequency adopted by the carrier signal into the gate drivers, has an effect on the size of the passive components, thermal management, as well as the efficiency and response time. A conservative 20000 Hz is selected for this application.

$$L = \frac{V_{out} \cdot (1 - D)}{f_{sw} \cdot I_{pp}} \quad (4.8)$$

As mentioned previously, an additional constraint for the system comes in the form of the MIL-STD-704F standards, which establishes the standards and characteristics for aircraft electrical power provided to the input terminals of equipment attached to the respective power bus. These standards for the 28VDC and 270VDC bus are given in table 4.1. A summary of the converter requirements governed by the author and MIL-STD-704F standards, is given in table 4.2.

As the system will rely on an interleaved H-bridge configuration, where by a complementing pair of switches to Q1, and Q2 are inserted, there is no requirement for diode sizing.

For the value of inductance,  $L$ , described by equation 4.8, in the context of the converter, this is described as the critical inductance value. The critical inductance value is the minimum inductance required in a power converter to ensure that it remains operating in a continuous conduction mode, and for values of inductance

Table 4.2: Non-Biased Multiphase DC-DC Buck Converter Specification

Parameter	Value
Phases, $n$	2
Input Voltage, $V_{in}$ [V]	270
Output Voltage, $V_{out}$ [V]	28
Output Current Max, $I_{out,max}$ [A]	40
Output Power, $P_{out}$ [W]	1120
Switching Frequency, $f_{sw}$ [Hz]	20000
Current Ripple, $\Delta I$ [%]	5
Output Voltage Peak, $V_{pk}$ [V]	29.5

used below the critical inductance value, places the converter into discontinuous conduction mode. The continuous conduction operation ensures that there is a stable output voltage, and permits for a smoother current waveform, where as operating in the discontinuous conduction mode results in higher peak currents, and increased conduction losses. Based on this and the requirement to operate the standard-inductor below the 20 Amp maximum phase value, an inductor saturation current of 10 Amps is selected, and when combined with equation 4.8, this yields a critical inductance value of 2.5 mH. A factor of safety will be added to this, and the next section considers the physical design of an inductor.

### 4.3 Inductor Design

The design specification for a physical inductor is dependent on a set of fundamental parameters, these being the converter switching frequency,  $f_{sw}$ , the peak currents observed by the phase,  $I_{phase}$ , rather than the total system current, the converter input voltage,  $V_{in}$ , and the inductance required,  $L$ , which itself is a function of the switching frequency and phase current, as well as the output voltage,  $V_{out}$ . As per the literature review, the cores selection is frequency dependent, and for higher frequencies, ferrite cores are well suited. Based on availability, and respectable frequency handling capabilities, this study will utilise the amorphous METGLAS

### 4.3. INDUCTOR DESIGN

Table 4.3: AMCC METGLAS © Alloy 2605SA1 Core Parameters

Core No.	Core Parameters									
	a (mm)	b (mm)	c (mm)	d (mm)	e (mm)	f (mm)	$l_m$ (cm)	$A_c$ (cm <sup>2</sup> )	$W_a$ (cm <sup>2</sup> )	AP (cm <sup>4</sup> )
AMCC10	11	13	40	20	35	62	15.4	1.8	5.2	9.4
AMCC100	16	20	70	45	52	102	25	5.9	14	82.6
AMCC1000	33	40	105	85	106	171	42.7	23	42	966
AMCC125	19	25	83	35	63	121	30.2	5.4	20.8	112.1
AMCC160	19	25	83	40	63	121	28.5	6.5	20.8	135.2
AMCC168S	20.4	30.2	155.2	20	71	196	45.4	3.35	45.7	153
AMCC16A	11	13	40	25	35	62	15.1	2.3	5.2	12
AMCC16B	11	13	50	25	35	72	16.9	2.3	6.5	15
AMCC1725	63.5	38.1	97.8	88.9	165.1	224.8	53.63	46.29	37.3	1725
AMCC20	11	13	50	30	35	72	17.5	2.7	6.5	17.6
AMCC200	19	25	83	50	63	121	29.8	7.8	20.8	162.2
AMCC211A	9.93	15.88	49.2	25.4	35.74	69.1	17.59	2.07	7.81	16
AMCC25	13	15	56	25	41	82	19.6	2.7	8.4	22.7
AMCC250	19	25	90	60	63	128	31.4	9.3	22.5	209.3
AMCC32	13	15	56	30	41	82	20	3.3	8.4	26.9
AMCC312A	19	19	67	45	57	105	25.45	7.01	12.73	89.25
AMCC320	22	35	85	50	79	129	32.5	9	29.8	267.8
AMCC367S	25.8	66	97.8	25	117.6	149.4	43.78	5.29	63.81	338
AMCC3100A	30	25.4	58.72	30	85.4	118.72	29.52	7.38	14.91	119
AMCC4	9	10.5	32.75	15.25	28.5	51	12.7	1.11	3.44	3.82
AMCC40	13	15	56	35	41	82	19.9	3.7	8.4	31.1
AMCC400	22	35	85	65	79	129	33.6	11.7	29.8	348.1
AMCC50	16	20	70	25	52	102	24.9	3.3	14	46.2
AMCC500	25	40	85	55	90	135	35.6	11.3	34	384.2
AMCC6.3	10	11	33	20	31	53	13.1	1.6	3.6	5.8
AMCC630	16	20	70	30	52	102	25.3	3.9	14	54.6
AMCC8	11	13	30	20	35	52	13.2	1.8	3.9	7
AMCC80	16	20	70	40	52	102	25.4	5.2	14	72.8
AMCC800A	25	40	85	85	90	135	35.6	17.4	34	591.6
AMCC800B	30	40	95	85	100	155	39.3	21	38	798

© Alloy 2605SA1, in the form of a C-core from the AMCC range. The material properties for this core material are presented in table E.1, within the appendix.

The Area Product (AP) methodology for inductor sizing is a commonly used practice; this allows for the selection of a core geometry, based on an AP value, typically provided by the core manufacturer; some examples for the AMCC range of the METGLAS © Alloy 2605SA1, C-cores, are provided in table 4.3, and their corresponding dimensions, according to figure 4.9, are also provided, as well as the mean magnetic path length,  $l_m$ ; these details will be used for the sizing of the most appropriate inductor for the converter. The AP is defined as the product of the core's area cross-section,  $A_c$ , and its window area,  $W_a$ , These parameters are shown in figure 4.10, and the corresponding equation 4.9.

$$AP = A_c \cdot W_a = \frac{2 \cdot E \cdot 10^4}{B_{max} \cdot J \cdot K} \quad (4.9)$$

Where:

$J$  = current density in the conductor coil,  $A/cm^2$

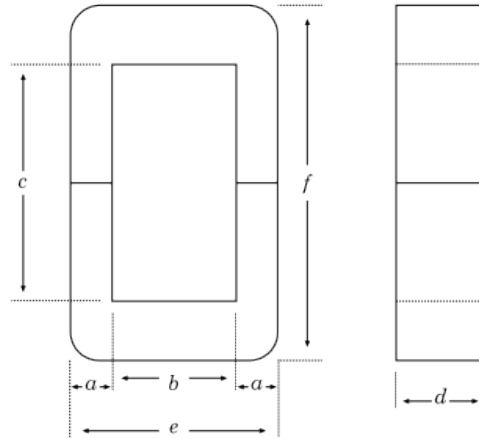


Figure 4.9: AMCC METGLAS © Alloy 2605SA1 General Core Dimensions

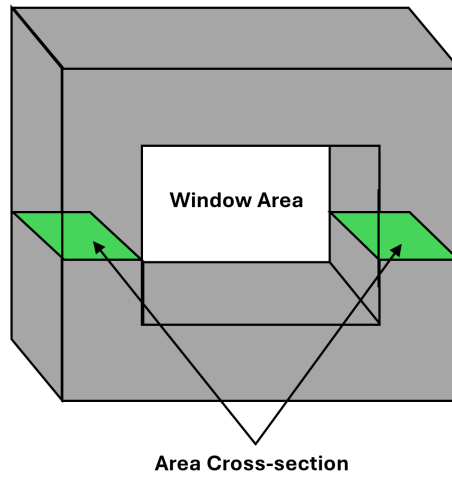


Figure 4.10: Inductor Core Cross-section and Window Area

$B_{max}$  = Maximum peak flux density during operation, Tesla. A value of 1.4T is used for this study; the maximum flux density for the material is given as 1.56T

$K_u$  = window utilisation factor. This represents the copper percentage within  $W_a$ . Typical values vary between 40% and 80%.

$E$  = Energy Product,  $J$

There are multiple ways to express the stored energy, commonly referred to as the energy product,  $E$ , for an inductor; usually given in Joules or Watt-Seconds. Equation 4.10 provides the energy both as a function of the inductance and current squared, but also in relation to the AP. The value for  $\Delta B$  is dependent upon the

condition at which the inductor operates at. As AC inductors use quadrant one and three of the BH curve, their  $\Delta B$  is double the saturation of the equivalent DC inductor; this gives  $\Delta B = B_{sat}$  for DC inductors, and  $\Delta B = 2 \cdot B_{sat}$  for AC inductors. The method adopted for this study, takes advantage of the initial equation from 4.10.

$$E = \frac{L \cdot I^2}{2} = \frac{AP \cdot \Delta B \cdot J \cdot K_u}{2} \quad (4.10)$$

Once the  $AP$  value has been determined, an appropriate core size, can be selected from the desired manufacturer; however, for this study, the selection is made from from table 4.3. The chosen core must have an  $AP$  value, slightly greater than the calculated requirements; this ensures that the core will have suitable performance.

Following the core selection, the initial number of turns,  $N$ , necessary to achieve the desired inductance, can be computed using equation 4.11. The equation also incorporates the peak current,  $I_{pk}$ , which represents the maximum instantaneous current experienced by the inductor. This value exceeds the steady state DC current. The peak current is determined using equation 4.12.

$$N = \frac{L \cdot I_{pk}}{B_{max} \cdot A_c} \quad (4.11)$$

$$I_{pk} = I_{DC} + \left( \frac{I_{pp}}{2} \right) \quad (4.12)$$

The relationship between the inductance and airgap length,  $l_g$ , is provided in the application notes for core material used in this study, and is expressed in equation 4.13. This equation also introduces  $\Delta\mu$ , which represents the incremental permeability at the operating point on the BH curve, and is specified as 1000.

$$L = \frac{0.4 \cdot \pi \cdot N^2 \cdot A_c \cdot 10^{-8}}{lg + \left(\frac{l_m}{\Delta\mu}\right)} \quad (4.13)$$

Equation 4.13, is rearranged to determine the airgap length,  $l_g$ , by substituting  $N$  and  $A_c$ , with  $I_{pk} \cdot 10^4$  and replacing  $L$ , with  $B_{max}$ . The resulting expression, given by equation 4.14, provides the total airgap length, rather than the gap per leg. When using the units from table 4.3, the airgap length is expressed in centimeters, and is required to be divided by two. For practical purposes, the value ascertained for the airgap, is rounded up to the nearest two decimal places.

$$lg = \frac{0.4 \cdot \pi \cdot N \cdot I_{pk} \cdot 10^{-4}}{B_{max}} - \left(\frac{l_m}{\Delta\mu}\right) \quad (4.14)$$

An additional nuance for inductors, surrounds the theory that magnetic flux does not always remain confined to the intended magnetic path, particularly in the presence of an airgap, where significantly increased reluctance compared to the core material, causes the flux to expand into free space. This phenomenon, known as fringing flux, affects the inductance of the inductor, by effectively increasing the magnetic field's distribution. In order to mitigate the effects of this, the number of windings can be adjusted, using a fringing flux factor,  $FF$ , which is dependent on the core dimensions and airgap length. This is given by equation 4.15.

$$FF = \frac{(a + lg) \cdot (d + lg)}{a \cdot d} \quad (4.15)$$

The fringing flux factor  $FF$ , is then incorporated into the calculation of the adjusted number of turns,  $N_{adjusted}$ , to compensate for the influence of the fringing flux on the effective cross-sectional area of the magnetic path. This adjustment is presented in equation 4.16, taken from the application notes of the core's manufacturer. Alternate methods for the adjustment of the number of windings are readily

available from stalwart magnetics design textbooks, such as that of [84].

$$N_{adjusted} = \sqrt{\frac{L \cdot [l_g + (l_m/\Delta\mu) \cdot 10^8]}{0.4 \cdot \pi \cdot A_c \cdot FF}} \quad (4.16)$$

Using the adjusted number of turns, in combination with equation 4.14 transposed to yield the value of the maximum flux density,  $B_{max}$  in the core, it is possible to check that the operating point of the inductor with the corrected number of turns still meets the requirements of the core material, and does not induce an over bias at the peak operating point. The updated equation is given in 4.17

$$B_{max} = \frac{0.4 \cdot \pi \cdot N \cdot I_{pk} \cdot 10^{-4}}{l_g + \left(\frac{l_m}{\Delta\mu}\right)} \quad (4.17)$$

As part of the inductor design process, it is necessary to make some assessment of the losses which will be experienced by the windings and the core. To support these calculations the AC flux density,  $B_{AC}$  within the core is considered, initially, and computed using equation 4.18; This will be used in the supporting calculation of the core losses. For further clarification, the  $B_{AC}$  term is representative of the fluctuation in the magnetic flux density as a function of the peak-to-peak current ripple. It is noted here, that although the theoretical losses are calculated as part of the inductor design process, the consideration of the losses does not form part of this study, which is primarily focused on mass and volume reduction.

$$B_{AC} = \frac{0.4 \cdot \pi \cdot N_{adjusted} \left(\frac{I_{pp}}{2}\right) \cdot 10^{-4}}{l_g} \quad (4.18)$$

Using the average current,  $I$ , expected in the windings of the inductor coil, in conjunction with the current density,  $J$ , presented previously, the cross section of an individual copper wire,  $A_{copper}$  can be determined using equation 4.19. The

current density for the copper in this study is taken to be, a reasonable  $6 \text{ A/mm}^2$ . Subsequently, the diameter of the copper wire,  $D_{copper}$  can then be determined through the simple geometric equations for a circle; this equation is not presented here.

$$A_{copper} = \frac{I}{J} \quad (4.19)$$

As the current also features a high frequency component, the resistance of the winding will increase, due to the skin effect, resulting in a new term, the skin depth,  $\delta_{copper}$ . The skin effect, in essence, causes the current to deviate away from the center of the conductors core, due to eddy currents, and concentrate towards the surface of the conductor, with the skin depth being the distance from the conductor's surface where the current density falls to approximately 37%. As the current is forced towards the surface of the copper conductor, the available cross-sectional area which is available for conducting the current is reduced. The skin effect is calculated using equation 4.20, and effects of the phenomenon, for high frequency designs can be minimised through the adoption of Litz wire or foil windings. Multiplying the skin depth by two, gives a usable diameter of the copper conductor, and the area of the copper wire is calculated using this value as the diameter.

$$\delta_{copper} = \sqrt{\frac{2 \cdot \rho_{copper}}{\mu \cdot \omega}} \quad (4.20)$$

Depending upon the copper cross-section,  $A_{copper}$  calculated previously, and the resulting area when using skin depth  $\delta_{copper}$  to generate the diameter for the new area calculation, it may be necessary to distribute the windings across a number of windings in parallel,  $N_{parallel}$ , this is given as the  $A_{copper}$ , divided by the resultant area given by the copper skin depth  $A_{\delta}$ . A factor of safety may also be applied; however, this will be to the detriment of mass and volume of the inductor.

It is possible to determine the length of the copper,  $l_{copper}$ , required to produce the coil(s). This is achieved by multiplying the mean length per turn, given by equation 4.21, which uses the dimensions of the cores geometry given in table 4.3, by the re-calculated number of turns; as per equation 4.22.

$$MLT = 2 \cdot (a + 2 \cdot b + d) \quad (4.21)$$

$$l_{copper} = MLT \cdot N_{adjusted} \quad (4.22)$$

The calculation of the DC resistance on the winding,  $R_{DC}$ , requires information regarding the resistivity of the copper,  $\rho_{copper}$ ; this is given as  $1.68 \cdot 10^{-8} \Omega m$ , at a temperature of  $20^\circ C$ , and is used in equation 4.23, to compute the winding resistance value.

$$R_{DC} = \frac{MLT \cdot N \cdot \rho_{copper}}{N_{parallel} \cdot A_\delta} \quad (4.23)$$

In addition to DC resistance, the inductor is also exposed to AC resistance, which needs accounting for. Empirical approximations are one method to determine this resistance, alternatively, the use Dowell's equations to estimate this value; these are not presented here. For a reasonable approximation the AC resistance,  $R_{AC}$  is calculated through an AC resistance factor,  $F_{R,AC}$ , multiplied by the DC resistance. This resistance factor is approximated by equation 4.24, using the skin depth, and the radius of the copper conductor,  $r_{copper}$ , given by the diameter divided by two. The AC resistance factor is then multiplied by  $R_{DC}$ , to yield the total AC resistance; this is computed with equation 4.25.

$$F_{R,AC} = 1 + \left( \frac{\delta_{copper}}{r_{copper}} \right)^2 \quad (4.24)$$

$$R_{AC} = R_{DC} \cdot F_{R,AC} \quad (4.25)$$

To total losses for the winding, commonly referred to as copper losses,  $P_{copper}$ , can be calculated using both the AC and DC resistance components previously calculated; This is achieved with equation 4.26.

$$P_{copper} = R_{DC} \cdot \left( I^2 + F_{R,AC} \cdot \left( \frac{I_{pk}}{3} \right)^2 \right) \quad (4.26)$$

Losses are also dissipated in the core of the ferromagnetic material, these are known as the iron losses,  $P_{Fe}$ . Data sheets from core manufacturers generally provide a plot to represent the volumetric power density loss. The core loss versus flux density plot for AMCC METGLAS © Alloy 2605SA1, at 25 °C across multiple operating frequencies, is available in figure 4.11. The plot presents the power density losses as a function of the AC magnetic flux density, in  $W/kg$ , based on the Steinmetz equation 4.27, and also presents a conversion factor to translate the results into another common quantity, that being  $mW/cm^2$ , at the ratio of 7.18 : 1. If the equation for power density losses are not presented on the data sheets, the work of [84] presents equation 4.28.

$$P_{Fe/kg} = 6.5 \cdot f_{sw}^{1.5} \cdot B^{1.74} \quad (4.27)$$

$$P_{Fe/kg} = K_{Fe} \cdot \Delta B^\beta \cdot A_c \cdot l_m \quad (4.28)$$

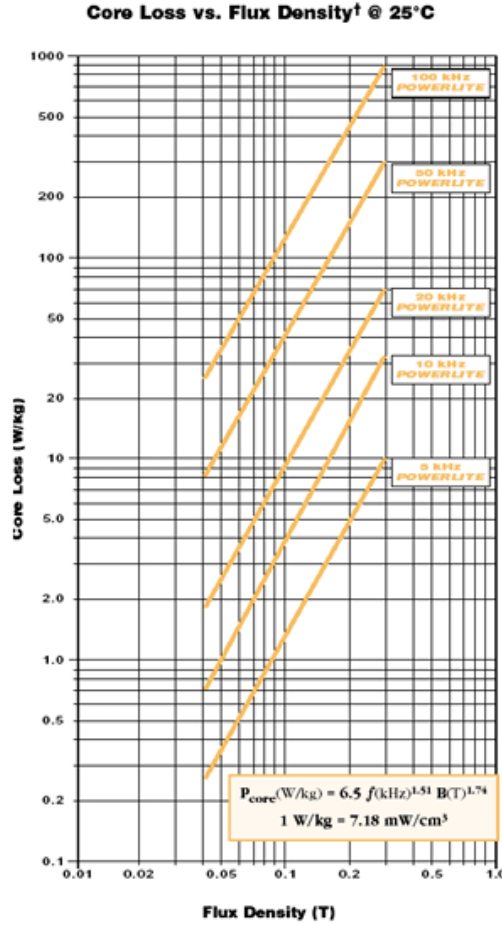


Figure 4.11: AMCC METGLAS © Alloy 2605SA1 Core Loss vs Flux Density

The coefficients  $\beta$  and  $K_{Fe}$  are determined empirically from the power density plot for the material, and the core volume is given by  $A_C \cdot l_m$ . The peak-to-peak flux density,  $\Delta B$  determines the iron losses. The final core power loss as a function of the core weight, is given by simply multiplying the core mass,  $M_{core}$  by the core loss per unit mass; this is described by equation 4.29.

$$P_{Fe} = P_{Fe/kg} \cdot M_{core} \quad (4.29)$$

The total power losses,  $P_{total}$ , can be calculated through the addition of the iron losses and the copper losses, given in equation 4.30.

$$P_{total} = P_{Fe} + P_{copper} \quad (4.30)$$

The final mass of the inductor is a function of the inductor core mass, and the mass of the copper windings. The core mass is presented as part of the manufacturer's data sheet, and the copper mass,  $M_{copper}$ , can be determined through equation 4.31, when the density of the copper,  $\rho_{copper}$  is given; for this study this is taken as  $8960 \text{ kg/m}^3$ .

$$M_{copper} = A_{\delta} \cdot N_{parallel} \cdot N_{adjusted} \cdot MLT \cdot \rho_{copper} \quad (4.31)$$

### 4.3.1 Experimental Inductor Sizing

The critical inductance described above, stipulates the minimum value of inductance required to ensure that the converter operates in continuous conduction mode. If the value of inductance is too small, the current can drop to zero during part of the switching cycle, causing the converter to enter discontinuous conduction mode, where the inductor does not store the required energy to meet the demands of the converter. Based on this, the value of inductance is enlarged, relative to the 2.5mH previously calculated. Using a higher value inductance provides a margin of safety in the event that the physical inductor does not conform to the values calculated from the design phase. The drawback to using a larger inductance value comes in the form of a larger time constant, and the potential for a physically larger inductor.

However, as this study focuses on investigating mass and volume reductions in a specific inductor topology within an interleaved buck converter, the physical size of the baseline inductor is relatively arbitrary. The primary objective is to demonstrate improvements independent of the initial design.

Table 4.4: 2.5mH Inductor Design

Parameter	Value	Parameter	Value
Inductance (mH)	2.5	Switching Frequency (kHz)	20
$I_{DC}$ (Amps)	10	Ripple Current (%)	5
$\Delta I$ (Amps)	0.5	$I_{pk}$ (Amps)	10.25
Energy Product (mJ)	131.33	Skin Depth (mm)	0.4674
Area Product (cm <sup>4</sup> )	7.82	MLT (cm)	20.2
Airgap Length (mm)	0.05	Number of Turns (-)	32
Peak Flux Density (T)	8.24	Wires in Parallel (-)	3

For reference, the 2.5mH inductor, designed to the original specifications, when using the AMCC-100 core, in conjunction with the previously described design methodology, are presented in table 4.4. As the table shows, the value of inductance for the AMCC-100 core is not suitable. Notably, the area product being approximately ten times larger than required, and the peak flux density exceeding to saturation limits of the core.

The baseline inductor will also require modifications to enable it to accept the magnets during biasing. This is not strictly an issue when the magnets are to be mounted to the area given by dimensions 'd' and 'f' of the core; however, a proposal to also place magnets within the airgap, to achieve additional novelty, requires additional consideration. This being, the thickness of commercially available magnets, with respects to the airgap length sized by the methodology; the minimum acceptable length for the airgap is set to 2mm, to allow for magnets of 1mm in thickness per airgap.

Using the methodology to sweep for a manageable airgap, within the confines of the operating parameters produces a suitable candidate for the pre-biased experimental inductor; presented in table 4.5. For a total of 196 winds, adjusted for fringing factor, it is possible to achieve a total airgap of 2mm, an inductance value for this configuration is found to be 0.0132 Henry, as per figure 4.12, which shows airgap and inductance versus non-adjusted number of turns.

#### 4.4. STANDARD INDUCTOR GALVANO ELECTROCHEMICAL IMPEDANCE SPECTROSCOPY TESTING

Table 4.5: Experimental Inductor Parameters

Parameter	Value	Parameter	Value
Inductance (mH)	13.2	Switching Frequency (kHz)	20
$I_{DC}$ (Amps)	10	Ripple Current (%)	5
$\Delta I$ (Amps)	0.5	$I_{pk}$ (Amps)	10.25
Energy Product (mJ)	693.41	Skin Depth (mm)	0.4674
Area Product (cm <sup>4</sup> )	41.27	MLT (cm)	20.2
Airgap Length (mm)	2	Number of Turns (-)	196
Peak Flux Density (T)	1.6	Wires in Parallel (-)	2

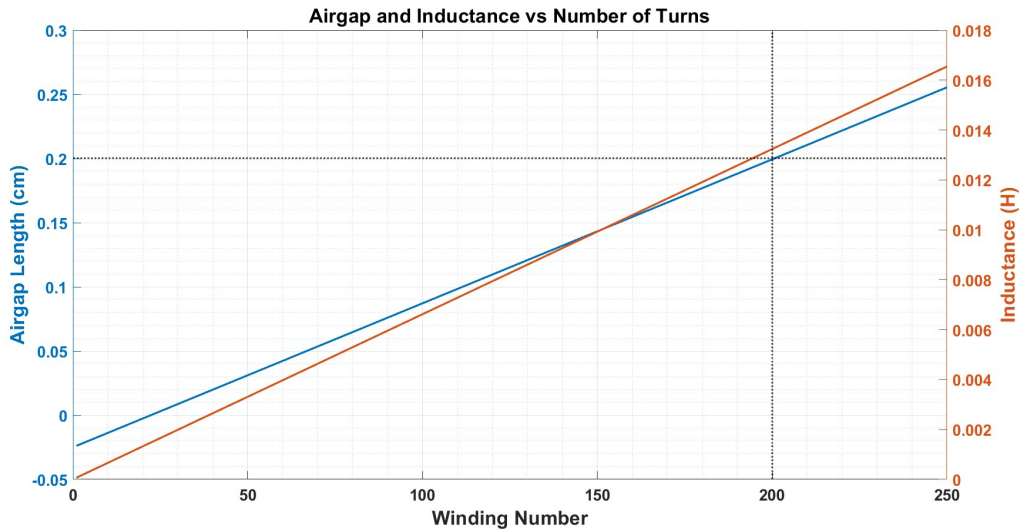


Figure 4.12: Airgap and Inductance vs Number of Turns

## 4.4 Standard Inductor Galvano Electrochemical Impedance Spectroscopy Testing

As a means of characterising an inductor with respects to varying input currents, operational frequency, and current ripple amplitude, without placing it directly into a converter, is possible through the use of Galvano Electrochemical Impedance Spectroscopy (GEIS). During GEIS testing, a constant galvanostatic (current) signal,  $I_s$ , is applied to the inductor's windings, in conjunction with an AC current waveform,  $I_a$ , as per figure 4.13, across various frequencies. The system's voltage is measured, and the impedance,  $Z$ , is calculated. It is then possible to use these values, to calculate the inductance of the inductor, in units of Henry, based on

equation 4.32.

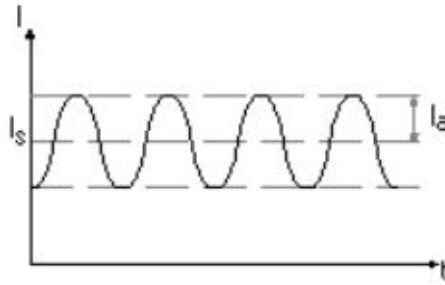


Figure 4.13: GEIS Inductor Current Input Waveform

$$L = \frac{-Z}{2 \cdot \pi \cdot f_{sw}} \quad (4.32)$$

The test equipment used to generate the experimental values, was the University of Nottingham's BioLogic SP-150 potentiostat / galvanostat [124], supplemented by a VMP3B-20 booster [125], to allow for testing at current values greater than the maximum of 1A permitted by the SP-150, alone. The experimental equipment is available in figure 4.14, with the SP-150 placed on top of the VMP3B-20 booster. The Spectroscopy machine is connected to the inductor, quite simply through the use of a "banana plugs" arrangement, and complementing connectors making a positive and negative connection on the terminals of the inductors windings, to complete the circuit.

#### 4.4.1 Galvano Electrochemical Impedance Spectroscopy Test: Inductance vs Current

Using the equipment described above, the experimental results of the GEIS testing, for currents sweeps of 0A to 18A, across frequencies ranging from 100Hz to 1kHz, for the experimental non-biased inductor are generated. In order to ensure that the test equipment did not reach an over load state before producing results, due to the

#### 4.4. STANDARD INDUCTOR GALVANO ELECTROCHEMICAL IMPEDANCE SPECTROSCOPY TESTING

---



Figure 4.14: University of Nottingham's Galvano Electrochemical Impedance Spectroscopy Equipment

impedance, the current ripple,  $I_a$ , was kept to the test equipment's lowest value, this being  $100 \mu A$ , and the frequency of inductors proposed operational value of 20kHz was not considered for these tests; however, this value will still be used for the interleaved buck converter hardware during further validation stages. Impedance will be discussed in the next section, to substantiate the decision making process for the tests completed in this section. The results for a sweep of 0A to 18A at 100Hz are presented in figure 4.15, and presented numerically in table 4.7. The results for the inductor at 100Hz represent the closest quasi-DC values attainable by the test equipment, in a bid to show the changing values of inductance, with current, without the effects of frequency.

#### 4.4. STANDARD INDUCTOR GALVANO ELECTROCHEMICAL IMPEDANCE SPECTROSCOPY TESTING

---

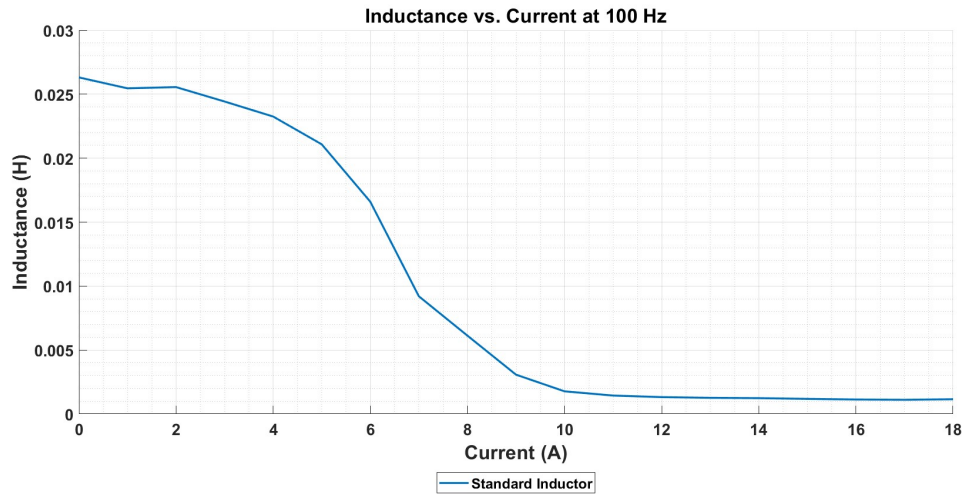


Figure 4.15: Experimental Inductor: Inductance vs Current at 100Hz

One of the first major observations comes from the initial inductance values between 0 and 1 Amps; the inductance value is considerably larger than the values calculated using the inductor sizing methodology; one possible explanation for this is the effects of frequency-dependent permeability of the core, whereby at low frequencies the permeability is higher, relative to the permeability at higher frequencies, due to impedance, core losses and eddy currents. Therefore, at frequency values closer to that of the designed 20kHz operating frequency should yield inductance values closer to those previously calculated; this is also supported by equation 4.32, and will be shown in the next section of the study which deals with frequency dependency. In this scenario however, the absolute value of inductance from the experimental inductor are somewhat irrelevant, as this section of the study is aimed at generating a baseline inductor for subsequent biasing, and re-testing; moreover, the inductance value, is, as before, suitably greater than the critical inductance value required by the converter.

Using both figure 4.15, and table 4.7, it is clear to see that the value of inductance remains stable, within 12% of the original value, across a current values between 0 and 4 Amps. Beyond this point, larger variations between the value of inductance

4.4. STANDARD INDUCTOR GALVANO ELECTROCHEMICAL  
IMPEDANCE SPECTROSCOPY TESTING

Table 4.6: Experimental Inductor: GEIS Experimental Results

Current (A)	Impedance ( $\Omega$ )	Inductance (H)	$\% \Delta L$ from 0A	$\% \Delta L$ from Previous
0	-16.539	0.0263	-	-
1	-16.002	0.0255	-3.24%	-3.24%
2	-16.063	0.0256	-2.89%	+0.38%
3	-15.354	0.0244	-7.16%	-4.41%
4	-14.616	0.0233	-11.63%	-4.81%
5	-13.251	0.0211	-19.88%	-9.34%
6	-10.431	0.0166	-36.93%	-21.28%
7	-5.783	0.0092	-65.03%	-44.56%
8	-3.849	0.00612	-76.72%	-33.43%
9	-1.932	0.00307	-88.32%	-49.82%
10	-1.112	0.00177	-93.28%	-42.45%
11	-0.905	0.00144	-94.53%	-18.61%
12	-0.828	0.00132	-95%	-8.54%
13	-0.794	0.00126	-95.79%	-4.1%
14	-0.777	0.00124	-95.2%	-2.09%
15	-0.742	0.00118	-95.52%	-4.55%
16	-0.71	0.00113	-95.71%	-4.22%
17	-0.696	0.00111	-95.79%	-2.02%
18	-0.724	0.00115	-95.63%	+3.95%

relative to the previous value begin to decrease exponentially, until approximately 11 Amps; this is best visualised using 4.16. This region beyond 4 Amps, to the 11 Amp mark, suggests that the core is entering saturation, as per figure 2.27 from the literature review. The value of inductance, and the relative difference between the inductance values begins to plateau at this point, as the inductor becomes entirely saturated, after reaching the peak of B-H curve.

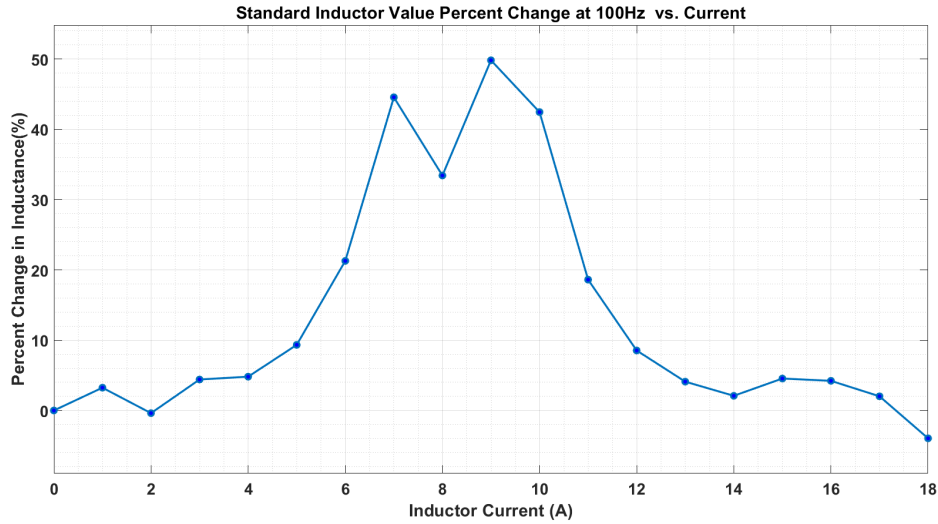


Figure 4.16: Standard Inductor Value Percent Change with Current at 100Hz

From the data sheet of the AMCC-100 core, it is suggested the core is fully saturated, with a flux density,  $B$  at 1.56T. it is indeed possible to determine  $B$  for the various values of current, through equation 4.33, using the experimental values of inductance and current, the magnetic path length, number of turns, and cross sectional area.

$$B_{experimental} = \left( \frac{L \cdot lm}{N^2 \cdot A_c} \right) \cdot \left( \frac{N \cdot I}{lm} \right) \quad (4.33)$$

However, using equation 4.33 in conjunction with the experimental results does not yield the corresponding  $B$  values beyond 6 Amps.

#### 4.4.2 Galvano Electrochemical Impedance Spectroscopy Test: Inductor Losses vs Frequency

Thus far, the models and waveforms of the buck converter which have been presented, only consider 'ideal' inductors, i.e. those which do not exhibit any loss. These losses are considered in this section, and delivered experimentally.

As discussed previously, within the inductor sizing section, it is possible to calculate the resistance of the windings, due to the DC component of the current wave form, and the equation for such is presented below for the reader's convenience as equation 4.34, and using equation 4.35 in conjunction with the current value, it is possible to attain the power losses in the copper windings,  $P_{cu}$ , due to the DC current component.

$$R_{DC} = \frac{MLT \cdot N \cdot \rho_{cu}}{A_W} \quad (4.34)$$

$$P_{cu} = I_{rms}^2 \cdot R_{DC} \quad (4.35)$$

As well as the DC resistance and power losses, it is also necessary to factor in the resistance and subsequent losses due to the AC component of the current waveform.

The combination of these resistances,  $R_{DC}$ ,  $R_{AC}$ , and  $R_{Core}$  [126], are commonly referred to as Equivalent Series Resistance (ESR), and allow for an 'ideal' inductor to be modelled with a resistance in series, which pertains to the loss characteristics of the inductor itself, as per figure 4.17. The  $R_{Core}$  losses arise from a combination of hysteresis and eddy current losses in the core material, while the  $R_{AC}$  losses are a function of skin effects, which force current towards the conductor's surface, thus reducing the conductor's usable cross-sectional area, and proximity effects at higher frequencies, which allow the influence of adjacent turns to induce circulating currents in the windings, increasing the resistance further.

In addition to methods for calculating the losses based on the design parameters of the inductor, it is also possible to calculate the ESR based on impedance,  $Z$ , measurements; for example, from experimental validation of inductor performance.

The impedance,  $Z_L$ , also given in the unit of Ohms, includes both resistance,  $R$ ,

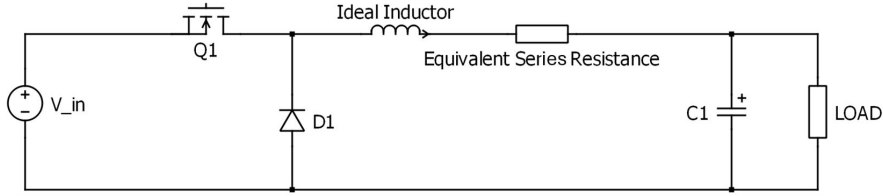


Figure 4.17: Simple Buck Converter with Additional ESR

and inductive reactance,  $X_L$ , and is the the vector sum of the two, as per equation 4.36. It is also possible to express impedance as a complex number, as per equation 4.37, where  $j$ , is the imaginary unit i.e.  $\sqrt{-1}$ . The impedance is complex, due to the fact that the 'real' part of the impedance, given by the  $R$  term, represents energy dissipation, akin a resistor, where as the imaginary part of the impedance, represents the reactive power component, which unlike the 'real' resistance, does not dissipate energy, instead, it stores and returns the energy.

$$Z_L = \sqrt{R^2 + X_L^2} \quad (4.36)$$

$$Z_L = R + jX_L \quad (4.37)$$

The  $X_L$  term for the impedance equation, is given as a positive, specifically for an inductor, and the inductive reactance is dependent on the frequency,  $f_{sw}$  of the AC signal, as shown in equation 4.38. Inversely, when dealing with capacitors, the capacitive reactance,  $X_C$  is dealt with as a negative. It therefore stands to reason that an inductor experiencing a high frequency or an inductor with a high value of inductance, will exhibit greater reactance than the equivalent inductor operating at a lower frequency, or inductor of lower inductance value.

$$X_L = \omega \cdot L \equiv 2 \cdot \pi \cdot f_{sw} \cdot L \quad (4.38)$$

#### 4.4. STANDARD INDUCTOR GALVANO ELECTROCHEMICAL IMPEDANCE SPECTROSCOPY TESTING

Table 4.7: Experimental Inductor: GEIS Experimental Results

Current (A)	100Hz		464Hz		1kHz	
	Impedance ( $\Omega$ )	Inductance (H)	Impedance ( $\Omega$ )	Inductance (H)	Impedance ( $\Omega$ )	Inductance (H)
0	-16.539	0.0263	-71.125	0.0244	-121.33	0.0193
1	-16.002	0.0255	-65.284	0.0224	-125.401	0.0199
2	-16.063	0.0256	-64.989	0.0223	-118.284	0.0188
3	-15.354	0.0244	-65.119	0.0223	-130.171	0.021
4	-14.616	0.0233	-60.538	0.0208	-122.602	0.0195
5	-13.251	0.0211	-58.283	0.0199	-110.131	0.0175
6	-10.431	0.0166	-49.819	0.0171	-107.064	0.0170
7	-5.783	0.0092	-24.883	0.0085	-56.57	0.009
8	-3.849	0.00612	-16.455	0.0057	-38.97	0.0062
9	-1.932	0.00307	-9.043	0.0031	-17.753	0.0028
10	-1.112	0.00177	-5.11	0.0018	-12.146	0.0019
11	-0.905	0.00144	-4.268	0.0015	-10.061	0.0016
12	-0.828	0.00132	-3.822	0.0013	-8.354	0.0013
13	-0.794	0.00126	-3.712	0.0013	-7.713	0.0012
14	-0.777	0.00124	-3.581	0.0012	-7.795	0.0012
15	-0.742	0.00118	-3.388	0.0012	-6.992	0.0011
16	-0.71	0.00113	-3.296	0.0011	-6.765	0.0011
17	-0.696	0.00111	-3.292	0.0011	-6.45	0.001
18	-0.724	0.00115	-3.209	0.0011	-8.327	0.0013

Having previously examined the GEIS results for the 100Hz near DC test, additional frequencies, at 464Hz, and 1kHz are presented in figure 4.18. As suggested by equation 4.38 and 4.32, the additional frequency has the effect of lowering the initial inductance value, However, at 6 Amps, all of the inductors converge on the same inductance value, as the inductors core begins to saturate.

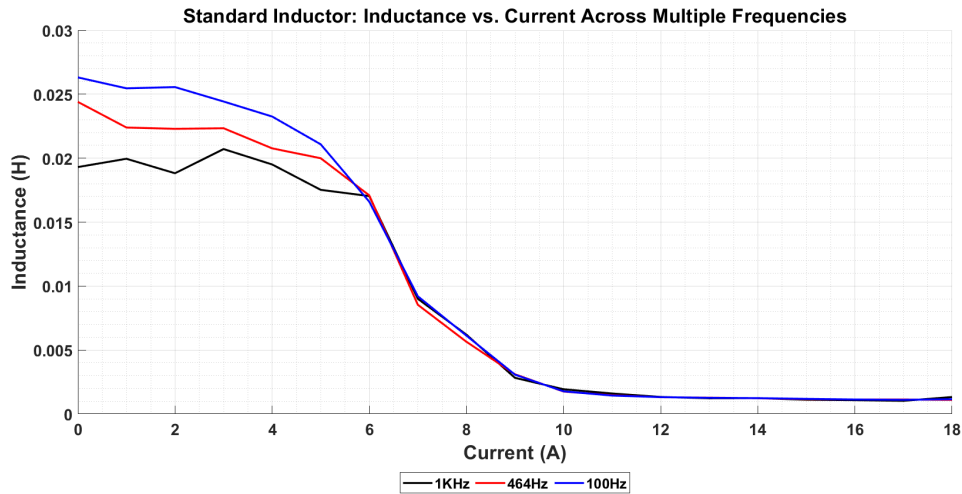


Figure 4.18: Standard Inductor Inductance Values Across Multiple Frequencies

From table 4.7, it can be observed that the increase in frequency, translates into an increase in the impedance values, due to the proportional relationship of inductive reactance,  $X_L$  to frequency. Table 4.7 also shows that as the inductor heads towards saturation, the impedance begins to decrease for all frequency cases, as the core's

permeability,  $\mu$  begins to reduce, this in effect causes a decrease in the effective inductance, which in turn reduces the inductive reactance, as the proportional frequency component is constant, but the proportional inductance component reduces, as per equation 4.38.

### 4.4.3 Galvano Electrochemical Impedance Spectroscopy Test: Summary

In summary the GEIS testing has permitted the exploration of the standard experimental inductor under consideration of various operating frequencies, and current conditions, for the determination of inductance versus current, and inductance versus frequency. The results of the test have also proven a 'mismatch' between the calculated values for the inductor value derived from the equations of [84], and experimental values. As the inductance value remains at a value which is considerably larger than the critical inductance value determined during the buck converter sizing.

## 4.5 Interleaved Buck Converter Inductor Simulations with Closed Loop Control

In order to achieve higher fidelity modelling of the inductors within the converter simulations, it is necessary to expand upon the 'simple inductor block' presented in any previous diagrams, and used for any simulations previously shown, with a view to expanding into a model which is more akin to a Magnetic Equivalent Circuit (MEC).

The MEC, which is analogous to an electrical circuit with respects to the use of

4.5. INTERLEAVED BUCK CONVERTER INDUCTOR SIMULATIONS  
WITH CLOSED LOOP CONTROL

---

resistors, and voltage / current sources, decomposes the 'simple inductor block' into the physical inductor's reluctance,  $\mathfrak{R}$ , including that of the core material,  $\mathfrak{R}_{Core}$ , and any airgaps,  $\mathfrak{R}_{airgap}$ , as well as any Magnetomotive Force (MMF) sources,  $F$ , which as the project expands will come from both the inductor windings and, an opposing  $F$ , from the permanent magnets. A representative example of the MEC is provided in figure 4.19b., and is based on simple inductor diagram shown in figure 4.19a. which comprises of a winding of ' $N$ ' turns, a ferromagnetic core, and an airgap.

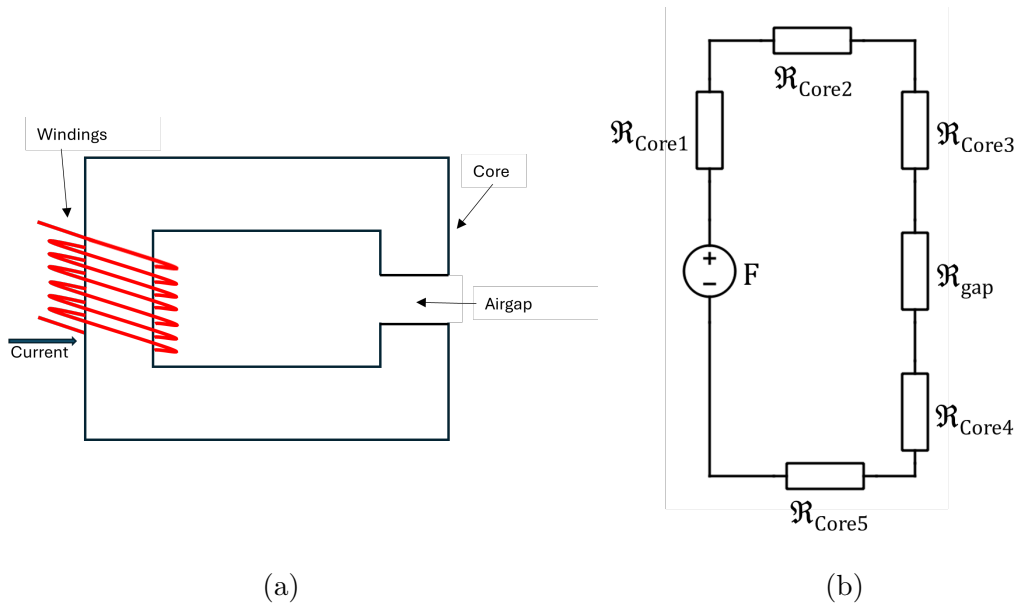


Figure 4.19: a) Simple Inductor Diagram. b) Magnetic Equivalent Circuit for Inductor presented in a.

One of the key advantages to the MEC is that with some known parameters, such as number of turns, which in this study are taken from the inductor design stage, the relative unsaturated permeability of the core's material,  $\mu_r$ , the core's saturated relative permeability, and the core dimensions, it is possible to determine the following:

- $\phi$  - Magnetic flux within the core; given in Webbers,  $Wb$  .
- $B$  - Magnetic flux density with in the core; given in Tesla,  $T$ .
- $H$  - Magnetic field intensity; given in Amp Turns,  $At$ .

- $F$  - Magnetic Motive Force; given in Amps,  $A$ .

The total reluctance of the core can be found through the sum of the individual core reluctance; for the inductor described by figure 4.19, this would be  $\mathfrak{R}_{Core} = \mathfrak{R}_{Core1} + \mathfrak{R}_{Core2} + \mathfrak{R}_{Core3} + \mathfrak{R}_{Core4} + \mathfrak{R}_{Core5}$ . The sum of the reluctance should also reflect the total mean magnetic path length,  $l_m$ , of the core. The core reluctance is then given by equation 4.39.

$$\mathfrak{R}_{core} = \frac{l_m}{\mu_r \cdot \mu_0 \cdot A_c} \quad (4.39)$$

Where:  $\mu_0$  = Permeability of free space, a constant given as  $4 \cdot \pi \cdot 10^{-7}$

It is possible to determine the airgap reluctance, with minor modifications to equation 4.39, this being the magnetic path length being replaced with the length of the airgap,  $l_g$ , and the removal of the relative permeability term, as now, the medium for the magnetic flux to pass through, is quite simply, free space. As with the inductor sizing process, the airgap cross section,  $A_g$ , is modified to account for any fringing; this is taken care of through equation 4.41, using the core geometry notation discussed in the inductor sizing section. The modified equation is presented in equation 4.40

$$\mathfrak{R}_{airgap} = \frac{l_g}{\mu_0 \cdot A_g} \quad (4.40)$$

$$A_g = \frac{((a + l_g) \cdot (d + l_g))}{(a \cdot d)} \quad (4.41)$$

For the MMF,  $F$ , term, this can be described as the product of the number of turns on the inductor's winding, multiplied by the applied current, or alternatively, using the magnetic terms, as the flux multiplied by the reluctance, as per equation 4.42.

$$F = N \cdot I \equiv \phi \cdot \mathfrak{R}_{total} \quad (4.42)$$

The PLECS simulation package has a number of programmable magnetic components, which have the ability to be integrated into an electrical circuit, such as the proposed interleaved buck converter. Further details regarding the development of the blocks, and pre-programmed fitting functions can be found in [127]. The ideal inductor cores are removed, in favor of the MEC equivalent circuits. An example of the experimental inductor when constructed from the programmable magnetics blocks is shown in figure 4.20. It can be observed that the winding, which sets up,  $F$ , is split, and connected in series, with half of the 196 turns on each coil; this is to ensure that the airgap is placed between the coils, as it would be in the practical inductor. It is important to also note the use of the reluctance blocks, which will be used to represent the reluctance of each half of the core, on either side of the airgap, and the value for this is given by equation 4.39. The ESR is also placed in series with the inductor's windings, with the value given by the inductor design phase; this value is given as 1.091 Ohms. Input parameters for the saturable core, and airgap blocks, are described in table 4.8 and 4.9 respectively.

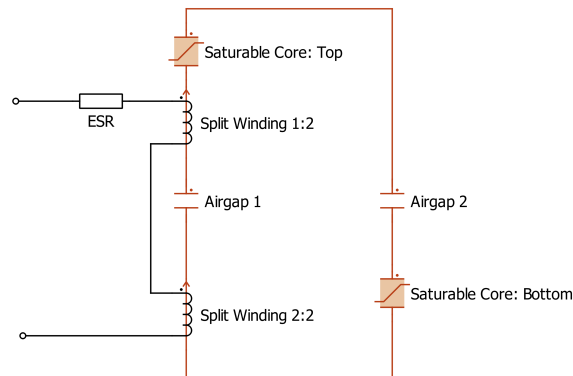


Figure 4.20: Single Inductor MEC Representation in PLECS Magnetics Blocks

Simulations are designed to align with the testing undertaken for the GEIS, where by the current is stepped up, in one Amp increments, at the inductor; these tests are

4.5. INTERLEAVED BUCK CONVERTER INDUCTOR SIMULATIONS  
WITH CLOSED LOOP CONTROL

---

Table 4.8: Saturable Core Input Parameters

Parameter	Value
Fitting Function	atan
Cross-sectional Area [m <sup>2</sup> ]	0.000591
Length of Flux Path [m]	0.125
Unsaturated Relative Permeability	3000
Saturated Relative Permeability	1
Flux Density at Saturation	1.56

Table 4.9: Airgap Input Parameters

Parameter	Value
Cross-sectional Area [m <sup>2</sup> ]	(0.016+0.005)*(0.045+0.005)
Length of Flux Path [m]	0.001

also to demonstrate the closed loop functionality, to maintain the output voltage at 28V, and within the limits of the MIL-STD requirements, presented previously. However, PLECS does not appear to have anyway of directly calculating the inductance, based on the magnetic circuit. It is possible however, to assess saturation based on an average reading of the flux density, and relating the measured value to the saturation flux density given by the data sheet, to yield a percent saturation per amp increment. It is worth noting that PLECS does have the ability to generate a B-H curve, using the probe blocks, however this does not provide sufficient details for reasonable analysis. The final results for the flux density of the MEC inductors within the closed loop simulation of the interleaved buck converter, are given in table 4.10. It is also possible to observe the flux waveform and output voltage for a converter load of 2 Amps, in figure F.12. The remainder of the results are presented in the appendix, for both completeness, and evidence of the work done. Note from figure F.12b. that the voltage is within the MIL-STD requirements.

The data presented in 4.10, as a stand alone set of value provide little information. To this end, and to make a comparison of the simulations against the physical non-biased inductor, the data for such at 1kHz was normalised against itself. This implies that as the current is stepped, the value of inductance is related to its initial

#### 4.5. INTERLEAVED BUCK CONVERTER INDUCTOR SIMULATIONS WITH CLOSED LOOP CONTROL

Table 4.10: PLECS MEC Inductor Simulation Results

Load Current (A)	Inductor Current (A)	Load Resistance ( $\Omega$ )	Average Flux Density (T)	% Saturation Relative to $B_{sat}$
2	1	14	0.211	13.52%
4	2	7	0.405	25.96%
6	3	4.6	0.614	39.36%
8	4	3.5	0.797	51.09%
10	5	2.8	0.983	63%
12	6	2.3	1.158	74.23%
14	7	2	1.279	81.99%
16	8	1.75	1.372	87.95%
18	9	1.5	1.443	92.5%
20	10	1.4	1.46	93.59%
22	11	1.27	1.484	95.12%
24	12	1.16	1.5	96.15%

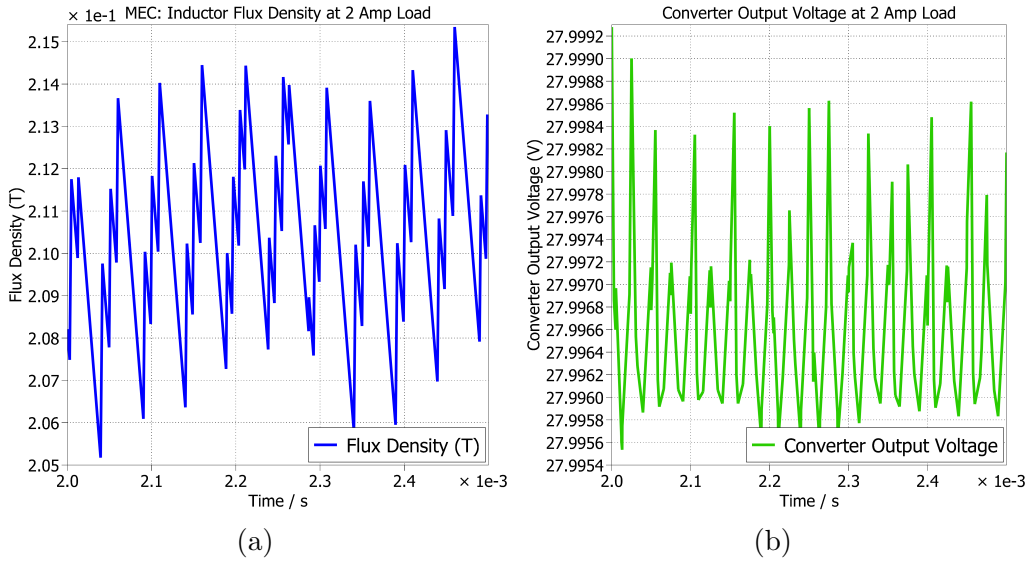


Figure 4.21: a) MEC Inductor Flux Density Waveform at converter Load of 2 Amps  
b) Output Voltage Waveform for Converter Load of 2 Amps

value to give a percent of the saturation, whereby at 0 Amps, the saturation would be 0%, and each step in current would then be a percent reduction of this initial value. These results are then placed against the results of saturation percentage of the simulated inductor for comparison. This data is presented in table 4.11.

As the results suggest, there is little confidence between the values. The simulated inductor saturates considerably earlier than the experimental inductor, achieving approximately 50% saturation at a converter load of 8 Amps, relative to the 14 Amps, for a similar saturation value of the experimental inductor. It has to be appreciated that PLECS, is not specifically designed for work on magnetics, and lends itself more the the simulation of electronics, and thermal losses.

4.5. INTERLEAVED BUCK CONVERTER INDUCTOR SIMULATIONS  
WITH CLOSED LOOP CONTROL

Table 4.11: PLECS Inductor Saturation Vs Experimental Inductor Saturation

Load Current (A)	PLECS Inductor % Saturation Relative to $B_{sat}$	Experimental % Saturation Relative to $B_{sat}$	$\Delta\%$
2	13.52%	+3.36%	16.88%
4	25.96%	2.51%	23.45%
6	39.36%	+7.28%	46.64%
8	51.09%	+1.05%	52.14%
10	63%	9.23%	54%
12	74.23%	11.76%	62.47%
14	81.99%	53.37%	28.62%
16	87.95%	67.88%	20.07%
18	92.5%	85.37%	7.13%
20	93.59%	89.99%	3.6%
22	95.12%	91.71	3.41%
24	96.15%	93.11%	3.04%

The idea for modelling the inductor as a MEC, was two fold. In addition to simulating the standard inductor, initial attempts were made to use the PLECS magnetics package in a novel manner, and implement a biased inductor, through the magnetic blocks, as per figure 4.22, which shows a coil, with a current source, acting in opposition to the coils of the inductor winding; this simulated electro-magnet would represent the biasing permanent magnets, and set up a biasing flux, in the opposite direction to the flux from the main inductor windings. However, PLECS does not have the capacity to compute such a simulation without experiencing difficulty, and does not yield any practical, or reasonable results. Based on this, the author attempted to use the ANSYS FLUENT, Finite Element Analysis package to simulate the inductor, in both a standard configuration and a biased configuration. Figure 4.23a. shows initial efforts to simulate a generic inductor, with a simple core and a winding, to assess the the saturation flux, and 4.23b. shows the same inductor, with an N38 grade permanent magnet placed on the exterior, with the resulting flux augmented away from the central leg. the Finite Element Analysis approach appeared to accept the biasing flux within the core, however, due to severe time constraints for the project, a full analysis to represent the experiments of the GEIS could not be taken further; this will be a point for future work in the conclusions

#### 4.5. INTERLEAVED BUCK CONVERTER INDUCTOR SIMULATIONS WITH CLOSED LOOP CONTROL

section.

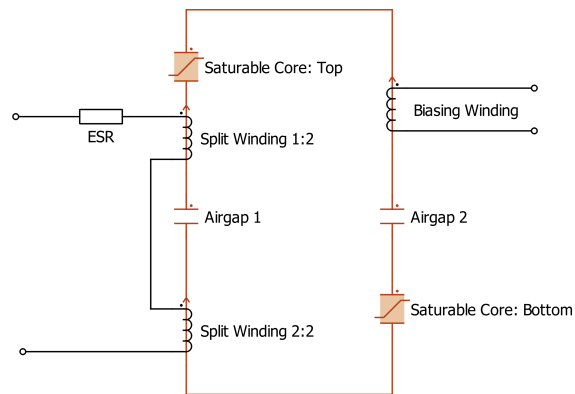


Figure 4.22: Single Inductor MEC Representation in PLECS Magnetics Blocks with Bias Winding

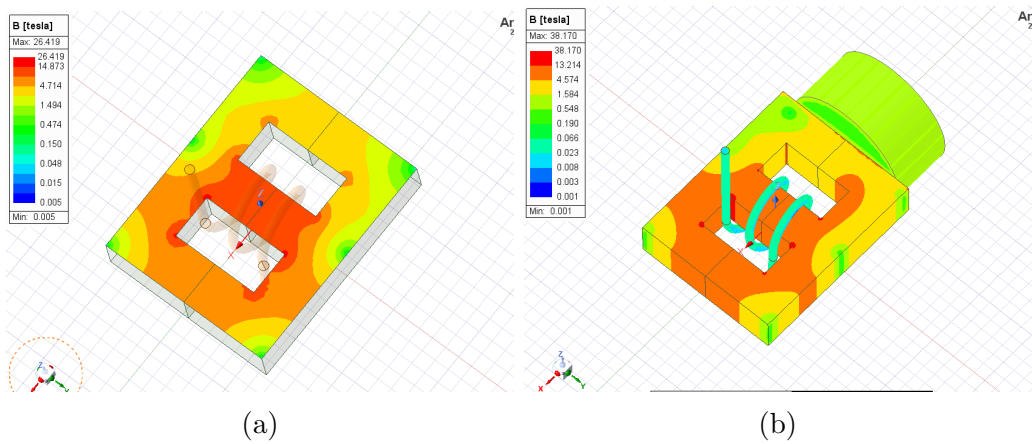


Figure 4.23: Preliminary FEA Investigations a) Inductor Core with Winding. b) Inductor Core with Winding and Biasing Magnet

---

## Chapter 5

# Biased Magnetics For Interleaved Converters

In a bid to reduce the mass and volume of most heavy and voluminous components of the DC-DC converters onboard the aircraft, this author suggests the implementation of biased magnetics; as discussed in the literature review.

From the literature review, it was stated that the topology described within the patent, given by [1] is of particular interest. The comprehensive review paper from [86], which goes into great detail regarding various topologies and arrangements of PMBI, only mentions the patent, rather than discussing it, and there is no supporting research to demonstrate any potential advantages of this topology, or mention of an application in which it has been implemented. This section aims to investigate this topology, and leverage the benefits of biasing a pair of inductor cores, with the same pair of permanent magnets by taking advantage of the interleaving methodology for power converters. This combination of features is novel, and potentially allows for reductions in mass and volume, as well as increases in efficiency for DC-DC converters. Additional novelty was sought, through the adaptation of the topology from the patent, with the addition of permanent magnets placed

---

within the air gap, to support both the biasing flux, and to create a continuous magnetic flux path for the biasing magnets placed between the two inductor cores, and hence the prerequisite discussed earlier for the larger air gaps, to accommodate the thickness of commercially available magnets. The image in figure 5.1 supports the description above, and shows how the proposed topology differs from that of the topology from the patent.

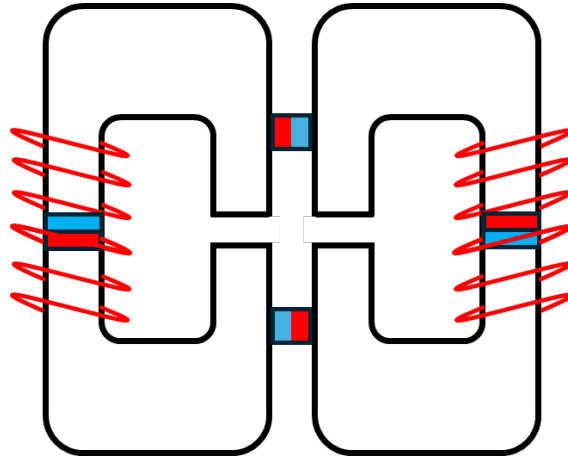


Figure 5.1: Proposed Biased Inductor with Airgap Magnets, and Side Mounted Biasing Magnets

When testing the inductor topology, solely with the magnets placed within in the air gap, this proved to be mechanically disadvantageous, due to the effects of demagnetisation, observed by the magnets after each test, potentially due to the currents forcing the magnets past the knee point on the extrinsic curve of the demagnetisation curve, and affecting the final remanent flux of the magnets when the current is removed from the windings. Based on this, and the potential for non-consistent data, the topology was discounted from any further studies; however, the results are given in the appendix section of this report, to highlight the initial benefits of placing magnets within the air gaps, although no official analysis is undertaken.

In order to achieve, and explore the topology given in [1], an initial set of tests was proposed, to be conducted on the GEIS test equipment, under identical conditions to those conducted previously, in order to experimentally determine any benefits, relative to the standard inductor.

Table 5.1: Magnetic Properties of the N52 Neodymium Material used in the Experimental Inductor

Remanence ( $B_r$ ), (T) min.-max.	Coercive Force ( $H_{cB}$ ), (kA/m) min.	Intrinsic Coercivity ( $H_{cJ}$ ), (kA/m) min.	Max Energy, Magnetic ( $BH_{max}$ ), (kJ/m <sup>3</sup> ) min-max.
1.43-1.47	$\geq 876$	$\geq 875$	398-422

The variable between each test, was the quantity of magnets, placed between the two inductor cores, forming what is colloquially referred to here, as a magnetic bridge, which forms a complete magnetic circuit between the two cores, as per figure 5.2a. These tests used commercially available magnets, in the form of N52 Neodymium block magnets, of dimensions 20mm length, 15mm width, and 5 mm in thickness; The magnetic properties of the N52 material are available in table 5.1.

The various combinations of magnetic bridge used for the tests, are termed as 1S2P, 2S2P, 3S2P, 4S2P, 5S2P, where 'S' represents the number of magnets in series to bridge the cores, and the actual number of magnets used is double this, as there is a requirement for a top and bottom bridge, to complete the magnetic circuit; this can be observed in figure 5.2c. The 'P' term refers to the number of magnets in parallel, and this is held constant, due to the limited space on the 'd' dimension of the AMCC-100 core, this is shown in figure 5.2b.; therefore with a '2P' configuration, the magnetic area per bridge is given in absolute terms as the magnet length and width multiplied by two.

The biasing of magnetics to increase converter power density, and reduce converter volume, as well as being a scientific endeavor, is also rooted in requirements to consider the use of rare earth materials, such as the Neodymium mentioned previously, and also commercial considerations, in regards to cost. Based on this, table 5.2 has been developed to show the costs, and dimensions of the configurations, which will be compared with the results of the GEIS testing. Each magnet has a mass of 0.0111kg, and a unit cost of £5.60. Increasing the length of the bridge has the

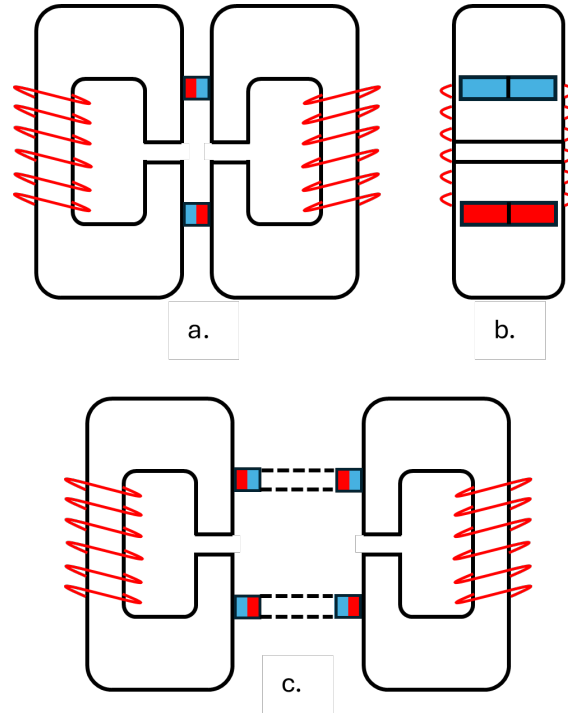


Figure 5.2: Experimental Inductor: Bias scheme with 'n' magnets in series and parallel

Table 5.2: Configuration Parameters for Experimental Inductor

Configuration	Total Magnets	Bridge Length (mm)	Bridge Mass (kg)	Bridge Cost (£)	Boxed Volume mm <sup>3</sup>
1S2P	4	5	0.0444	£22.4	343350
2S2P	8	10	0.0888	£44.8	359100
3S2P	12	15	0.1332	£67.2	374850
4S2P	16	20	0.1776	£89.6	390600
5S2P	20	25	0.222	£112	406350

effects of increasing the 'boxed' volume of the overall biased cores package, and the volumes to describe each topology, excluding the windings, are also included in table 5.2, and will be used to assess the relationship between biasing and volume. Each core has a length of 70mm, a width of 52mm and a depth of 45mm, hence a volume of 163800mm<sup>3</sup> each, and the combination of the two, yields a core volume of 327600mm<sup>3</sup>; the magnetic bridge length extends the 'boxed'; volume of the two cores.

## 5.1 Biased Inductor Galvano Electrochemical Impedance Spectroscopy Testing

Repeating the GEIS testing from the previous section, with the biased inductors described above, in place of the standard, non-biased inductor, a series of new data sets was created, and can be viewed in figure 5.3, for the 100Hz quasi-DC frequency. The standard inductor is included within the plot to allow for easy visual reference of the immediate benefits of biasing the inductor cores, and acts as the baseline for a comparison of the results.

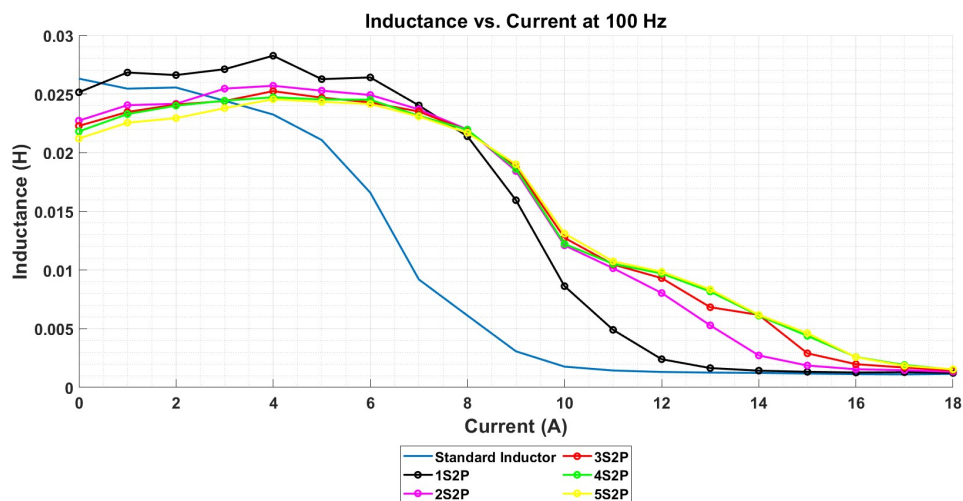


Figure 5.3: Experimental Biased Inductors: Inductance vs Current at 100Hz

Using the standard inductor as a baseline, the percent differences in inductance value per amp, are presented in table 5.7, and can be visualised in figure 5.4. As shown in figure 5.4, the inductance percent difference relative to the baseline, remain relatively consistent between 0 Amps and 8 Amps. However, beyond 8 Amps, the 1S2P configuration deviates from the the other configurations, due to the biasing flux beginning to be exceeded by the magnetising flux of the coils. This results in the flux density, reaching the low permeability region of the BH curve, and heading towards saturation. The remaining configurations, remain in close agreement, until approximately 9 Amps, beyond which, each configuration

5.1. BIASED INDUCTOR GALVANO ELECTROCHEMICAL IMPEDANCE SPECTROSCOPY TESTING

begins to diverge. Notably, between 12 Amps and 18 Amps, there is decrease in the inductance percent difference relative to the baseline, which occurs sequentially, as the number of magnets in the magnet bridge increase. For instance the 2S2P configuration reaches saturation before the 3S2P configuration and so forth.

This variation in the percent change among the different configurations, can be explained using the MEC theory, introduced earlier. While the 5S2P configuration exhibits greater reluctance, due to the magnetic length,  $l_m$ , being increased by a factor of five, for a single bridge, it also benefits from an increased MMF, as described by equation 5.1. Here,  $H_m$  represents the magnet field intensity, and this MMF contributes to the biasing flux,  $\phi_{bias}$ , which can be determined using the bridge reluctance,  $\mathfrak{R}_{bridge}$ , based on equation 5.2.

$$F_{magnet} = H_m \cdot l_m \quad (5.1)$$

$$\phi_{bias} = \frac{F_{magnet}}{\mathfrak{R}_{bridge}} \quad (5.2)$$

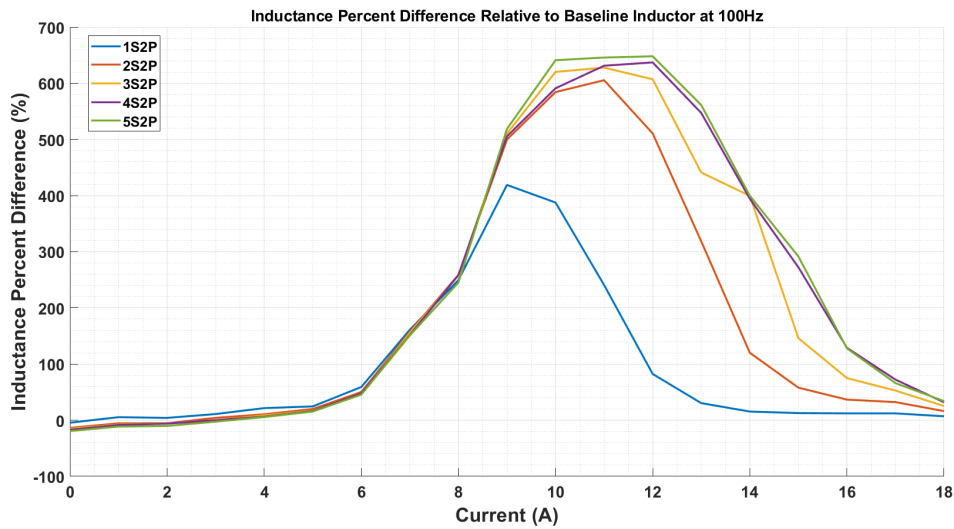


Figure 5.4: Experimental Biased Inductors: Inductance Percent Difference Relative to Baseline Inductor at 100Hz

5.1. BIASED INDUCTOR GALVANO ELECTROCHEMICAL IMPEDANCE  
SPECTROSCOPY TESTING

---

Table 5.3: Inductance Percent Change Relative to Increase in Magnet Count per Amp

Current (A)	1S2P	2S2P	3S2P	4S2P	5S2P
0	-4.42%	-13.61%	-15.31%	-17.09%	-19.39%
1	+5.4%	-5.53%	-7.81%	-8.51%	-11.39%
2	+4.15%	-5.43%	-5.67%	-6.05%	-10.22%
3	+11%	+4.22%	-0.1%	0%	-2.59%
4	+21.55%	+10.54%	+8.57%	+6.33%	+5.61%
5	+24.6%	+19.95%	+17.12%	+16.41%	+15.43%
6	+59.17%	+50.16%	+46.39%	+47.72%	+45.5%
7	+161.17%	+157.55%	+155.51%	+151.61%	+150.98%
8	+249.42%	+258.81%	+257.64%	+258.61%	+245.2%
9	+419.09%	+499.95%	+510.57%	+505.56%	+518.78%
10	+387.71%	+584.45%	+620.41%	+591.22%	+641.23%
11	+240.82%	+605.6%	+627.96%	+631.41%	+645.97%
12	+82.37%	+510.87%	+607.27%	+637.28%	+648.2%
13	+30.43%	+318.65%	+441.19%	+547.28%	+561.33%
14	+15.43%	+120.18%	+399.79%	+394.44%	+399.79%
15	+12.7%	+57.99%	+146.19%	+272.46%	+291.69%
16	+12.17%	+36.67%	+75.07%	+128.97%	+127.86%
17	+12.21%	+32.29%	+52.78%	+72.31%	+66.04%
18	+6.99%	+16.17%	+25.27%	+31.88%	+34.02%

Using figure 5.3 as a visual reference, it is evident that the addition of magnets to the circuit yields diminishing returns. Table 5.4, which presents the percent change in inductance relative to the 1S2P configuration. However, a more comprehensive approach, is considered, integrating the improvements made to the baseline inductor, while enabling assessment of diminishing returns.

The baseline inductor remained within approximately 12% of its initial inductance value, between 0 Amps and 4 Amps. Accordingly, the biased configurations are evaluated under the same criterion, comparing each configuration to its own initial inductance, rather than to the baseline inductor. The approach allows for the determination of the current beyond 4 Amps, at which the inductor begins to saturate, permitting for useful inferences regarding any performance improvements. If the 12% reduction point falls between two current values, the midpoint is taken as the transition threshold.

5.1. BIASED INDUCTOR GALVANO ELECTROCHEMICAL IMPEDANCE  
SPECTROSCOPY TESTING

---

Table 5.4: Inductance Percent Change Relative to 1S2P Configuration per Amp

Current (A)	1S2P	2S2P	3S2P	4S2P	5S2P
0	-	-9.62%	-11.39%	-13.25%	-15.66%
1	-	-10.38%	-12.53%	-13.21%	-15.94%
2	-	-9.19%	-9.43%	-9.79%	-13.79%
3	-	-6.1%	-10%	-9.89%	-12.24%
4	-	-9.06%	-10.68%	-12.53%	-13.11%
5	-	-3.74%	-6%	-6.58%	-7.37%
6	-	-5.66%	-8.03%	-7.91%	-8.57%
7	-	-1.39%	-2.16%	-3.66%	-3.9%
8	-	+2.69%	+2.35%	+2.63%	+1.37%
9	-	+15.58%	+17.62%	+16.66%	+19.21%
10	-	+40.34%	+47.71%	+41.73%	+51.98%
11	-	+107.03%	+113.59%	+114.60%	+118.88%
12	-	+234.96%	+287.82%	+304.28%	+310.26%
13	-	+220.97%	+314.92%	+396.26%	+407.03%
14	-	+90.76%	+332.99%	+328.36%	+332.99%
15	-	+40.18%	+118.44%	+230.48%	+247.54%
16	-	+21.84%	+56.08%	+104.12%	+103.14%
17	-	+12.87%	+30.34%	+47.01%	+41.66%
18	-	+8.58%	+17.08%	+23.26%	+25.26%

Table 5.5: Experimental Biased Inductors: Biasing Improvements Relative to Baseline Inductor

Configuration	Current at 12% L Decrease (A)	% Current Increase From Baseline	% Current Increase From 1S2P
1S2P	7.5	+87.5%	-
2S2P	8.5	+112.5%	+13%
3S2P	8.5	+112.5%	+13%
4S2P	8.5	+112.5%	+13%
5S2P	9	+125%	+20%

Table 5.5 presents the current levels at which the inductance of each configuration decreases to approximately 12% of its initial inductance value. Additionally, it quantifies the percent increase, in current relative to both the baseline, non-biased inductor, as well as the 1S2P configuration.

As shown in the table, the minimum number of magnets required to establish a bias (1S2P), results in a substantial 87% increase in the current threshold, before reaching the equivalent saturation point of the non-biased inductor. The data also indicates a plateau between the 2S2P and 4S2P configurations, where the equiva-

*5.1. BIASED INDUCTOR GALVANO ELECTROCHEMICAL IMPEDANCE  
SPECTROSCOPY TESTING*

---

Table 5.6: Experimental Biased Inductors: Energy Product, Cost, Mass and Volume per Additional Amp Data

Configuration	£/Additional Amp (£)	mass/Additional Amp (kg)	Volume/Additional Amp (mm <sup>3</sup> )	Energy Product (J)
1S2P	6.4	0.0127	4500	0.654
2S2P	£9.95	0.0197	7000	0.84
3S2P	14.93	0.0296	10500	0.84
4S2P	19.91	0.0395	14000	0.84
5S2P	22.4	0.0444	15750	0.942

lent saturation currents are equivalent, at 8.5 Amps. This corresponds to a 112.5% increase in current capacity, before reaching saturation, relative to the non-biased equivalent, but only a 13% improvement, when compared to the 1S2P configuration. The final configuration, 5S2P, exhibits the most significant improvement, reaching 9 Amps, before experiencing a 12% decline in inductance. This represents a 125% increase relative to the non-biased inductor; however, the gain over the 1S2P configuration is limited to 20%.

These results can be further analysed in terms of cost, mass and volume per additional amp. Additionally, the energy product for the biased cores is determined by combining the non-biased inductor's inductance at the 12% reduction threshold, with the corresponding saturation currents of the biased configurations, providing further insights into any additional performance improvements, and an element of competition between the configurations, to determine the optimum candidate to take forward into the experimental buck converter. This information is provided in table 5.6.

Based on the data from table 5.6, the 1S2P configuration demonstrated the highest cost, mass and volume efficiency; however, it also exhibits the lowest energy product among all the configurations. The 2S2P configuration provides a balanced trade-off, offering an additional 112.5% increase in current capacity, while incurring a 50% increase in cost per additional Amp, a 52.1% increase in mass per additional Amp, and a 55.5% increase in volume per additional Amp. Additionally, it achieves a 28.4% increase in energy product, when compared to the 1S2P configuration.

*5.1. BIASED INDUCTOR GALVANO ELECTROCHEMICAL IMPEDANCE  
SPECTROSCOPY TESTING*

---

Table 5.7: Inductance Percent Change Relative to Standard Non-Biased Inductor per Amp

Current (A)	1S2P	2S2P	3S2P	4S2P	5S2P
0	-4.42%	-13.61%	-15.31%	-17.09%	-19.39%
1	+1.98%	-8.6%	-10.79%	-11.48%	-14.27%
2	+1.15%	-8.15%	-8.39%	-8.75%	-12.8%
3	+3.05%	-3.24%	-7.26%	-7.14%	-9.57%
4	+7.42%	-2.31%	-4.06%	-6.03%	-6.67%
5	-0.17%	-3.9%	-6.16%	-6.73%	-7.52%
6	+0.39%	-5.29%	-7.67%	-6.82%	-8.21%
7	-8.68%	-9.95%	-10.66%	-12.02%	-12.24%
8	-18.67%	-16.48%	-16.75%	-16.53%	-17.55%
9	-39.37%	-29.93%	-28.69%	-29.27%	-27.73%
10	-67.22%	-53.99%	-51.58%	-53.54%	-50.18%
11	-81.36%	-61.4%	-60.18%	-59.99%	-59.19%
12	-90.88%	-69.43%	-64.61%	-63.11%	-62.56%
13	-93.74%	-79.91%	-74.03%	-68.94%	-68.27%
14	-94.58%	-89.66%	-76.52%	-76.77%	-76.52%
15	-94.95%	-92.92%	-88.96%	-83.3%	-82.44%
16	-95.18%	-94.13%	-92.48%	-90.17%	-90.21%
17	-95.07%	-94.43%	-93.57%	-92.75%	-93.01%
18	-95.32%	-94.91%	-94.52%	-94.23%	-94.14%

The 3S2P and 4S2P configurations exhibit diminishing returns in energy product, despite the associated increase in cost, mass and volume. This suggests that beyond a certain threshold, the addition of extra magnets, does not yield proportional performance improvements. Finally, while the 5S2P configuration achieves the highest energy product, it also imposes the greatest penalties with regard to cost, mass and volume. As a result, this configuration is most suitable for applications where mass or volume aren't critical attributes.

Building on the improvements observed in the experimental results, the findings can be related back to the literature review, specifically the Bias Improvement Factor (BIF) as described by [85]. This concept allows for theoretical adaptations of the inductor by modifying key design parameters, such as the core cross-sectional area,  $A_c$ , number of turns,  $N$ , or current handling capacity.

For clarity, the equations defining the BIF are repeated below for the reader's

5.1. BIASED INDUCTOR GALVANO ELECTROCHEMICAL IMPEDANCE  
SPECTROSCOPY TESTING

---

Table 5.8: Inductance Percent Change Relative to Increase in Magnet Count per Amp

Current (A)	1S2P	2S2P	3S2P	4S2P	5S2P
0	-	-9.62%	-11.39%	-13.25%	-15.66%
1	-	-4.37%	-6.67%	-7.39%	-10.3%
2	-	-3.9%	-4.15%	-4.53%	-8.76%
3	-	+1.24%	-2.96%	-2.84%	-5.38%
4	-	+2.21%	+0.39%	-1.69%	-2.34%
5	-	+0.59%	-1.81%	-2.42%	-3.24%
6	-	-0.91%	-3.4%	-2.51%	-3.96%
7	-	-5.78%	-6.52%	-7.95%	-8.18%
8	-	-12.62%	-12.9%	-12.66%	-13.74%
9	-	-26.68%	-25.39%	-25.99%	-24.38%
10	-	-51.86%	-49.33%	-51.38%	-47.87%
11	-	-59.61%	-58.33%	-58.14%	-57.30%
12	-	-68.02%	-62.97%	-61.4%	-60.83%
13	-	-78.98%	-72.83%	-67.5%	-66.8%
14	-	-89.17%	-75.43%	-75.69%	-75.43%
15	-	-92.59%	-88.45%	-82.71%	-81.62%
16	-	-93.86%	-92.13%	-89.71%	-89.76%
17	-	-94.18%	-93.27%	-92.41%	-92.69%
18	-	-94.68%	-94.27%	-93.96%	-93.87%

convenience. However this study proposes modifications to the original methodology to better align with the experimental results.

$$BIF = \frac{\Delta B_{PMBI}}{\Delta B} = \frac{B_{bias} + B_{sat}}{B_{sat}}$$

$$L \cdot I_{max,PMBI} = \frac{B_{sat} \cdot A_c \cdot N}{BIF}$$

Rather than using the flux density differentials ( $\Delta B$  and  $\Delta B_{PMBI}$ ), it is proposed that the saturation threshold currents of the standard and biased inductor are to be used instead. These values, denoted as  $I_{max,standard}$  and  $I_{max,biased}$ , provide a more direct experimental approach. The biased maximum current,  $I_{max,biased}$ , is calculated using equation 5.3, which incorporates the experimentally determined percent increase in current handling capability. Subsequently, equation 5.4 is used

Table 5.9: Bias Improvement Factor for each Experimental Inductor Topology

Topology	BIF
1S2P	1.87
2S2P	2.125
3S2P	2.125
4S2P	2.125
5S2P	2.25

to compute the BIF, based on the measured values. The BIF for each of the various topologies from the experimental data, are shown in table 5.9.

$$I_{max,bias} = I_{max,standard} \cdot (1 + \%I_{Improvement}) \quad (5.3)$$

$$BIF = \frac{I_{max,bias}}{I_{max,standard}} = \frac{I_{max,standard} \cdot (1 + \%I_{Improvement})}{I_{max,standard}} \quad (5.4)$$

With the BIF determined for each topology, it is now possible to evaluate theoretical adaptations of the inductor by modifying key design parameters based on the  $LI$  product equation, presented in the literature review. Rather than presenting absolute values for the inductor, the results are expressed as a percentage of a normalised reference value, when the full BIF is allocated to a single design parameter.

The proportional changes in each design parameter, when adjusted, relative to the non-biased inductor's baseline design parameters, provide insight into how performance can be synthesised to match that of the standard non-biased inductor. These proportional reductions are summarised in 5.10.

Utilising the equations from the inductor design section of this report, it is possible to determine how the reductions in the number of turns,  $N$ , and core cross-sectional area,  $A_c$ , influence the DC resistance,  $R_{DC}$ , and mean length per turn,  $MLT$ ; both of which may impact inductor efficiency and mass.

5.1. BIASED INDUCTOR GALVANO ELECTROCHEMICAL IMPEDANCE  
SPECTROSCOPY TESTING

---

Table 5.10: Proportional Reductions in Design Parameter Relative to Non-Biased Inductor

Topology	N reduction	$A_c$ reduction
1S2P	53% N	53% $A_c$
2S2P	47% N	47% $A_c$
3S2P	47% N	47% $A_c$
4S2P	47% N	47% $A_c$
5S2P	40% N	40% $A_c$

When evaluating the effect of the BIF on  $R_{DC}$ , it is assumed that the window area and fill factor remain constant, therefore allowing for a doubling of the conductor's cross-sectional area. Adjustments are required to assess the influence of BIF on  $MLT$ , ensuring that calculations are specific to the AMCC-100 core, by aligning with the application notes provided by the manufacturer.

The  $MLT$  given in the application notes is calculated through equation 5.5, which uses dimensions 'a', 'b' and 'd', from the inductor schematic as presented earlier in this study, to calculate the  $MLT$  for the baseline inductor. The  $MLT$  for the biased topology,  $MLT_{biased}$ , is then calculated using a modified version of the original equation, incorporating the proportional reductions in design parameters,  $PRDP$ , for core cross-sectional area adjustments, as expressed by by equation 5.6.

The percent difference between the baseline and biased  $MLT$  values, serves as a scaling factor, against which the original  $MLT$  value is multiplied. Given that  $R_{DC}$  is directly proportional to the  $MLT$ , the same factor is used to determine changes in  $R_{DC}$ . Additionally, When the core area is reduced, the core volume, and as such core mass is affected proportionally. The results for this analysis, are presented in table 5.11.

$$MLT = 2 \cdot (a + 2 \cdot b + d) \tag{5.5}$$

5.1. BIASED INDUCTOR GALVANO ELECTROCHEMICAL IMPEDANCE  
SPECTROSCOPY TESTING

---

Table 5.11: Bias Improvement Factor Influence on  $MLT$  and  $R_{DC}$

Topology	$R_{DC}$	MLT
1S2P, 53% N	28% $R_{DC}$	-
1S2P, 53% $A_c$	92.57% $R_{DC}$	92.57% MLT
2S2P, 47% N	22% $R_{DC}$	-
2S2P, 47% $A_c$	91.5% $R_{DC}$	91.5% MLT
3S2P, 47% N	22% $R_{DC}$	-
3S2P, 47% $A_c$	91.5% $R_{DC}$	91.5% MLT
4S2P, 47% N	22% $R_{DC}$	-
4S2P, 47% $A_c$	91.5% $R_{DC}$	91.5% MLT
5S2P, 40% N	16% $R_{DC}$	-
5S2P, 40% $A_c$	90.5% $R_{DC}$	90.5% MLT

$$MLT_{biased} = 2 \cdot ((a \cdot (PRDP)) + 2 \cdot b + d) \quad (5.6)$$

From the data presented in table 5.11, it is evident that reducing the number of turns, has the most significant effect on lowering the value of  $R_{DC}$ . However, this parameter change primarily reduces mass, through decreasing copper requirements, where as reducing the cross-sectional area,  $A_c$ , leads to reductions in both copper and core mass, as well as volume.

To quantify potential reductions in core mass, when selecting core cross-sectional area as the primary parameter for modification, the baseline core cross-sectional area is divided by the baseline core mass. This yields a scaling factor which is then multiplied by the proportional reduction in  $A_c$ , to determine the new core mass for each topology. Based on datasheet information, the core exhibits an approximate mass to area ratio of  $0.0018 \text{ kg/mm}^2$ . The corresponding mass data for each topology, is presented in table 5.12.

If the biased inductor is not explicitly designed to take advantage of the increased current handling capacity, provided by the magnets, and instead prioritises reductions in core mass, through a reduction in core cross-sectional area,  $A_c$ , the BIF values suggest that higher values result in greater core mass reductions. However,

Table 5.12: Bias Improvement Factor Influence on Core Mass

Topology	Biased Core Mass (kg)
1S2P, 53% $A_c$	0.563
2S2P, 47% $A_c$	0.499
3S2P, 47% $A_c$	0.499
4S2P, 47% $A_c$	0.499
5S2P, 40% $A_c$	0.425

this comes at the expense of an increased magnet count, which in turn raises the total 'boxed volume', and adds additional weight. While the added magnet weight is relatively minor compared to the mass savings from the core reduction, and should be considered in any practical applications, dependent on the intended use and proposed function of the set of inductors.

### 5.1.1 Biased Inductor Galvano Electrochemical Impedance Spectroscopy Test: Summary

In summary, it has been possible to show that with the addition of magnets, placed between the sides of the inductor cores, forming a magnetic circuit, an effective bias can be achieved, such that the inductor's saturation thresholds with respects to current, have been augmented. Additionally, it has been shown that when a bias is achieved, variations in design parameters, permits for a cores with reduced windings or cross-sectional area, and which is shared by both cores, The 1S2P configuration is to be taken forward for incorporation into the experimental buck converter. This chapter has shown the possible benefits of biasing an inductor, with regards to energy storage. These studies support overarching objective of the project, to reduce the mass, and volume of of the inductors with DC-DC converters, and as such the mass and volume of the converters themselves, or alternatively the power density, for the same volume and mass.

---

## Chapter 6

# Experimental Interleaved Buck Converter Hardware & Supporting Equipment

In order to validate the results of the GEIS testing, and demonstrate the novelty of PMBI technology when used in an interleaved buck converter configuration, an experimental rig developed by the Power Electronics and Machine Control (PEMC) research group has been modified in order to accommodate the new hardware and testing scenarios. The hardware of the interleaved DC-DC boost converter rig is discussed in this section.

A two channel interleaved buck converter capable of handling both standard and magnetically biased inductors, is developed through modification of a converter rig used previously for experimental work within the PEMC. The converter rig is constructed with four half bridges, taking advantage of Silicon Carbide (SiC) semiconductor devices, connected to the DC Bus for the input voltage, and the output of the half bridges is connected to an electronic load, with an output filtering capacitor placed between the positive and negative terminals; additionally, a DC

---

link capacitor is placed between the positive and negative rail of the half bridges on the DC bus, for filtering on the supply side. As this study is focused on a two phase interleaved buck converter, only two of the four channels will be used. Having four channels permits for the future development of an interleaved converter with a greater number of phases.

The experimental rig takes advantage of a TMS320C6713 digital signal processing board, to implement the control algorithms for the control of the half bridges, via a series of optocouplers, and gate driver boards. The current and voltage measurements are captured with the use of independent current and voltage sensors, connected to the digital signal processing board, and will be discussed separately. The signal processing board is also equipped to transmit data back to a host computer via USB, to enable both the upload of the control software developed in the Texas Instruments Code Composer Studio software, and to receive information from the voltage and current sensors for visualisation on a display screen, as well as supporting the over current protection system built into the code. the digital signal processing board can be observed in figure 6.1.

As depicted in the schematics for the interleaved buck converter from the previous chapters, the output of the half bridge, is connected to the input terminal of the inductor, and the inductor's output terminal is connected via a node, to the positive side of the electronic load; this is the same for both inductors. With the use of M6 threads, washers and nuts, along with the terminals of the biased and non-biased inductors terminating with crimped ring connectors, this permits for easy swapping of the inductors between tests, and allows for an electrically sound connection; the connections are securely wrapped with non-conductive tape to prevent accidental contact to either operators, of the rig or to the workbench.

Figure 6.2 shows the electrically insulating Paxoline board, mounted with the eight driver PCB boards, required to switch the half bridge MOSFETS, which are in



Figure 6.1: Buck Converter Digital Signal Processing Board

turn connected to the copper bus bars, placed above. Each of the four MOSFET packages are mounted to an aluminum heat sink, which in turn sits above a cooling fan, to prevent the modules from overheating.

The critical components which comprise the converter rig, are detailed in table 6.1. As previously discussed, the maximum output current for the experiments is slated to be 40 Amps maximum, and as can be taken from table 6.1, the components are suitably within specification for the power levels which they will experience during testing.

Although the rig was inherited from previous work, a thorough understanding of the sensing equipment on the measurement board was developed, to accommodate potential modifications, or sensor upgrades. The sensing equipment and measurement board are available in figure 6.3. The measurement board interfaces with the digital signal processing FPGA via a 23-D connector cable. Current measurements

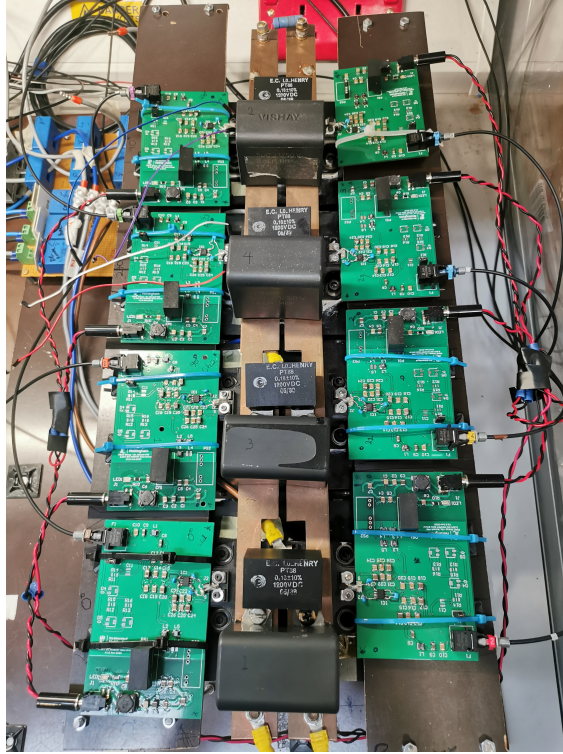


Figure 6.2: Buck Converter Gate Driver Board

Table 6.1: Critical Equipment of Experimental Rig

Equipment	Details
Digital Signal Producer	TMS230C6712 FPGA
Optocouplers	PWM Signal Transmission
SiC Power Module	CAS100H12AM1
	1.2kV, 100A Half Bridge Module [128]
Sensing	LEM LA-55P Current Sensing Module
	LV-25P Voltage Sensing Module

are obtained using hall effect transducers, which converts the measured current into a corresponding voltage via a burden resistor, mounted to the digital signal processing board. The current is measured from the high side, where a proportional signal is then taken to digital signal processing board, and subsequently scaled by the burden resistor to yield a usable voltage for the FPGA to interpret and use within the control software.

Voltage transducers are connected across the positive and negative rails of their respective high or low side of the converter, to provide voltage readings for the DC

Table 6.2: Sensing Module Specifications

Parameter	Current Sensing Module	Voltage Sensing Module
Module Variant	LEM LA-55P	LV-25P
Operational Range	-50A to +50A	10V to 500V
Linearity Error	<0.15%	<0.2%
Primary RMS current	50A	10mA
Turns Ratio $N_p/N_s$	1:1000	2500:1000
Resistor Values	$R_{\text{burden}} = 140\Omega$	$R_{\text{burden}} = 140\Omega$ $R_1 = R_2 = 50k\Omega$ $R_v = \frac{R_1+R_2}{R_1+R_2} = 25k\Omega$

link, and at the load respectively. The current sensors are placed in series with the current they are measure, specifically for this study, the input currents into inductor one and inductor two. The specifications for the sensing equipment is provided in table 6.2.

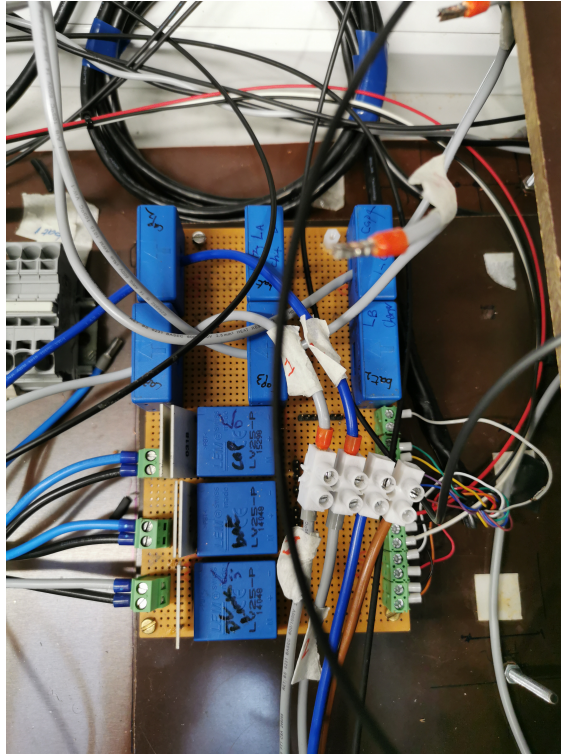


Figure 6.3: Buck Converter Sensor Board

The burden resistors are integrated into the digital signal processing board to ensure that the output voltage remains within a limit of  $\pm 5V$ . As per the current sensor's data sheet, the sensor has a turns ratio of 1:1000, meaning that a 40 Amp

---

primary side current, which is the maximum that will be observed during testing, is translated into a 40 mA secondary side current. As the voltage into the FPGA as already described, is limited to  $\pm 5V$ , the required burden resistor value is given by  $5V/40 \cdot 10^{-3}mA$ , which is  $125\Omega$ . This calculation aligns with datasheet's recommended burden resistor range of  $50\Omega$  to  $160\Omega$  when taking advantage of the full 50 Amp capability of the sensor. A  $140\Omega$  resistor is pre-soldered to the digital signal producing board, from previous testing, and this was deemed adequate for this study.

A similar procedure is applied to the voltage transducer. The datasheet for the LV 25-P specifies that the voltage transducer has an upper operating range of 500V. When a voltage is measured, it passes through a set of external resistors ( $R_1$  and  $R_2$ ), which, by Ohm's law produces an output signal in the form of a current, that is interpreted by the voltage transducer.

For example, to measure a 250V primary side voltage, and given the nominal primary current of 10 mA, the required resistance of  $R_1$  will be given by  $250V/10 \cdot 10^{-3}mA$ , and results in a 25 k $\Omega$  resistor. The secondary side current of the LV 25-P of 25 mA will therefore require a burden resistor given  $5V/25 \cdot 10^{-3}mA$ , with a resulting value of  $200\Omega$ . The datasheet for the LV 25-P recommends a burden resistor of  $100\Omega$  to  $300\Omega$ . As before, a pre-soldered  $140\Omega$  is installed and, deemed sufficient for this study.

The voltage and current sensors have previously been calibrated using pre-existing software to scale the relationship between the readings taken from measured signals to the analogue to digital converter. Additionally previous work has already performed calibration activities to compensate for the deviation from the readings, resulting from temperature changes in the resistors and traducers.

## 6.1 Support Equipment

In addition to the hardware required exclusively for the buck converter, a plethora of supporting hardware was also required. This additional hardware was required to provide power to the gate drivers, as well as providing the power to the load. A number of measurement devices are placed across the rig for the measurements of current and voltages, and finally an oscilloscope was required to translate the measurements from the voltage and current probes into usable, exportable data.

### Power Supply

To supply the required 270V to the DC bus for the half bridges, one of the PEMC's 0 to 360V, 0 to 40 Amp, 0 to 5kW power supply was utilised. These power supplies take advantage of the 400V, three phase sockets provided on the lab benches in the PEMC drives lab, and all required health and safety documents were completed prior to powering up this high power equipment. The positive and negative of the output terminals was placed onto the positive and negative terminal blocks of the converter rig, which act as nodes, for the remaining components of the converter to be attached to, with their positive and negative terminals, respectively.



Figure 6.4: 5 kW Power Supply Unit for the DC Bus

## Current & Voltage Probes

A selection of current and voltages probes were strategically placed along the circuit, which in turn feed into the oscilloscope, mentioned in the forthcoming subsection. To begin with, a differential voltage probe was placed across the input terminal of inductor one, and the input terminal of inductor two; the logic being, that it allows the visualisation of the interleave, and ensures that the converter is interleaving correctly, the differential voltage probe can be seen in 6.5.



Figure 6.5: Differential Voltage Probe

Additionally, a Rogowski coil was placed in line with the input terminal of inductor one. Rogowski coils are not designed to measure DC currents, however, they can accurately detect changes in current, without necessarily providing the absolute value of the current running through the cable itself. The Rogowski coil plays one of the most important roles within the sensing arrangements, as this will ultimately be the measurement which allows the determination of any saturation in the inductor core, based on the  $di/dt$  value measured. The Rogowski coil can be seen in figure

6.6.



Figure 6.6: Rogowski Coil

## Oscilloscope

In order to capture the signals from the current and voltage probes, such that the readings could be saved and extracted into MATLAB for post processing, a 4 channel YOKOGAWA oscilloscope was employed to work in conjunction with the rig; this is shown in figure 6.7. Each probe required programming into the machine, based in their individual attenuation values, and acceptable frequency ranges.

## Electronic Load

As opposed to using the resistor bank which was inherited with the converter rig, for the experimental testing, it was decided that an alternate approach would be taken to guarantee the current on the output side of converter was correct, and as such

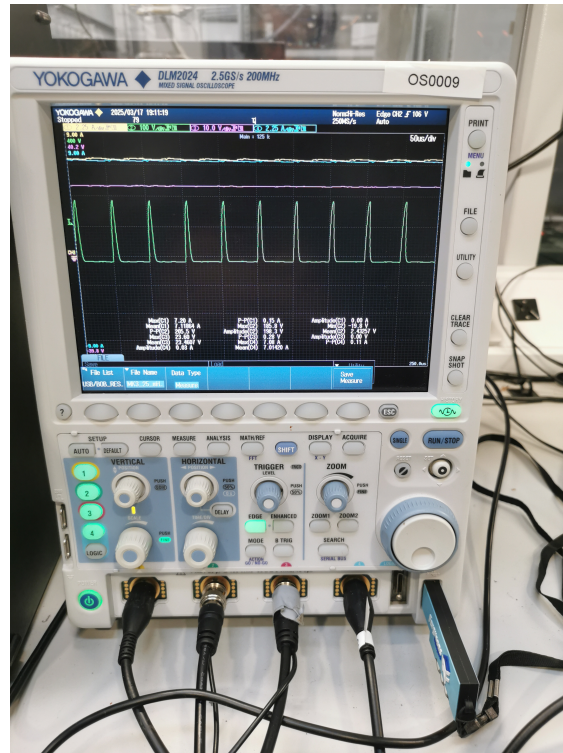


Figure 6.7: YOKOGAWA DLM2024

the current across the inductor. The equipment utilised here, is referred to as an electronic load, and has multiple functionalities, including the setting of a constant current demand. With the constant current set on the electronic load, and the the input voltage set on the input power supply, the necessary current is drawn from the supply, to meet the demand at the load. The control panel permits for the stepping of the current for every test, which allows the experiments to align well with the GEIS testing process. Additionally, it is possible to connect the controllable load to a host computer, where dedicated software can be used to perform more dynamic testing, such a current ramps, rather than the stepped approach which is used for this study.



Figure 6.8: Interleaved Buck Converter Programmable Load

---

## Chapter 7

# Experimental Results

Using the experimental interleaved buck converter rig described above, alongside the non-biased inductor, and the 1S2P configuration biased inductor, it was possible to run a series of tests to validate the potential benefits brought about through biased inductors, and assess the correlations to the results given by the GEIS testing, under quasi-DC conditions. In alignment with the previous GEIS experiments, the current is stepped, such that each inductor experiences an increment of 1A per step; this is achieved by applying a 2A step on the electronic load; as the current across the inductors is split, the load current is halved between the two inductors.

Traditionally, the value of inductance per current step,  $L_x$ , is calculated, quite simply, through the instantaneous voltage,  $V_x$ , and change in current with respects to time, as per equation 7.1, and akin to the plots seen for the GEIS testing, it would be possible to plot the inductance with respects to current. However, due to the use of current clamps, which generate considerable noise on the oscilloscope, and yield somewhat questionable outputs, an alternate method to determine the saturation points of the inductors is adopted.

---

$$L_x = \frac{V_x}{(di/dt)} \quad (7.1)$$

The experimental test equipment section has already detailed the use of the Rogowski coil; which in this experimental work was 'connected' to the input terminal of a single inductor phase. Rogowski coils, do not have the ability to measure a pure DC current waveform, however, they have the ability to measure changes in current waveforms, i.e.  $di/dt$  values. The measurements are therefore not absolute values of current, but a representation of how the current is changing. Taking the  $di/dt$  values for the respective inductors, biased and non-biased, at each current step, and comparing the values, is one means of providing some indication as to whether the cores are becoming saturated. Another means is given as, when the value of  $di/dt$  increases, relative to previous lower current measurements, this represents the core heading towards saturation, and it stands to reason that when the core is in the non-saturated region, the values of the  $di/dt$  should be low, in comparison to the saturated values, and both the biased and non-biased inductor should exhibit similar values. As the current is ramped up in stages, the biasing validation should be observed by the  $di/dt$  values of the standard inductor deviating away from both the steady state values observed at lower currents, and away from the  $di/dt$  values experienced by the biased inductor.

In order to assess these changes in  $di/dt$ , an examination of the waveforms is undertaken to observe how they vary as the current across the inductors is increased. The waveforms discussed in this section represent part of the full data set, which is available to the reader in the appendix, as both reading matter and evidence of experimental work undertaken by the author, in support of this project.

Beginning with the results for a load current of 2 Amps, the results for the Rogowski coil output waveform are shown in figure 7.1, with the top image representing a single pulse of the 10kHz frequency, and the lower plot showing the continuous waveform,

---

for reference. During the course of the  $5 \times 10^{-5}$  second switching cycle, a number of distinct events occur within the converter. These will now be discussed

At a time of  $t = 0$  seconds, the MOSFET associated with the inductor being measured by the Rogowski coil, is switched on. Immediately after this switch on event, a transient ripple is observed, and lasts until approximately  $t = 0.25 \times 10^{-5}$  seconds. This ripple, appears to be a transient response to the MOSFET switching event, rather than a classical inrush current, generally observed when the inductor is provided with current, from fully discharged state. This is likely caused by parasitic inductances in the circuit. However, in both the standard and biased inductor cases, the ripple settles almost identically after this period, and the current subsequently continues to increase linearly, until the end of MOSFET's duty cycle.

The interval from  $t = 0$  seconds, to the end of the duty cycle, is the region utilised to determine the  $dt$  component of  $di/dt$ . The change in current,  $di$ , is defined as the difference between the current at  $t = 0$  seconds, and the current at the end of the duty cycle. This is denoted by a dashed iso-bar on the x-axis, at the moment the duty cycle ends, referred to as 'Max Current Time'.

At the end of the duty cycle, the source-side MOSFET switches off, and a significant decrease in inductor current is observed. This marks the transition from the source-driven mode, to the freewheeling mode, where the inductor discharges through the freewheeling MOSFET path. The sudden drop in inductor current during the transition suggests a brief delay between the two phases, where the inductor should be discharging through the freewheeling synchronous MOSFET. Between these two phases, likely caused by the dead time, which is incorporated to prevent shoot through, the inductor is temporarily disconnected from the circuit, resulting in an incomplete current path, causing what can be observed on the figure, as a temporary dip in the inductor current, before the freewheeling MOSFET is switched on, and the current can discharge, linearly, without interruption, as previously described.

Table 7.1:  $di/dt$  for Biased and Non-Biased Inductor at Converter Load of 2A

Inductor	$di/dt$ (A/S)	% difference to Non-Biased Inductor
Non Biased	8947.28	-
Biased	9317.67	+4.14%

Between, approximately  $2.5 \times 10^{-5}$  seconds, and  $3.75 \times 10^{-5}$  seconds, along the linear discharge region, low-amplitude ripples are observed. These ripples are attributed to the switching of the MOSFETs in the second phase of the interleaved buck converter. As these MOSFETS are operating out of phase with those shown in the figure, which represent the first phase, the resulting disturbances can be classified as noise in the measured waveform of the first phase.

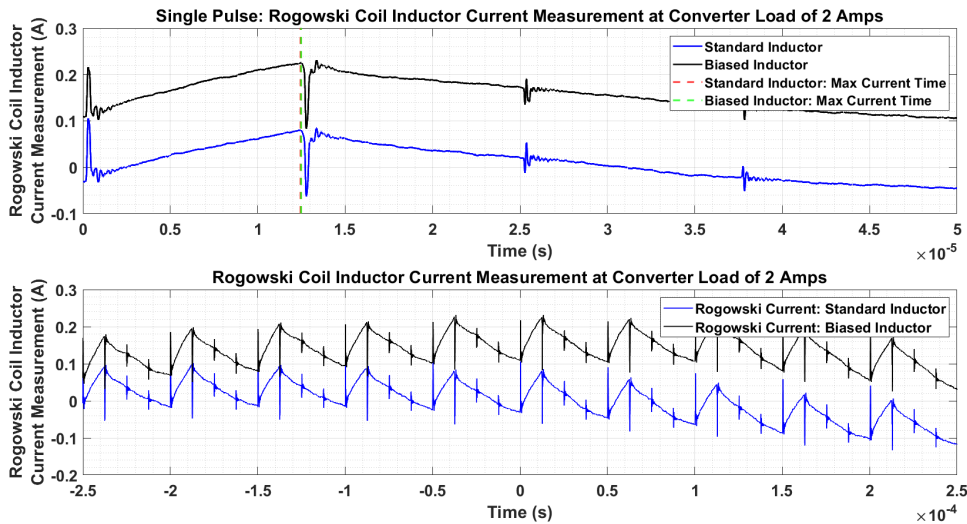


Figure 7.1: Rogowski Coil Inductor Current Measurement at Converter Load of 2A

The values for the  $di/dt$ , given in Amps per second at a converter load of 2 amps, for the standard and biased inductor, are presented in table 7.1. As the table suggests, there is approximately a 4.14% increase in the  $di/dt$  between the non-biased and biased inductor, this represents a small value of difference and does not suggest any biasing at this low current, well below the designed saturation point of the inductor, and that observed during GEIS testing.

Increasing the converter load to 8 Amps, yields the waveform shown in figure 7.2.

Table 7.2:  $di/dt$  for Biased and Non-Biased Inductor at Converter Load of 8A

Inductor	$di/dt$ (A/S)	% difference to Non-Biased Inductor
Non Biased	9793.75	-
Biased	9213.71	-6.92%

It is clear that the shape and events are nearly identical, albeit with an increase in the current amplitude, during the switch on transient of the MOSFET at  $t = 0$  seconds, and similar values presented for the  $di/dt$ , in table 7.2, with an increase of approximately 10% for the non-biased inductor, and minor decrease of 1.1% for the biased inductor.

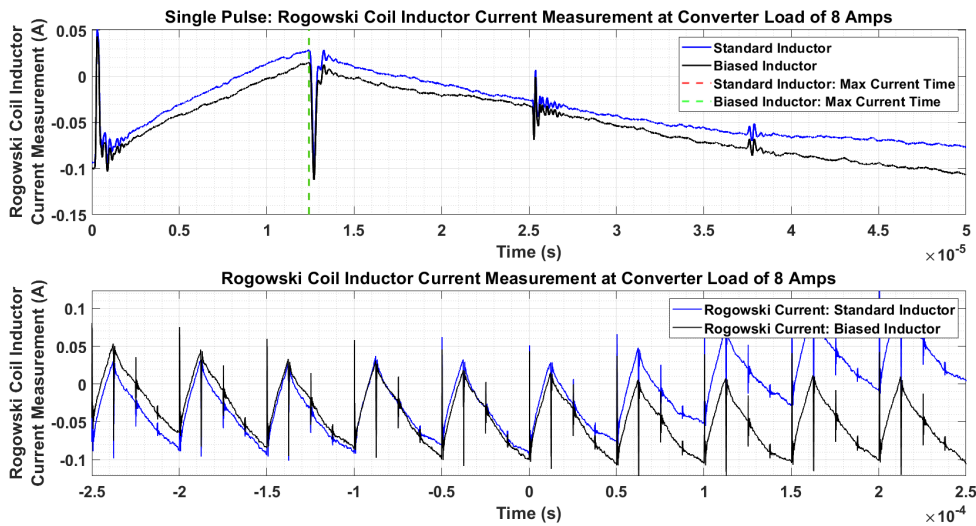


Figure 7.2: Rogowski Coil Inductor Current Measurement at Converter Load of 8A

Aligning the waveforms of the Rogowski coil inductor current measurements, from the 2 Amp load test, and the 8 Amp load test, such that the initial values of the non-biased inductor are the same for both tests, while negating the absolute values of current, and similarly for the biased inductor, it is possible to present figure 7.3. This figure provides a visual reference for the changes in  $di/dt$  between each test. As previously described, the values for the biased inductor remain relatively unchanged, and this is reflected in the near-perfect overlap of the waveform currents; the same cannot be stated for the standard inductor, whereby a larger gradient is evident at the higher current test, relative to the lower current test. This figure also

supports the -6.29% difference in  $di/dt$  experienced by the biased inductor, relative to the non-biased inductor.

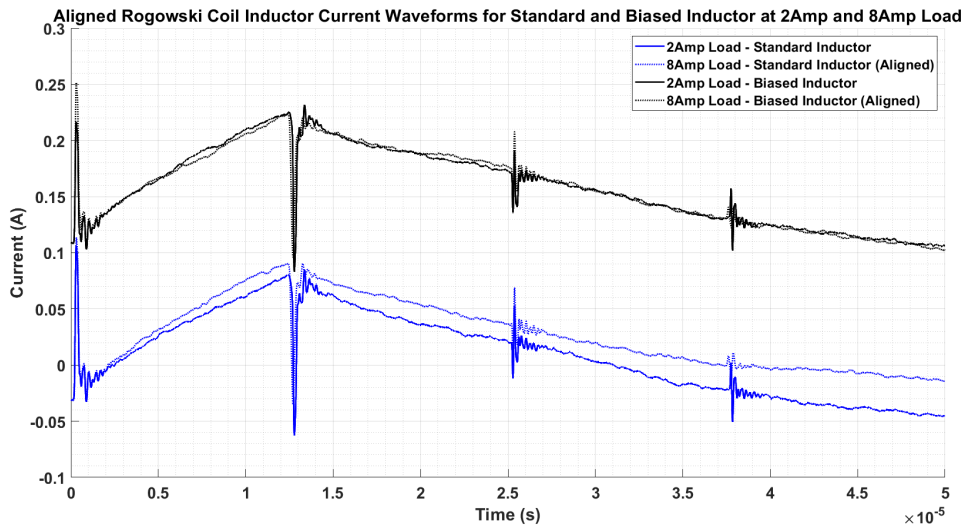


Figure 7.3: Aligned Rogowski Coil Inductor Current Waveforms for Standard and Biased Inductor at 2Amp and 8Amp Load

Increasing the load current further again, to 16 Amps, with a resulting 8 Amps across each inductor, shown in figure 7.4, it is clear to see the increased disparity between the gradients of  $di/dt$ , for each inductor variant. As with the previous tests, the events observed in the wave forms are in essence identical. The values for the  $di/dt$ , are provided in table 7.3, and the visual disparity observed in the figure is validated numerically, with the biased inductor expressing a 43.19% lower value of  $di/dt$  relative to the non-biased inductor. This result, is suggestive of a condition described previously, whereby, the standard inductor  $di/dt$ , has deviated considerably from that of the biased inductor, and indicates that it is heading towards saturation, while the biased inductor is further away from this point, and indicates that the biasing due to the magnets is allowing for the inductor to accept more current, and thus increasing the energy product, before reaching saturation, again relative to the non-biased inductor. The previous descriptions of the variations in the  $di/dt$  are also aligning with the results of the GEIS testing, whereby, initial current values see both inductors at relatively the same value, but as the current is increased, a deviation between the inductances of the two inductors, become more

Table 7.3:  $di/dt$  for Biased and Non-Biased Inductor at Converter Load of 16A

Inductor	$di/dt$ (A/S)	% difference to Non-Biased Inductor
Non Biased	34737.5	-
Biased	19734.7	-43.19%

apparent.

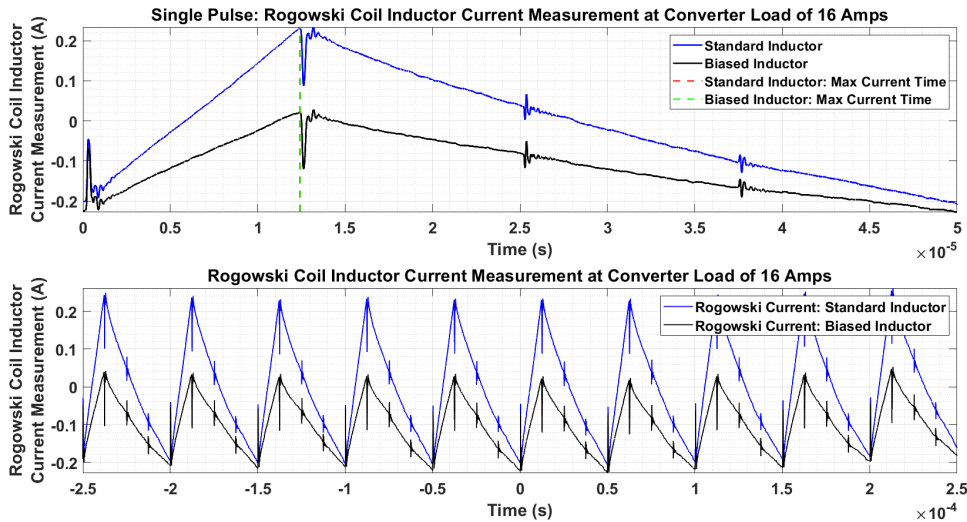


Figure 7.4: Rogowski Coil Inductor Current Measurement at Converter Load of 16A

As before, the currents of the most recent test, are aligned with the previous test; in this case, the 8 Amp load test with the 16 Amp load test; this is available in figure 7.5. The first observation here, comes from the disparity between the 8 Amp and 16 Amp test for the standard inductor; here a difference of 254% is experienced, relative to the 114.18% for the biased inductor; a considerable difference between the two, and further validating the advantages of biased magnetics.

Moving towards a higher current test, the 24 Amp load is now considered, and the results of the waveform for the Rogowski coil are shown in figure 7.6. At this current, the results are somewhat different to the previous result, although the events that are captured are the same, the waveforms for the non-biased inductor, and the biased inductor, are almost visually identical in terms of their gradients of  $di/dt$ , the values of which can be taken from 7.4. It can be seen that at this current

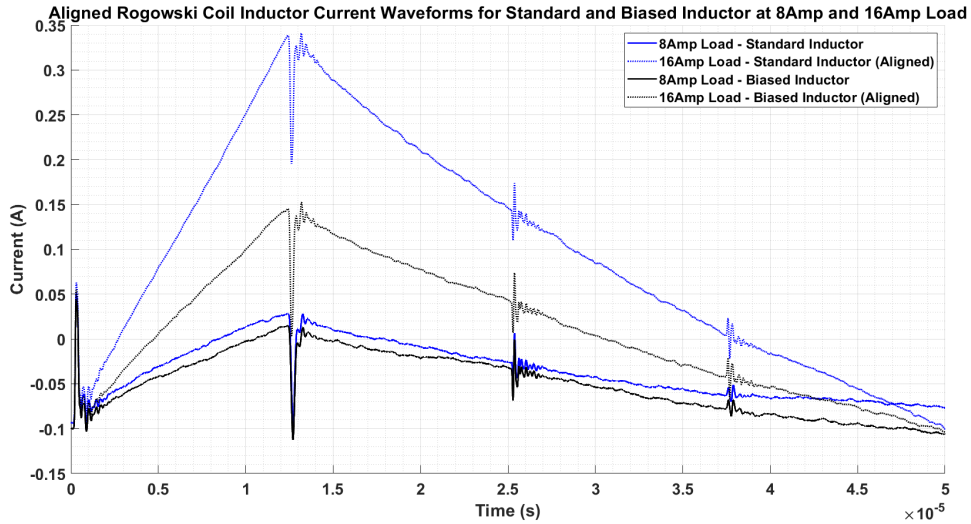


Figure 7.5: Aligned Rogowski Coil Inductor Current Waveforms for Standard and Biased Inductor at 8Amp and 16Amp Load

level, there is only a 4.34% difference, between the two, similar to that observed during the 2 Amp test. However, at this value it has become apparent that the high values of  $di/dt$ , limited deviation between the two results and having already progressed through a region of large disparity, the inductors are clearly, nearing their full saturation point.

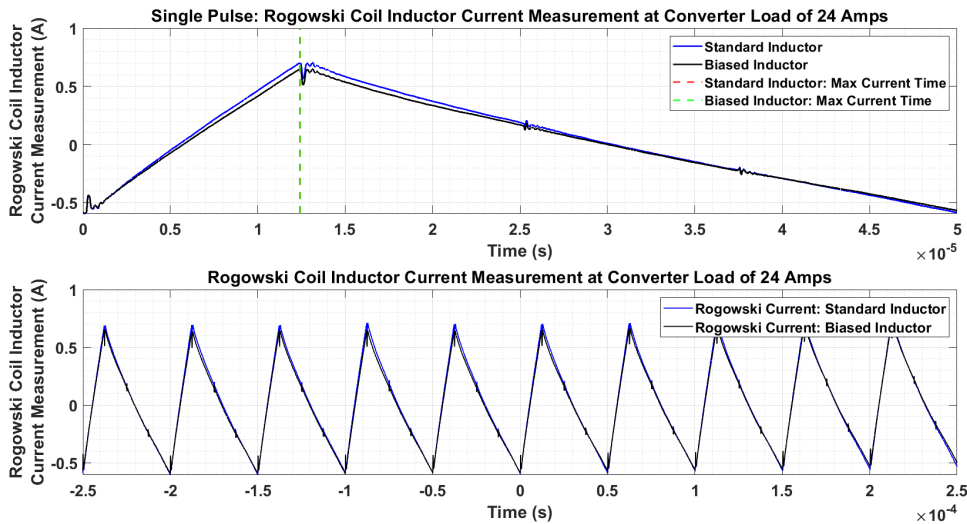


Figure 7.6: Rogowski Coil Inductor Current Measurement at Converter Load of 24A

The plot for the aligned waveforms, for tests at 16 Amps and 24 Amps, can be

Table 7.4:  $di/dt$  for Biased and Non-Biased Inductor at Converter Load of 24A

Inductor	$di/dt$ (A/S)	% difference to Non-Biased Inductor
Non Biased	103838	-
Biased	99334.4	-4.34%

observed in figure 7.7. it is immediately clear that the  $di/dt$  gradients, are considerably greater for both the non-biased and biased inductor at the 24 Amp test, relative to the 16 Amp test. This is given as a near 200% increase in  $di/dt$  for the non-biased inductor, and over 400% increase in  $di/dt$ , for the biased inductor. it is conclusive to say at this stage that the biased inductor has also reached a saturated condition.

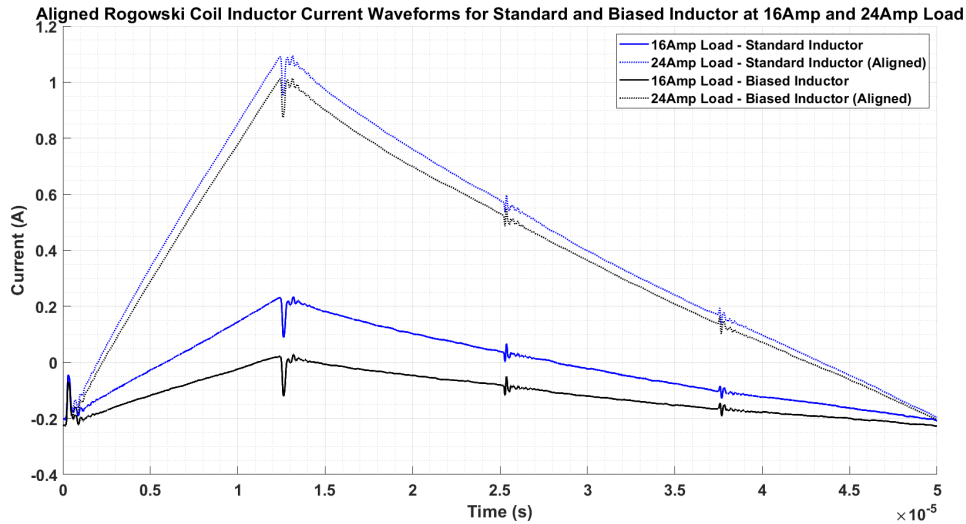


Figure 7.7: Aligned Rogowski Coil Inductor Current Waveforms for Standard and Biased Inductor at 16Amp and 24Amp Load

The final set of Rogowski coil current results, for a converter load at 40 Amps, is shown in figure 7.8. In this scenario, the gradients for the  $di/dt$  appear to be almost identical, as is validated by table 7.5, with a mere 0.81% difference between the non-biased and biased inductors. When considering the results of the 40 Amp test, in conjunction with the results of the 24 Amp test, the difference between the  $di/dt$  values are extremely close. This again supports the notion that the inductor is saturated at this point, as the biased inductor, has now reached equivalent  $di/dt$

Table 7.5:  $di/dt$  for Biased and Non-Biased Inductor at Converter Load of 40A

Inductor	$di/dt$ (A/S)	% difference to Non-Biased Inductor
Non Biased	121091	-
Biased	122073	+0.81%

values to that of the non biased, and both have traversed through the region of greater disparity at lower current values.

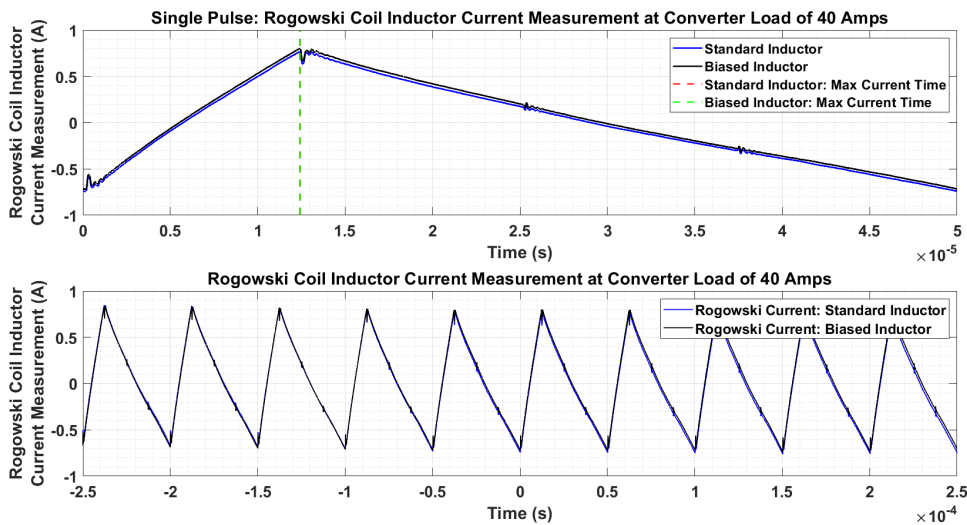


Figure 7.8: Rogowski Coil Inductor Current Measurement at Converter Load of 40A

Figure 7.9, also helps to show the limited increase in  $di/dt$  for both inductor variants, between the 24 Amp test and the 40 Amp test, relative to the region of greater disparity, at lower current vales. A difference of 16.62% is observed for the the non biased inductor, and a difference of 22.89% for the biased.

Based on the results presented in tables 7.1 to 7.5, the changes in current with respect to time, initially begin at relatively similar values, at low currents, below the designed saturation point. As the currents are increased, the disparity between the  $di/dt$  increases with respects to the non-biased inductor achieving considerably higher values, relative to the non biased, and finally towards the maximum current used for the experimental results, the values once again align, albeit with values of  $di/dt$  multiple factors greater than their lower current counterparts. In order to

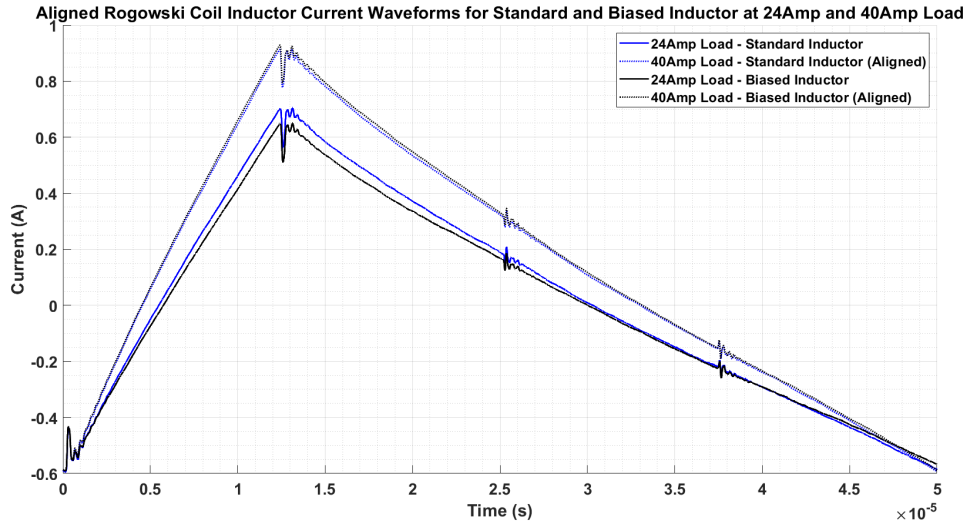


Figure 7.9: Aligned Rogowski Coil Inductor Current Waveforms for Standard and Biased Inductor at 24Amp and 40Amp Load

visualise the  $di/dt$  fully, the final results of the  $di/dt$  for both inductor variants, when plotted against one another for the full range of currents, is shown in figure 7.10.

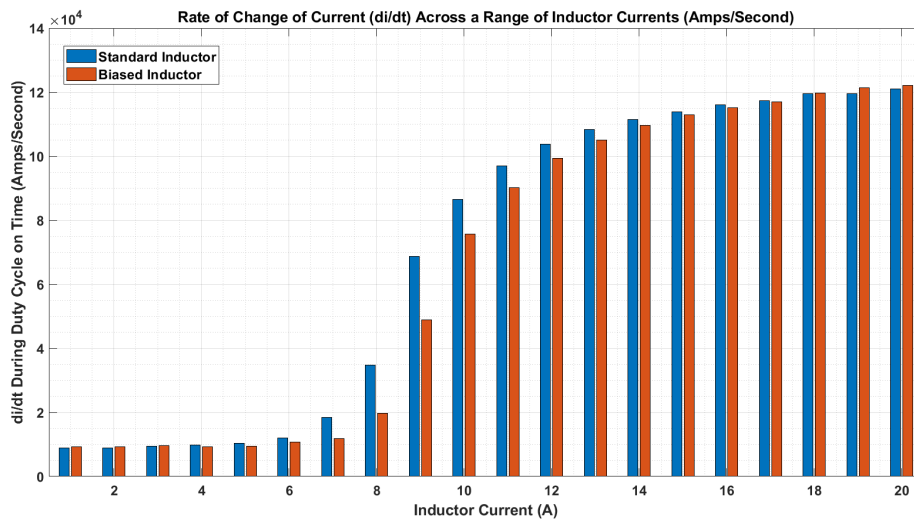


Figure 7.10: Rate of Change of Current ( $di/dt$ ) Across a Range of Inductor Currents (Amps/Second)

From figure 7.10, it can be clearly observed that the standard non-biased inductor, begins to see saturation at currents lower than that of the biased inductor. This profile is visually the inverse of the plots for the GEIS experiments, where as for

---

these test we see lower values of metric increasing to higher values of metric, with current increase, rather than higher metric to lower metic, with current increase. However, the deviation between the two as current is increased, and the converge towards saturation is clearly identifiable in beth sets of experiments. This proves that the biased inductor, when used in the interleaved buck converter, has the capacity to handle larger current values relative to the standard inductor, which in turn increases the power density of the converter, or alternatively yields the option for geometric alterations to the core and / or its windings, to again, increase the power density of the converter.

---

## Chapter 8

# Conclusions and Future Work

This project has applied various methods and frameworks, meaningfully, to generate original ideas, permitting for the analysis of their implications. The main goals of this research were to implement a novel hydrogen-electric aircraft simulation tool, capable of determining optimised propulsion system parameters, based on Top Level Aircraft Requirements (TLARs), and hybridisation of power, as inputs into a mission analysis, while also allowing for capabilities to perform trade studies for the assessment of the impact of various power converter technology levels, and various drag polars, on overall aircraft mass. Additionally, the second objective of this research was aimed at improving the performance of magnetics within an interleaved buck converter, through the implementation of magnets to simultaneously bias a pair of inductors, based on AMCC-100 cores.

### 8.1 Main Contributions

The main contributions of this research are as follows:

A novel hydrogen-electric aircraft sizing methodology has shown that the selection

of aerodynamic model, i.e. the simple or complex drag polar, in combination with the quality of the input parameters from either CFD studies or equivalent aircraft parameters, referenced in conceptual aircraft design textbooks, has an adverse affect on the quality and accuracy of the results for the final MTOM, when considering a like-for-like aircraft.

Evaluation using the novel hydrogen-electric aircraft sizing methodology shows that the most mass sensitive propulsion system components, outside of the  $\text{GH}_2$  tank, are the DC-DC converters, and more so for the hydrogen branch of the aircraft propulsion system. This supported the efforts to reduce the most heavy and voluminous parts of the converter, in a bid to yield greater power density, or reduce volume and as a byproduct, mass.

Using the novel hydrogen-electric aircraft sizing methodology, it has been possible to show that adding the operational mode of in-flight recharging, has both positive and negative side effects. A down side to in-flight recharging has shown an increase in aircraft mass relative to the non-in-flight recharge counterpart; however, this mass increase never exceeds 1% in all cases. Operational advantages have been gained, though having the potential for a fully recharged aircraft, ready for deployment, immediately after landing, with no requirements for the operator to have to recharge the aircraft, which would otherwise require the energy for take-off climb and diversion climb, before the aircraft is available for deployment again.

The development of a simplified fuel cell model has supported the rapid calculation of competing aircraft, without the necessity for complex Nernst equations, or in depth sizing of fuel cell balance of plant equipment. In addition, the efficiency of the fuel cell, has the capacity to be an input parameter to any future trade studies.

Evaluation of the use of the PLECS simulation tool to model permanent magnet biased inductors, when modelled as a MEC, with a magnetising coil in place of the permanent magnet, has shown poor results, and a conclusion could be drawn that

although PLECS was useful for the simulation of the closed loop interleaved buck converter, its magnetic package is limited, relative to the superior ANSYS Fluent Finite Element Analysis package.

Experimental validation of the inductor topology described by patent [1] , to generate original data, under the influence of varying degrees of magnetic bias, under consideration of GEIS testing, have shown positive improvements to the current handling and energy product capabilities, in addition to the theoretical improvements to the inductor parameters, including number of turns, and volume, should the full current potential not be required from the biasing flux.

Additionally, experimental validation has shown that the use of permanent magnet biased inductors, based on the topology of [1], when used in combination with an interleaved buck converter configuration has effects of improving the power density of the converter, by permitting for the delay of the on set of inductor saturation, relative to the non-biased counterparts.

## **8.2 Future Work**

During the course of this project, a number of thoughts for future work have arisen do to a number of factors including, the authors limited knowledge of a subject, but desire to see the science improved, additional time constrains have moved certain elements into future work, as well as a desire for scientific endeavour.

The drag polar information used to supplement the corresponding drag polar equations, pertains to information gleaned from research. It would be desirable to undertake additional Computer Fluid Dynamics work, or practical wind tunnel testing to develop new drag polars for experimental, blended wing body, or geometrically novel aircraft.

Future work would also consider the development of improved models for the balance of plant, and fuel cell system as a whole; this has been limited in this study, due to the author's limited knowledge of the intricacies of fuel-cell dynamics. This additional work would also attempt to capture an enhanced time response model for the fuel cell.

It was not possible to experimentally validate the 20kHz inductor with the spectroscopy machine due to its limited power; however it would be advantageous to find a new spectroscopy machine with the capabilities to complete this experiment.

Finally, attempts were made to model permanent magnet biased inductors using the PLECS software package, with minimal success. Future work would suggest continuation of the use of ANSYS, to emulate the results of the GEIS testing.

# Bibliography

- [1] P. Pieteris, ““Permanent Magnet DC inductor”,” 2015.
- [2] “IATA - 20 Year Passenger Forecast.” [Online]. Available: <https://www.iata.org/en/publications/store/20-year-passenger-forecast/>
- [3] “Number of Flights Worldwide in 2022/2023: Passenger Traffic, Behaviors, and Revenue - Financesonline.com.” [Online]. Available: <https://financesonline.com/number-of-flights-worldwide/>
- [4] M. Arifeen, “Air travel is taking flight again — The Economist.” [Online]. Available: <https://www.economist.com/business/2022/06/09/air-travel-is-taking-flight-again>
- [5] “Flightpath 2050 - Publications Office of the EU.” [Online]. Available: <https://op.europa.eu/en/publication-detail/-/publication/296a9bd7-fef9-4ae8-82c4-a21ff48be673>
- [6] P. Thalin, R. Rajamani, J.-C. Maré, and S. Taubert, *Fundamentals of Electric Aircraft: Revised Edition*, 2nd ed. Warrendale: SAE International, 2023.
- [7] “Home - ZeroAvia.” [Online]. Available: <https://zeroavia.com/>
- [8] K. Gundry, “Universal Hydrogen Successfully Completes First Flight of Hydrogen Regional Airliner — Universal Hydrogen,” 2023. [Online]. Available: <https://hydrogen.aero/press-releases/universal-hydrogen-successfully-completes-first-flight-of-hydrogen-regional-airliner/>

- [9] E. J. Adler and J. R. R. A. Martins, “Hydrogen-Powered Aircraft: Fundamental Concepts, Key Technologies, and Environmental Impacts,” Tech. Rep., 2023.
- [10] “Energy Management Systems for a Hybrid Electric Source (Application for a More Electric Aircraft) - MATLAB & Simulink - MathWorks United Kingdom.” [Online]. Available: <https://uk.mathworks.com/help/sps/ug/energy-management-systems-for-a-hybrid-electric-source-application-for-a-more-electric-aircraft.html>
- [11] “2019 Toyota Mirai - Toyota USA Newsroom.” [Online]. Available: <https://pressroom.toyota.com/vehicle/2019-mirai/>
- [12] “PemGen Solutions — Nedstack.” [Online]. Available: <https://nedstack.com/en/pemgen-solutions>
- [13] “Boeing tests first hydrogen powered plane.” [Online]. Available: <https://www.thetimes.com/article/boeing-tests-first-hydrogen-powered-plane-bwlfbjf6wrh>
- [14] J. Zhang, *PEM fuel cell testing and diagnosis*, J. Zhang, Ed. Amsterdam: Elsevier, 2013.
- [15] C. E. Thomas, “Fuel cell and battery electric vehicles compared,” *International Journal of Hydrogen Energy*, vol. 34, no. 15, pp. 6005–6020, 8 2009.
- [16] N. M. Souleman, O. Tremblay, and L. A. Dessaint, “A generic fuel cell model for the simulation of fuel cell power systems,” *2009 IEEE Power and Energy Society General Meeting, PES '09*, pp. 1722–1729, 2009.
- [17] A. Yulianto, M. Simic, D. Taylor, and P. Trivailo, “Modelling of full electric and hybrid electric fuel cells buses,” *Procedia Computer Science*, vol. 112, pp. 1916–1925, 1 2017. [Online]. Available: <https://www.sciencedirect.com/science/article/pii/S1877050917313777>

- [18] M. Lukic, P. Giangrande, C. Klumpner, and M. Galea, “Trade-off Analysis of Energy Storage Systems for Helicopter Landing Gear Electromechanical Actuator,” *IEEE International Symposium on Industrial Electronics*, vol. 2021-June, 6 2021.
- [19] D. P. Raymer, *Aircraft design : a conceptual approach*, sixth edition. ed., ser. AIAA education series. American Institute of Aeronautics and Astronautics, Inc., 2018.
- [20] S. Gudmundsson, *General aviation aircraft design : applied methods and procedures*, second edi ed. Butterworth-Heinemann, 2022.
- [21] D. F. Finger, *Methodology for Multidisciplinary Aircraft Design under Consideration of Hybrid-Electric Propulsion Technology*, 2020, no. September.
- [22] D. Hernandez Lugo, S. Clarke, T. Miller, M. Redifer, and T. Foster, “X-57 Maxwell Battery From cell level to system level design and testing,” Tech. Rep.
- [23] “Velis Electro - Pipistrel.” [Online]. Available: <https://www.pipistrel-aircraft.com/products/velis-electro/>
- [24] “spirit-of-innovation-factsheet.”
- [25] H. Budde-Meiwes, J. Drillkens, B. Lunz, J. Muennix, S. Rothgang, J. Kowal, and D. U. Sauer, “A review of current automotive battery technology and future prospects,” *Proceedings of the Institution of Mechanical Engineers, Part D: Journal of Automobile Engineering*, vol. 227, no. 5, pp. 761–776, 2013.
- [26] A. S. Sengupta, A. K. Chakraborty, and B. K. Bhattacharyya, “Modeling super capacitor discharge profile,” *1st IEEE International Conference on Power Electronics, Intelligent Control and Energy Systems, ICPEICES 2016*, 2 2017.
- [27] “Elysian Aircraft.” [Online]. Available: <https://www.elysianaircraft.com/>

- [28] “Heart Aerospace — Electrifying regional air travel.” [Online]. Available: <https://heartaerospace.com/>
- [29] Y. Chen, E. MacLi, and M. Poncino, “Workload-driven frequency-aware battery sizing,” in *Proceedings of the International Symposium on Low Power Electronics and Design*. Institute of Electrical and Electronics Engineers Inc., 8 2017.
- [30] O. Tremblay and L.-A. Dessaint, “Experimental Validation of a Battery Dynamic Model for EV Applications,” Tech. Rep.
- [31] A. K. Kundu, *Conceptual aircraft design : an industrial approach*, M. Price and D. Riordan, Eds. Wiley, 2019.
- [32] C. Pernet, C. Gologan, P. C. Vratny, A. Seitz, O. Schmitz, A. T. Isikveren, and M. Hornung, “Methodology for sizing and performance assessment of hybrid energy aircraft,” *Journal of Aircraft*, vol. 52, no. 1, pp. 341–352, 2015.
- [33] A. J. Colozza, “Hydrogen Storage for Aircraft Applications Overview,” Tech. Rep., 2002. [Online]. Available: <http://www.sti.nasa.gov>
- [34] J. O. Jensen, A. P. Vestbø, Q. Li, and N. J. Bjerrum, “The energy efficiency of onboard hydrogen storage,” *Journal of Alloys and Compounds*, vol. 446-447, pp. 723–728, 10 2007.
- [35] A. L. Dicks and D. A. J. Rand, *Fuel Cell Systems Explained (3rd Edition)*, third edition ed. Newark: John Wiley & Sons, 2018.
- [36] B. Gou, “Fuel cells : modeling, control, and applications,” Boca Raton, Fla. ;, 2010.
- [37] A. F. Abu Kasim, M. S. Chan, and E. J. Marek, “Performance and failure analysis of a retrofitted Cessna aircraft with a Fuel Cell Power System fuelled with liquid hydrogen,” *Journal of Power Sources*, vol. 521, 2 2022.

- [38] G. L. M. Vonhoff, “Conceptual Design of Hydrogen Fuel Cell Aircraft Flying on hydrogen for a more sustainable future by,” TUDelft, Tech. Rep., 2021. [Online]. Available: <http://repository.tudelft.nl/>.
- [39] S. N. Motapon, O. Tremblay, and L.-A. Dessaint, “Development of a generic fuel cell model: application to a fuel cell vehicle simulation of a generic fuel cell model: application to a fuel cell vehicle simulation’,” Tech. Rep. 6, 2012.
- [40] A. EL-Refaie and M. Osama, *High Specific Power Electrical Machines: A System Perspective*. IEEE, 2017.
- [41] P. Xie, G. Vakil, and C. Gerada, “Sizing, design, and modelling of aerospace electric drive system with long feeder cables,” *2019 IEEE International Electric Machines and Drives Conference, IEMDC 2019*, pp. 993–1000, 9 2019. [Online]. Available: <http://research.nottingham.edu.cn/en/publications/sizing-design-and-modelling-of-aerospace-electric-drive-system-wi>
- [42] H. Radmanesh, “Sizing Equations of Axial Flux Permanent Magnet (AFPM) Machine Based on an Analytical Method,” *Journal of applied research in Electrical Engineering*, vol. 1, no. 1, pp. 14–21, 2021.
- [43] G. L. Fidone, G. Migliazza, E. Carfagna, D. Benatti, F. Immovilli, G. Buticchi, and E. Lorenzani, “Common Architectures and Devices for Current Source Inverter in Motor-Drive Applications: A Comprehensive Review,” *Energies*, vol. 16, no. 15, 8 2023.
- [44] “Three-Phase Voltage Source Inverter Impact of Basic VSI Modulation Schemes on Harmonics.”
- [45] D. J. Roskam, “Roskam Airplane Design Part 1 : Preliminary Sizing Of Airplanes,” p. 187, 1985.
- [46] E. Aretskin-Hariton, M. Bell, S. Schnulo, and J. Gray, “Power Cable Mass Estimation for Electric Aircraft Propulsion,” Tech. Rep.

- [47] P. Abolmoali et al, “Integrated Propulsive and Thermal Management System Design for Optimal Hybrid Electric Aircraft Performance,” in *AIAA Propulsion and Energy 2020 Forum - Propulsion and Energy 2020 Forum*. American Institute of Aeronautics and Astronautics (AIAA), 2020, pp. 1–1.
- [48] K. Kitts, “CONTACTORS FOR AEROSPACE GROW SMARTER AND MORE CAPABLE,” Tech. Rep.
- [49] —, “EVC 250 Main Contactor White Paper from TE Connectivity,” Tech. Rep.
- [50] “BSBC8V-500A High Voltage DC Contactor for EV Applications.” [Online]. Available: [https://bsbelectric.com/product/c8v-500a-high-voltage-dc-contactor/?utm\\_source=chatgpt.com](https://bsbelectric.com/product/c8v-500a-high-voltage-dc-contactor/?utm_source=chatgpt.com)
- [51] “1000V 200A DC Contactor for EV — BSB Electric.” [Online]. Available: [https://bsbelectric.com/product/c8v-200a-dc-contactor-for-ev/?utm\\_source=chatgpt.com](https://bsbelectric.com/product/c8v-200a-dc-contactor-for-ev/?utm_source=chatgpt.com)
- [52] “DC contactor high current - 12-1000V DC Contactor,EVQ Series.” [Online]. Available: [https://www.hotsoninternational.com/product/evq500/?utm\\_source=chatgpt.com](https://www.hotsoninternational.com/product/evq500/?utm_source=chatgpt.com)
- [53] “EV200 electric vehicle contactor - 12-1000V DC Contactor,EVQ Series.” [Online]. Available: [https://www.hotsoninternational.com/product/evq200/?utm\\_source=chatgpt.com](https://www.hotsoninternational.com/product/evq200/?utm_source=chatgpt.com)
- [54] J. G. Coffin, “A STUDY OF AIRPLANE RANGES AND USEFUL LOADS,” Tech. Rep., 1920.
- [55] M. Cavcar, “Bréguet range equation?” *Journal of Aircraft*, vol. 43, no. 5, pp. 1542–1544, 2006.
- [56] C. H. Latimer Needham, *Sailplanes their Design Construction and Pilotage*, 1937.

- [57] D. P. Raymer, *Enhancing Aircraft Conceptual Design Using Multidisciplinary Optimization*, 2002, no. May.
- [58] L. M. L. M. Nicolai, *Fundamentals of aircraft and airship design. Volume 1, Aircraft design*, ser. AIAA educational series, G. Carichner and L. M. L. M. Nicolai, Eds. Reston, Va.: American Institute of Aeronautics and Astronautics, 2010.
- [59] J. Roskam, *Airplane design*. Lawrence, Kan.: DARcorporation, 2003.
- [60] D. Scholz and M. Nita, “Preliminary Sizing of Large Propeller Driven Aeroplanes,” Tech. Rep., 2009. [Online]. Available: <http://www.vzlu.cz/>.
- [61] “DORNIER A-5 AIRFOIL (doa5-il).” [Online]. Available: <http://airfoiltools.com/airfoil/details?airfoil=doa5-il>
- [62] “The Incomplete Guide to Airfoil Usage.” [Online]. Available: <https://m-selig.ae.illinois.edu/ads/aircraft.html>
- [63] “NACA 0012 AIRFOILS (n0012-il).” [Online]. Available: <http://airfoiltools.com/airfoil/details?airfoil=n0012-il>
- [64] G. Anilkumar, N. Puneetha, G. V. Brahmendra Kumar, K. Palanisamy, and A. Gupta, “Design and testing of proton exchange membrane fuel cell (PEMFC) power pack for platform vehicle,” in *IOP Conference Series: Materials Science and Engineering*, vol. 937, no. 1. IOP Publishing Ltd, 10 2020.
- [65] M. Pettes-Duler, X. Roboam, and B. Sareni, “Integrated Optimal Design for Hybrid Electric Powertrain of Future Aircrafts,” *Energies*, vol. 15, no. 18, 9 2022.
- [66] J. Ebersberger, L. Fauth, R. Keuter, Y. Cao, Y. Freund, R. Hanke-Rauschenbach, B. Ponick, A. Mertens, and J. Friebe, “Power Distribution

- and Propulsion System for an All-Electric Short-Range Commuter Aircraft - A Case Study,” *IEEE Access*, vol. 10, pp. 114 514–114 539, 2022.
- [67] N. J. Lawson, H. Jacques, J. E. Gautrey, A. K. Cooke, J. C. Holt, and K. P. Garry, “Jetstream 31 national flying laboratory: Lift and drag measurement and modelling,” *Aerospace Science and Technology*, vol. 60, pp. 84–95, 1 2017.
- [68] Y. Liu, A. Elham, P. Horst, and M. Hepperle, “Exploring vehicle level benefits of revolutionary technology progress via aircraft design and optimization,” *Energies*, vol. 11, no. 1, 1 2018.
- [69] S. Mane, “Aircraft Electrical System: Short Review,” Tech. Rep. 2, 2024. [Online]. Available: [www.ijaresm.com](http://www.ijaresm.com)
- [70] T. Roinila, T. Messo, R. Luhtala, R. Scharrenberg, E. C. De Jong, A. Fabian, and Y. Sun, “Hardware-in-the-Loop Methods for Real-Time Frequency-Response Measurements of on-Board Power Distribution Systems,” *IEEE Transactions on Industrial Electronics*, vol. 66, no. 7, pp. 5769–5777, 7 2019.
- [71] V. Madonna, P. Giangrande, and M. Gaela, “Electrical Power Generation in Aircraft.”
- [72] R. Wilkinson, *Aircraft Structures and Systems*, 1st ed. Mechaero Publishing, 2001, vol. 1.
- [73] R. Erickson and D. Maksimovic, *Fundamentals of Power Electronics*, 1st ed. New York, NY: Springer, 2013.
- [74] A. Castaldo, “Switching regulator fundamentals Application Report Switching regulator fundamentals,” Tech. Rep., 2012. [Online]. Available: [www.ti.com](http://www.ti.com)
- [75] N. Mohan, “Power Electronics Converters, Applications and Design 3rd,” *John Wiley & Sons*, p. 811, 2003.

- [76] “How to Understand Power Inductors Parameters for DC/DC Converters — SOS ELECTRONIC,” 2017. [Online]. Available: <https://www.soselectronic.com/en-gg/articles/sos-supplier-of-solution/how-to-understand-power-inductors-parameters-for-dc-dc-converters-2005>
- [77] H. Wang, “Design and control of a 6-phase Interleaved Boost Converter based on SiC semiconductors with EIS functionality for Fuel Cell Electric Vehicle,” Tech. Rep., 2019. [Online]. Available: <https://theses.hal.science/tel-02185678v1>
- [78] G. R. Chandra Mouli, J. H. Schijffelen, P. Bauer, and M. Zeman, “Design and comparison of a 10-kW interleaved boost converter for PV application using Si and SiC devices,” *IEEE Journal of Emerging and Selected Topics in Power Electronics*, vol. 5, no. 2, pp. 610–623, 6 2017.
- [79] A. Ikriannikov, “Considerations for the Output Current and Voltage Ripple in a Multiphase Buck with Coupled Inductors — Analog Devices,” 2024. [Online]. Available: <https://www.analog.com/en/resources/analog-dialogue/articles/output-current-and-volt-ripple-in-multiphase-buck.html>
- [80] C. Parisi, “Multiphase Buck Design From Start to Finish (Part 1),” Tech. Rep., 2021. [Online]. Available: [www.ti.com](http://www.ti.com)
- [81] G. Calderon-Lopez, J. Scoltock, Y. Wang, I. Laird, X. Yuan, and A. J. Forsyth, “Power-Dense Bi-Directional DC-DC Converters with High-Performance Inductors,” *IEEE Transactions on Vehicular Technology*, vol. 68, no. 12, pp. 11 439–11 448, 12 2019.
- [82] J. W. Kolar, U. Drogenik, J. Biela, M. L. Heldwein, H. Ertl, T. Friedli, and S. D. Round, “PWM converter power density barriers,” in *Fourth Power Conversion Conference-NAGOYA, PCC-NAGOYA 2007 - Conference Proceedings*, 2007.

- [83] R. Saeed, “Design and Characterisation of a High Energy-Density Inductor,” Tech. Rep., 2017.
- [84] W. T. McLyman, *Transformer and Inductor Design Handbook.*, 4th ed. Taylor & Francis Group, 2011.
- [85] Andres Revilla Aguilar, “Permanent Magnet Biased Inductors: And Additional investigations on: Biasing topologies for AC applications, Parametric transformers using permanent magnets, and Optimization of conduction losses on planar transformer windings,” 2023. [Online]. Available: <https://vbn.aau.dk/en/publications/permanent-magnet-biased-inductors-and-additional-investigations-o>
- [86] A. R. Aguilar, S. Munk-Nielsen, F. B. Bendixen, Z. Ouyang, M. Duffy, and H. Zhao, “Permanent Magnet Biased Inductors; an Overview,” *IEEE Open Journal of Power Electronics*, 2024.
- [87] J. T. Ludwig, “Inductors Biased with Permanent Magnets Part I-Theory and Analysis,” Tech. Rep.
- [88] G. M. Shane and S. D. Sudhoff, “Design and Optimization of Permanent Magnet Inductors.”
- [89] “Mn-Zn Ferrite Material Characteristics,” Tech. Rep.
- [90] “NiZn Ferrite Core,” Tech. Rep. [Online]. Available: [www.abracon.com](http://www.abracon.com)
- [91] “Metglas AMCC Series Cut Core,” Tech. Rep.
- [92] S. P. McDonald, G. J. Atkinson, R. Martin, and S. Ullah, “Magnetically biased inductor for an aerospace switched reluctance drive,” in *Proceedings - 2015 IEEE International Electric Machines and Drives Conference, IEMDC 2015*. Institute of Electrical and Electronics Engineers Inc., 2016, pp. 1272–1278.

- [93] C. Heitsch, “Sensitivity Analysis for Design Variables of Hybrid Electric General Aviation Aircraft,” Tech. Rep., 2019.
- [94] D. Felix Finger, R. de Vries, R. Vos, C. Braun, and C. Bil, “A comparison of hybrid-electric aircraft sizing methods,” in *AIAA Scitech 2020 Forum*, vol. 1 PartF. American Institute of Aeronautics and Astronautics Inc, AIAA, 2020.
- [95] Taylor Ryan, “G-HFZA — Dornier Do-228-200 — ZeroAvia — Ryan Taylor — JetPhotos,” 2024. [Online]. Available: <https://www.jetphotos.com/photo/11304799>
- [96] F. T. Jane, *Jane’s All the world’s aircraft*, 87th ed., ser. Jane’s yearbooks, P. A. Jackson, Ed. Coulsdon: Jane’s Information Group, 1996.
- [97] EASA, “Easy Access Rules for Normal, Utility, Aerobatic and Commuter Category Aeroplanes (CS-23) (Initial issue),” Tech. Rep.
- [98] “SUAVE.” [Online]. Available: <https://suave.stanford.edu/>
- [99] “OpenVSP.” [Online]. Available: <https://openvsp.org/>
- [100] “Boeing 787 Dreamliner : Analysis.” [Online]. Available: <https://www.lissys.uk/samp1/index.html>
- [101] J. D. Mattingly, *Aircraft Engine Design.*, 2nd ed., ser. AIAA Education Series, W. H. Heiser and D. T. Pratt, Eds. American Institute of Aeronautics and Astronautics, 2000.
- [102] “TPE331-10 TURBOPROP ENGINE,” Tech. Rep., 2016.
- [103] E. Torenbeek, *Synthesis of Subsonic Airplane Design*, 1977, vol. 22.
- [104] L. M. L. M. Nicolai, G. Carichner, and L. M. L. M. Nicolai, “Fundamentals of aircraft and airship design. Volume 2 Airship Design and Case Studies,” 2010.

- [105] D. Hao, J. Shen, Y. Hou, Y. Zhou, and H. Wang, “An Improved Empirical Fuel Cell Polarization Curve Model Based on Review Analysis,” *International Journal of Chemical Engineering*, vol. 2016, 2016.
- [106] J. Ryes, W. Chapman, S. L. Schnulo, and M. P. Nitzsche, “Development of a Thermal Management System for Electrified Aircraft,” Tech. Rep., 2020. [Online]. Available: <http://www.sti.nasa.gov>
- [107] T. Leo, “Fuel Cell Efficiency Explained — FuelCell Energy,” 2023. [Online]. Available: <https://www.fuelcellenergy.com/blog/fuel-cell-efficiency>
- [108] U. Bossel and B. Eliasson, “Energy Hydrogen Economy,” Tech. Rep.
- [109] R. M. Dell, P. T. Moseley, and D. A. Rand, “Towards Sustainable Road Transport,” *Towards Sustainable Road Transport*, pp. 1–345, 1 2014. [Online]. Available: <http://www.sciencedirect.com:5070/book/9780124046160/towards-sustainable-road-transport>
- [110] “Horizon Educational - What’s the Molar Mass of Hydrogen?” [Online]. Available: <https://www.horizeducational.com/what-s-the-molar-mass-of-hydrogen/t1496?currency=usd>
- [111] “Dornier 228 Advanced Commuter Facts and Figures,” Tech. Rep.
- [112] “Aircraft Ferry Tanks.” [Online]. Available: <https://www.turtlepac.com/photo-gallery/aircraft-ferry-tanks/>
- [113] “Airplane Shippers — Transporting Aircrafts — Heavy Haulers.” [Online]. Available: <https://www.heavyhaulers.com/airplane-transport.php>
- [114] “Aerotow - Lesson 16.” [Online]. Available: <https://www.gliding.world/index.php/gliding-the-basics/4-16-aerotow>
- [115] “Airspeed Horsa Glider — BAE Systems.” [Online]. Available: <https://www.baesystems.com/en-uk/heritage/airspeed-horsa-glider>

- [116] J. Chisholm, “FUNDAMENTALS OF GAS LAWS,” Tech. Rep.
- [117] “Hydrogen Compressibility at different temperatures and pressures — H2tools — Hydrogen Tools.” [Online]. Available: <https://h2tools.org/hyarc/hydrogen-data/hydrogen-compressibility-different-temperatures-and-pressures>
- [118] “The Power of Electric Flight D500 (1K T ),” Tech. Rep. [Online]. Available: [www.evolito.aero](http://www.evolito.aero)
- [119] M. Pettes-Duler, X. Roboam, and B. Sareni, “Integrated Optimal Design for Hybrid Electric Powertrain of Future Aircrafts,” *Energies*, vol. 15, no. 18, 9 2022.
- [120] N. E. Anderson, S. H. Loewenthal, J. D. Black, A. Gas, and T. Operations, “AN ANALYTICAL METHOD TO PREDICT EFFICIENCY OF AIRCRAFT GEARBOXES,” Tech. Rep., 1984.
- [121] M. H. Jahanbakhshi and M. Etezadinejad, “Modeling and Current Balancing of Interleaved Buck Converter Using Single Current Sensor,” in *ICEE 2019 - 27th Iranian Conference on Electrical Engineering*. Institute of Electrical and Electronics Engineers Inc., 4 2019, pp. 662–667.
- [122] R. Walmsley, “Design of a Permanent Magnet Synchronous Motor Drive System with Comprehensive Tuning,” University of Newcastle, Tech. Rep., 2021.
- [123] M. Jaberipour, E. Khorram, and B. Karimi, “Particle swarm algorithm for solving systems of nonlinear equations,” *Computers and Mathematics with Applications*, vol. 62, no. 2, pp. 566–576, 7 2011.
- [124] “EC-lab Products SP-50/150,” Tech. Rep. [Online]. Available: [www.artisanng.com](http://www.artisanng.com)
- [125] “Installation and Configuration Manual for VMP3-based Instruments,” Tech. Rep.

- [126] “Coilcraft Inductor Losses,” 2018.
- [127] J. Allmeling, W. Hammer, and J. Schönberger, “Transient Simulation of Magnetic Circuits Using the Permeance-Capacitance Analogy,” Tech. Rep., 2012.
- [128] “CAS100H12AM1-475725.”

# Appendices

# Appendix A

## Part Power Tables for Honeywell

### TPE331-10

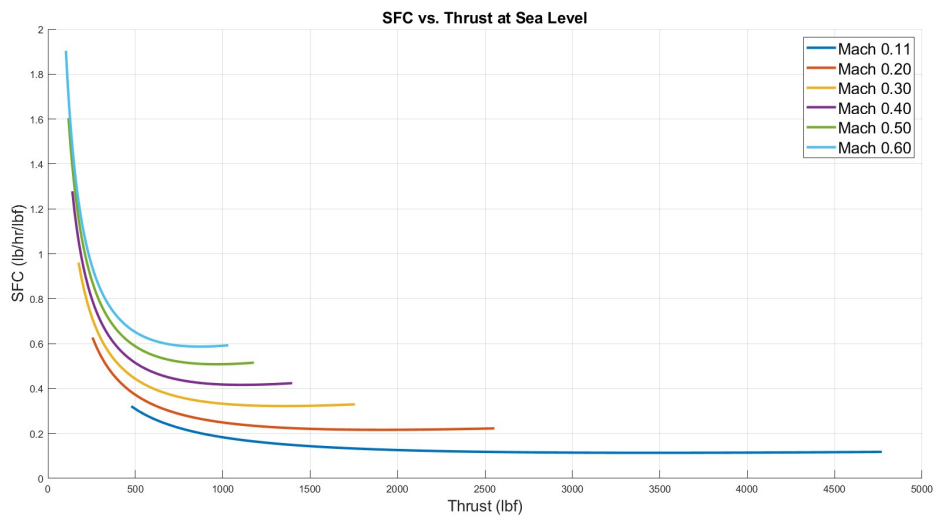


Figure A.1: Specific Fuel Consumption (SFC) with Altitude and Mach Number

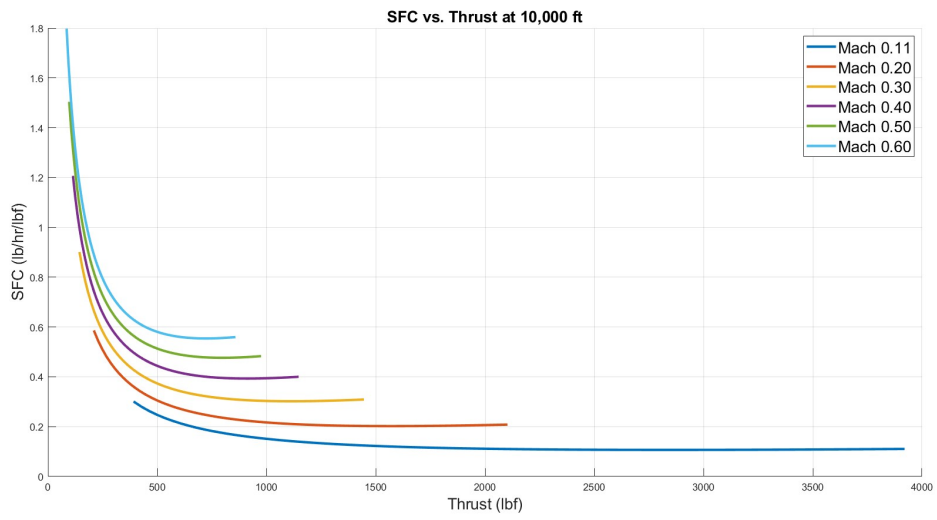


Figure A.2: Specific Fuel Consumption (SFC) with Altitude and Mach Number

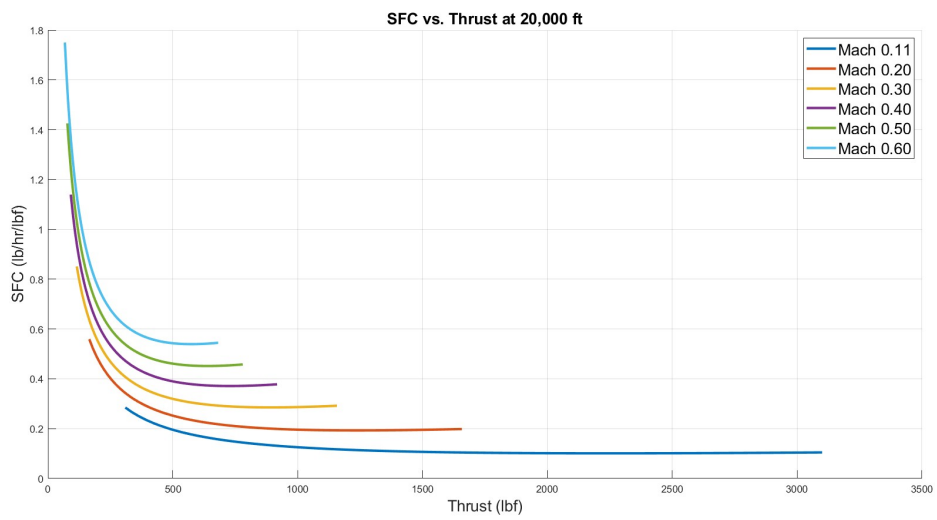


Figure A.3: Specific Fuel Consumption (SFC) with Altitude and Mach Number

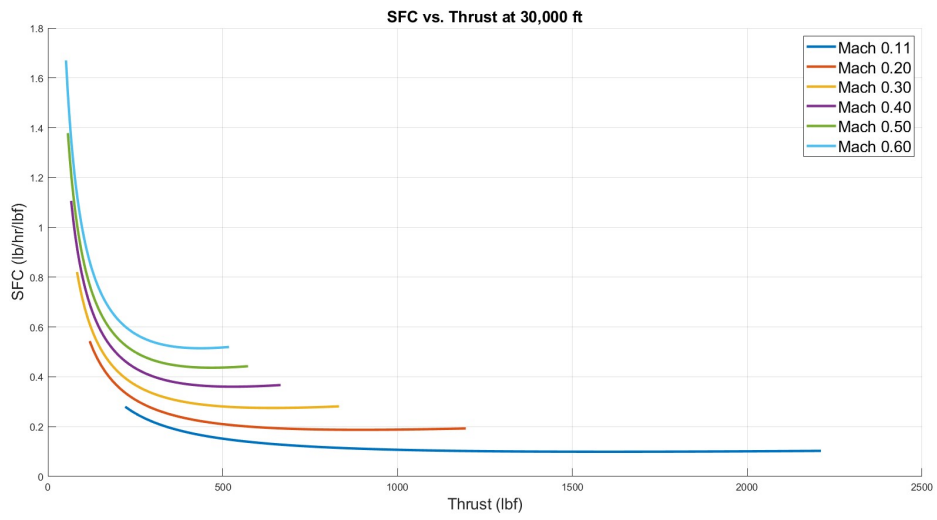


Figure A.4: Specific Fuel Consumption (SFC) with Altitude and Mach Number

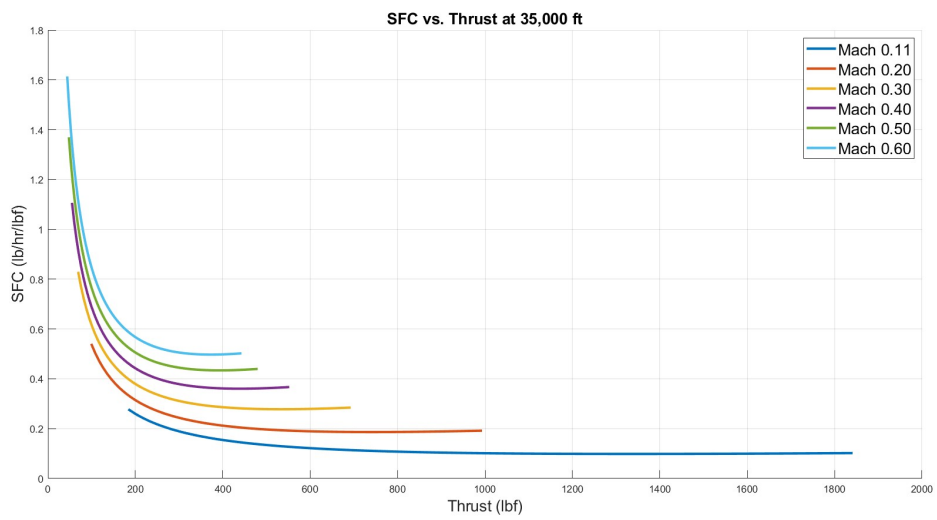


Figure A.5: Specific Fuel Consumption (SFC) with Altitude and Mach Number

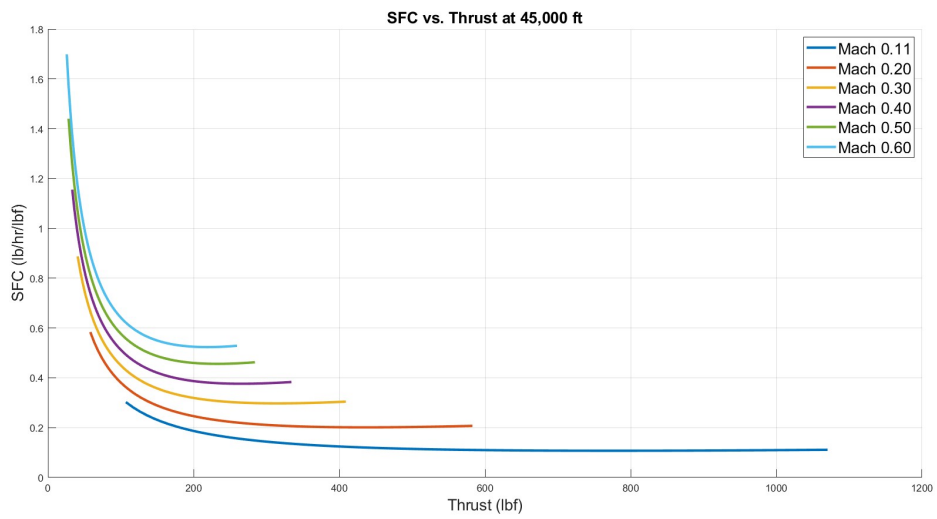


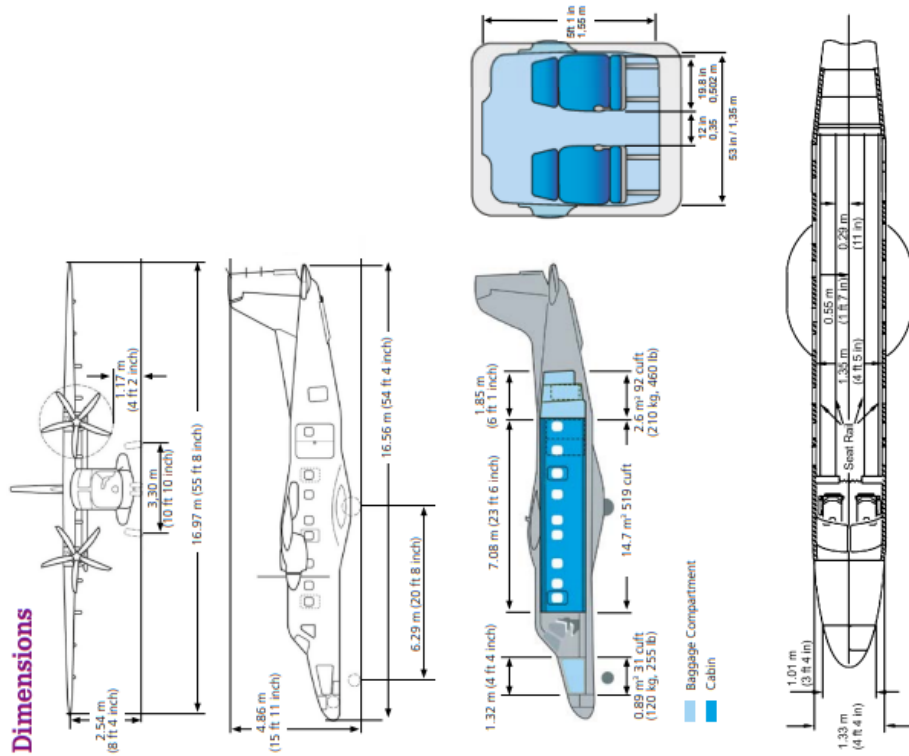
Figure A.6: Specific Fuel Consumption (SFC) with Altitude and Mach Number

# Appendix B

## Dornier 228 Brochure Specifications

# Aircraft Specifications

## Dimensions



Principal dimensions	
Overall height	15 ft 11 in (4.86 m)
Overall length	54 ft 4 in (16.56 m)
Wing	
Span	55 ft 8 in (16.97 m)
Area	344.3 ft <sup>2</sup> (32.00 m <sup>2</sup> )
Aspect ratio	9.0
Taper ratio	0.7
Sweepback of leading edge inboard	0°/outboard 8°
Vertical stabilizer	
Height	8 ft 10 in (2.70 m)
Area	64.6 ft <sup>2</sup> (6.0 m <sup>2</sup> )
Aspect ratio	1.50
Taper ratio	0.46
Rudder area	16.1 ft <sup>2</sup> (1.5 m <sup>2</sup> )
Rudder deflection	-24°/+24°
Passenger compartment	
Overall length, max.	23 ft 3 in (7.08 m)
Maximum width	4 ft 4 in (1.328 m)
Maximum height	5 ft 1 in (1.55 m)
Horizontal stabilizer	
Span	21 ft 2 in (6.45 m)
Area	89.6 ft <sup>2</sup> (8.33 m <sup>2</sup> )
Aspect ratio	5.00
Taper ratio	1.00
Elevator deflection	-30°/+25°
Ailerons	
Span	8 ft 10 in (2.69 m)
Area	2x14.5 ft <sup>2</sup> (2x1.345 m <sup>2</sup> )
Deflection (Flaps 0°)	25° up/18° down
Chord	30%
Doors (height x width)	
Cockpit door	2 ft 9 in x 2 ft 2 in (0.84 m x 0.65 m)
Passenger airstair door	4 ft 5 in x 2 ft 1 in (1.34 m x 0.64 m)
Passenger/cargo door (both door panels are open)	4 ft 5 in x 4 ft 2 in (1.34 m x 1.28 m)
Baggage door (front)	3 ft 11 in x 1 ft 8 in (1.2 m x 0.5 m)
Baggage door (rear)	2 ft 11 in x 1 ft 9 in (0.89 m x 0.53 m)
Emergency exits (3)	2 ft 2 in x 1 ft 7 in (0.67 m x 0.48 m)

## Weights

	lb	kg
Max. take-off weight (MTOW*)	14,110	6,400
Max. landing weight	13,448	6,100
Max. zero fuel weight (MZFW)	13,095	5,940
Operating weight empty (with 2 Pilots) (OWE)	8,598	3,900
Mission equipment (incl. operator and console)	1,047	475
Max. fuel	4,156	1,885

\* e.g. optional MTOW increase to 6,575 kg (14,550 lbs) possible

Figure B.1: Dornier 228 Specification Sheet

# Appendix C

## 85kW Fuel Cell Time Response Fitting Plots

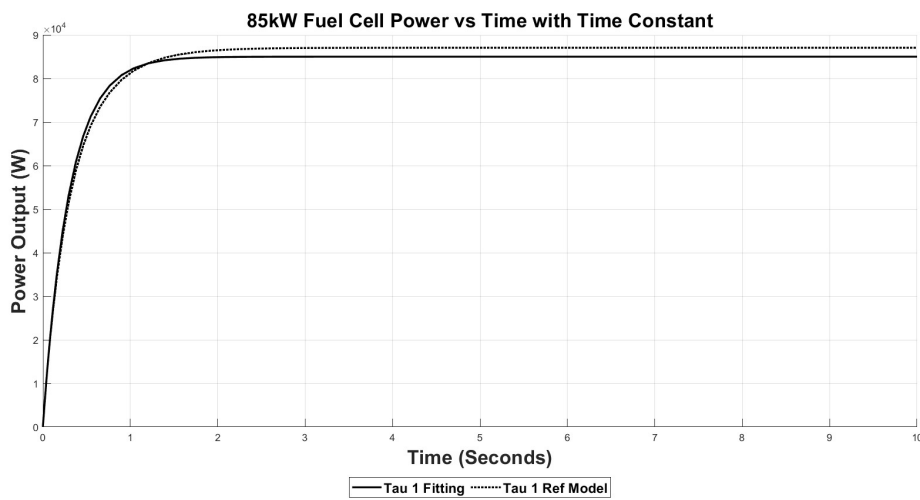


Figure C.1: Tau1

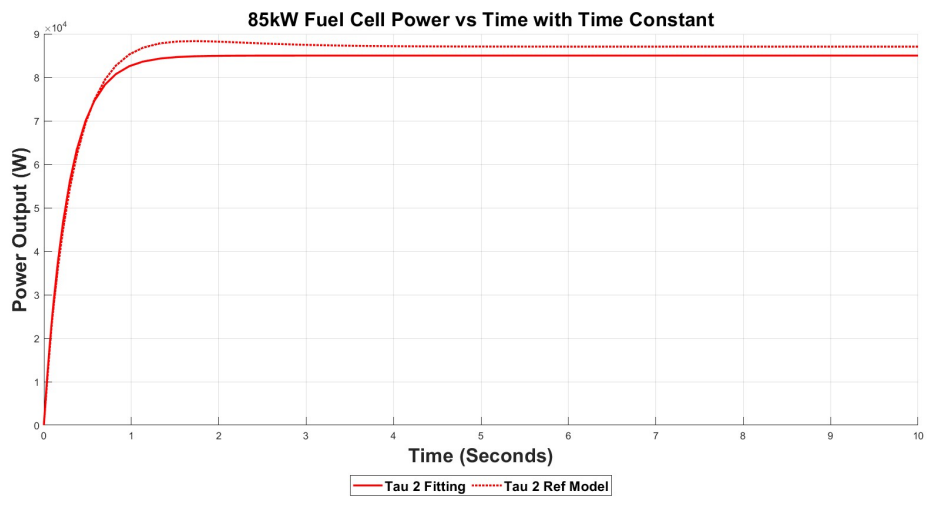


Figure C.2: Tau2

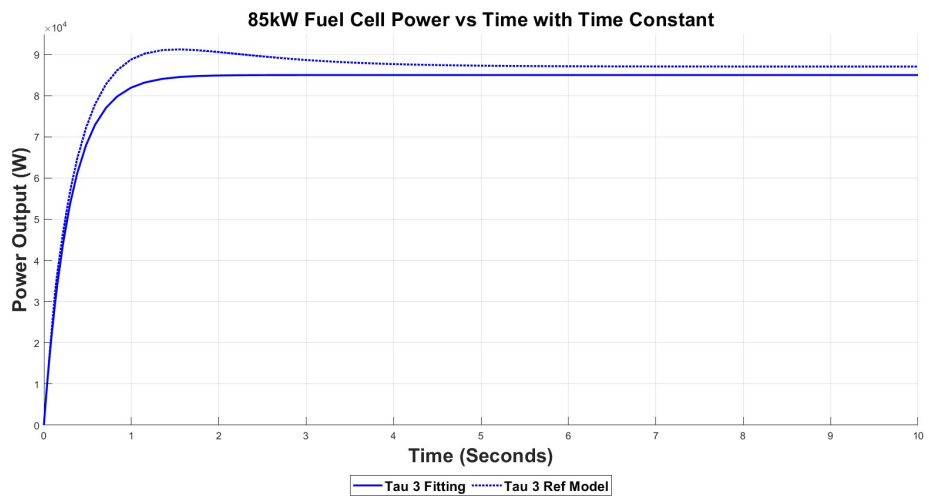


Figure C.3: Tau3

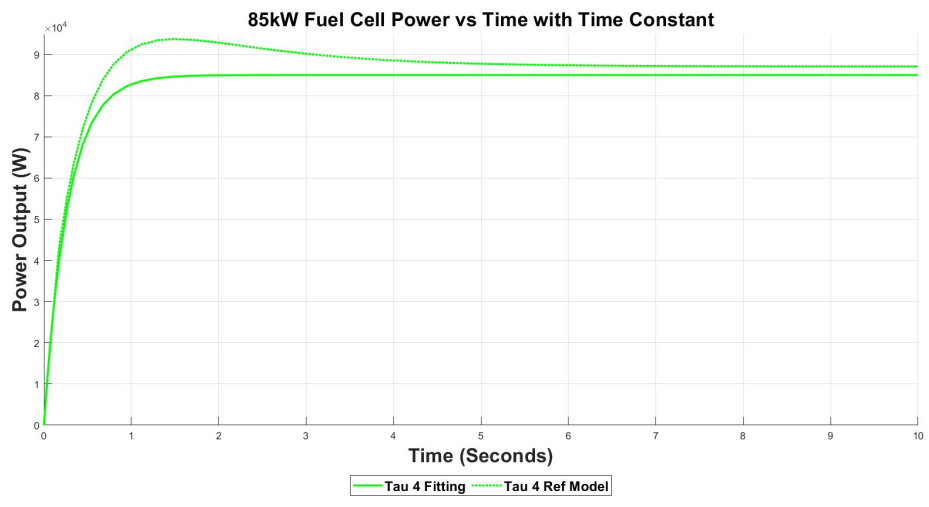


Figure C.4: Tau4

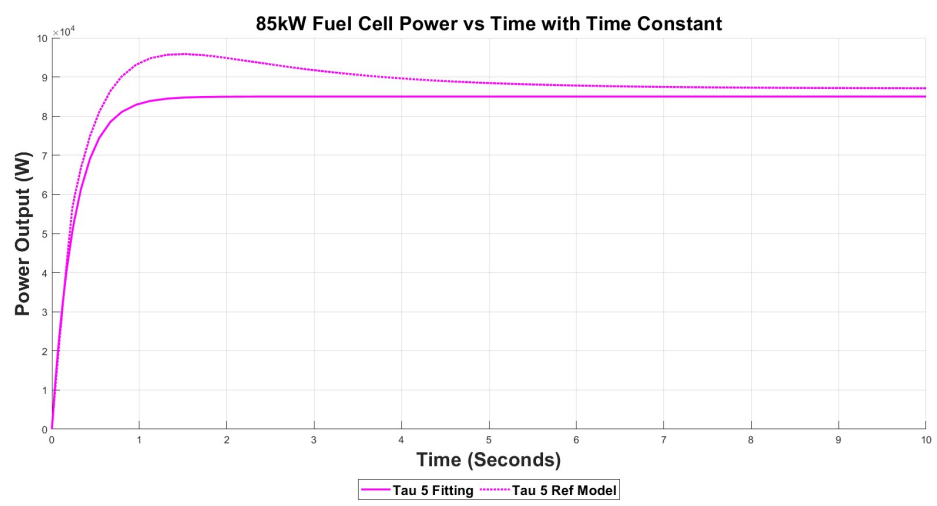


Figure C.5: Tau5

# Appendix D

## Evolito D500 Data Sheet

# D500 (1K<sub>T</sub>)

AXIAL FLUX ELECTRIC MOTOR

**Evolito**  
The Power of Electric Flight

Electrified aerospace applications where the D500 is suitable:

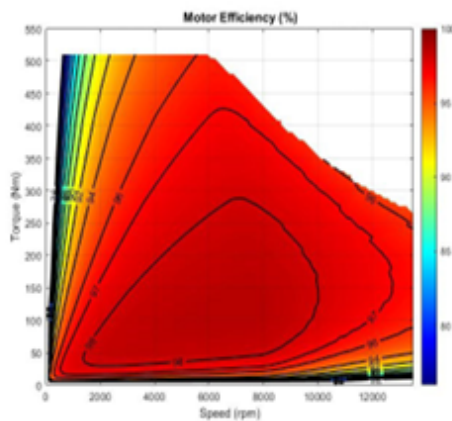
- For single and multi-propellor, fixed wing aviation applications
- E-VTOL and UAM applications
- Rotary aircraft solutions
- For indirect (geared) propulsion applications



Evolito's eMotors are the smallest and lightest in their performance class. The eMotors use less material to yield higher torque and power densities than comparable motor types.

Versatile form factor allows options for design integration with the ability to increase performance by stacking motors.

Fig1. Efficiency map for D500 machine only, using an 800Vdc capable system.



Notes: Peak data are based on a coolant inlet temperature of 55°C, flow rate of 15 l/min and 30°C ambient temperature. Actual performance will vary with drive cycle, cooling and installing details.

Please contact us to discuss your application requirements. We can then supply detailed information on the Evolito products and options that may be suitable for you.

## Key Specifications

(Preliminary data)

Maximum TO Torque	500Nm
Maximum TO Power	300kW @ 6,000rpm
Maximum Cruise Torque*	280Nm
Maximum Cruise Power*	230kW @ 8,000rpm
Max Speed	9,000rpm
Mass	~28kg
Size	345mm X 123mm

\*Continuous

## Key Benefits

- Best in class torque density.  
Peak torque density > 18 Nm/kg
- Dimensions just 345mm (D) x 123mm (L)
- Integrated position and temperature sensors
- Through-shaft mounting, may be stacked for increased torque and power
- Customisable winding options available, to suit different applications and optimise performance points

www.evolito.aero | +44 (0) 1865 967700 | sales@evolito.aero

©2022 Evolito Ltd. | Private & Confidential - not to be shared with third parties. | Registered in England and Wales No. 11308921

V4

Figure D.1

# D500 (1K<sub>T</sub>)

AXIAL FLUX ELECTRIC MOTOR

**Evolito**  
The Power of Electric Flight

## Peak and Continuous Torque

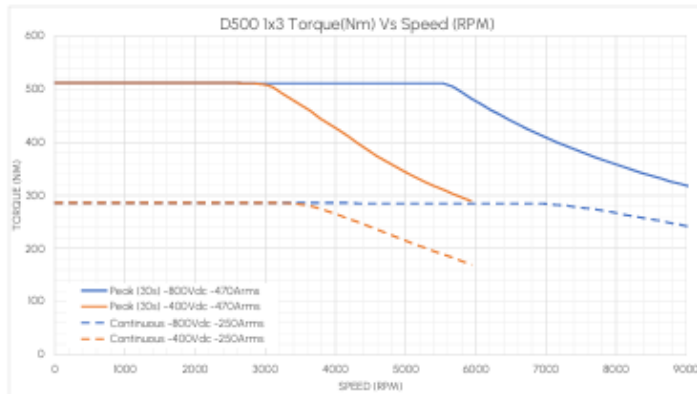


**Fig2.** The Evolito D500 is capable of maintaining 280Nm torque for continuous periods of time, setting a new benchmark in continuous torque delivery from a lightweight production intent design, whilst also delivering best in class torque density of 18Nm/Kg.

## Peak and Continuous Power



**Fig3.** The Evolito D500 achieves a continuous 230 kW and up to 300kW during peak testing conditions. This industry leading product offering is breaking conventional radial limits, boasting greater than 10kW/Kg+.

www.evolito.aero | +44 (0) 1865 967700 | sales@evolito.aero

©2022 Evolito Ltd. | Private & Confidential - not to be shared with third parties. | Registered in England and Wales No. 11308921

V4

Figure D.2

# Appendix E

**AMCC METGLAS © Alloy**

**2605SA1 Core Material Properties**

Table E.1: AMCC METGLAS © Alloy 2605SA1 Core Material Properties

Physical Properties of METGLAS Alloy 2605SA1	
Parameter	Value
Ribbon Thickness ( $\mu m$ )	23
Density ( $\frac{g}{m^3}$ )	7.18
Thermal Expansion ( $\frac{ppm}{^\circ C}$ )	7.6
Crystallisation Temperature ( $^\circ C$ )	508
Curie Temperature ( $^\circ C$ )	399
Continuous Service Temperature ( $^\circ C$ )	150
Tensile Strength ( $\frac{MN}{m^2}$ )	1k-1.7k
Elastic Modulus ( $\frac{GN}{m^2}$ )	100-110
Vicker's Hardness (50g load)	900
Magnetic Properties of METGLAS Alloy 2605SA1	
Parameter	Value
Saturation Flux Density ( $T$ )	1.56
Permeability (depending on gap size)	VARIABLE
Saturation Magnetostriction ( $ppm$ )	27
Electrical Resistivity $\mu\Omega.cm$	130

# Appendix F

## PLECS Closed Loop Simulation

### Results for MEC Inductor

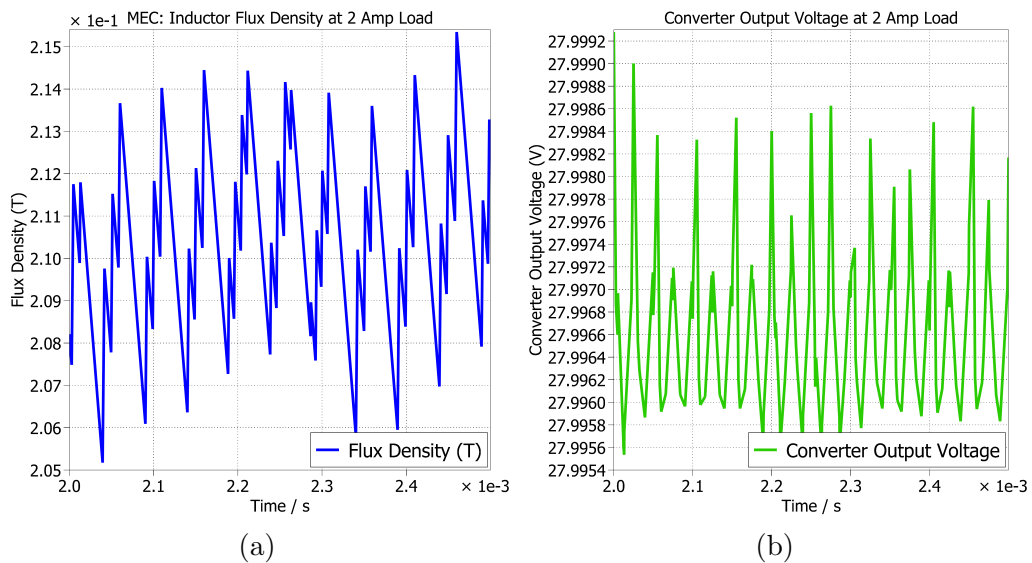


Figure F.1: a) MEC Inductor Flux Density Waveform at converter Load of 2 Amps  
b) Output Voltage Waveform for Converter Load of 2 Amps

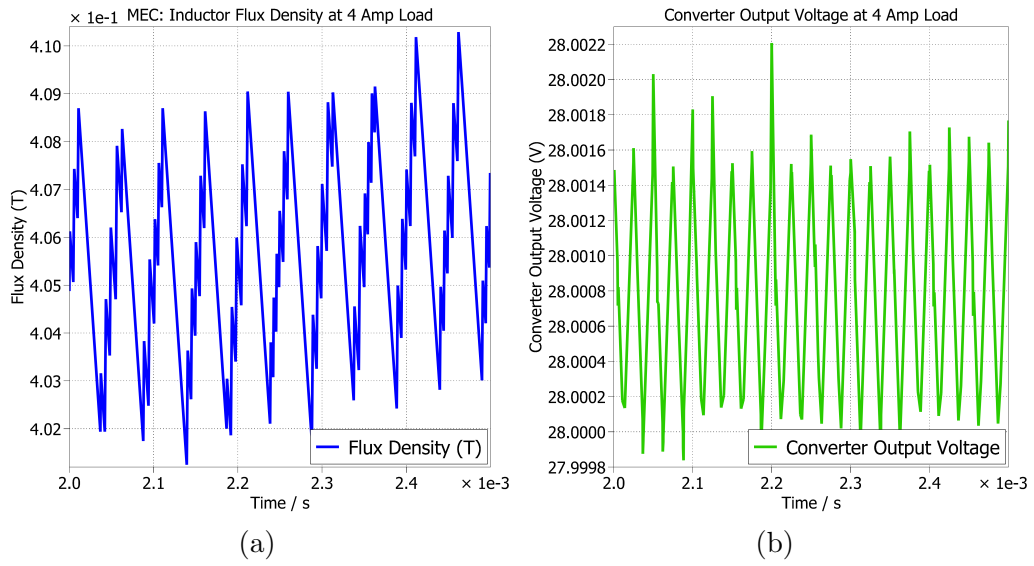


Figure F.2: a) MEC Inductor Flux Density Waveform at converter Load of 4 Amps  
 b) Output Voltage Waveform for Converter Load of 4 Amps

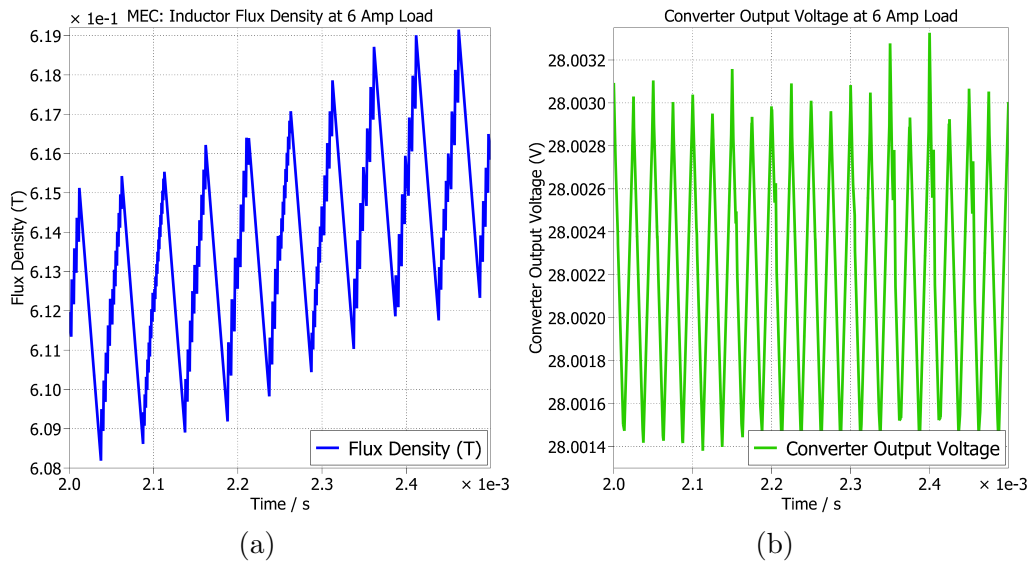


Figure F.3: a) MEC Inductor Flux Density Waveform at converter Load of 6 Amps  
 b) Output Voltage Waveform for Converter Load of 6 Amps

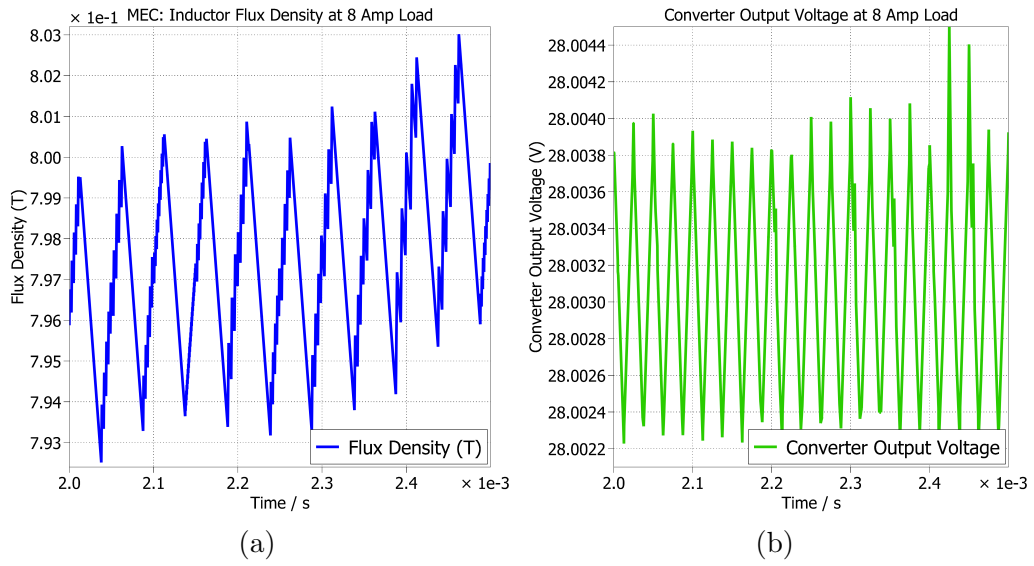


Figure F.4: a) MEC Inductor Flux Density Waveform at converter Load of 8 Amps  
 b) Output Voltage Waveform for Converter Load of 8 Amps

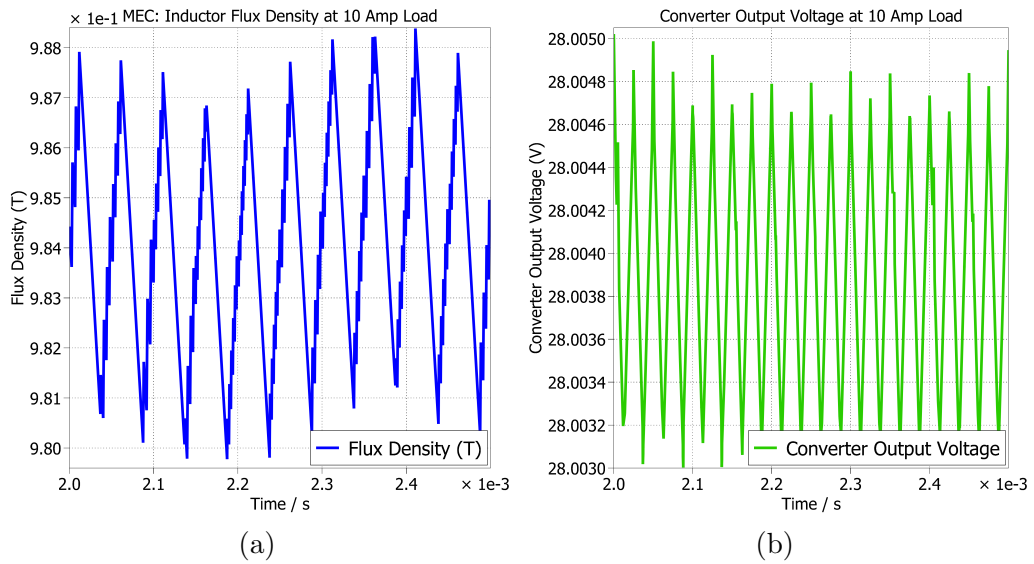


Figure F.5: a) MEC Inductor Flux Density Waveform at converter Load of 10 Amps  
 b) Output Voltage Waveform for Converter Load of 10 Amps

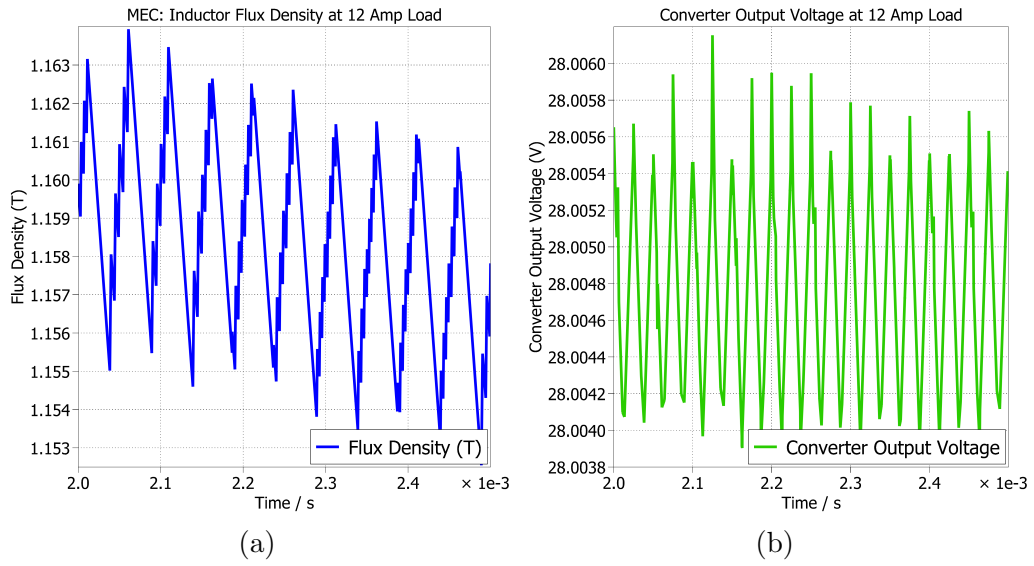


Figure F.6: a) MEC Inductor Flux Density Waveform at converter Load of 12 Amps  
 b) Output Voltage Waveform for Converter Load of 12 Amps

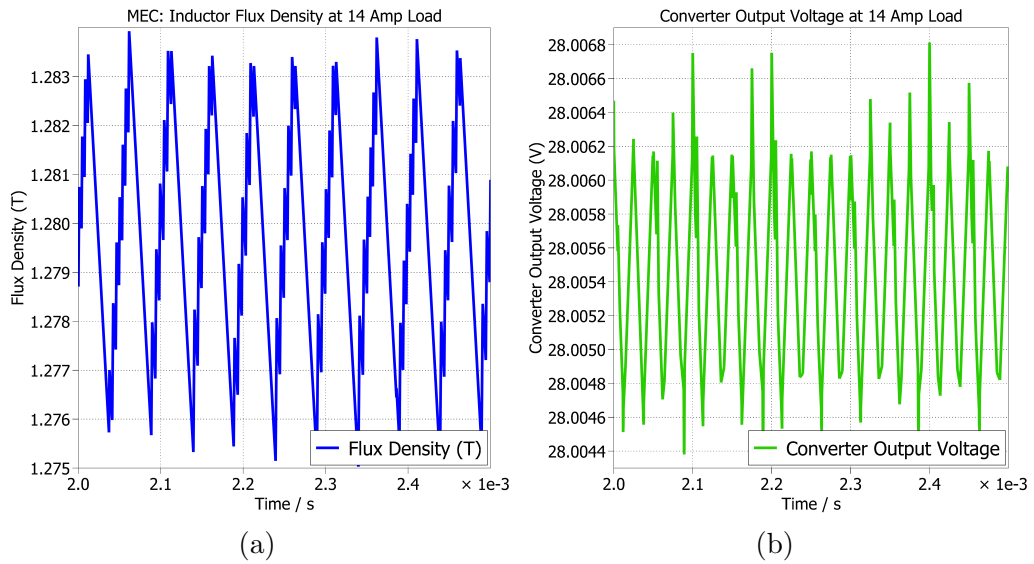


Figure F.7: a) MEC Inductor Flux Density Waveform at converter Load of 14 Amps  
 b) Output Voltage Waveform for Converter Load of 14 Amps

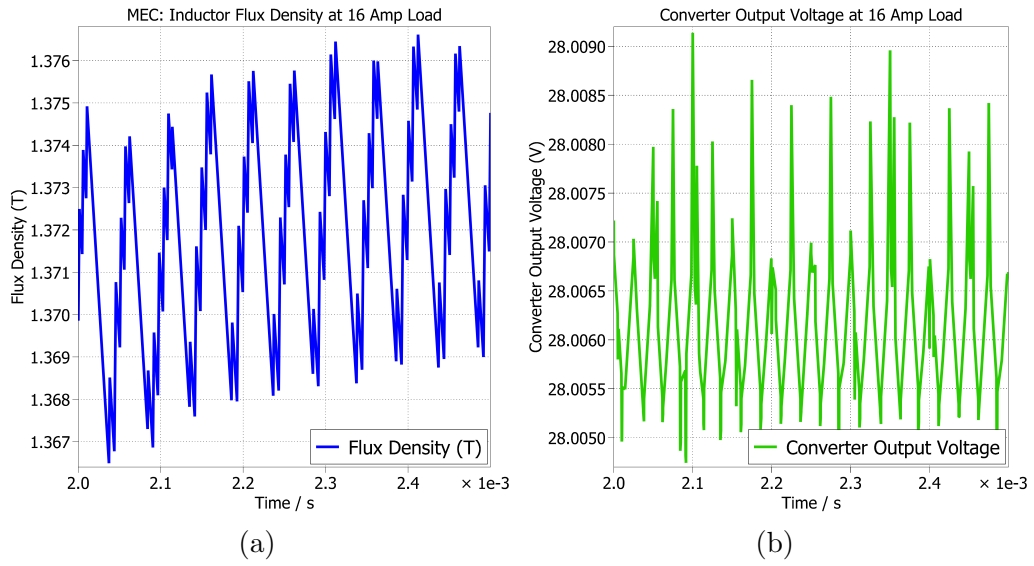


Figure F.8: a) MEC Inductor Flux Density Waveform at converter Load of 16 Amps  
 b) Output Voltage Waveform for Converter Load of 16 Amps

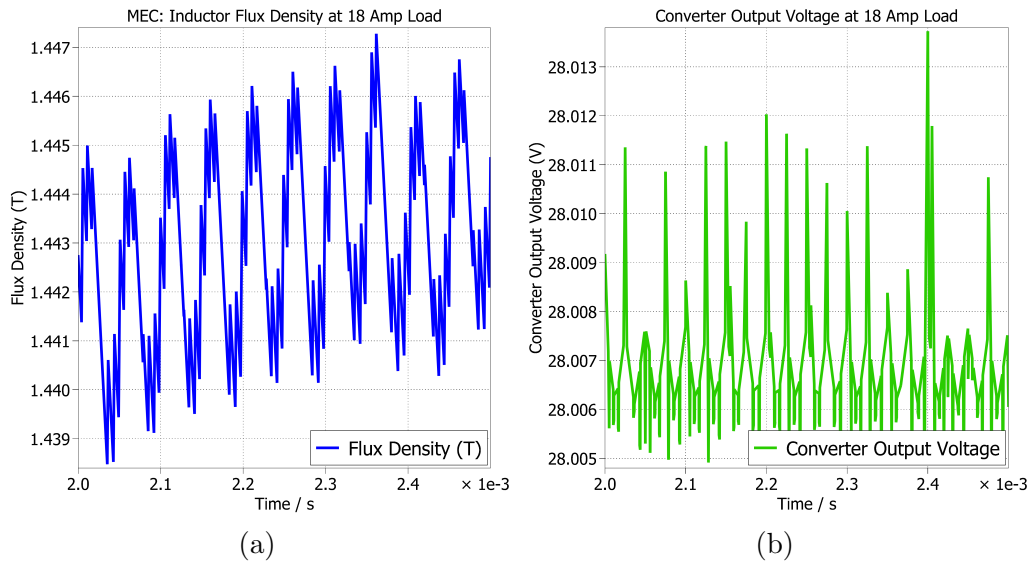


Figure F.9: a) MEC Inductor Flux Density Waveform at converter Load of 18 Amps  
 b) Output Voltage Waveform for Converter Load of 18 Amps

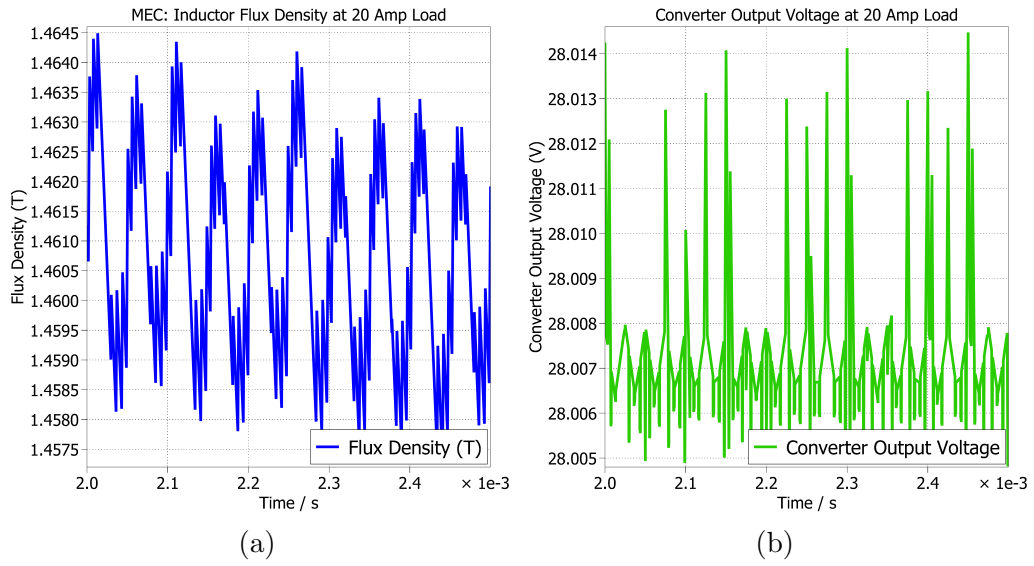


Figure F.10: a) MEC Inductor Flux Density Waveform at converter Load of 20 Amps b) Output Voltage Waveform for Converter Load of 20 Amps

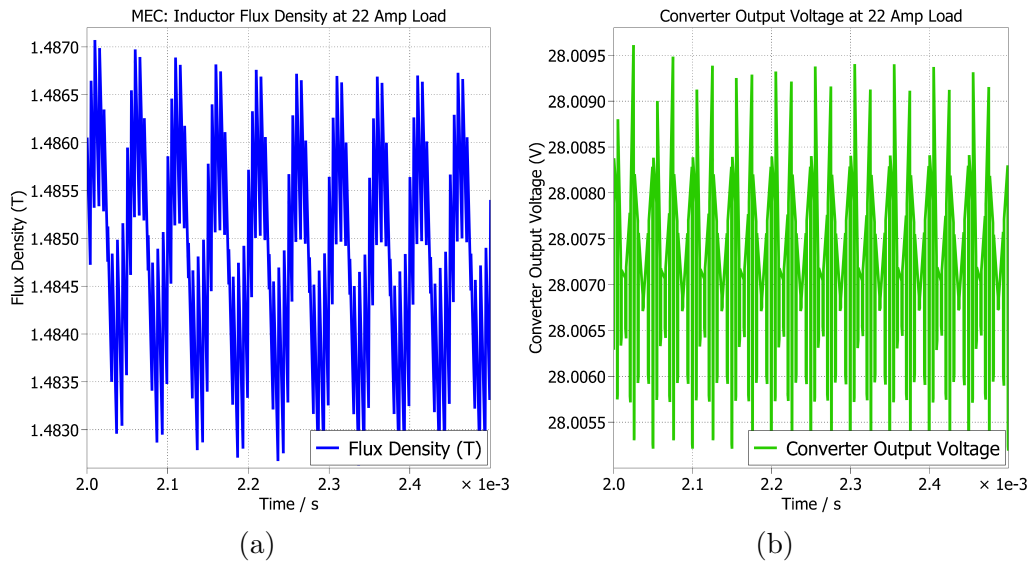


Figure F.11: a) MEC Inductor Flux Density Waveform at converter Load of 22 Amps b) Output Voltage Waveform for Converter Load of 22 Amps

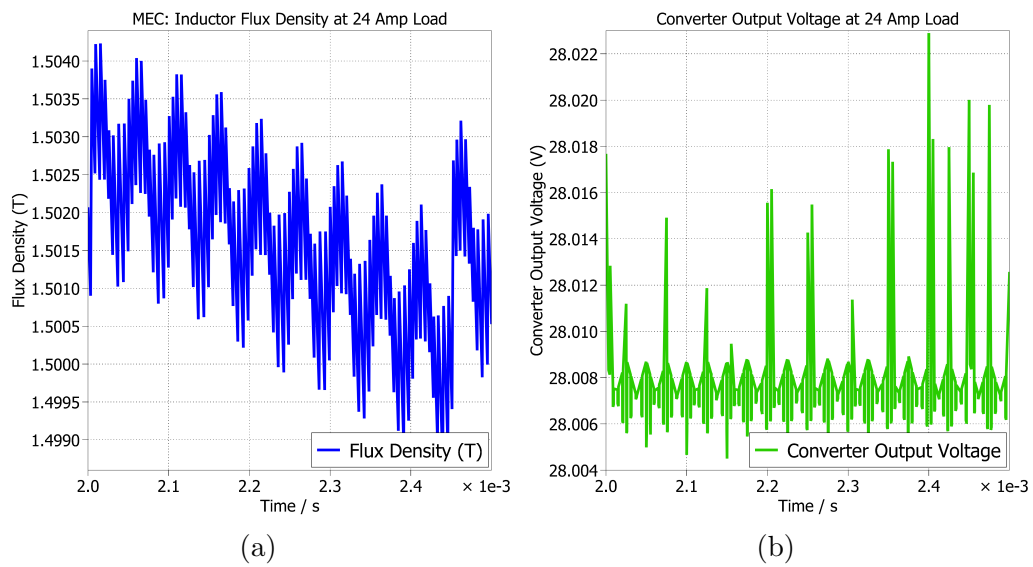


Figure F.12: a) MEC Inductor Flux Density Waveform at converter Load of 24 Amps b) Output Voltage Waveform for Converter Load of 24 Amps

# Appendix G

## Biased Inductor Galvano

## Electrochemical Impedance

## Spectroscopy Testing for Magnets

## within Inductor Airgap

The results of the biasing, caused by the magnets in the airgap show some positive results. However, the effects of demagnetisation of the magnets after each test ruled out this particular addition to the proposed inductor design. The results for this test are available to view in figure G.1, which clearly shows the benefits of increased current capacity before saturation is reached, relative to the non-biased inductor.

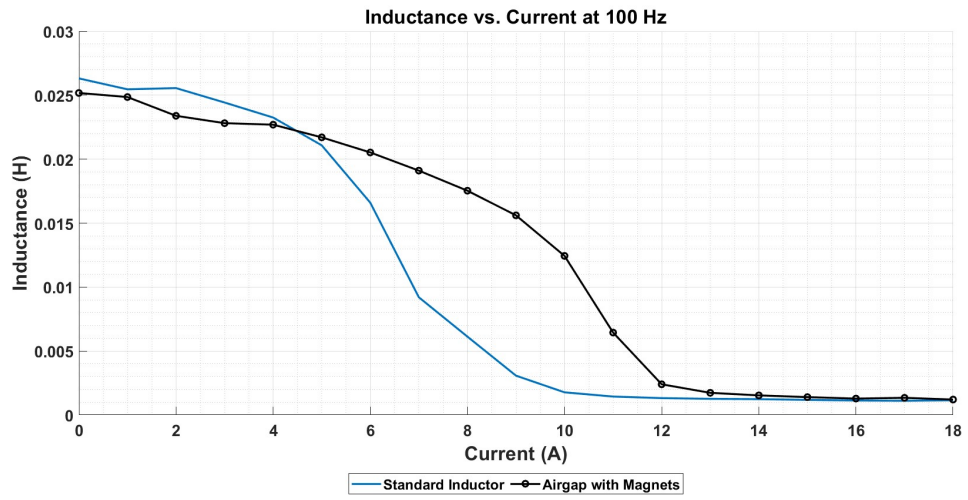


Figure G.1: Inductance vs Current for Inductor with Magnets in Airgap



Figure G.2: Button Magnets Placed on Cross-sectional Area of the Inductor Core

# Appendix H

## Experimental Interleaved DC-DC Buck Converter Waveforms

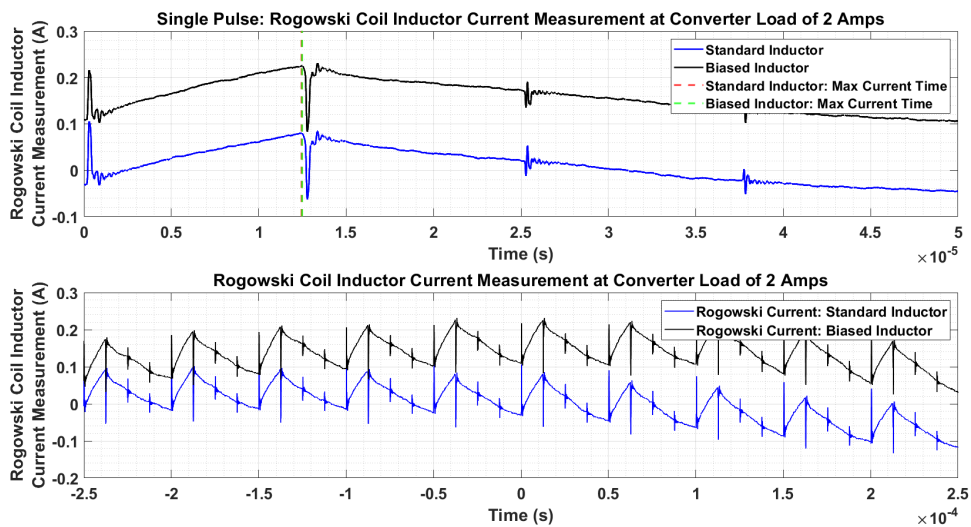


Figure H.1: Rogowski Coil Inductor Current Measurement at Converter Load of 2A

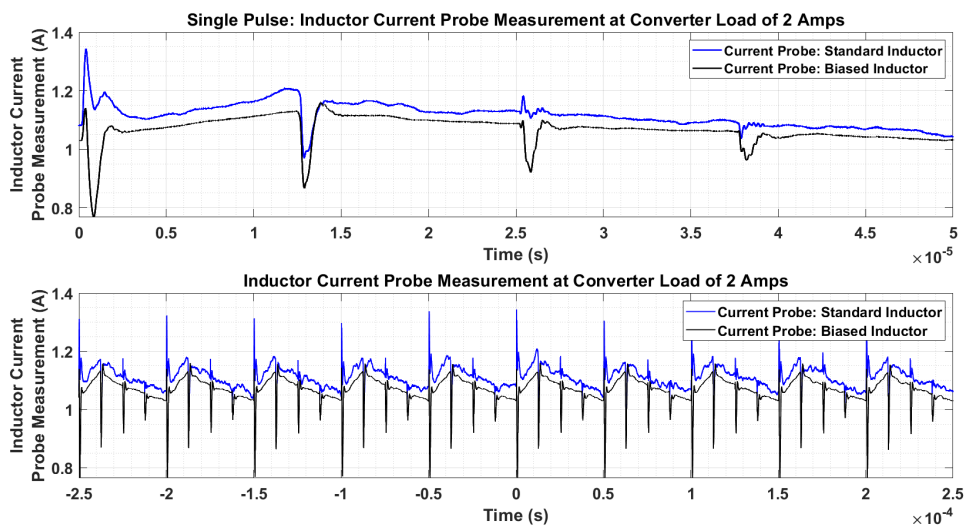


Figure H.2: Inductor Current Probe Measurement at Converter Load of 2A

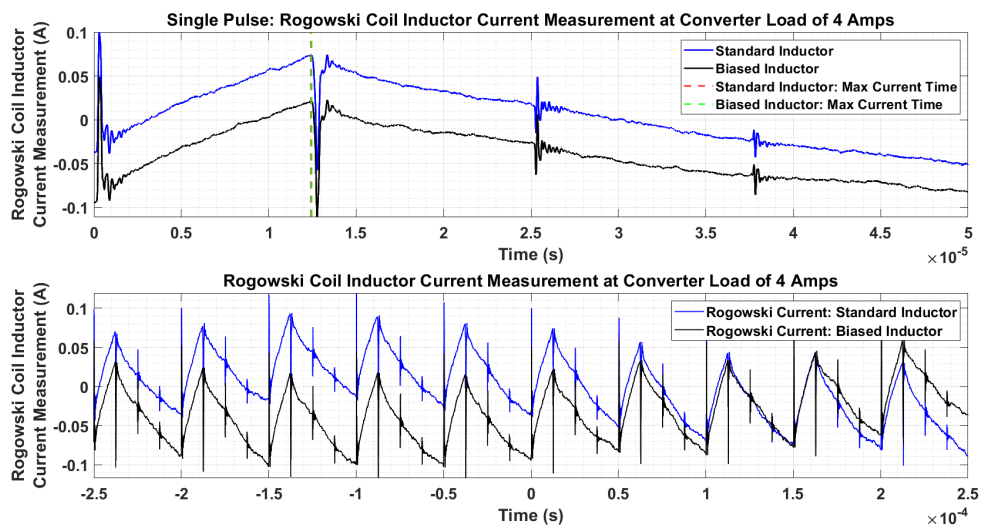


Figure H.3: Rogowski Coil Inductor Current Measurement at Converter Load of 4A

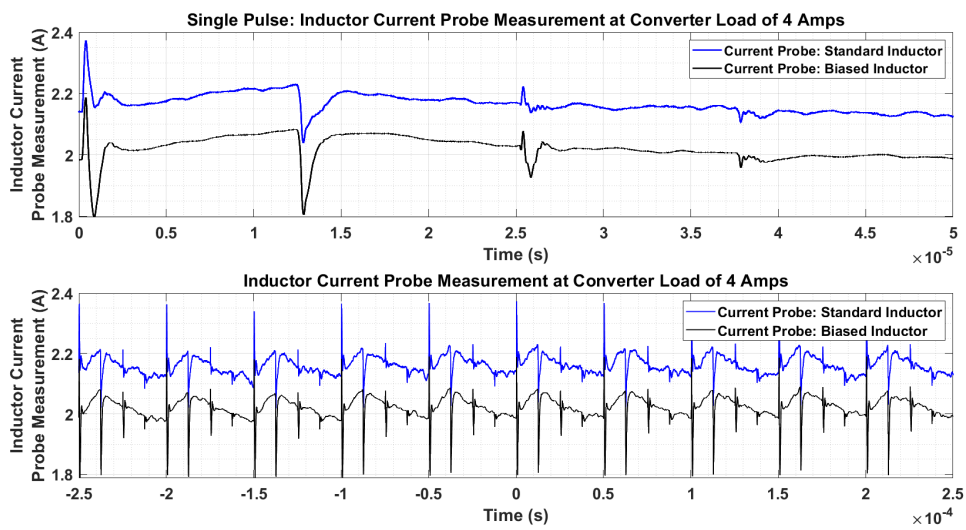


Figure H.4: Inductor Current Probe Measurement at Converter Load of 4A

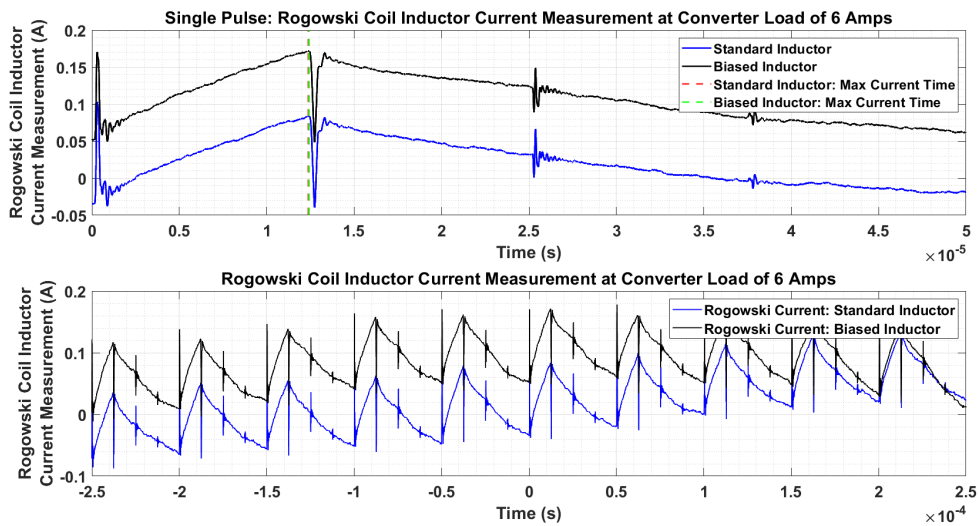


Figure H.5: Rogowski Coil Inductor Current Measurement at Converter Load of 6A

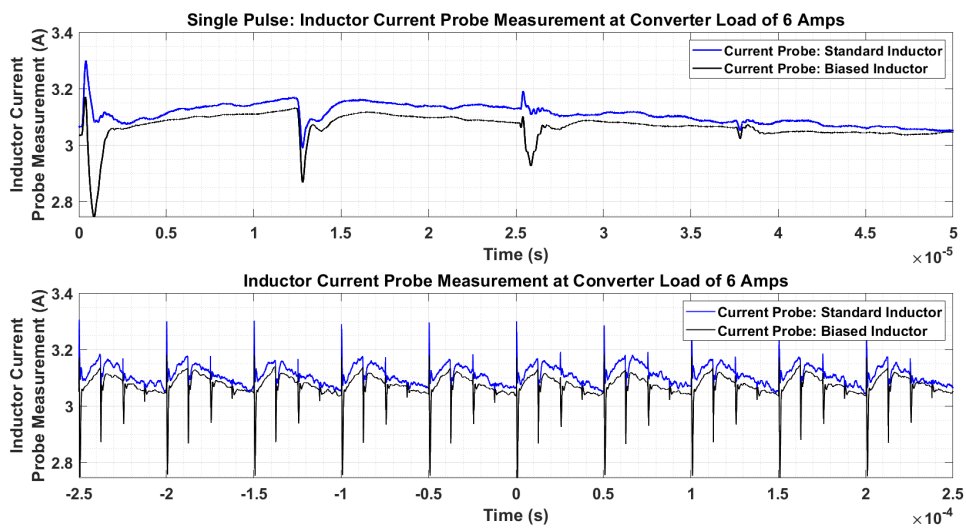


Figure H.6: Inductor Current Probe Measurement at Converter Load of 6A

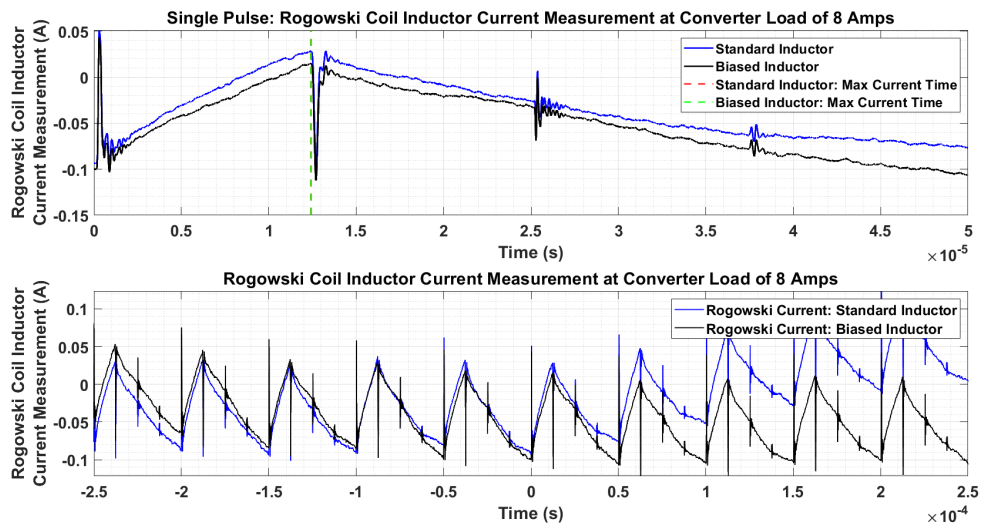


Figure H.7: Rogowski Coil Inductor Current Measurement at Converter Load of 8A

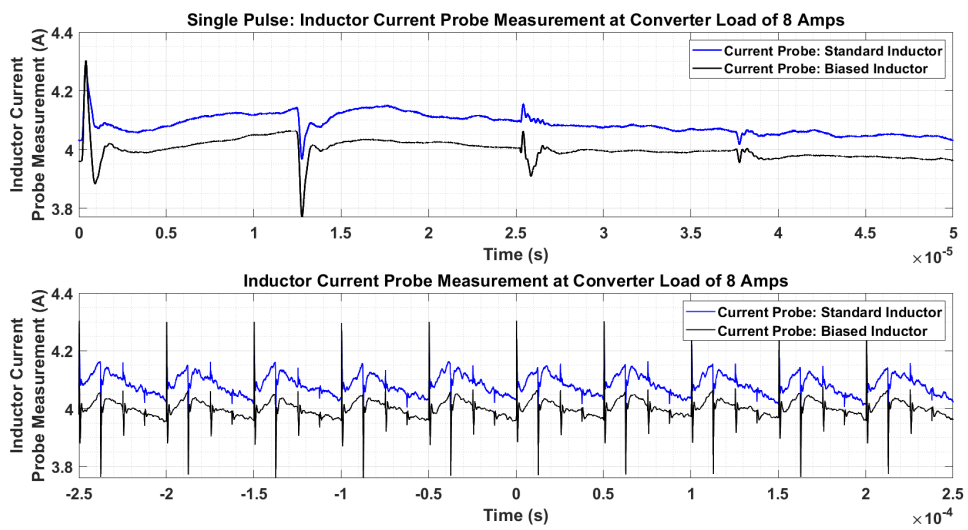


Figure H.8: Inductor Current Probe Measurement at Converter Load of 8A

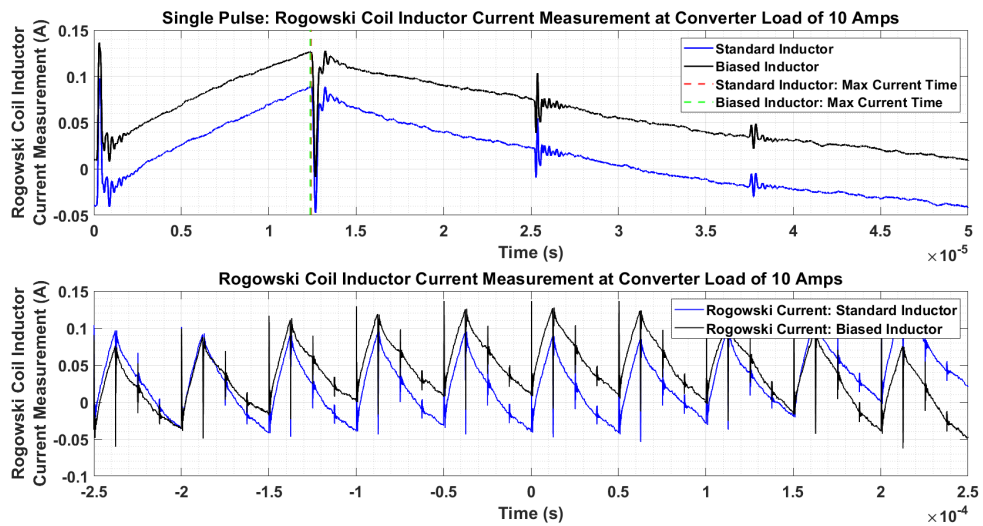


Figure H.9: Rogowski Coil Inductor Current Measurement at Converter Load of 10A

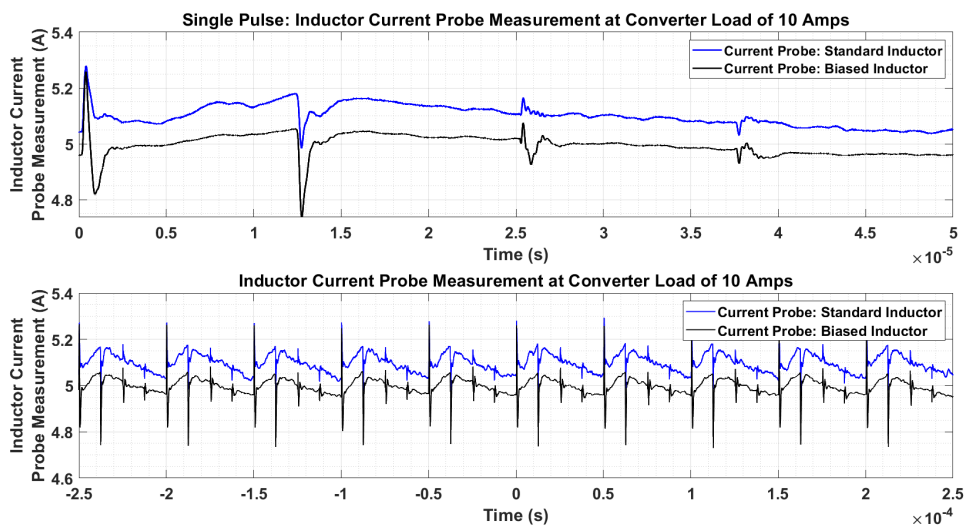


Figure H.10: Inductor Current Probe Measurement at Converter Load of 10A

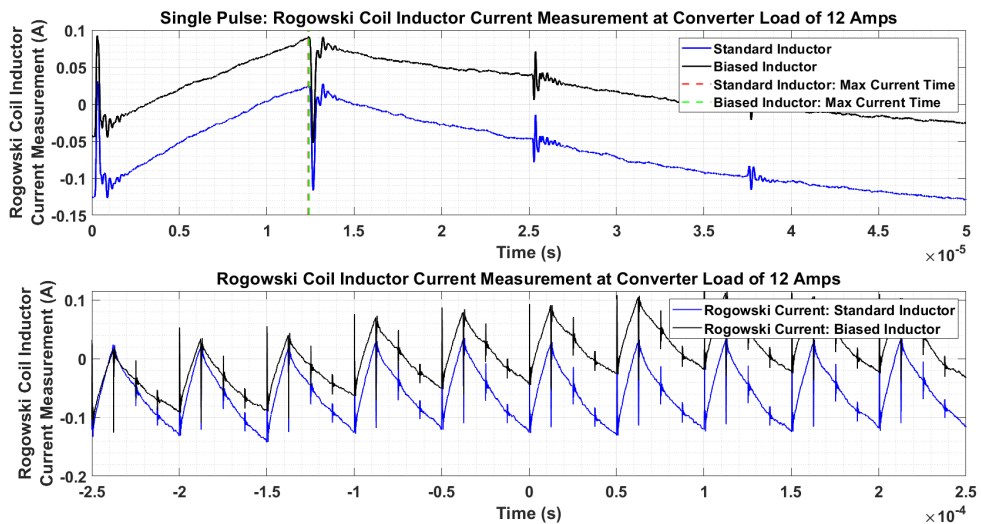


Figure H.11: Rogowski Coil Inductor Current Measurement at Converter Load of 12A

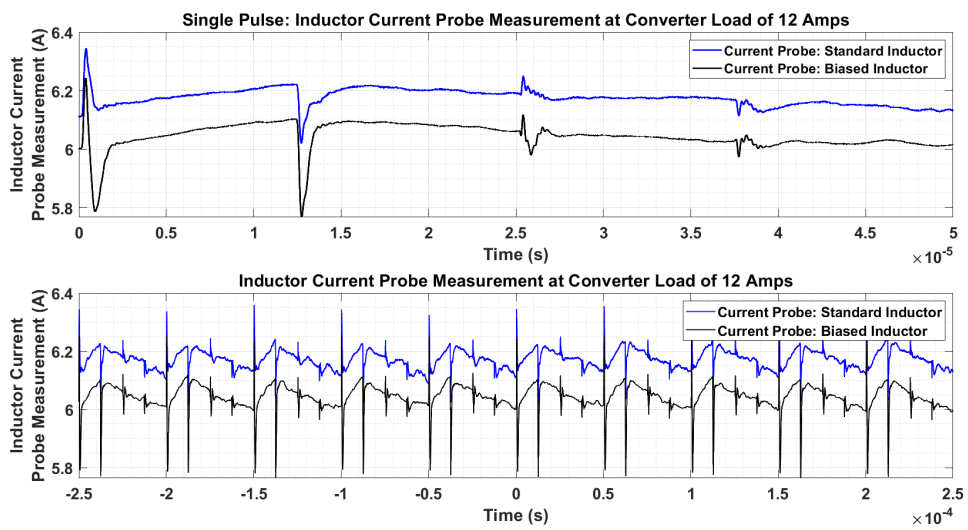


Figure H.12: Inductor Current Probe Measurement at Converter Load of 12A

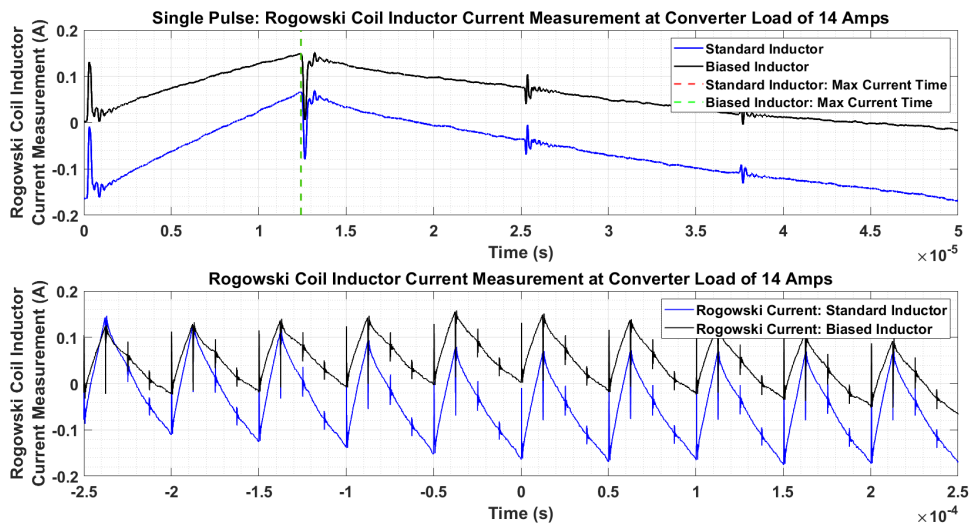


Figure H.13: Rogowski Coil Inductor Current Measurement at Converter Load of 14A

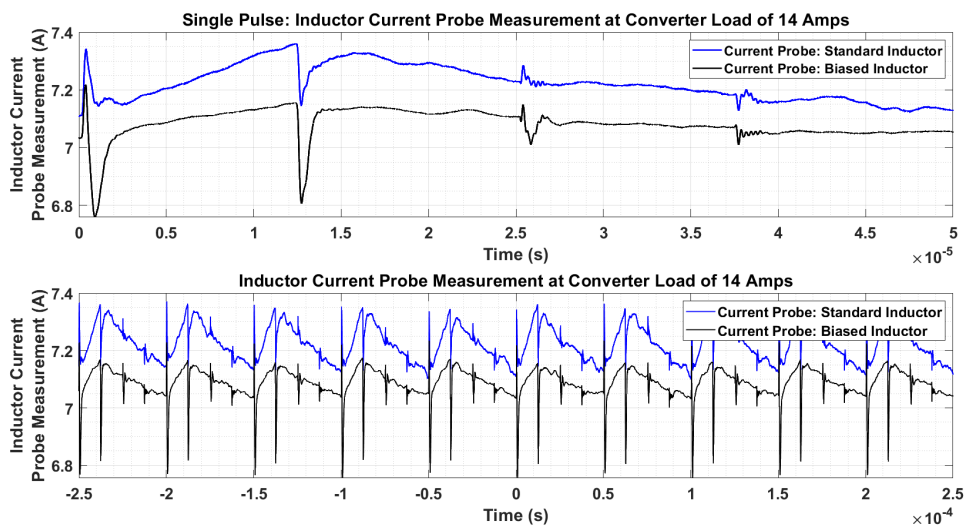


Figure H.14: Inductor Current Probe Measurement at Converter Load of 14A

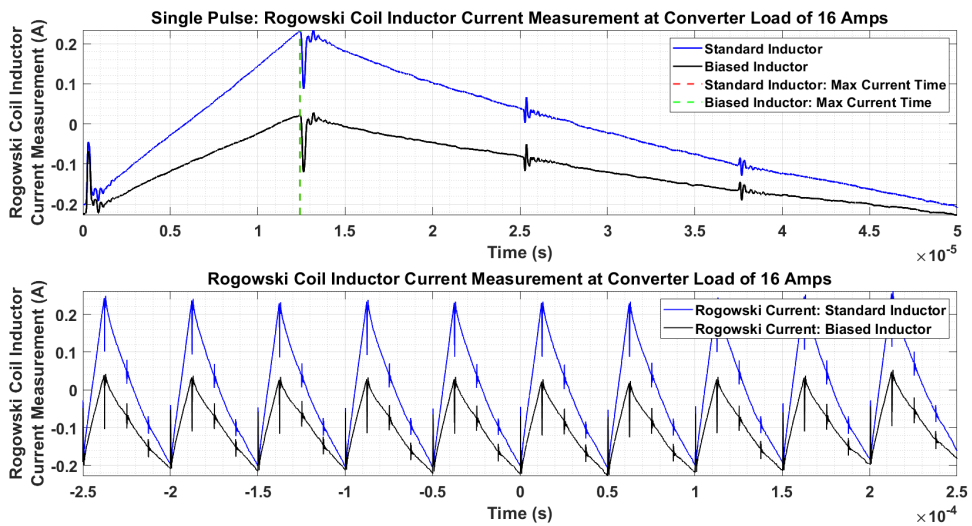


Figure H.15: Rogowski Coil Inductor Current Measurement at Converter Load of 16A

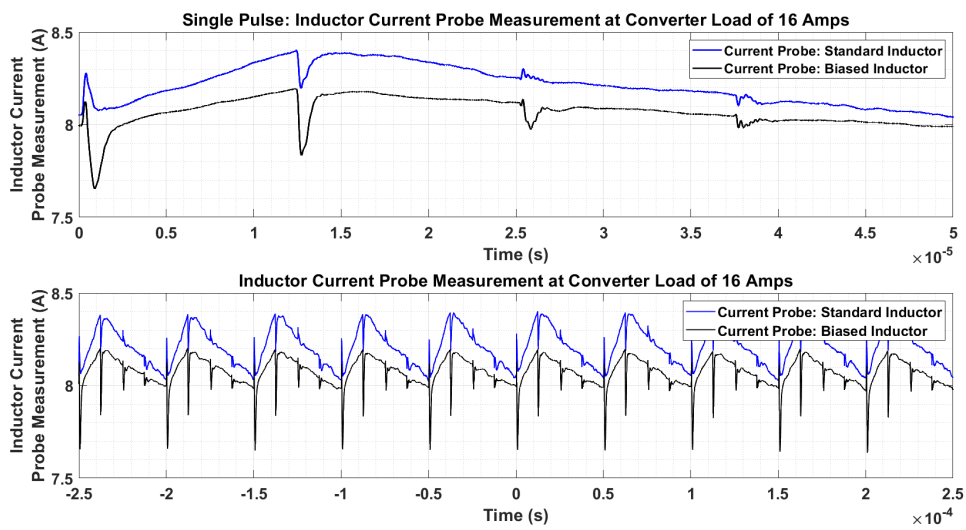


Figure H.16: Inductor Current Probe Measurement at Converter Load of 16A

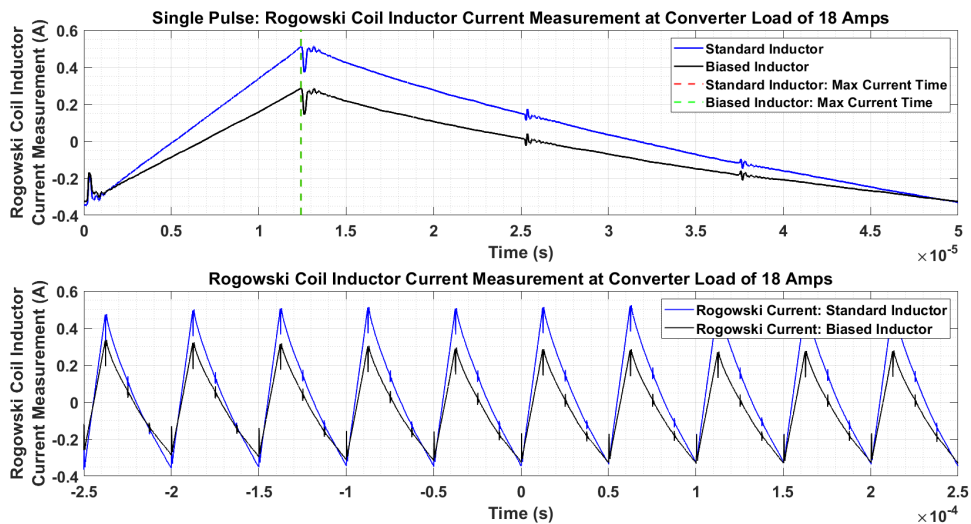


Figure H.17: Rogowski Coil Inductor Current Measurement at Converter Load of 18A

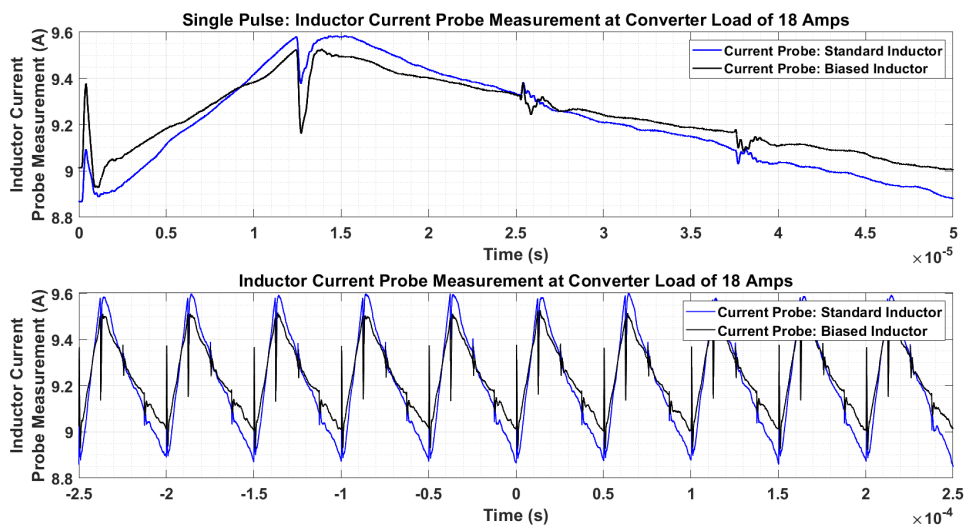


Figure H.18: Inductor Current Probe Measurement at Converter Load of 18A

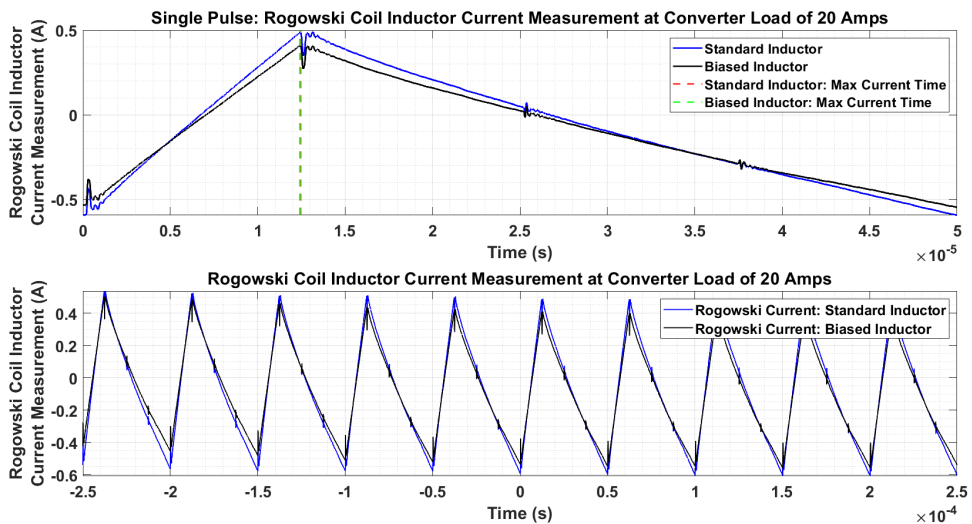


Figure H.19: Rogowski Coil Inductor Current Measurement at Converter Load of 20A

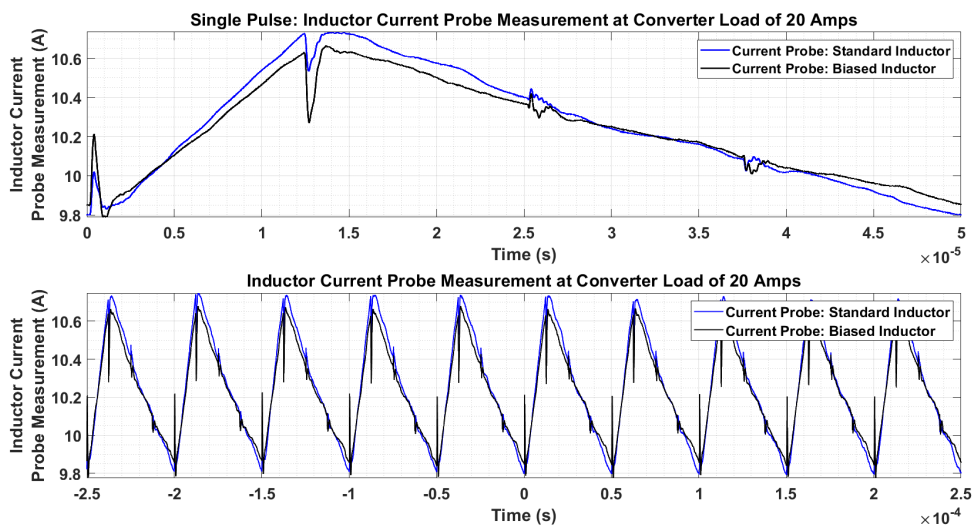


Figure H.20: Inductor Current Probe Measurement at Converter Load of 20A

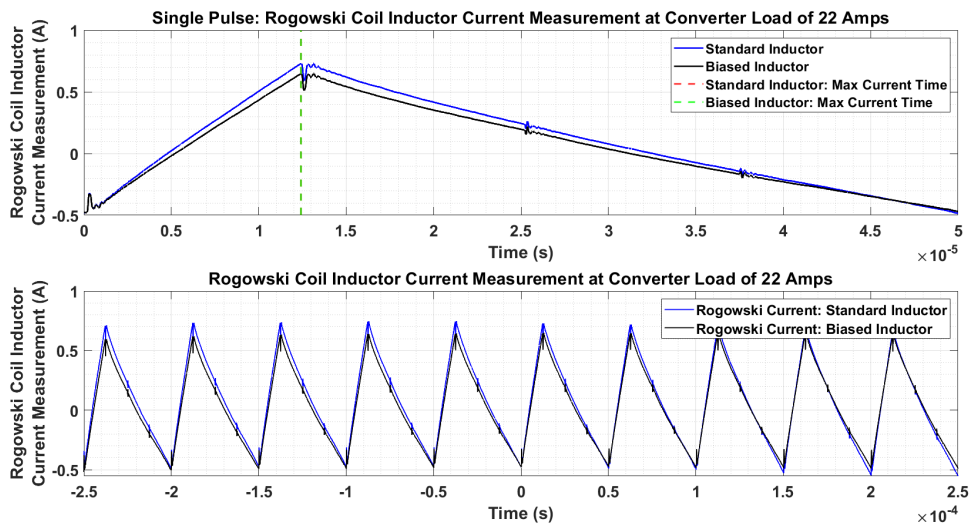


Figure H.21: Rogowski Coil Inductor Current Measurement at Converter Load of 22A

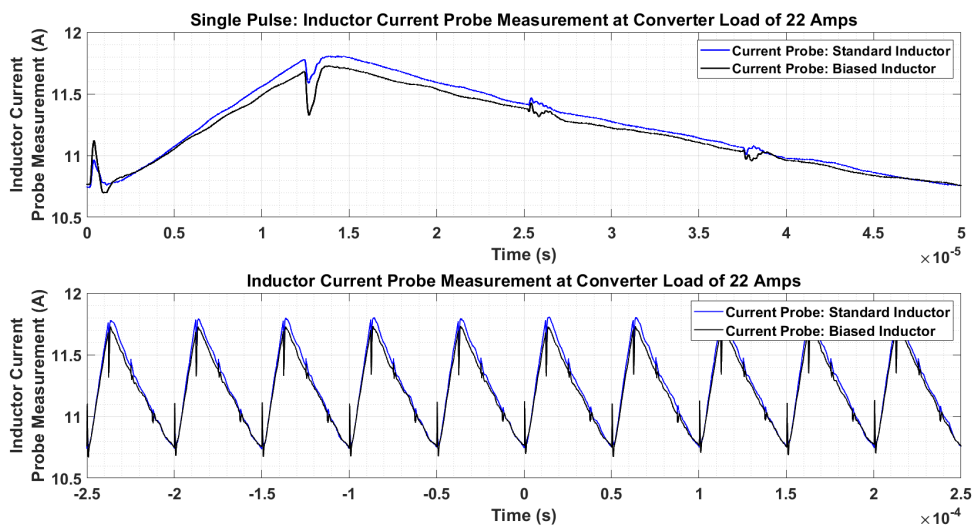


Figure H.22: Inductor Current Probe Measurement at Converter Load of 22A

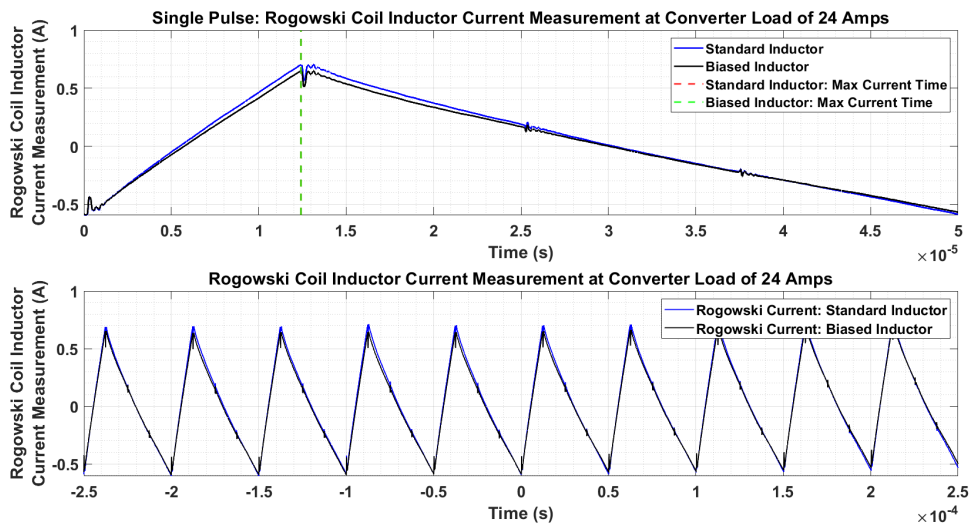


Figure H.23: Rogowski Coil Inductor Current Measurement at Converter Load of 24A

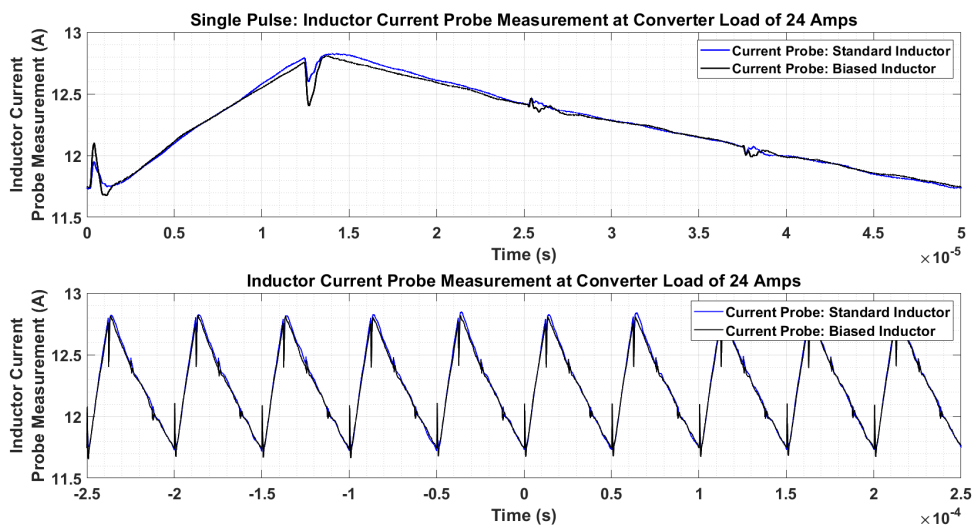


Figure H.24: Inductor Current Probe Measurement at Converter Load of 24A

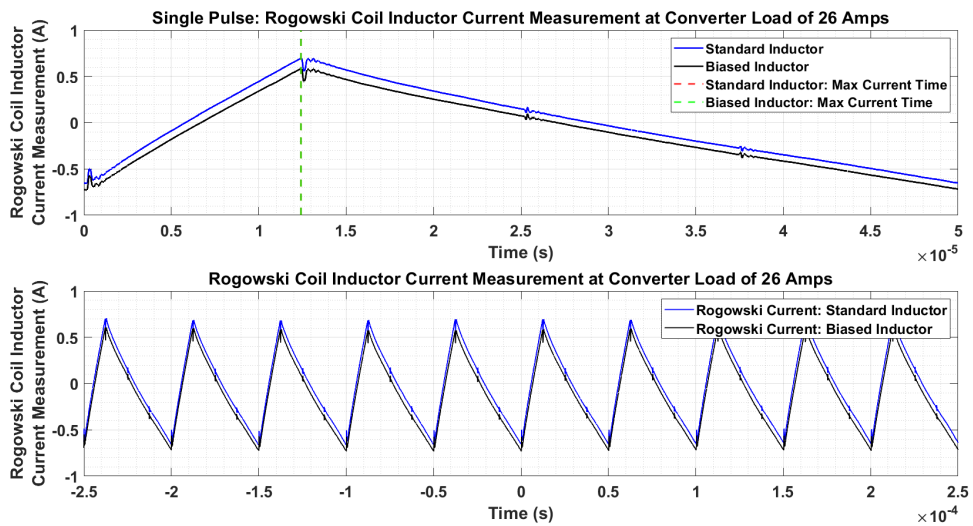


Figure H.25: Rogowski Coil Inductor Current Measurement at Converter Load of 26A

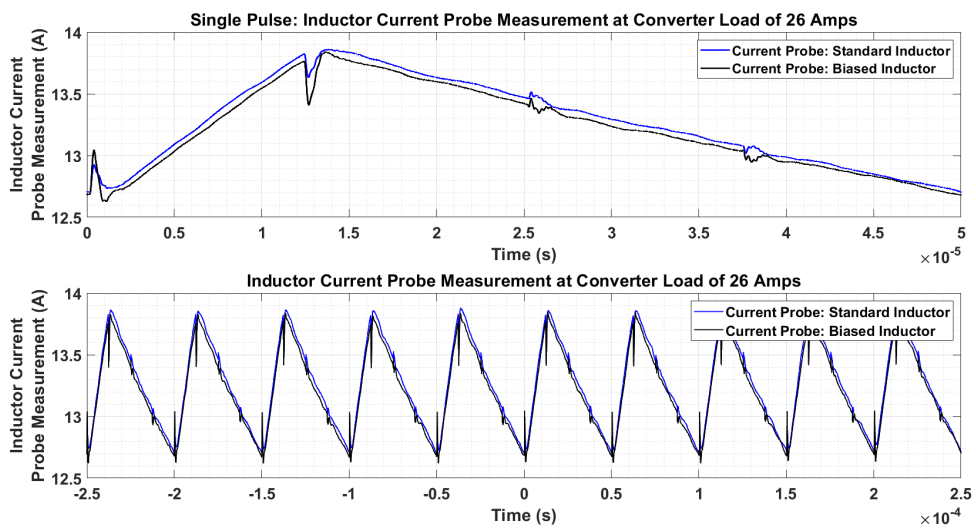


Figure H.26: Inductor Current Probe Measurement at Converter Load of 26A

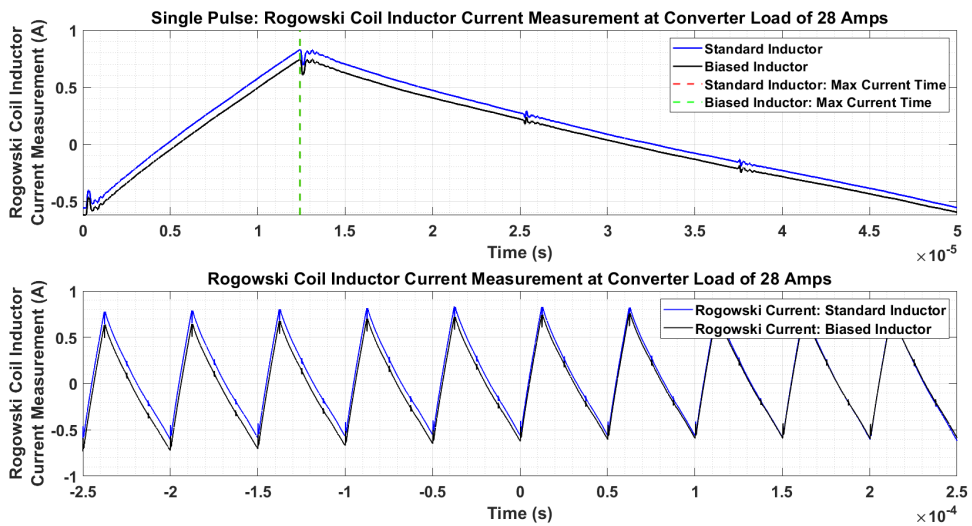


Figure H.27: Rogowski Coil Inductor Current Measurement at Converter Load of 28A

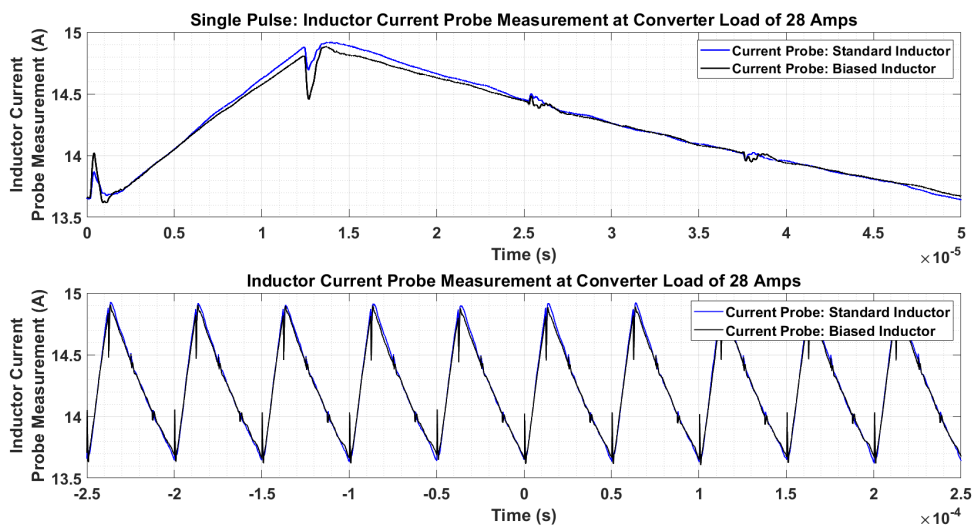


Figure H.28: Inductor Current Probe Measurement at Converter Load of 28A

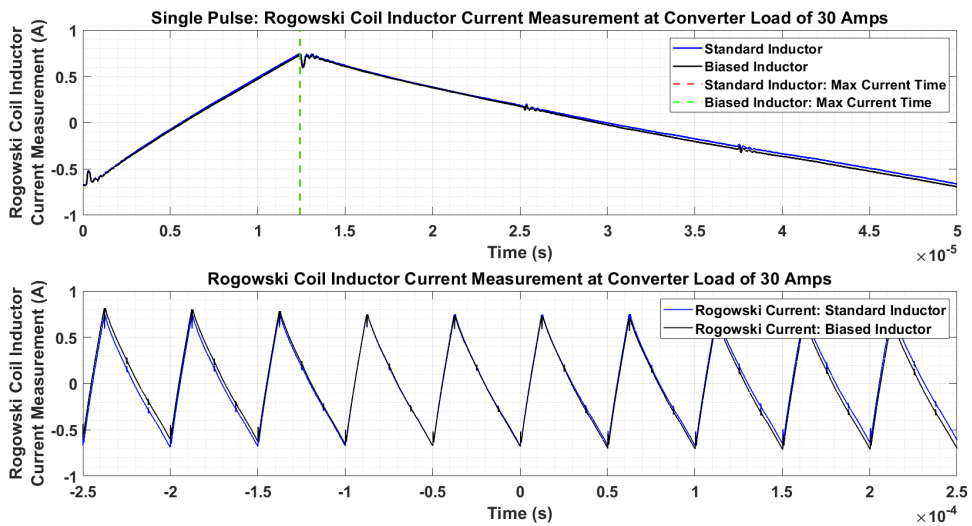


Figure H.29: Rogowski Coil Inductor Current Measurement at Converter Load of 30A

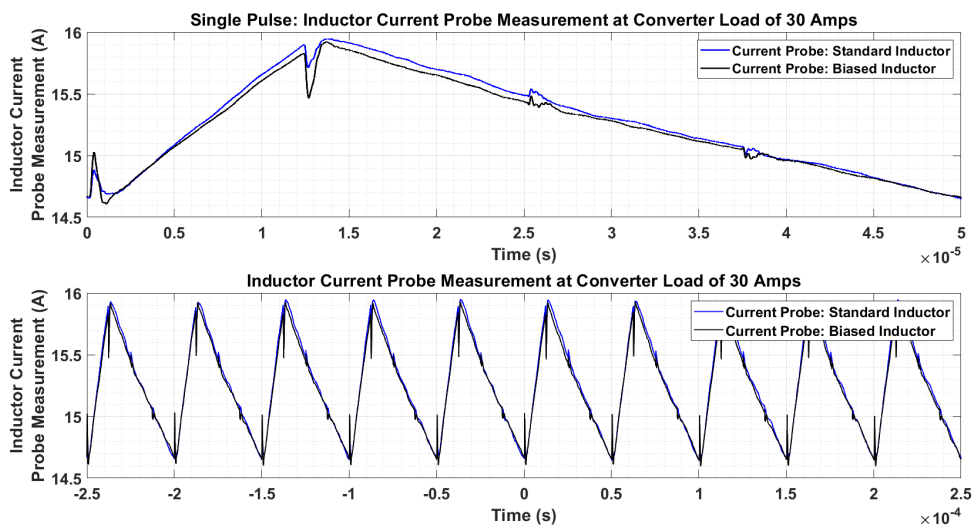


Figure H.30: Inductor Current Probe Measurement at Converter Load of 30A

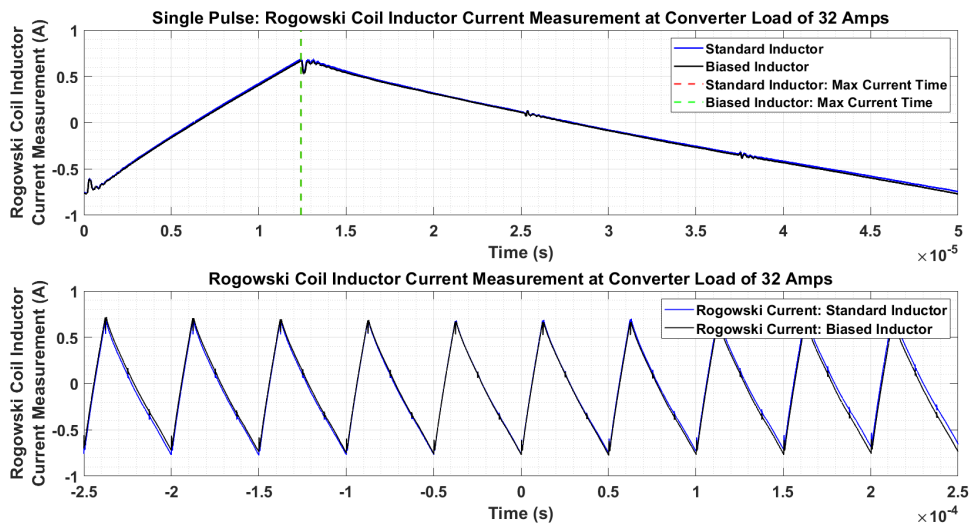


Figure H.31: Rogowski Coil Inductor Current Measurement at Converter Load of 32A

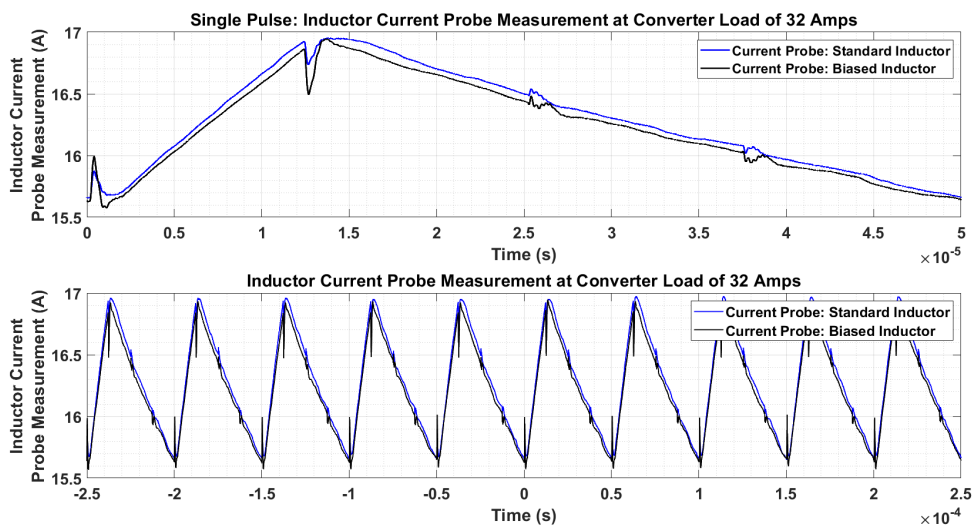


Figure H.32: Inductor Current Probe Measurement at Converter Load of 32A

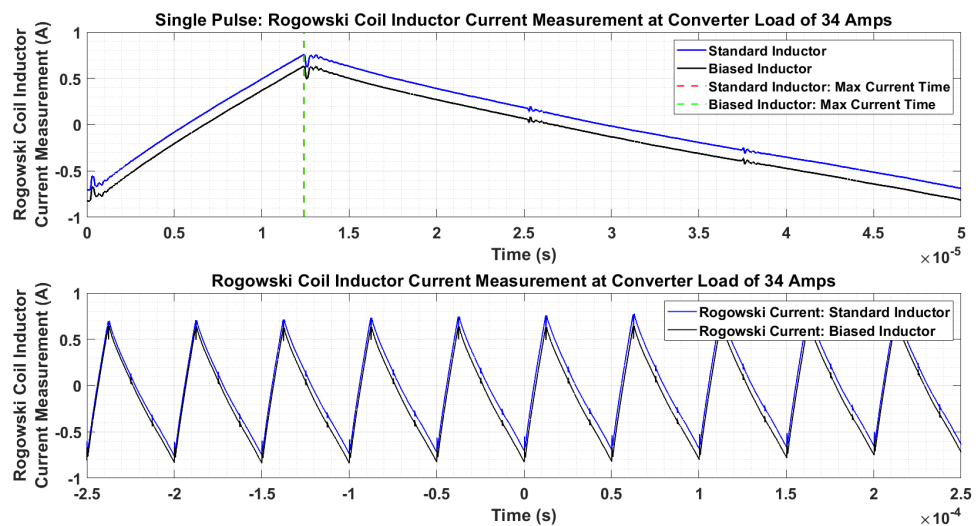


Figure H.33: Rogowski Coil Inductor Current Measurement at Converter Load of 34A

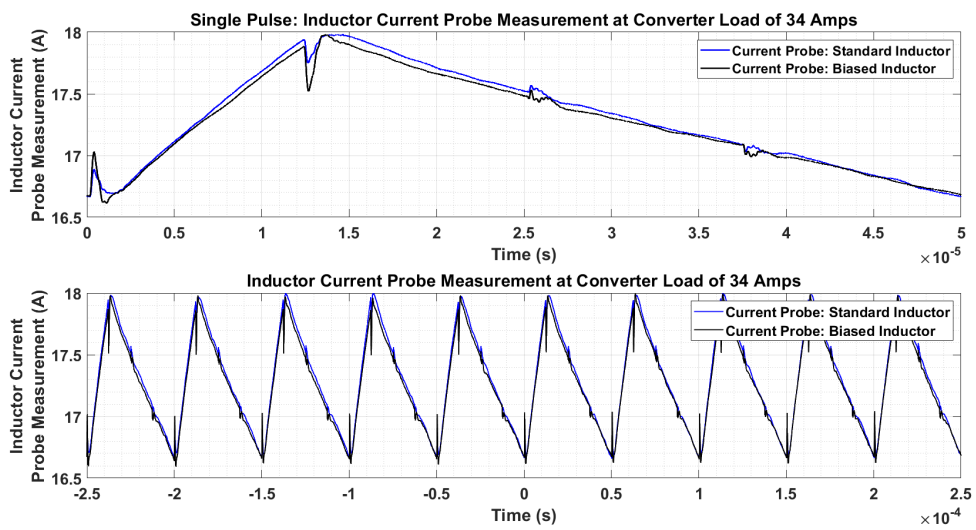


Figure H.34: Inductor Current Probe Measurement at Converter Load of 34A

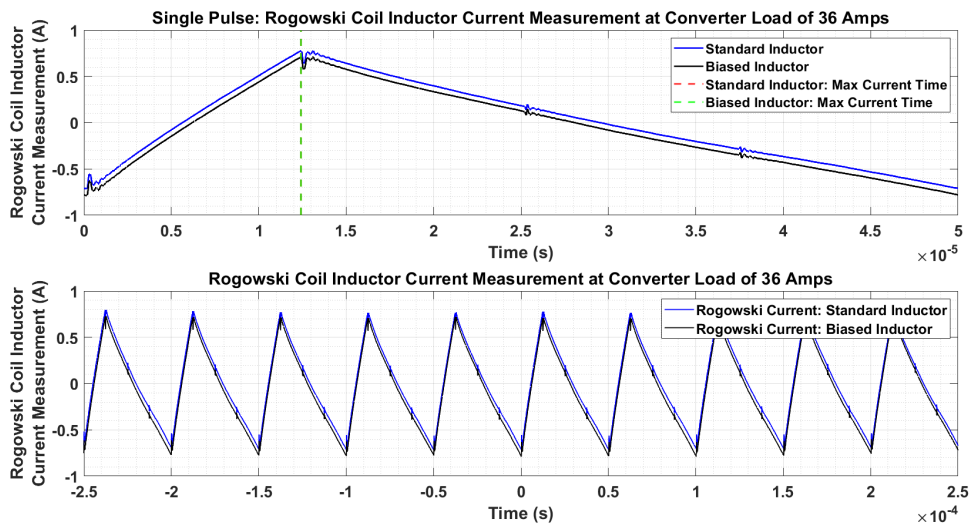


Figure H.35: Rogowski Coil Inductor Current Measurement at Converter Load of 36A

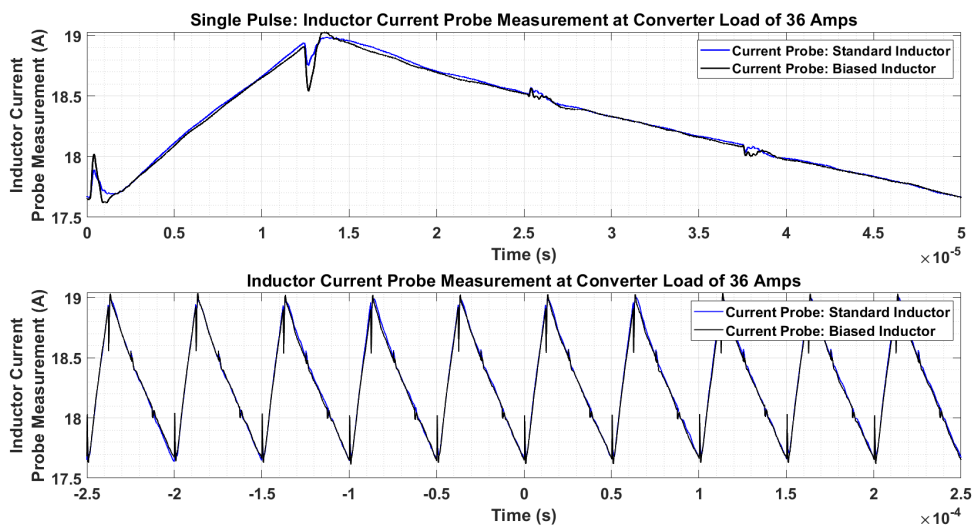


Figure H.36: Inductor Current Probe Measurement at Converter Load of 36A

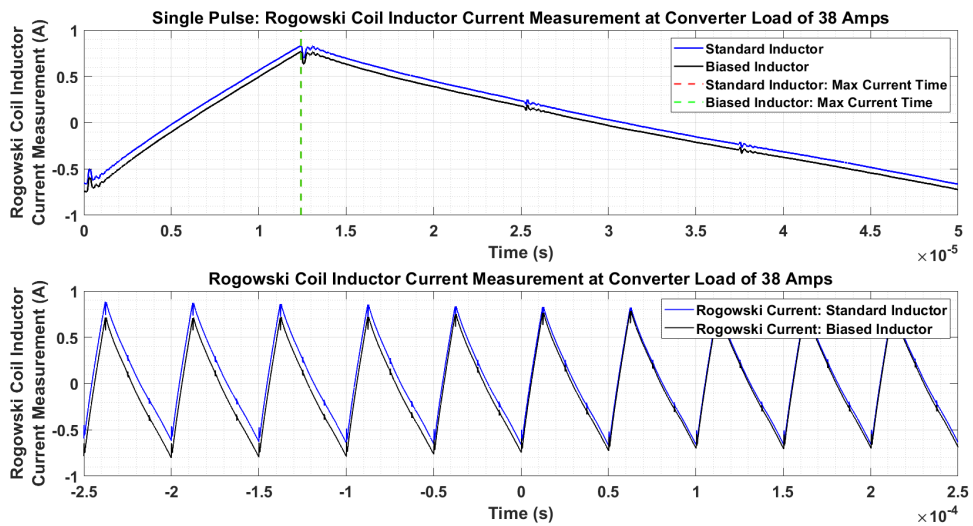


Figure H.37: Rogowski Coil Inductor Current Measurement at Converter Load of 38A

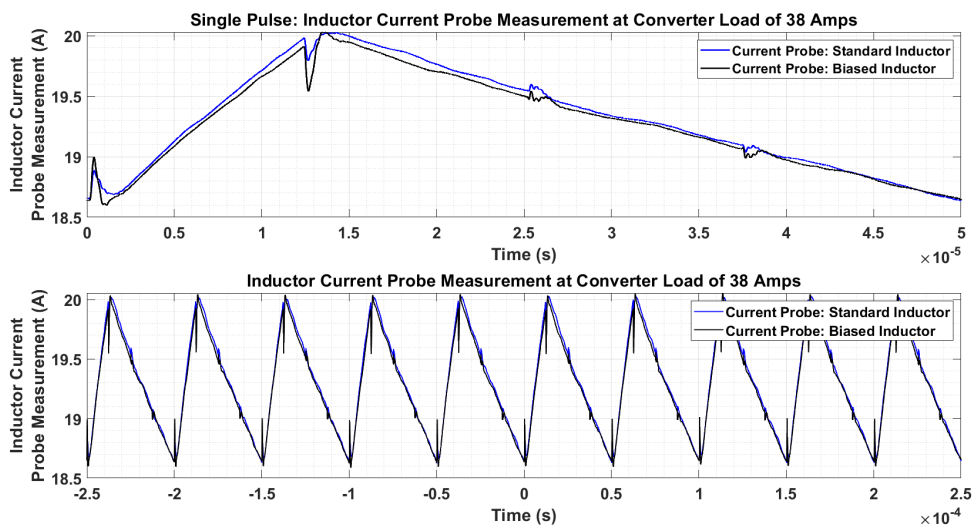


Figure H.38: Inductor Current Probe Measurement at Converter Load of 38A

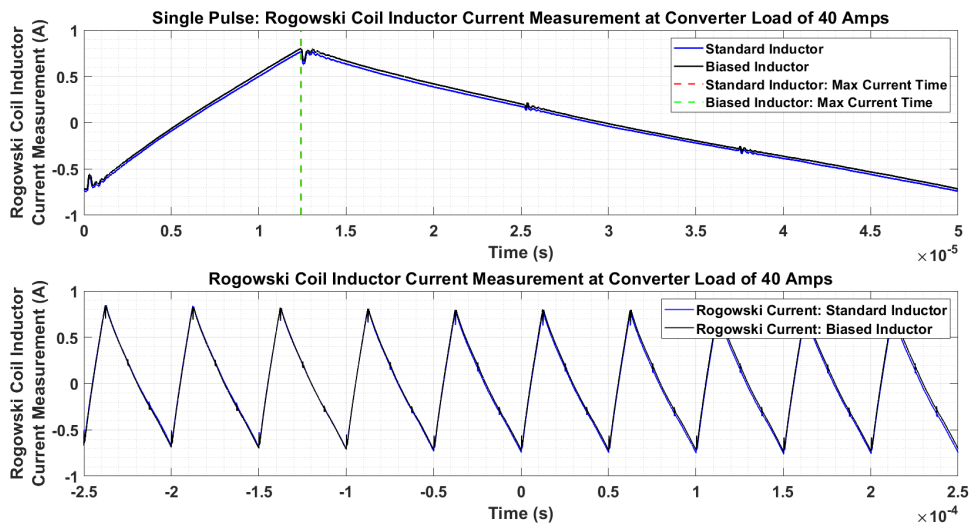


Figure H.39: Rogowski Coil Inductor Current Measurement at Converter Load of 40A

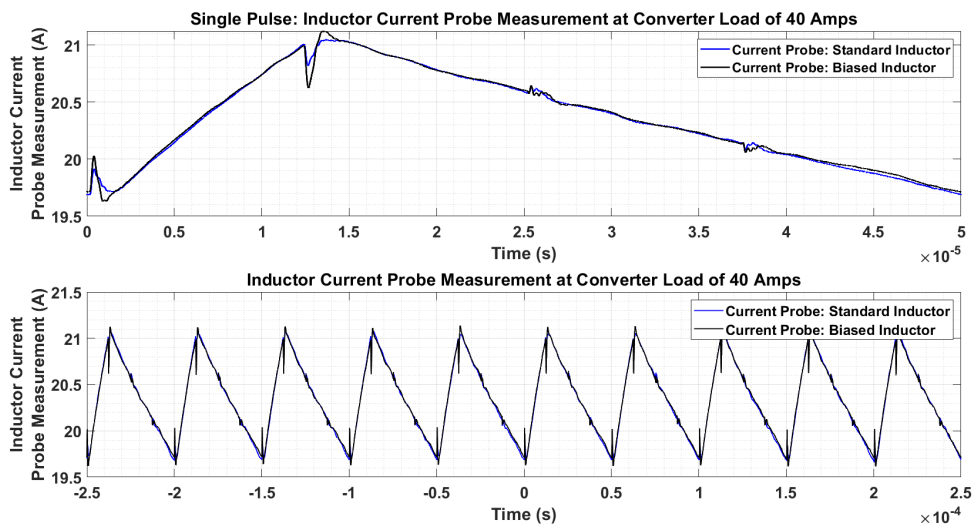


Figure H.40: Inductor Current Probe Measurement at Converter Load of 40A

# Appendix I

## Voltage Waveforms

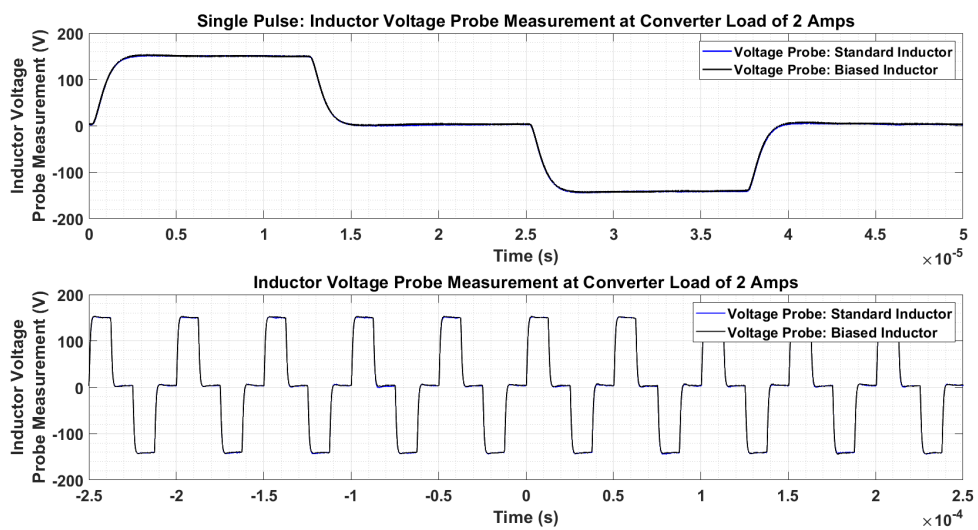


Figure I.1: Inductor Voltage Probe Measurement at Converter Load of 2A

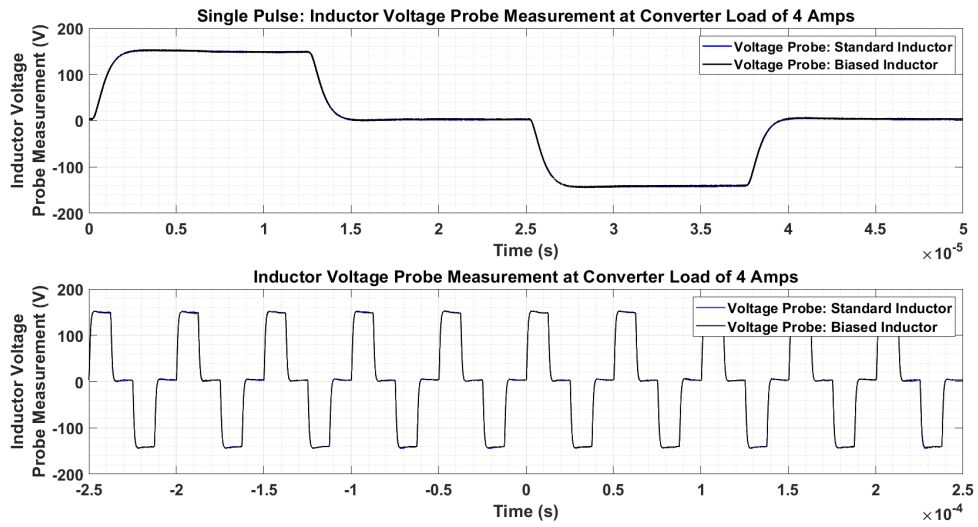


Figure I.2: Inductor Voltage Probe Measurement at Converter Load of 4A

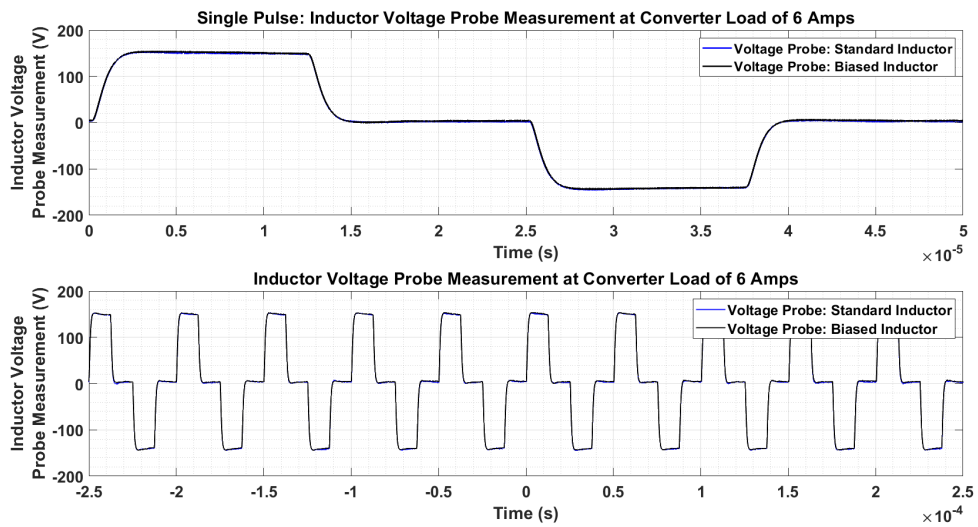


Figure I.3: Inductor Voltage Probe Measurement at Converter Load of 6A

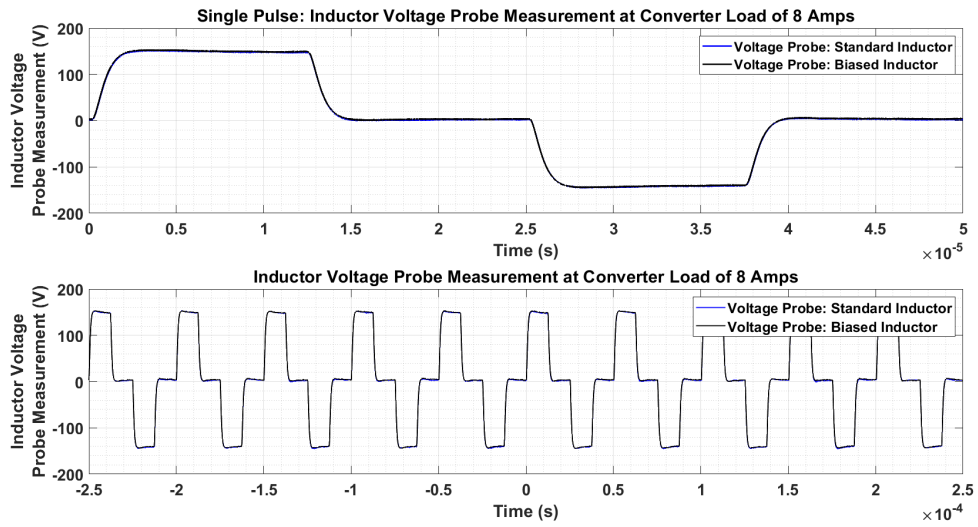


Figure I.4: Inductor Voltage Probe Measurement at Converter Load of 8A

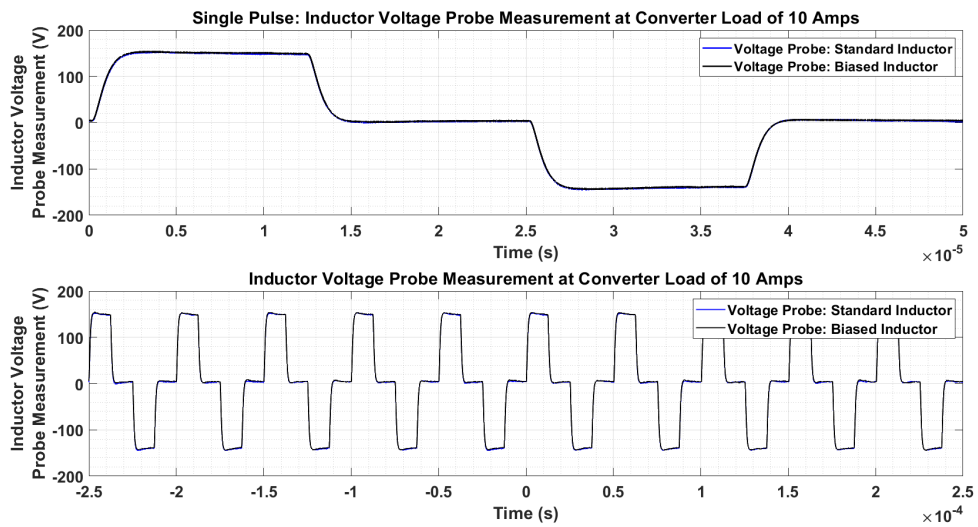


Figure I.5: Inductor Voltage Probe Measurement at Converter Load of 10A

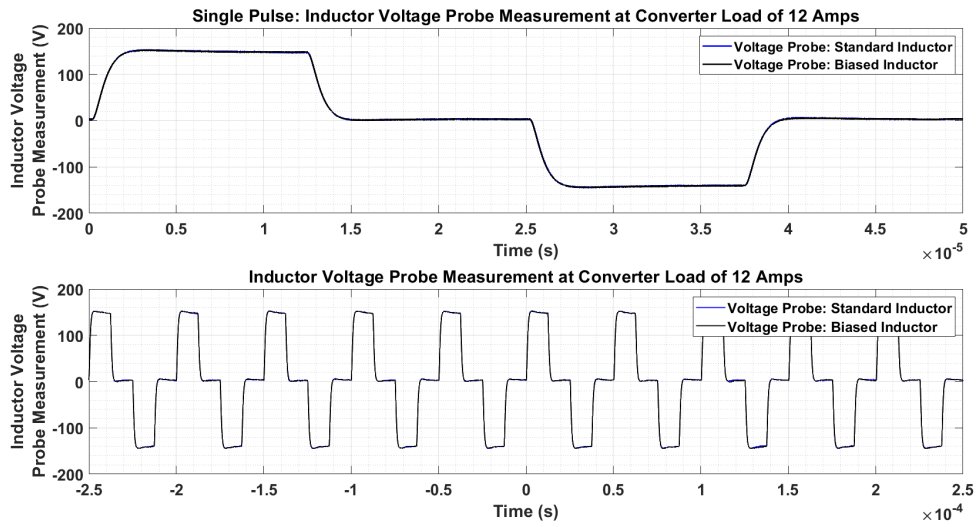


Figure I.6: Inductor Voltage Probe Measurement at Converter Load of 12A

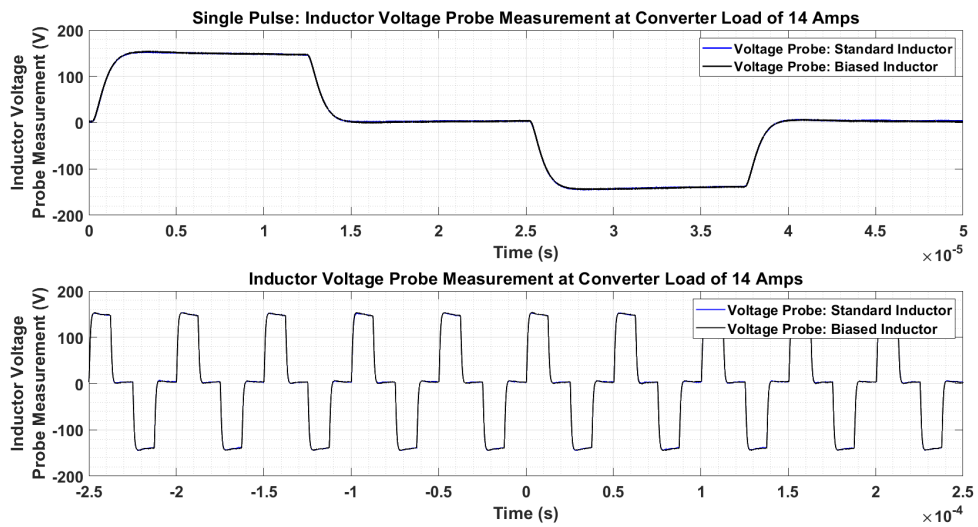


Figure I.7: Inductor Voltage Probe Measurement at Converter Load of 14A

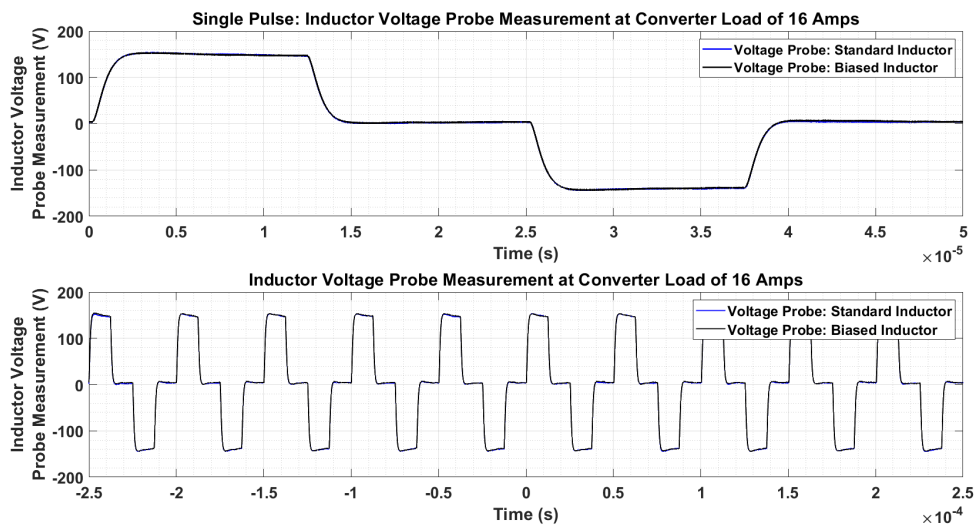


Figure I.8: Inductor Voltage Probe Measurement at Converter Load of 16A

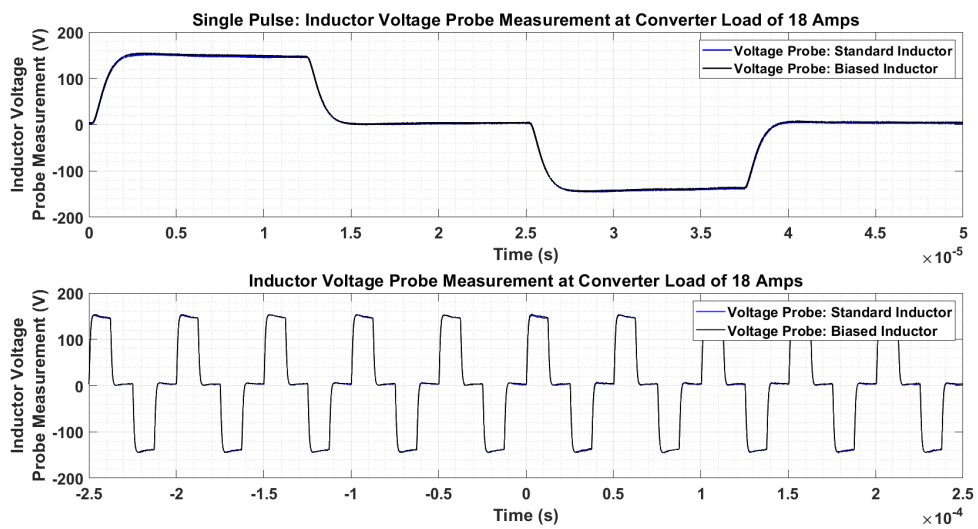


Figure I.9: Inductor Voltage Probe Measurement at Converter Load of 18A

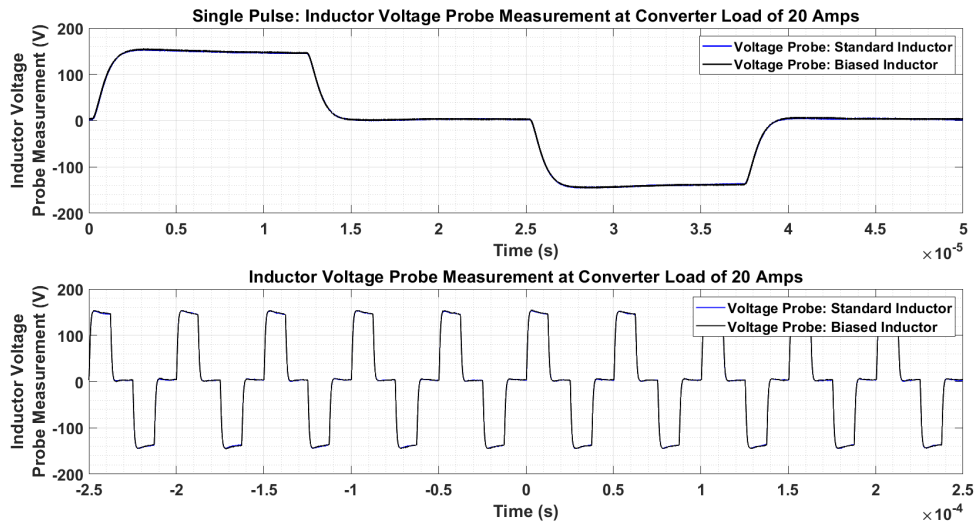


Figure I.10: Inductor Voltage Probe Measurement at Converter Load of 20A

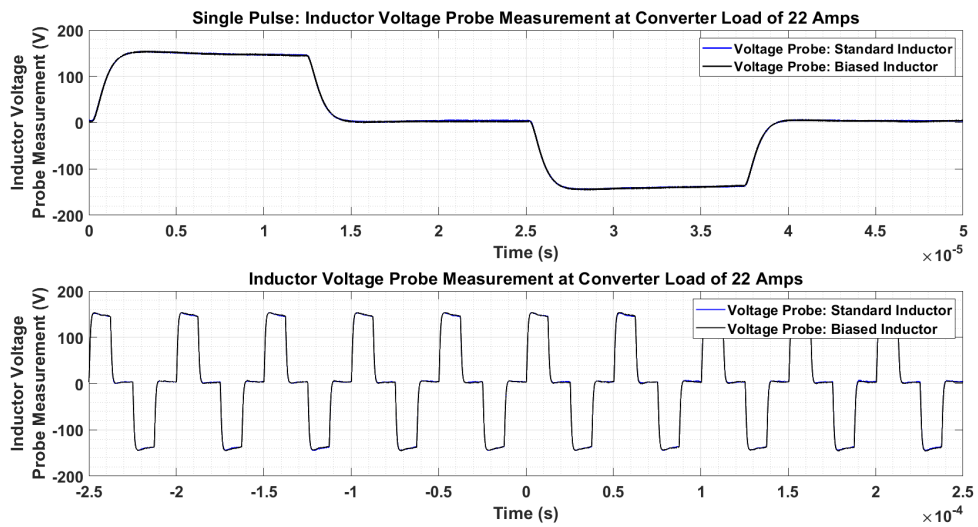


Figure I.11: Inductor Voltage Probe Measurement at Converter Load of 22A

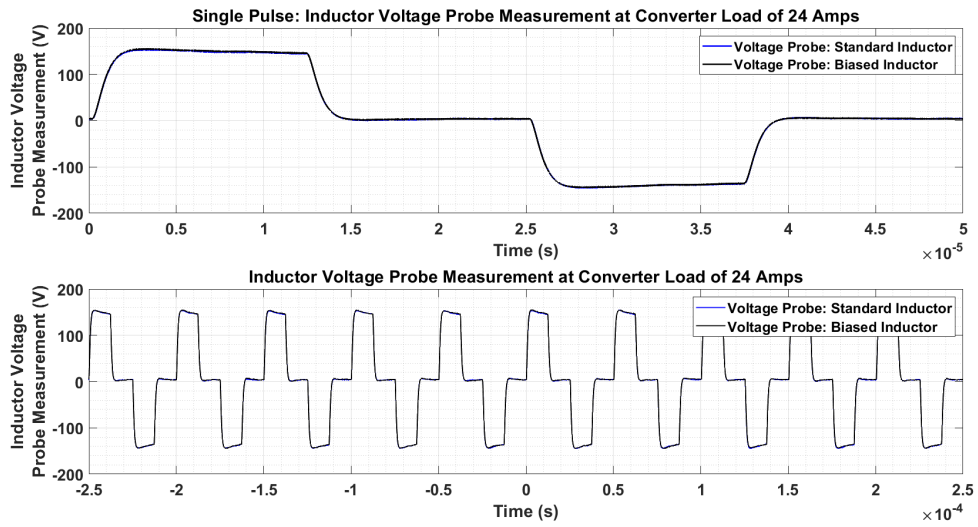


Figure I.12: Inductor Voltage Probe Measurement at Converter Load of 24A

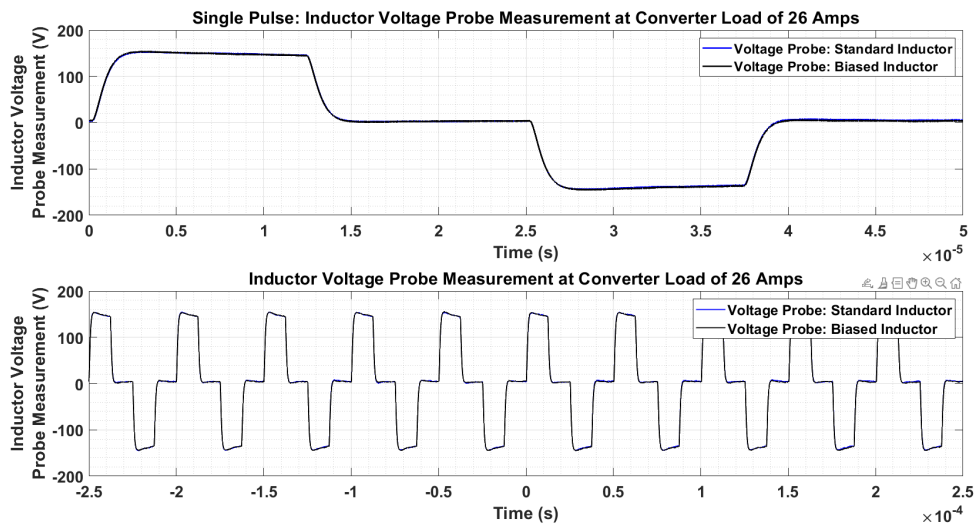


Figure I.13: Inductor Voltage Probe Measurement at Converter Load of 26A

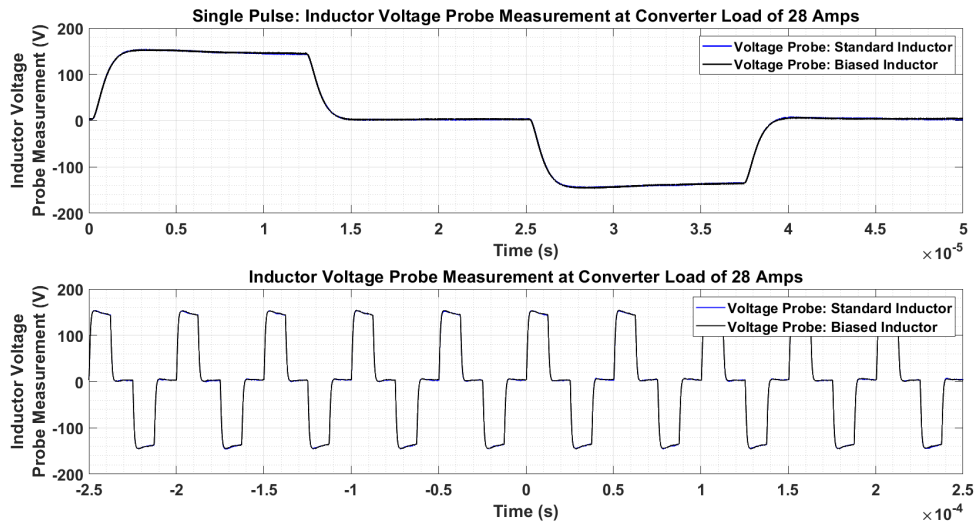


Figure I.14: Inductor Voltage Probe Measurement at Converter Load of 28A

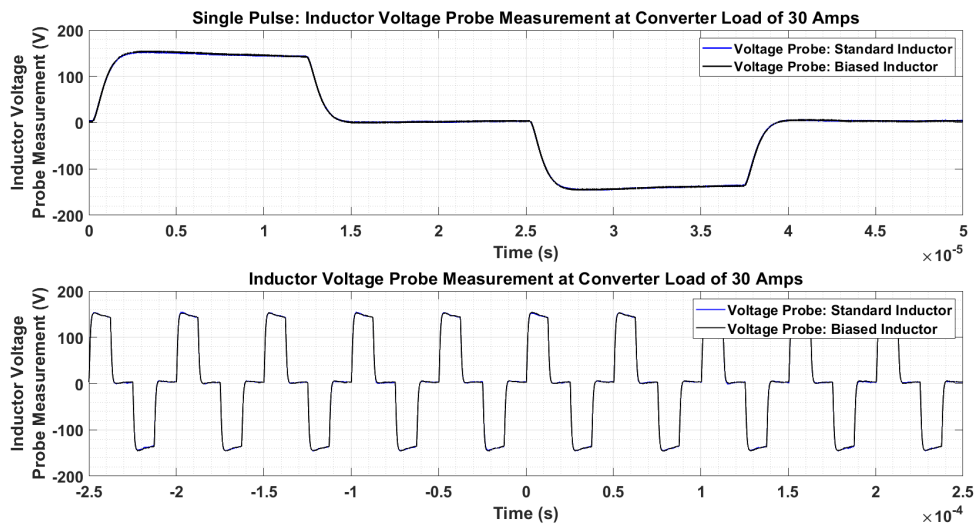


Figure I.15: Inductor Voltage Probe Measurement at Converter Load of 30A

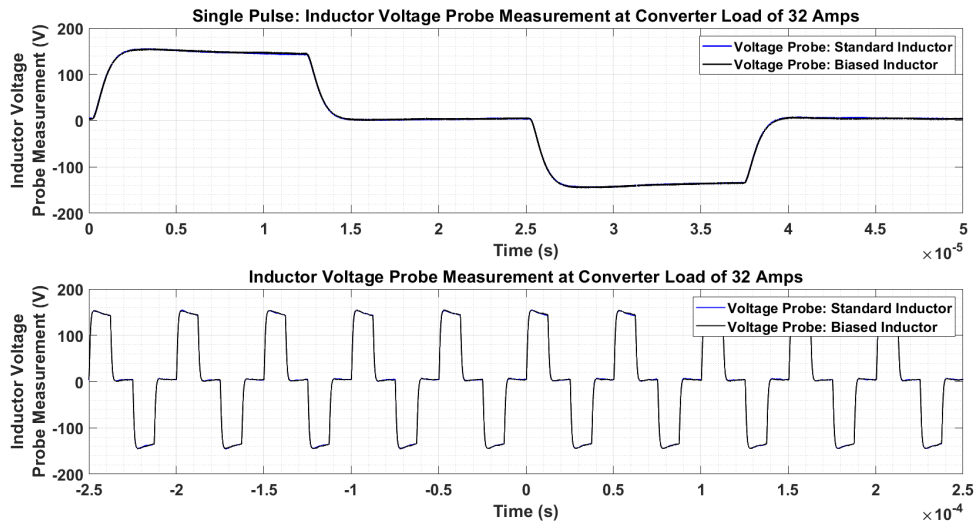


Figure I.16: Inductor Voltage Probe Measurement at Converter Load of 32A

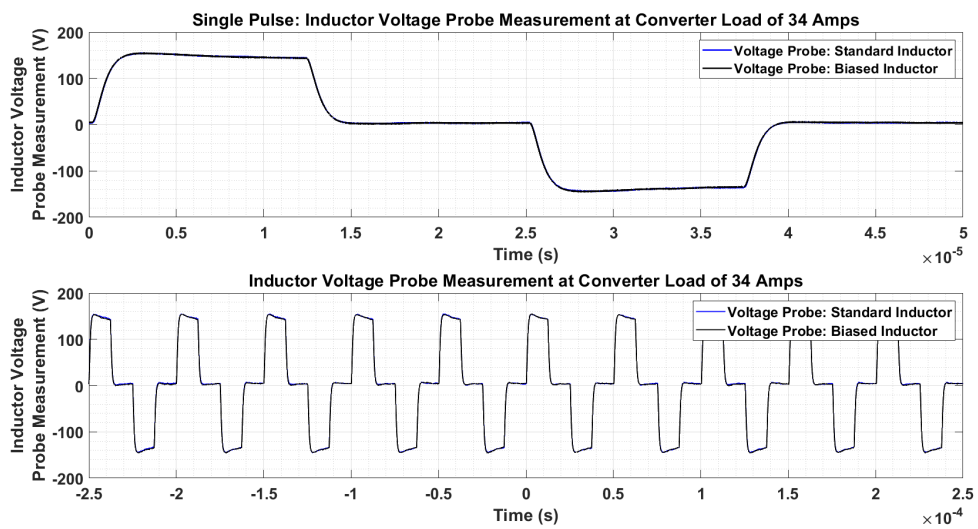


Figure I.17: Inductor Voltage Probe Measurement at Converter Load of 34A

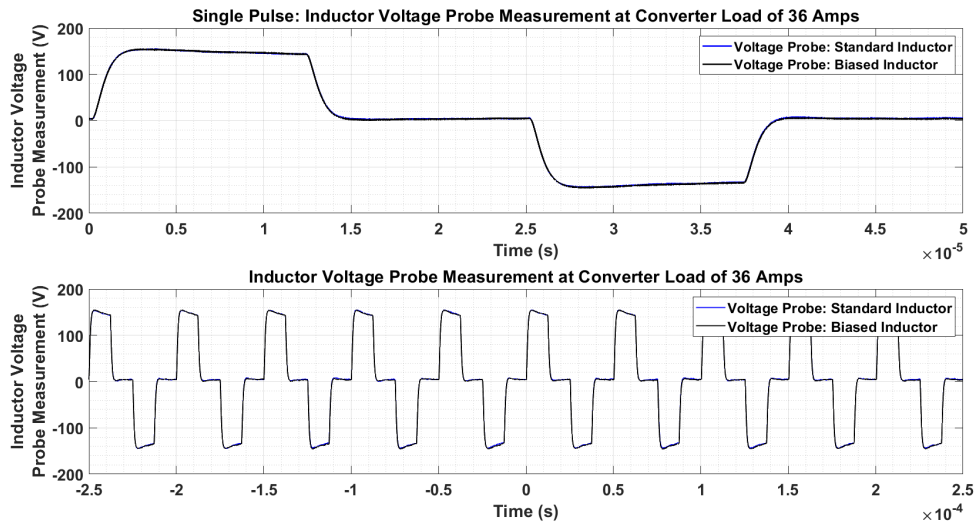


Figure I.18: Inductor Voltage Probe Measurement at Converter Load of 36A

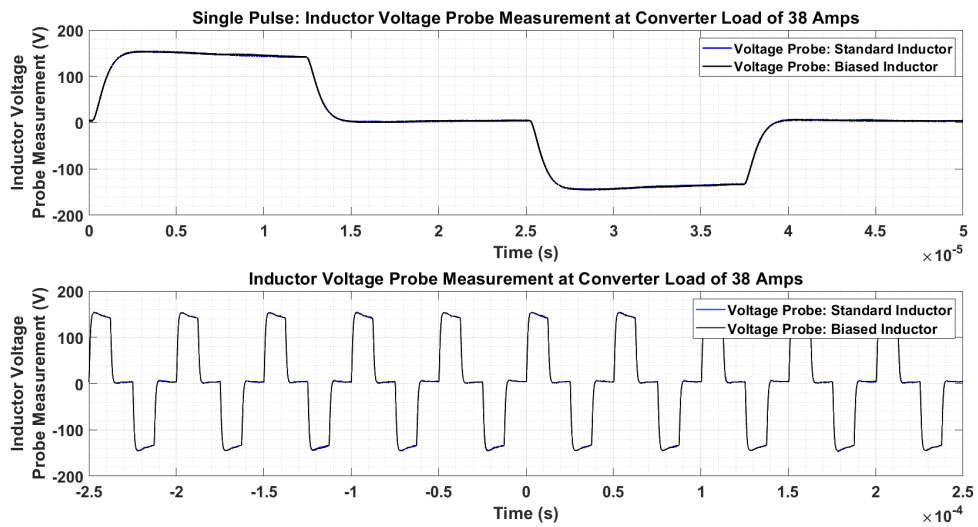


Figure I.19: Inductor Voltage Probe Measurement at Converter Load of 38A

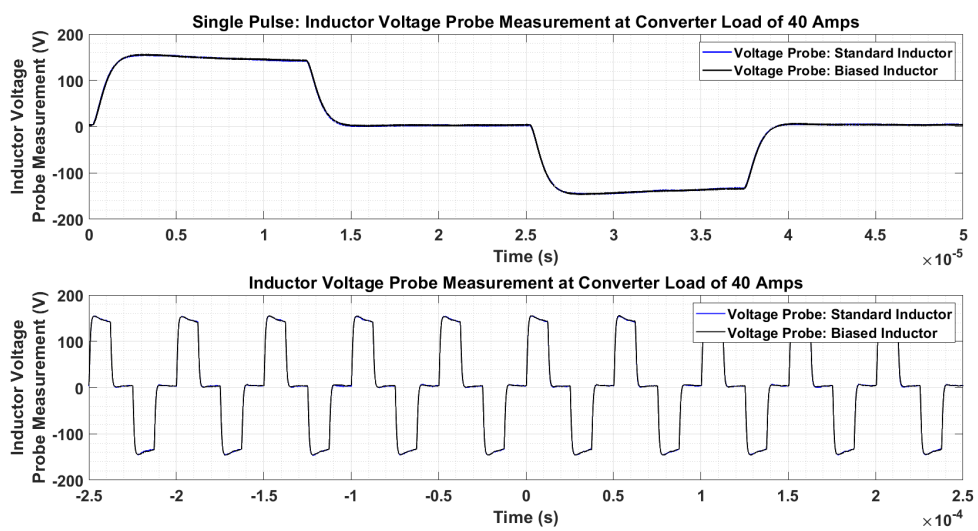


Figure I.20: Inductor Voltage Probe Measurement at Converter Load of 40A

# Appendix J

## Magnetising Current Waveforms

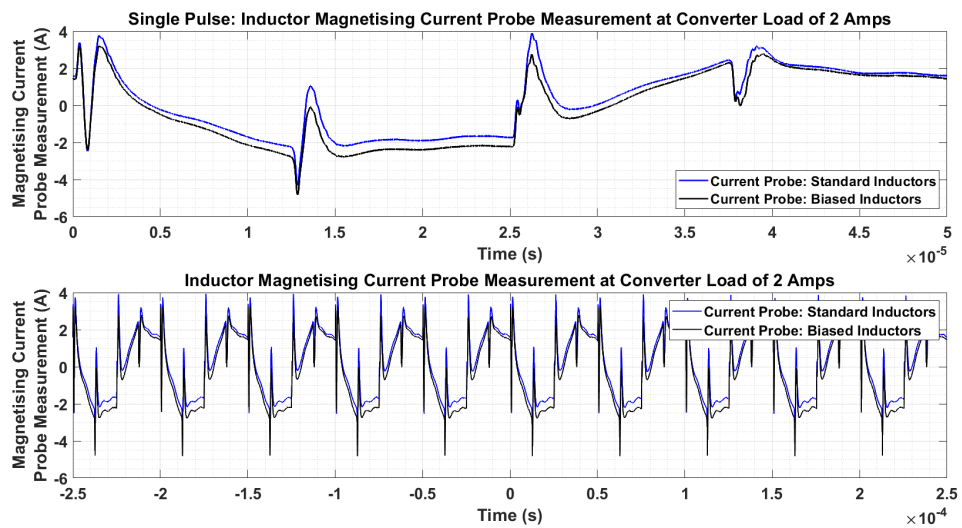


Figure J.1: Inductor Magnetising Current Probe Measurement at Converter Load of 2A

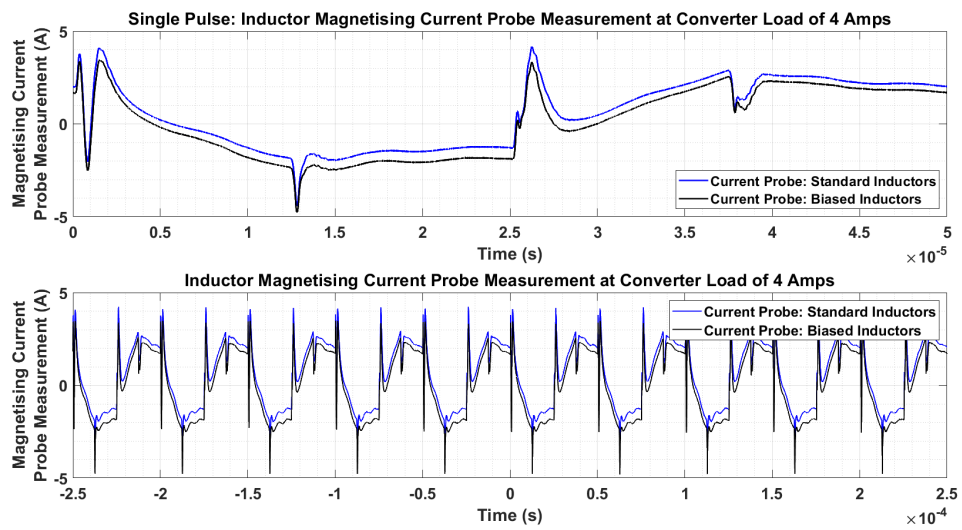


Figure J.2: Inductor Magnetising Current Probe Measurement at Converter Load of 4A

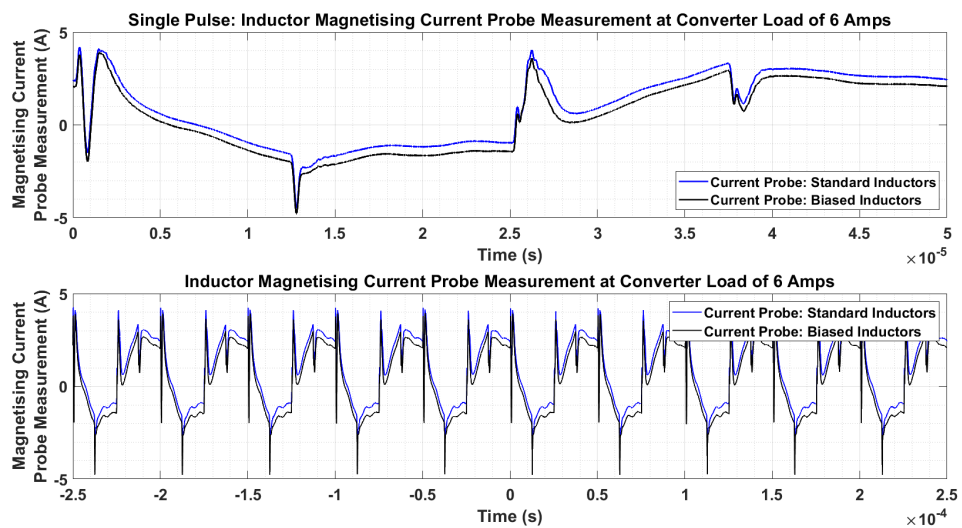


Figure J.3: Inductor Magnetising Current Probe Measurement at Converter Load of 6A

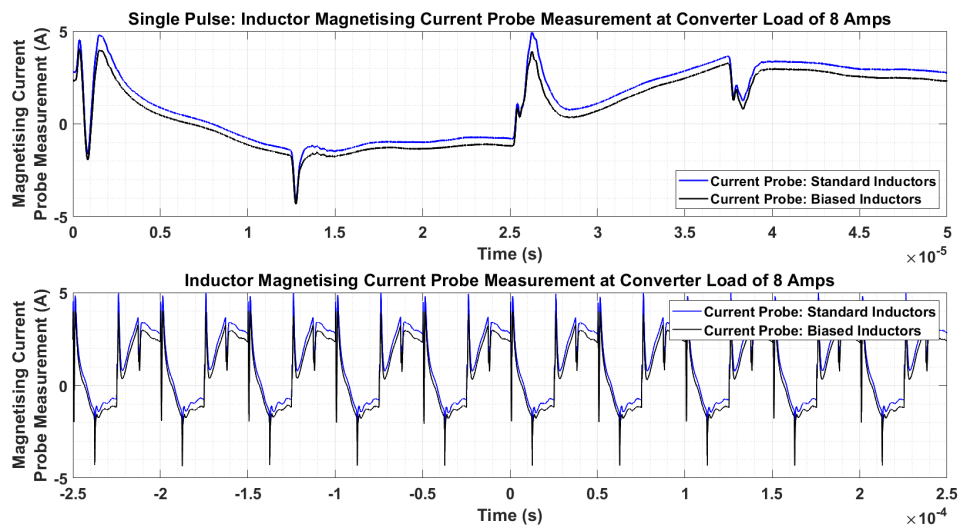


Figure J.4: Inductor Magnetising Current Probe Measurement at Converter Load of 8A

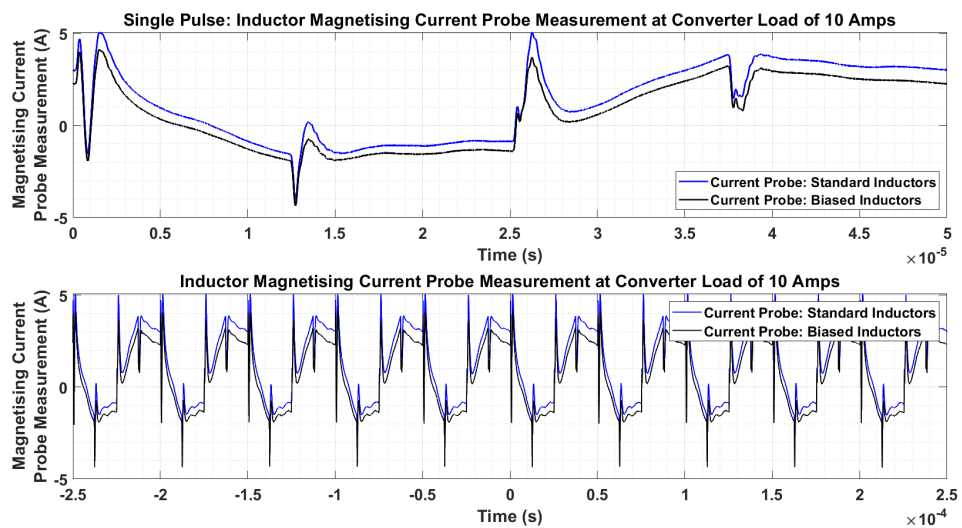


Figure J.5: Inductor Magnetising Current Probe Measurement at Converter Load of 10A

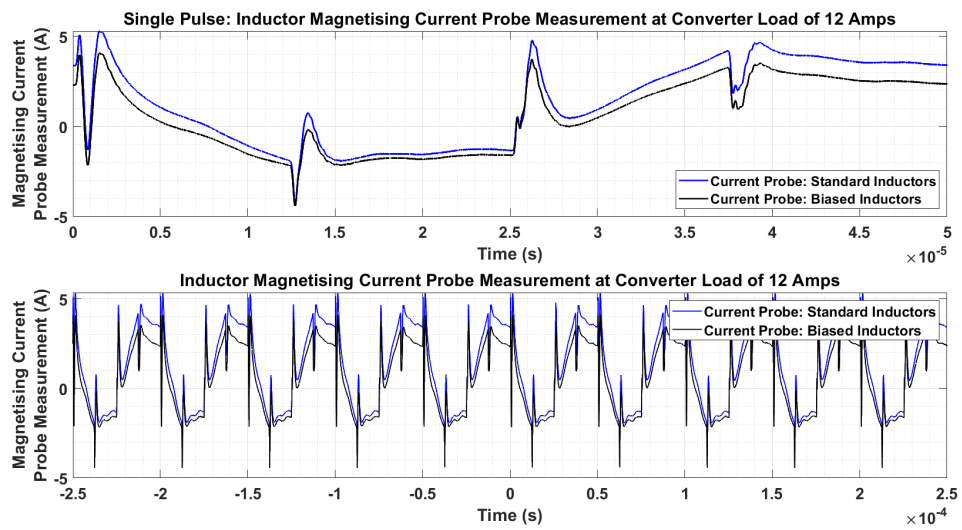


Figure J.6: Inductor Magnetising Current Probe Measurement at Converter Load of 12A

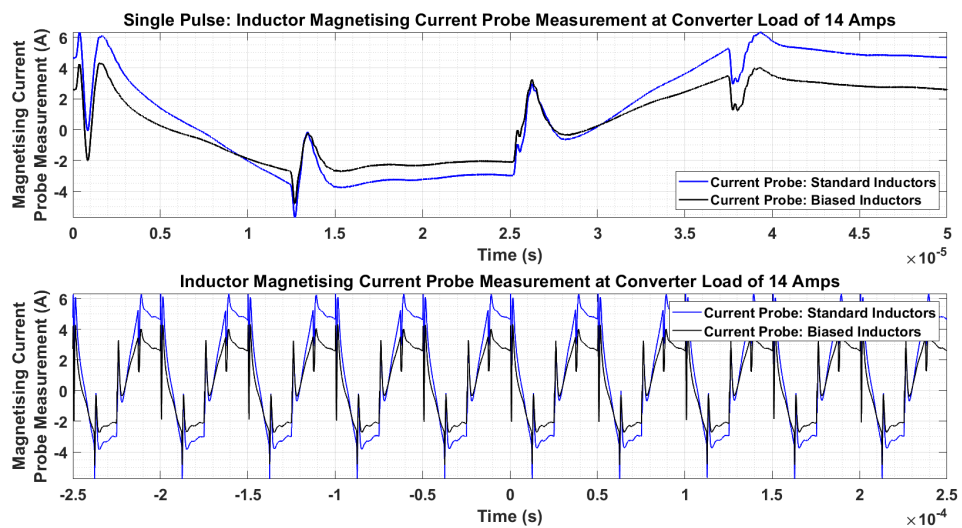


Figure J.7: Inductor Magnetising Current Probe Measurement at Converter Load of 14A

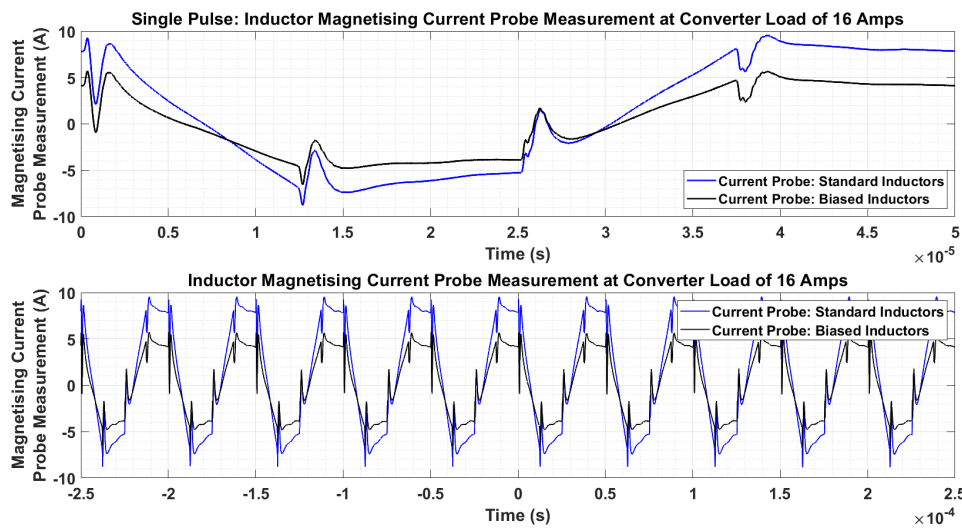


Figure J.8: Inductor Magnetising Current Probe Measurement at Converter Load of 16A

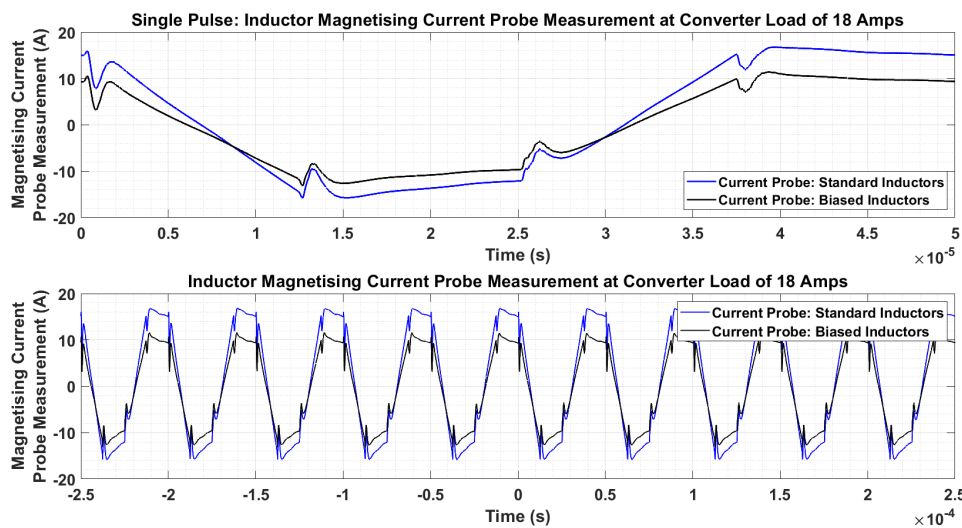


Figure J.9: Inductor Magnetising Current Probe Measurement at Converter Load of 18A

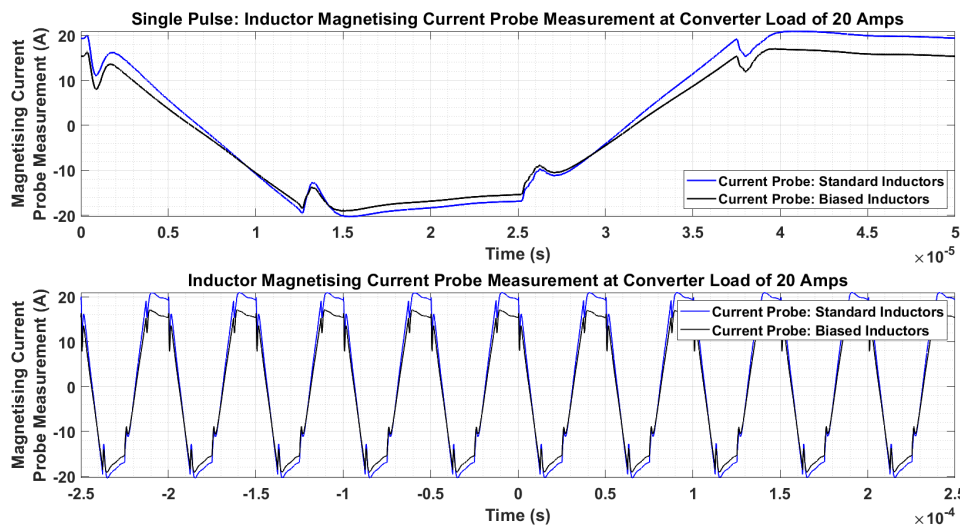


Figure J.10: Inductor Magnetising Current Probe Measurement at Converter Load of 20A

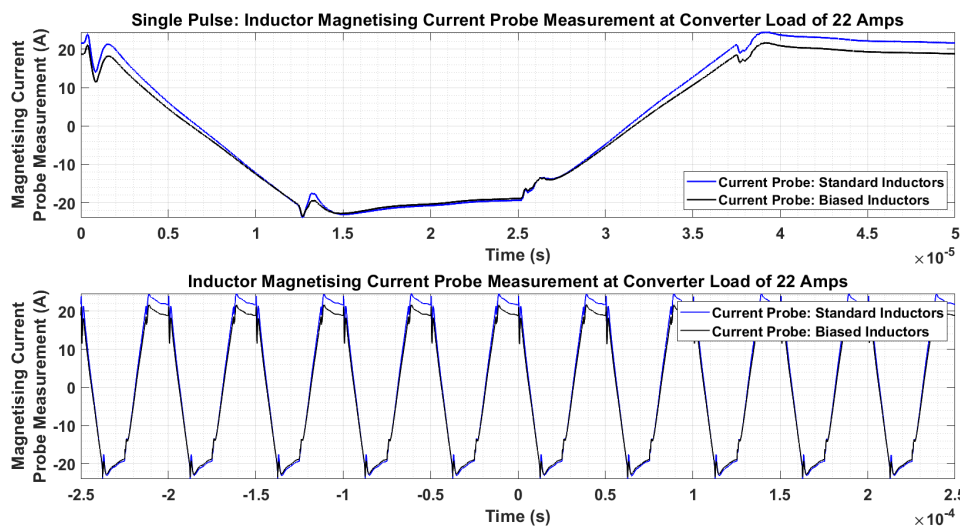


Figure J.11: Inductor Magnetising Current Probe Measurement at Converter Load of 22A

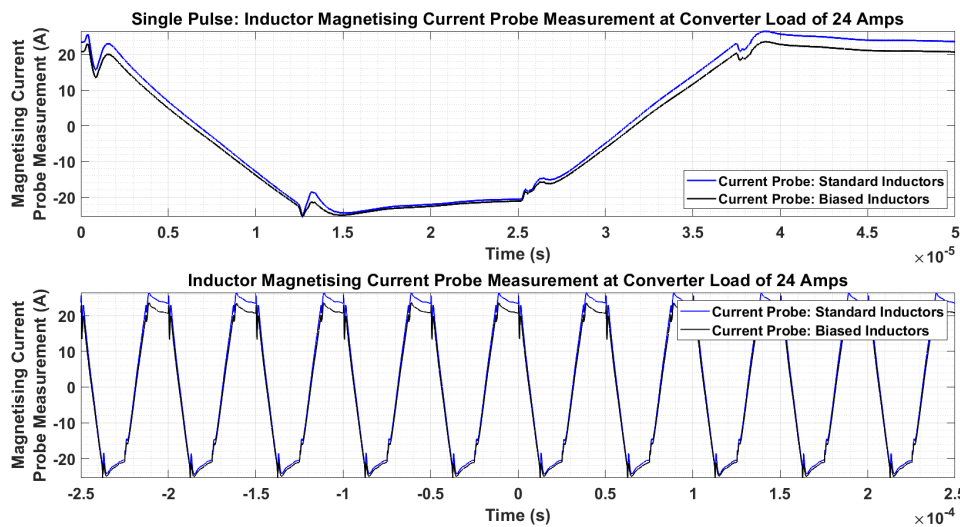


Figure J.12: Inductor Magnetising Current Probe Measurement at Converter Load of 24A

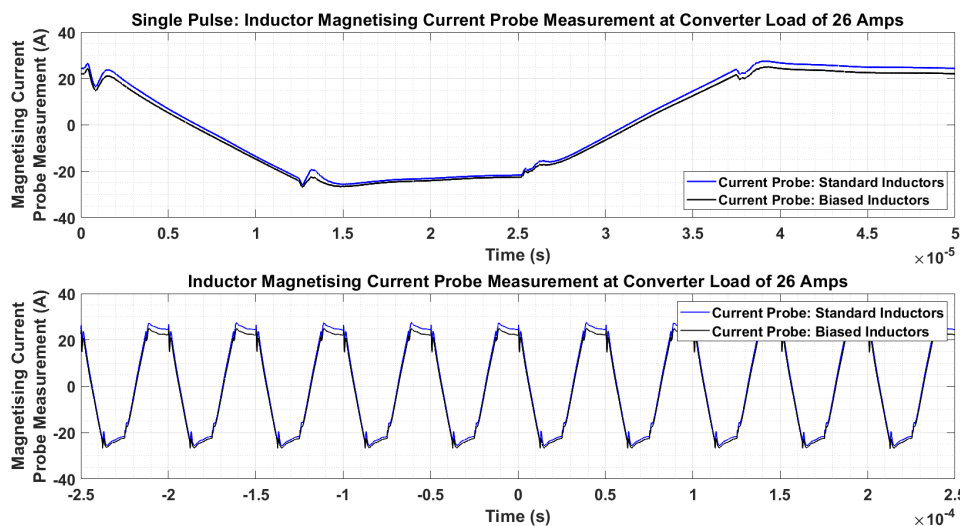


Figure J.13: Inductor Magnetising Current Probe Measurement at Converter Load of 26A

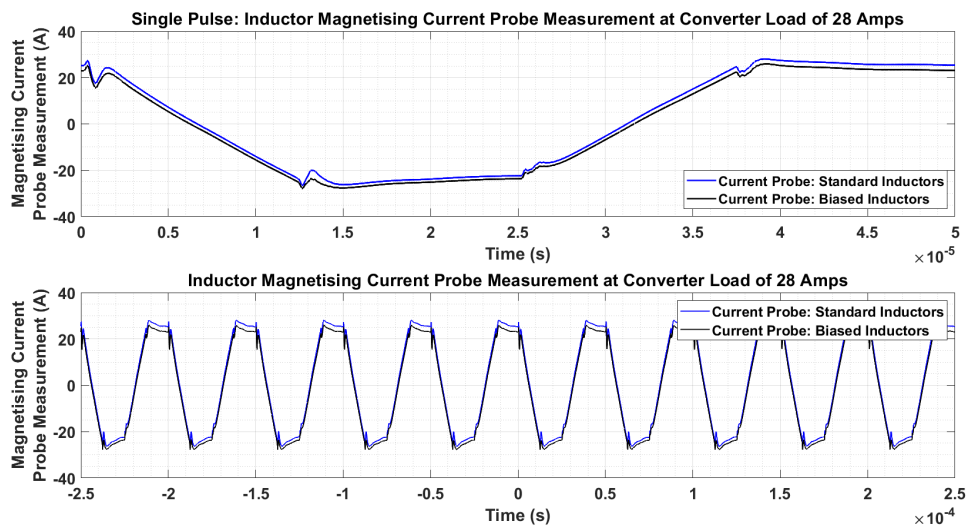


Figure J.14: Inductor Magnetising Current Probe Measurement at Converter Load of 28A

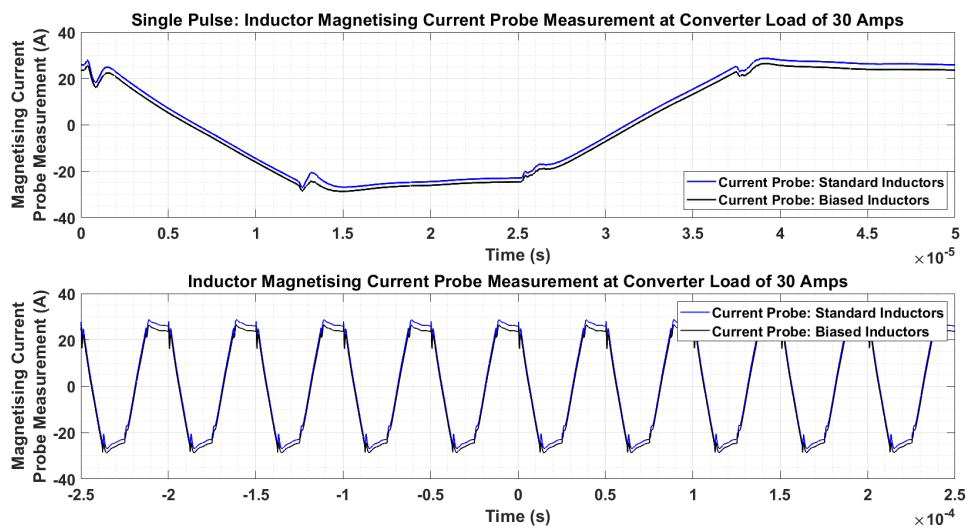


Figure J.15: Inductor Magnetising Current Probe Measurement at Converter Load of 30A

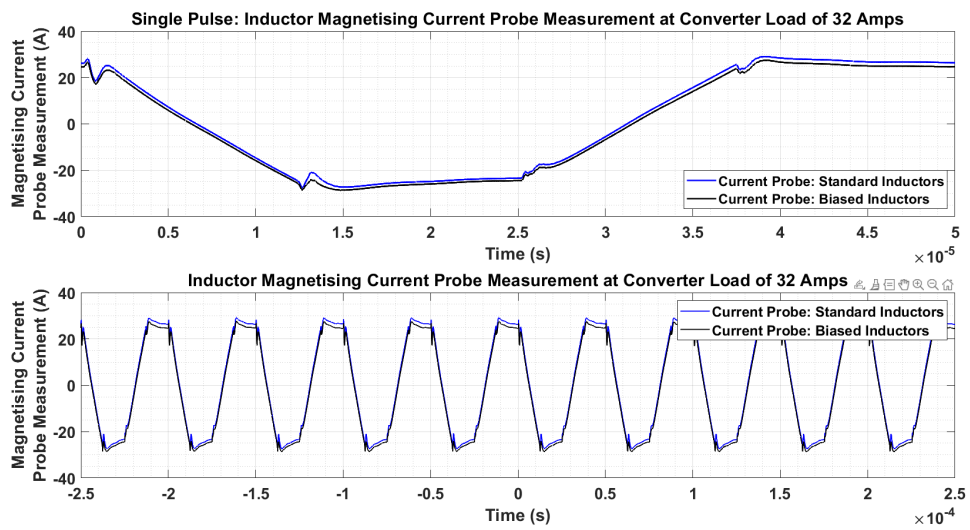


Figure J.16: Inductor Magnetising Current Probe Measurement at Converter Load of 32A

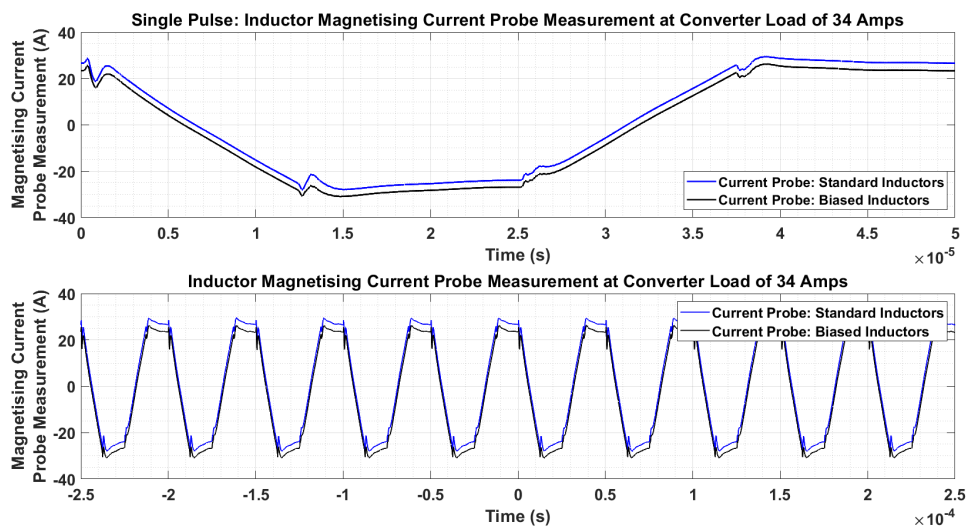


Figure J.17: Inductor Magnetising Current Probe Measurement at Converter Load of 34A

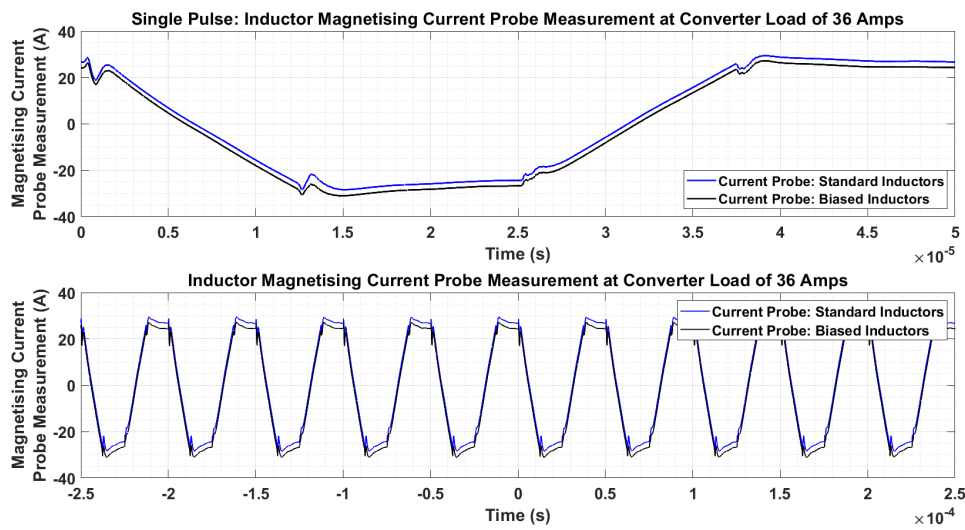


Figure J.18: Inductor Magnetising Current Probe Measurement at Converter Load of 36A

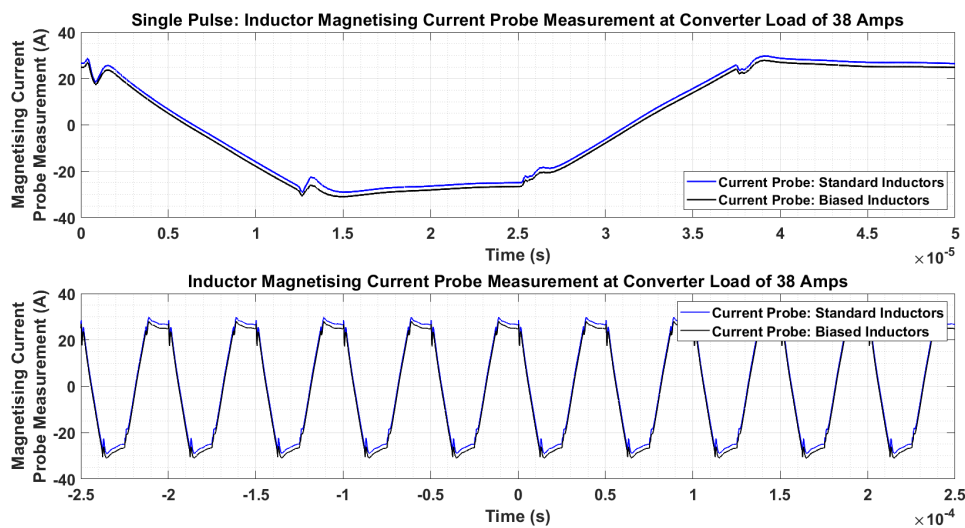


Figure J.19: Inductor Magnetising Current Probe Measurement at Converter Load of 38A

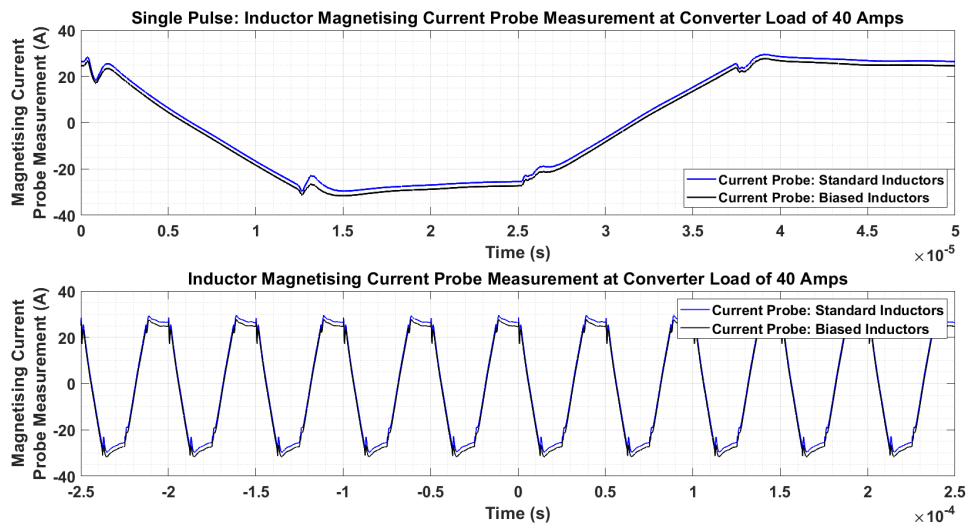


Figure J.20: Inductor Magnetising Current Probe Measurement at Converter Load of 40A